Imperial College London

Charge Transport, Injection and Optical Properties of Fluorene Based Copolymers

Mohammad Yaqub Chaudhary

Department of Physics

Imperial College London

August 2015

Submitted in fulfilment of the requirements of the degree of

Doctor of Philosophy

In the name of Allah, the Beneficent, the Merciful

The work described in this thesis was undertaken within the Centre for Plastic Electronics and the Experimental Solid State Physics group in the Department of Physics at Imperial College London from October 2011 to July 2015 under the supervision of Professor Donal Bradley and with EPSRC funding.

The work presented herein has been conducted by the author except where specific reference is made to the contributions of others.

Abstract

In this work we investigate the charge transport, injection and optical properties of several series of fluorene based copolymers. These properties are key areas for polymer semiconductor research studies that are intended to address the challenges of achieving electrically pumped polymer lasing.

In general, high charge carrier mobility and luminescence efficiency have been found to be mutually exclusive, however, optimising both together, as well as demonstrating high optical gain will be a significant step to offset losses associated with the mechanisms for lasing. A further requirement is that it is necessary to achieve efficient charge injection in the particular materials that are found to have both of these properties optimised.

We concentrate our investigation on fluorene-based copolymers, which have been amongst the earliest classes of materials of interest for polymer lasers (including studies in optically pumped polymer lasers), and since it has previously been shown that high hole mobility and luminescence efficiency may be achieved in fluorene based copolymers with simple alterations to side chain configurations. However, ohmic hole injection into poly(9,9-dioctylfluorene) (PFO) has been difficult to achieve because of its deep-lying highest occupied molecular orbital (HOMO) level of ~5.8eV below the vacuum level.

Therefore, in our first experimental study, we revisit the charge transport properties of PFO based on recent developments in the use of transition metal oxides as hole injecting electrodes. With the ability to achieve ohmic injection in PFO, we are able to use Dark Injection Space Charge Limited Current (DI-SCLC) and field effect transistor (FET) techniques, both of which require ohmic injecton for charge transport measurements, and make comparisons with measurements from Time-of-Flight (ToF) photocurrent experiments. Together, these techniques span several orders of magnitude in charge carrier density, which provides an additional perspective on charge transport and the presence of charge traps.

The subsequent chapters introduce three series of fluorene-based copolymers. The first series of blue emitting polymers has a resemblance to familiar fluorene based polymers with hexyloxyphenyl substituents instead of linear alkyl side chains and the series contains copolymers with a phenoxazine (BPPX) unit derived from more familiar triarylamine structures. Optical measurements show these polymers are free of morphologies such as the beta-phase and we obtain a hole mobility of ~10^{-3} cm^2/Vs, photoluminescence quantum efficiency (PLQE) of 65.7% and optical gain of 41cm^{-1} for poly(9,9-di(4-hexyloxyphenyl)fluorene). Transient DI-SCLC measurements are used to show differences in charge trapping behaviour in the series.

The final chapter of experimental results is based on novel poly(indenofluorene-fluorene) and poly(indenopyrazine-fluorene) copolymers. In the poly(indenofluorene-fluorene) series we consider the role of increased backbone rigidity compared to polyfluorene and the variation of side chain length and structure on charge transport and optical properties. Copolymers in this series yield a time-of-flight hole mobility of ~10^{-2} cm^2/Vs, PLQE of 61.5% and optical gain of 43cm^{-1}. Finally, we show that optical gain is possible in the indenopyrazine-fluorene series, which has been designed with the aim of achieving balanced electron and hole mobility.

Acknowledgements

All praise is due to Allah, the Exalted, and salutations on his Messenger, Muhammad, the best of creation, and on his family and companions.

After gratitude to Allah for all subtle and manifest blessings, I gratefully acknowledge many individuals for their contributions, assistance and advice. I am particularly grateful to Prof. Donal Bradley, under whose supervision this research has been conducted by providing invaluable guidance, lucid explanations that clarified my understanding of polymer physics, enlightening discussions and highly detailed comments on all pieces of work.

This research would not have been possible without the indenofluorene copolymers synthesised by Dr. Shahid Ashraf and Dr. Bob Schroeder in the group of Prof. Iain McCulloch, the indenopyrazine copolymers synthesised by Dr. George Barnes in the group of Prof. Martin Heeney and the blue polymers synthesised by the Sumitomo Chemical Company.

I greatly thank Dr. Sam Foster for enjoyable and thorough introductions to the laboratory and experimental techniques for time-of-flight measurements, and Dr. Colin Belton and Dr. Cora Cheung for their introductions to optical measurement techniques. I have also been greatly assisted by being able to draw on the expertise and sophisticated approach towards organic field-effect transistor fabrication preparation and testing of Dr. Jeremy Smith and Dr. Hendrik Faber in the lab of Prof. Thomas Anthopolous.

I am grateful to Dr. Paul Stavrinou and Dr. Xuhua Wang for the great benefits of their advice and I thank all of the individuals who ensured the activities peripheral to this research project have run smoothly, in particular, CPE programme manager Dr. Sophie Armstrong-Brown and Lisa Cheung, and Carolyn, Bhavna and Juraci in the EXSS group office.

I must finally acknowledge the most important individuals who have played a role outside the research environment, namely my mother, Nasreen, and father, Ahmed, then my siblings and, more recently, the Ali family who I have joined via their daughter during the production of this thesis.

CONTENTS

List of Figures

CHAPTER 1

1 INTRODUCTION

The field of plastic and organic electronic materials has gathered a tremendous amount of interest with a range of devices demonstrating exceptional characteristics such as organic light emitting diodes (OLEDs), polymer solar cells with efficiencies over 10% (You *et al.* 2013) and organic field effect transistors (OFETs). However, the electrically pumped polymer laser remains undiscovered, despite research interest since the earliest days of plastic electronics.

The state of plastic electronics has been advancing rapidly in academia. For example, OFET mobilities have risen from $\sim 10^{-5}\ cm^2/Vs$ in the first OFETs based on polythiophenes (Tsumura *et al.* 1986) to being comparable to their amorphous silicon thin-film transistor counterparts in 2006 with mobilities of up to 0.6 cm^2/Vs (McCulloch *et al.* 2006). They now reach mobilities as high as 10 cm^2/Vs and 40 cm^2/Vs in solution processed polymers (Li *et al.* 2012) and organic single crystal FETs, respectively (Hasegawa & Takeya 2009; Lezama & Morpurgo 2013).

Organic electronic technology has had tremendous commercial success as illustrated by its integration in widespread devices such as the small molecule OLED displays in the smartphones of major manufacturers. Organic electronics are transforming the functionality of digital devices and creating new environments of interaction by the commercialisation of entirely new consumer device classes such as recent devices with curved-edge displays, smart-watches, smart-eyewear, transparent and foldable large area displays and virtual reality headsets, all of which have been made possible by organic electronic technology.

Thus, organic semiconductor technology has resulted in ubiquitous devices that have moulded into human activities and mould new lifestyles. From the industrial perspective, they present the possibility of low intensity manufacturing to produce energy efficient, recyclable, lightweight and flexible devices, which may be fabricated by a wide range of techniques from solution deposition to roll-to-roll printing in a manner that is mechanically flexible and robust. The materials themselves offer the possibility of self-assembling microstructures and a very broad range of tuning optoelectronic properties for particular applications at low costs of materials and substrates.

Yet a device class that is conspicuously absent is the electrically pumped polymer laser, despite the robust state of the technology. Since the first demonstration of a coherent light source in the form of a solid state ruby LASER by Maiman in 1960 (Maiman 1960), the applications of lasers have been in every field, from communications, medicine, industry, spectroscopy, and semiconductor development itself.

Organic dye lasers have been the most significant class of lasers operating in the UV region with applications in optical lithography and data storage where shorter wavelengths are desired to reduce the diffraction limit to probe smaller features. Whilst Blu-ray discs are becoming deprecated as a storage medium for home users in favour of network-based delivery, the largest data centres are embracing the technology to store petabytes of data on optical discs to be retrieved robotically.

Organic semiconductors have drawn significant attention from researchers as a potential alternative class of materials in which solid state lasing may be realised. Several years after electroluminescence was demonstrated in the conjugated polymer, poly(p-phenylenevinylene) [PPV], by Burroughes et al. (1990) there have been numerous demonstrations of the lasing ability of plastic electronic materials by optical pumping, beginning with the demonstration of lasers using conjugated polymers in solution in 1992 (Moses 1992). This led to the development of a 545 nm laser based on solid films of poly(p-phenylenevinylene) (PPV) in a microcavity (Tessler *et al.* 1996) and shortly after, at 392 nm (Berggren *et al.* 1997).

Since then optically pumped lasers have been demonstrated extensively using a variety of materials and device structures. However, the challenges towards achieving electrically pumped polymer lasing lie in several key areas. Firstly, from fundamental physical phenomena, such as, exciton quenching and the yield of non-radiative triplet excitons by electrical injection of hole and electrons. Secondly, from research into novel polymer structures with high charge carrier mobility, luminescence efficiency and optical gain to offset losses. Thirdly, it will be necessary to inject sufficient charge carriers into these materials to reach the lasing threshold exciton density and finally, the material and electrodes must be incorporated into a suitable device structure to provide the necessary optical feedback and minimise losses at the electrodes.

Technologies such as organic light emitting transistors have emerged as researchers sought to achieve electrically pumped polymer lasing. These devices allow high charge current densities, control over electron and hole mobility and charge recombination amongst other novel features, which make them potential precursor devices towards electrically pumped polymer lasers.

One may ask why attempt to research new technologies for lasers when there are already numerous technologies available for lasing and thousands of types of laser. A key reason is that semiconductor lasers are particularly desirable for operational versatility in numerous applications, yet there are significant gaps in electrically driven inorganic semiconductor lasers in the 450 to 570 nm region of blue to green. In fact, this technology is itself quite recent and we note that blue light emitting diodes based on inorganic semiconductors were only demonstrated for the first time in the early 1990s and blue laser emission based on the same GaN technology was demonstrated in 1995 to 1996. The significance of these discoveries was recognised recently in the 2014 Nobel Prize in Physics.

One may then query why research attention should be given to plastic electronic materials for lasing. The reason for this is that plastic electronic materials exhibit a range of highly desirable intrinsic properties that make them worthy research materials for lasing, such as the fact that they are four-level systems. We note that at the same time as the aforementioned inorganic blue emitting semiconductors, was the introduction of blue light emitting polyfluorene in 1993 in plastic electronics.

From the challenges toward electrically pumped polymer lasing, we take the view in this thesis, that the most important areas for research are the properties of the materials themselves and efficient charge injection. Hence, the focus of this thesis is to develop a better understanding of fluorene based copolymer materials in particular in terms of their charge injection, transport and optical properties.

The main requirements, with respect to materials, for the realisation of electrically pumped lasing are simultaneously high charge carrier mobility and luminescence efficiency so that sufficient charge can be injected to reach the lasing threshold density of excitons (Yap *et al.* 2008). However, high mobility has generally been achieved where there is a good alignment of π-electron systems and close contact between neighbouring chains in a film, which thus improves interchain interactions and therefore charge transport, yet this leads to more rapid energy transfer that may quench luminescence (Cornil *et al.* 2001). Consequently, there appears to have been two divergent trends in the development of polymers, one yielding high luminescence efficiency and the other favouring high charge-carrier mobility. A key motivation for this work has been the demonstration of high charge carrier mobility and luminescence efficiency in fluorene based co-polymers by Bradley and co-workers (Yap *et al.* 2008), discussed in detail in the following chapter.

Following an overview of the background theory covering the basis of the semiconducting properties of plastic electronic materials, charge transport, charge injection and organic laser physics, the experimental results in this thesis begin with a charge injection study of polyfluorene using MoO_3 as the injection interlayer. Proceeding from this, the later chapters are arranged according to the various classes of fluorene based copolymers. The first series has been synthesised by Sumitomo Chemical and bears a resemblance to familiar fluorene and triarylamine based polymers. The final chapter of experimental results is based on novel indenofluorene-fluorene and indenopyrazine-fluorene copolymers that have been synthesised at Imperial College London by the McCulloch and Heeney groups, respectively.

CHAPTER 2

2 THEORY

2.1 π-Conjugated Organic Plastic Electronic Materials

At the time of the production of this thesis, the underlying physics and theoretical principles behind plastic electronic materials are generally well developed and documented widely in numerous reviews in the literature and book publications. In this section, we draw together and highlight the particular and most essential aspects of π-conjugated plastic electronic materials that comprise the necessary knowledge and understanding that are required for the work presented in this thesis.

The particular category of plastic electronic materials of interest here are polymeric materials rather than small molecules and may be referred to as organic π-conjugated polymer semiconductors. They are referred to as organic molecules because carbon is the dominant atom and π-conjugated due to the delocalisation of electrons arising from the overlap of carbon p_z-orbitals. The materials we are interested in are polymers formed of chains comprising a large number of repeated monomer units in distinction to conjugated small molecules or oligomers, which are formed of a single, or a small number of repeated, units, respectively.

The polymer itself may comprise of only one type of monomer such that it is known as a homopolymer or a combination of two or more different repeat units, yielding a copolymer (Fig. 2.1). This combination of different repeated monomers in a copolymer may be according to several patterns of repetition, namely alternating, block or statistical. The incorporation of different functional groups and substituent groups on the polymer backbone allows for an almost unlimited number of possibilities in tuning the properties of these materials, which has been the reason for widespread interest as researchers have explored different material configurations to target specific device applications.

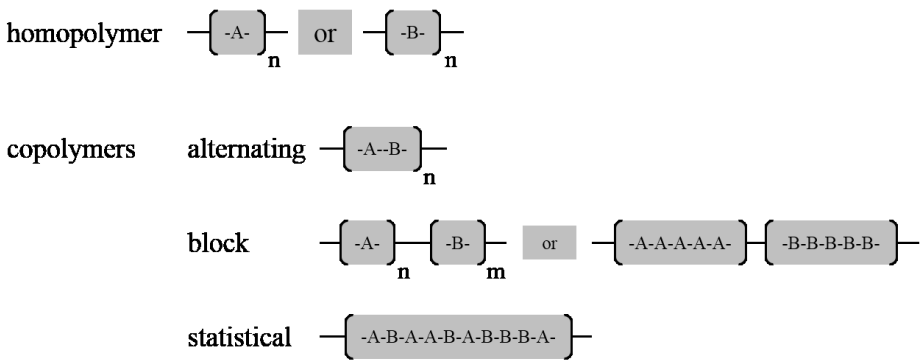

Fig. 2.1 Illustration of different polymer configurations showing the repeated units of homopolymers, and alternating, block and statistical copolymers.

The optical and electronic properties of π-conjugated organic plastic electronics materials are based on carbon chemistry, orbital hybridisation and conjugation. The most common isotope of carbon is carbon-12, which has an electronic configuration of $1s^2 2s^2 2p^2$. The two electrons of carbon in the 1s orbital are strongly bonded to its nucleus and thus not involved in bonding. However, the 2s and 2p orbitals can hybridise to allow the formation of three distinct bonding configurations. Such bond formation is energetically favourable despite the energy required in the promotion of the 2s electrons involved in hybridisation of the orbitals.

Hybridisation that involves the 2s and all of the 2p orbitals and results in the formation of four single bonds is known as sp^3 hybridisation. However, sp^2 and sp hybridisation, in particular, are operative in giving rise to the semiconducting properties of plastic electronic materials and hence will be described in more detail here.

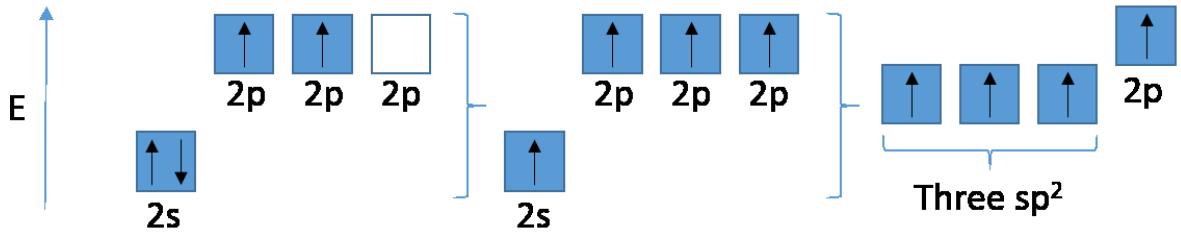

Fig. 2.2 Illustration of sp^2 hybridisation of a carbon atom in which one 2s electron is promoted into an empty p_z orbital

In sp^2 hybridisation, one 2s electron is promoted to the empty p_z orbital (Fig. 2.2) and hybrid orbitals are formed with the 2s, $2p_x$ and $2p_y$ orbitals, and named sp^2 orbitals. These sp^2 orbitals lie in plane and are separated by 120 degrees.

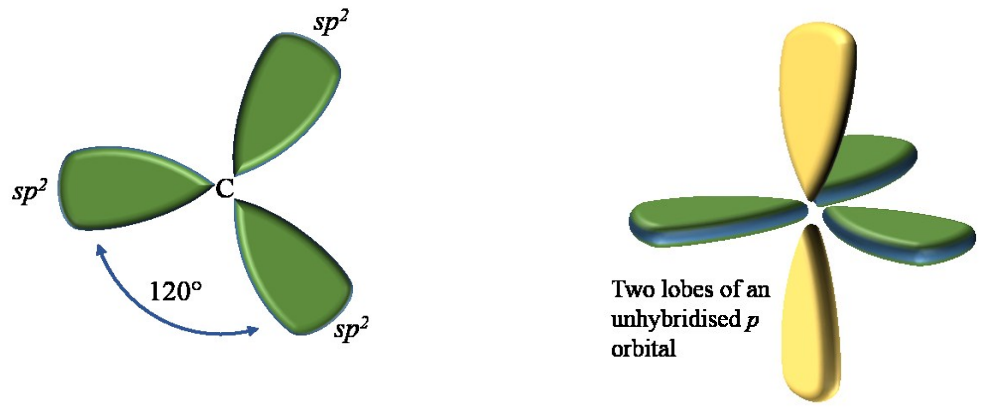

Fig. 2.3 Hybrid sp^2 orbitals lying in plane at separated by 120° (left) and the lobes of a un-hybridised p_z lying out of plane (right).

The remaining un-hybridised $2p_z$ orbital lies perpendicular to the plane of the three sp^2 hybridised orbitals (Fig. 2.3). When the sp^2 orbitals of two carbon atoms intersect to share an sp^2 electron a σ-bond is formed. This also causes the p_z orbitals to overlap above and below the molecule, forming a delocalised orbital known as a π-bond.

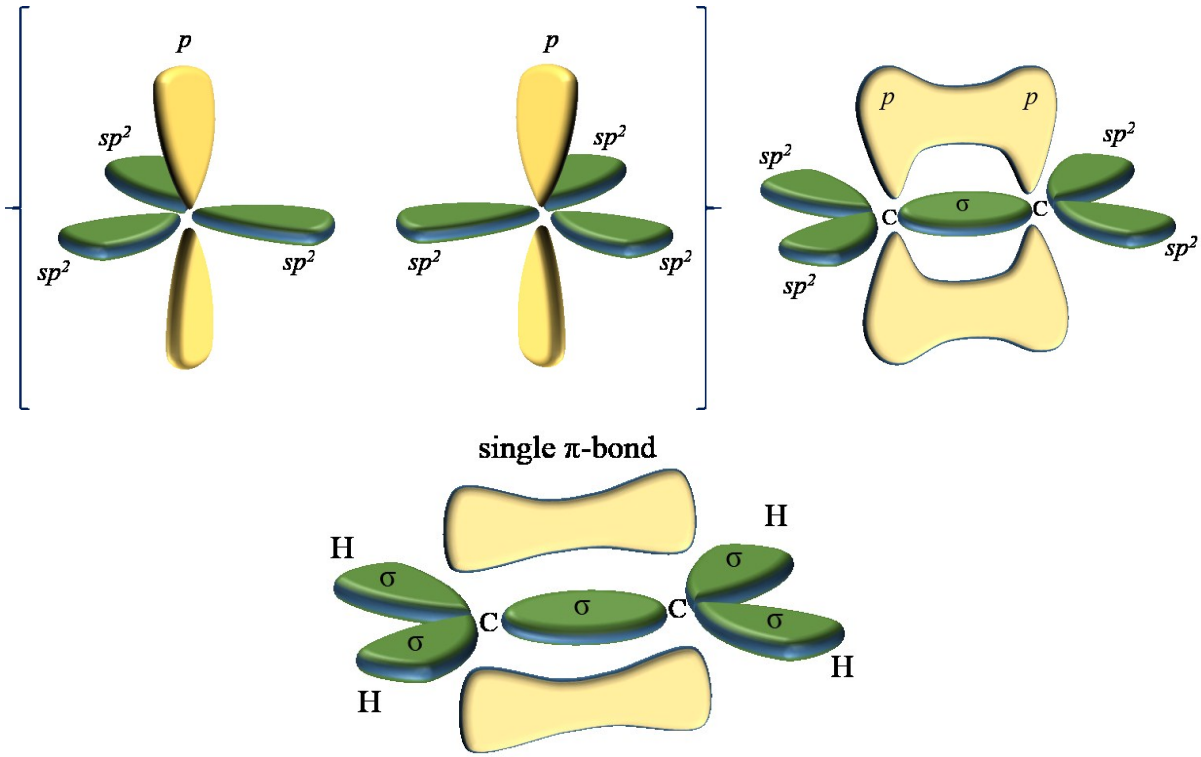

Fig. 2.4 Illustration of the overlap of p_z electrons of two molecules forming a delocalised orbital above and below the molecule (π-bond) (top) and an illustration of a double bond in which unfilled sp^2 orbitals form σ-bonds with hydrogen (bottom).

Thus, a double bond of one σ-bond and π-bond is established between the two carbon atoms (Fig. 2.4) where the electrons of the σ-bond are highly localised whereas the delocalised nature of the electrons in the case of the π-bond are the basis of the semiconducting properties of conjugated polymers.

These semiconducting properties are understood by considering the overlap of electron wavefunctions arising in these bonds and their occurrence in phase, known as bonding orbitals, and out of phase, known as anti-bonding orbitals, which are denoted by an asterisk. The bonding orbitals are more stable because of a high electron density between the atomic nuclei.

In the case of polymers with single bonds based on sp^3 hybridisation, the energy separation of their sigma and sigma* orbitals is larger than the ionisation potential, such that polymers with such single bonds are insulating.

In a conjugated system of n repeat units, the molecular orbitals are approximated with n linear combinations of p_z atomic orbitals based on the Hückel approximation. In such a system, the π and π^* orbitals may be considered to be a standing wave such that the orbital energy increases in accordance with the number of nodes. Hence, the discrete energy levels become continuous where n is very large. However, semiconducting properties are induced by Peierls distortion, which is a structural distortion that lowers the energy of the filled electron states and pushes up the energy of the empty states. This results in an energy gap.

We may now consider the case of the benzene ring in which six carbon atoms are joined in a ring and bonded in plane by sp^2 σ-bonds, which prevent dissociation of the molecule. The six un-hybridised $2p_z$ orbitals of each carbon within the ring lie out of plane from that ring and overlap with each other to form a system of delocalised electrons above and below the molecular plane. In these bonds, six electrons are shared in total to form three π and three π^* orbitals with different energies.

The two orbitals of interest are the highest occupied molecular orbital (HOMO) and the lowest unoccupied molecular orbital (LUMO). The HOMO has an ionisation energy, which is the energy required to remove an electron from the HOMO and the LUMO has a particular energy required to add an electron to it known as its electron affinity.

Adding or removing a charge from a molecule results in the redistribution of charge to minimise the energy of the system. This change is manifested in variation of bond length, bond angles and nuclear positions. Together the charge and the change in the molecular lattice are known as a polaron and as the energy of the system is reduced, they result in energy levels between the HOMO and LUMO energies.

Polarons may exists as either electron or hole polarons (Fig. 2.5), which may combine to form an exciton. The bound electron and hole of an exciton are bound by an energy known as the exciton binding energy, which is also the energy required to separate the bound pair into free charges.

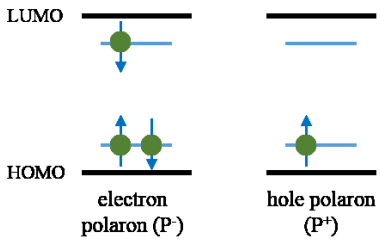

Fig. 2.5 Electron and hole polarons showing new energy levels within the HOMO-LUMO gap. The spin of the upper electron in the electron polaron may be up or down and the polarons may combine to form a singlet exciton (as depicted) or a triplet exciton.

The charge carrier species in plastic electronic materials are thus polaronic in nature, that is, they are both an electron or hole combined with a molecular distortion.

Electrical injection of charge carriers generates polarons directly, whereas optical excitation leads to a geminate pair of an electron polaron and a hole polaron with strong coulombic attraction between them, that is, an exciton. The presence of an exciton leads to a change in molecular geometry to reach the lowest energy state and the electron-hole pair has a wavefunction extending over conjugated segments of several repeat units.

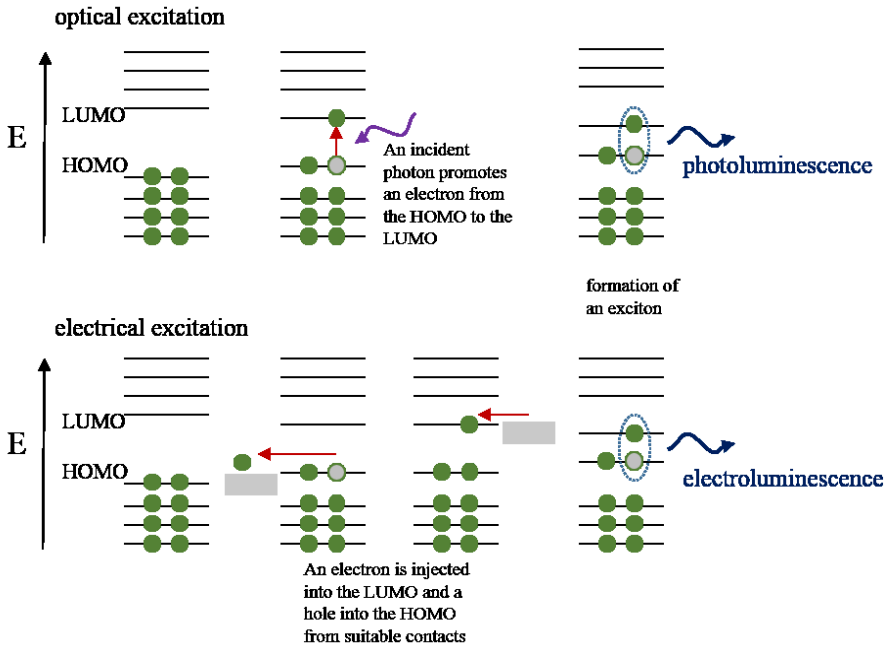

Fig. 2.6 Illustration of the different mechanisms involved in optical and electrical excitation. In optical excitation, an incident photon promotes an electron from the HOMO to the LUMO to form an exciton and causes photoluminescence. In electrical excitation, an electron is injected into the LUMO and a hole into the HOMO and results in electroluminescence.

In the case of optical excitation, a photon with sufficient energy promotes an electron from the HOMO to the LUMO. In the case of electrical injection, an electron is injected into the LUMO and a

hole into the HOMO (Fig. 2.6), which has significant consequences based on the spin statistics of the injected electrons and holes.

The excitons in organic semiconductors are Frenkel excitons, which are characterised by being tightly bound, that is confined to one polymer chain and highly localised, as opposed to Mott-Wannier excitons that primarily occur in inorganic semiconductors, which typically have a large separation between the electron and hole and a lower binding energy.

The wavefunction of an exciton may spread over several units where there are no breaks or defects in the polymer conjugation. However, in shorter chains or segments of conjugation, the electron-hole pair of the exciton is more closely confined and this additional energy, beyond the equilibrium energy of their separation, increases the energy gap. Hence, disorder in conjugated polymers that results in different segments of conjugation hinders the delocalisation of exciton wavefunctions, resulting in different energy gaps in each segment.

This distribution of conjugated segments and energies may be modelled as a Gaussian distribution of states through which rapid energy transfer of an exciton may occur to reach neighbouring sites of lower energy. Such exciton energy transfer, or exciton diffusion, occurs between absorption and emission in plastic electronic materials, which results in different features visible in the spectra for absorption and emission.

The combination of an electron polaron and hole polaron may form an exciton. However, depending on the spin configuration of the polarons, one of two types of exciton may be formed known as singlet (Fig. 2.7) and triplet excitons (Fig. 2.8).

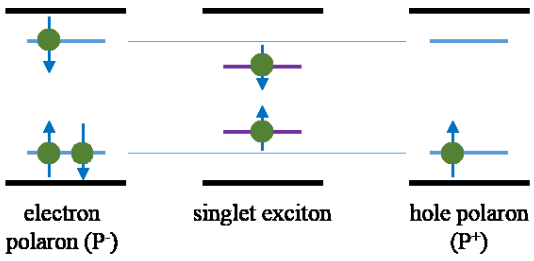

Fig. 2.7 Illustration of the formation of a singlet exciton from electron and hole polarons.

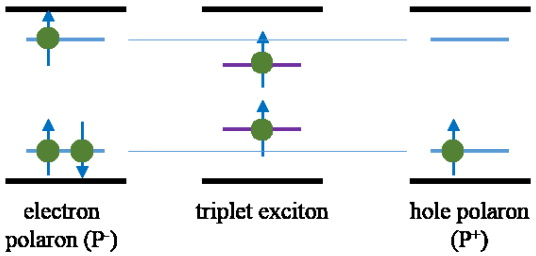

Fig. 2.8 Illustration of the formation of a triplet exciton from electron and hole polarons.

The total electronic spin, S, of an exciton may be either 0, in which case it is a singlet or 1, in which case it is a triplet. The spin wavefunction of the singlet exciton is anti-symmetric and symmetric in the case of the triplet.

As required by the Pauli Exclusion Principle, the spin wavefunction must have opposite symmetry to the spatial wavefunction. Hence, if we consider the confining potential of two atoms, the anti-symmetric spatial wavefunctions of triplets has a much smaller overlap between two electrons compared to the overlap of the symmetric spatial wavefunctions of a singlet. This results in less coulomb repulsion between electrons in the case of triplet wavefunctions such that the triplet state is at a lower energy compared to the singlet state by an amount known as the exchange energy (Fig. 2.9). In conjugated polymers, this is estimated to be between 0.3 and 1.0 eV (Köhler & Beljonne 2004).

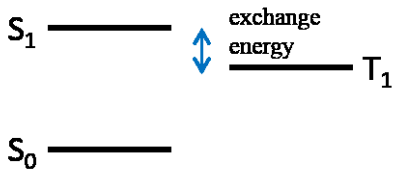

Fig. 2.9 The exchange energy between the first excited singlet and triplet states.

Electronic transitions by absorption and emission may occur between different singlet states in which the spin state is conserved. Whereas, direct optical transitions from singlet states to triplets are forbidden because of the requirement for spin conservation. However, this may be possible by inter-system crossing from a singlet to a triplet level by spin-orbital coupling where the large angular momentum of the electrons of a heavy atom are used to mix the electron spins of singlet and triplet states. The excited 'triplet' may then decay radiatively to the singlet ground state to produce phosphorescence.

In the case of electrical charge injection, triplet excitons are formed directly, which represents one of the most significant loss mechanisms for electrically driven light emission. Electrical excitation requires the injection of a hole into the HOMO level and an electron into the LUMO, which combine

to form an exciton (Fig. 2.10). However, the electrons remaining in the HOMO and electrons injected in the LUMO have a random orientation of spins, which may lead to the formation of either singlet or triplet excitons with a yield of 25% and 75%, respectively, based on random spin statistics.

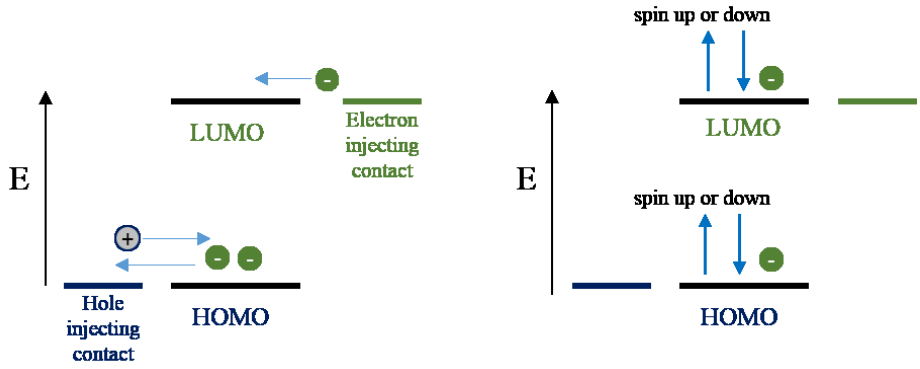

Fig. 2.10 Illustration of random spin orientations from electrical injection leading to formation of singlet or triplet excitons.

After formation, excitons may decay radiatively or non-radiatively, dissociate into free charges or undergo an exciton-exciton annihilation process, which is more likely to occur at high exciton densities.

There are several energy transfer mechanisms by which excitons may migrate to other sites. First, the most basic form of energy transfer is where light emitted by a donor molecule is absorbed by an acceptor molecule by the same process the donor absorbed the initial excitation. There are several factors that may influence the probability of this type of transfer, such as the spectral overlap between the emission of the donor and absorption of the acceptor, coupled with the luminescence quantum efficiency of the donor and absorption coefficient of the acceptor and the relative density of donor and acceptor molecules.

A second energy transfer processes is by dipole-dipole interaction between the donor and acceptor molecules, which is known as Förster Transfer. In this case, excitation of the donor creates an oscillating dipole that induces an oscillating dipole in the acceptor by dipole-dipole interaction. This coupling promotes an electron to an excited state on the acceptor and results in de-excitation of the excited electron of the donor. This is the dominant transfer mechanism for singlet excitons and has a sensitive dependence on the overlap between the donor emission and acceptor absorption spectra and on the relative orientation of the molecules and their separation distance.

Finally, Dexter transfer is the case where energy transfer occurs by a tunnelling process of electron exchange, that is, the excited electron from the donor is transferred to the acceptor while it receives a ground state electron from the acceptor. This requires a significant spatial overlap of the donor and acceptor wavefunctions and is therefore a short range mechanism.

The type of exciton to which we have thus far referred is of an intrachain character in which the electron and hole are localised on one chain segment. In the case of the excitation existing between units on different chains, that is, interchain, or different segments of the same chain and there being no ground state interaction between those segments, the resulting excitation is named an excimer (excited state dimer). In addition, where the interchain or intersegment excitation is shared between two chemically different polymer units, it is known as an exciplex.

2.2 Light Absorption and Emission in Organic Molecules

When considering the nature of light interaction with matter we may adopt one of two ways of describing it. This may be in its form as an electromagnetic wave of wavelength $\lambda = c/\nu$, where c is the speed of light and ν is its frequency, with perpendicular oscillating electric and magnetic fields that may be expressed mathematically in the form of wave equations.

Alternatively, we may adopt the quantum mechanical description of light based on its quantisation in the form of photons. In this case, a molecule in the ground state may absorb a photon that causes a transition between two energy levels, E_2 and E_1, where $E_2 > E_1$, when the photon energy is

$$E = h\nu = E_2 - E_1 = h \times \frac{c}{\lambda}. \qquad 2.1$$

From the macroscopic perspective of an absorbing medium, the Beer-Lambert law is used to analyse the attenuation of light as it passes through the medium, where the absorbed intensity is given by

$$I(\nu) = I_0 \times e^{-\alpha(\nu)\times d} \qquad 2.2$$

where $\alpha(\nu)$ is the absorption coefficient of the medium at frequency ν and d is the thickness of the medium through which the light traverses.

If we assume that the Born-Oppenheimer approximation is valid, that is, the approximation that nuclei remain stationary during an electronic transition since electronic transitions occur much more rapidly than nuclear rearrangement, then we may write the total wavefunction of an organic molecule as the product of electronic, vibrational and rotational wavefunctions. The total energy is then the sum of their energies and the rotational contribution may be ignored because it is generally insignificant in comparison to the electronic and vibrational energies.

The optical transitions may be depicted using a configuration coordinate diagram, on which the potential energy of a state is plotted against a parameter of physical distortion in the polymer, such as a change in bond length. For example, the electronic transitions in an organic molecule are illustrated in the energy level diagram in Fig. 2.11.

The different energy levels correspond to different electron configurations in the molecular orbitals and triplet states are slightly lower than corresponding singlet states because of the exchange energy arising from the lower overlap of electron spatial wavefunctions in the triplet state.

For each singlet and triplet electronic energy level there are a set of vibronic levels associated with the vibrational modes. Electronic transitions from the ground state then follow the Franck-Condon principle, whereby the vibronic level with the largest overlap with the ground state wavefunction will be preferentially occupied. If there were to be no displacement in configuration coordinate between ground and excited state, then only the 0-0 transition would be allowed.

In the process of absorption, the molecule is thus excited from the singlet ground state to an upper singlet state, represented by an S_0 to S_n transition. Absorption occurs simultaneously, without selectivity (other than through wavefunction overlap), to a range of chains with different conjugation lengths, and hence, to different excited states and vibronic energy levels (denoted by the second number in the subscript, i.e. $S_{n,x}$). As a result, the absorption spectrum of an organic molecule is typically broad and undefined as it encompasses transitions to an ensemble of molecules with slightly differing geometries and orientations.

Following absorption to a particular excited state, an exciton relaxes to the lowest vibrational energy level of that state then diffuses by exciton energy transfer to the lowest excited state ($S_{1,0}$) energy level, that is, a neighbouring segment with the longest conjugation, before emission occurs.

Since the exciton is in the lowest energy state, emission is at a lower energy than absorption (i.e. a longer wavelength), which is known as the Stokes shift. Therefore, light is not necessarily emitted from the same polymer segment at which it was absorbed because of the rapid energy transfer arising from exciton diffusion to neighbouring segments at lower energy levels. Thus, emission spectra may display more of the structure of the vibronic energy levels than the generally featureless absorption spectra.

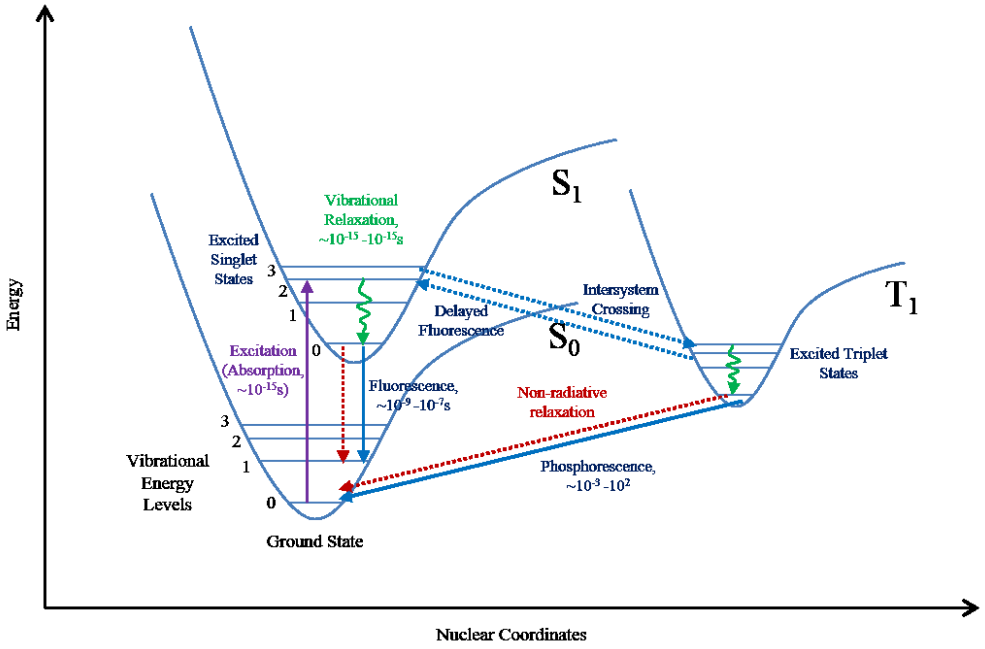

Fig. 2.11 Configuration coordinate diagram also showing energy levels and key transitions.

2.3 Optical Gain in Molecular Materials

The excited state and vibronic energy levels of molecular materials are highly favourable for optical gain since they provide a four-level system in which to achieve population inversion required for amplified emission.

In a two energy level system, a molecule in the ground state may reach an excited state after absorbing an incident photon. If the molecule is already in an excited state, the interaction of an incoming photon results in the stimulated (induced) emission of another photon. An excited state to ground state transition may also occur spontaneously and results in emission of a photon. These processes are described by Einstein A and B coefficients, which are a measure of the probability of each process. The coefficient for spontaneous emission is A_{21}, the coefficient for absorption is B_{12} and $B_{21}$for stimulated emission. In a two level system, the processes of induced absorption and induced emission have the same probability of occurring, and it is not possible to have net gain.

In order to achieve optical gain, the excited state is required to have a higher population than the ground state, which is defined as population inversion. However, at room temperature, the population of excited states is vanishingly small and a molecule occupies the lowest vibrational level of the ground state since the difference between vibronic energy levels of $\sim 0.15\ eV$ is much greater than kT of $\sim 0.025\ eV$.

Population inversion may be achieved via a higher energy third level that rapidly transfers its excitations to the first excited state such that induced emission becomes more probable than

absorption. A relatively long lifetime for the first excited state is also beneficial for population inversion.

The four level system of plastic electronic materials is therefore more favourable for optical gain as it enables population inversion to be achieved at a lower threshold. This is because the ground state, to which the first excited state decays, is empty at room temperature (since vibronic energy levels are much greater than kT) and hence population inversion occurs as soon as the excited state is occupied.

2.4 Spontaneous and Stimulated Emission in a Four Level System

We consider the four level system of an organic molecule with each of the four levels corresponding to the ground state, $S_{0,0}$ and its vibronic energy levels, $S_{0,n}$, and the lowest vibration level of the excited state, $S_{1,0}$ and its higher order vibronic energy levels, $S_{1,n}$. The energies of these levels are defined as E_0, E_1, E_2 and E_3, respectively (Fig. 2.12). Such a system is initially in the E_0 ground state, since $E_1 - E_0 \gg kT$ and an incident energy of at least $^{hc}/_{\lambda} \geq E_2 - E_0$ is needed to excite the molecule to the E_2 excited energy level (that is, the vibrational ground level of the excited state $S_{1,0}$) or higher.

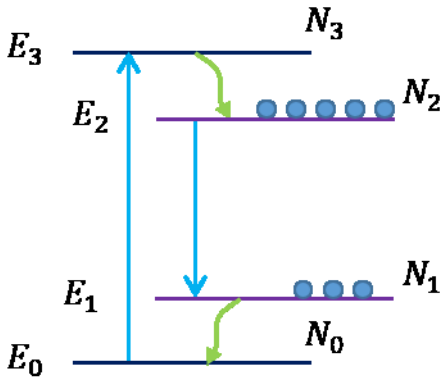

Fig. 2.12 Illustration of a four energy level system with energy level E_0 to E_4 with population densities N_0 to N_4. A transition from E_0 to a higher level is absorption (an E_0 to E_3 transition is depicted). Transitions from E_2 to E_1 may be spontaneous or stimulated emission and green arrows represent internal conversion.

The probability W_{03} of an electronic transition from $S_{0,0} \rightarrow S_{0,n}$ as the number of transitions per unit time is given by (Kneubühl & Sigrist 2005; Wellinger 2010)

$$P_{03} = \frac{dW_{03}}{dt} = u(\lambda)B_{03} \qquad 2.3$$

where B_{03} is the Einstein coefficient for absorption, $u(\lambda)$ is the wavelength dependent photon energy density which shows that the transition rate for induced absorption is proportional to the photon energy density.

The population density of an excited state at an energy level n is denoted by N_n, hence, the population of the vibrationally excited upper energy level, E_3 will increase in an interval of time according to

$$dN_{03} = N_0 dW_{03} = N_0 \mu(\lambda) B_{03} dt. \quad 2.4$$

This is followed by relaxation to the vibrational ground state of the same excited level, E_2 where they persist for an average lifetime, τ_{sp} then decay spontaneously to E_1 by a radiative or non-radiative transition. In the former case, this is with the emission of an incoherent photon of energy $E_2 - E_1 = {}^{hc}/_{\lambda}$.

The probability of a transition between these energy levels W_{21}, during the period dt is

$$dW_{21} = A_{21} dt \quad 2.5$$

where A_{21} is the Einstein coefficient for spontaneous emission and $A_{21} = 1/\tau_{sp}$. The change of population density N_2 of E_2 by spontaneous emission is therefore

$$dN_{21} = -N_2 dW_{21} = -N_2 A_{21} dt. \quad 2.6$$

A downward transition from E_2 to E_1 may also occur by an interaction with an incident photon, which is known as stimulated emission and results in a coherent photon with the same energy, phase and direction as the incident photon. The corresponding transition probability $\overline{W}_{21}$ in terms of the Einstein coefficient for stimulated emission, B_{21} is

$$d\overline{W}_{21} = \mu(\lambda) B_{21} dt \quad 2.7$$

which we note is proportional to the photon energy density, $\mu(\lambda)$ and may be written per period dt as

$$dN_{21} = N_2 d\overline{W}_{21} = N_2 \mu(\lambda) B_{21} dt. \quad 2.8$$

This is the rate of electron transitions to the lower vibrationally excited energy level, E_1, which has a very short lifetime before relaxation to the vibrational ground state, E_0.

From this description of the spontaneous and stimulated emission processes in a four level system, rate equations may be developed that describe the rate of change of the population density in each energy level. In these equations, which we do not reproduce here, the rates for the following processes are summarised:

- N_0 of E_0 is decreased by pumping to E_3 and increased by rapid relaxation from E_1
- N_1 of E_1 is decreased by relaxation to E_0 and increased by spontaneous and stimulated emission
- N_2 of E_2 is decreased by spontaneous and stimulated emission and increased by rapid relaxation from E_3

In order for amplification, a higher population in the upper energy level E_2 than the lower E_1 is required, which is known as population inversion, and the overall rates of stimulated absorption and emission are downwards in energy.

2.5 Amplified Spontaneous Emission (ASE)

The transition probability of stimulated emission is based on the incident photon energy density, hence at a certain threshold excitation, the stimulated emission dominates the spontaneous emission resulting in the characteristic spectral narrowing and gain of amplified spontaneous emission (ASE).

The ASE characteristics are an excellent means of identifying materials suitable for lasing applications. In an ASE measurement, spontaneous emission is waveguided along a one-dimensional stripe pumped region that stimulates the emission of further photons, resulting in a superlinear increase in light output intensity, around a narrow spectral line.

As light propagates through the gain medium in the z-axis, the light intensity from stimulated emission is given by

$$\frac{dI(\lambda)}{dz} = g_{net}(\lambda)I(\lambda) \qquad 2.9$$

where g_{net} is the net gain per unit of length, which is combined with the intensity from spontaneous emission as follows,

$$\frac{dI}{dz} = gI + A_{21}N_2 h\nu \left(\frac{\Omega}{4\pi}\right). \qquad 2.10$$

The second term is the contribution from spontaneous emission where A_{21} is the Einstein coefficient of spontaneous emission, that is, the rate of change of atoms in excited state N_2 such that $^{dN_2}/_{dt} = -A_{21}N_2$, h is Planck's constant and ν is the emission frequency. $^{\Omega}/_{4\pi}$ is a factor accounting for a small fraction of initial spontaneous emission that travels in the direction of amplification and Ω may be approximated as $^{A}/_{L^2}$, where A is the cross-sectional area of the amplifier and L is the length of the amplifier (Svelto 2010; Cheung 2010).

The solution for the differential equation is

$$I(\lambda, z) = \left(\frac{A_{21}N_2 h\nu}{g}\right)\left(\frac{A}{4\pi L^2}\right)(e^{gz} - 1) \qquad 2.11$$

and if $e^{gz} \gg 1$, this may be approximated to

$$I(\lambda, z) \approx \left(\frac{A_{21} N_2 h\nu}{g}\right)\left(\frac{A}{4\pi L^2}\right)(e^{gz}). \qquad 2.12$$

This shows that ASE is exponentially dependent on the length of the amplifying medium (Casperson & Yariv 1972; Costela et al. 2008).

ASE is measured in polymer waveguides in which the thickness of the polymer layer and its refractive index are chosen for total internal reflection to occur at the interface of the film and its surrounding layers and hence allow confinement of a guided mode.

In the most simple case, this is achieved in a planar waveguide with a thin film on a substrate with asymmetric refractive indices such that $n_a < n_s < n_p$, where n_a, n_s and n_p are the refractive indices of air, the substrate and the polymer, respectively.

2.6 Charge Transport in Plastic Electronic Materials

Polymer semiconductors have a low intrinsic charge carrier concentration hence free charges must be generated by photoexcitation or by charge carrier injection. Free charge carriers generated in an organic material by photogeneration require dissociation of singlet excitons into free charge carriers passing via an intermediate stage in which a geminate pair (i.e. a more loosely bound electron-hole pair) is formed.

The exciton binding energy of singlet excitons in conjugated polymers is up to ~0.5eV. The binding energy may vary depending on the degree to which the excited state possesses charge transfer character. For example, donor-acceptor copolymer are expected to have lower binding energies than homopolymers. In either case, dissociation into electrons and holes can require significantly more energy than the thermal energy at room temperature ($kT \sim 25\ meV$).

Such a large value of E_b will mean that the rate of exciton dissociation cannot compete with intrinsic decay processes such as radiative decay by fluorescence, hence a strong electric field or a favourable interface with a suitable step in potential is required for dissociation of excitons into free charges.

Charge carrier transport is by a hopping process in which an electron is localised to the lowest unoccupied molecular orbital (LUMO) of a molecule before hopping to a neighbouring molecule, similarly, a hole hops between the highest occupied molecular orbitals (HOMOs) of neighbouring molecules. The HOMO and LUMO have a distribution of energy levels based on the disorder of conjugated polymers, which is typically modelled as a Gaussian distribution of energy levels with a width σ. Charge carrier transport may be driven by an applied electric field and proceeds by hopping between neighbouring molecular units until collection at a counter electrode occurs or until a trap is encountered.

In plastic electronic materials, charge transport occurs on two key scales, first by intrachain charge transport along the conjugated backbone of the polymer by motion within the delocalised π-electron system and secondly between neighbouring polymer chains or chain segments, that is, interchain, by thermally activated charge hopping. The former may be affected by factors such as the chemical structure, number and types of defects, conformation of the polymer backbone and molecular weight and the latter is affected by factors such as supramolecular structure, morphology, order and orientation.

Several theories have been developed to describe charge transport in polymer semiconducting materials, in particular, the most instructive for describing the intermolecular hopping transport of conjugated polymer is the Marcus theory for hopping transport arising from weak electronic coupling between molecules rather than band-like transport that arises from strong electronic coupling. Marcus theory takes into account molecular distortion relevant to understanding the polaronic nature of charges in polymer semiconductors.

As the interchain hopping nature of charge transfer sets the limit for transport in conjugated polymers, (since chains do not typically span from one electrode to the other) ignoring the intramolecular charge transfer along a polymer chain is considered a suitable approximation.

The key parameters controlling the charge transfer rate that emerge from the theory are the reorganisation energy, λ, which accounts for the energy expended in changes to nuclear positons when charges are lost or accepted, the electronic transfer integral, J_{if}, and the energy difference between the initial and final states, ΔE. The non-adiabatic Marcus electron transfer rate is:

$$\Gamma_{if} = \frac{2\pi}{\hbar} |J_{if}|^2 \frac{1}{\sqrt{4\pi\lambda kT}} e^{-(\Delta E+\lambda)^2/4\lambda kT}. \qquad 2.13$$

By comparing the transfer integral and reorganisation energy, the theory provides a definition for the limit of weak electronic coupling when $J_{if} \ll \lambda$ and the limit of strong coupling when $J_{if} \approx \lambda$.
In the former limit, which is relevant in the case of most organic semiconductors, charge is localised on one molecular chain or another and the mode of transport is by hopping, and in the latter, charge is delocalised over both molecules for a large range of nuclear coordinates and transport assumes a band like character.

According to this view, charge transport may be considered as the macroscopic property that results from uncorrelated charge transfer hops between discrete sites and the rate of transfer is given by Marcus theory.

The parameters derived from Marcus theory provide a way of understanding disorder where variations in ΔE are termed energetic disorder and variations in J_{if} are termed configurational disorder. Hence, disorder may be consider to be on-site or inter-site. On-site disorder arises from conjugation length, defects and conformation and has an effect on the site energy and reorganisation energy. Inter-site disorder may arise from intermolecular separation, conformation, molecular orientation, coulombic interactions and affects transfer integrals, J_{if}, and ΔE.

Both types of disorder have a significant effect on charge hopping rates and are further differentiated as being temperature independent or dependent parameters in determining the rate of charge hopping.

An example of temperature independent variation on the rate of charge hopping is variation of the electronic transfer integral J_{if} that is a result of an increase in intermolecular separation. For example, an increase in separation of as little as 0.25 nm can reduce $|{J_{if}}^2|$ in equation 2.13 by a factor of $\sim 10^5$ (Athanasopoulos *et al.* 2007).

The transfer rate is in effect the product of two terms in which temperature, T, is a key variable, firstly related to the configuration disorder, $\left|J_{if}\right|^2 \frac{1}{\sqrt{4\pi\lambda kT}}$, and secondly to the energetic disorder, $e^{-(\Delta E+\lambda)^2/4\lambda kT}$. Hence, as T becomes very large, the term related to energetic disorder tends to unity such that the rate is determined by configurational disorder alone. This indicates that the extent of electron transfer integral coupling between molecules is the rate determining factor at sufficiently high temperatures.

When $1/\Gamma$ is in the same temporal range as a transient measurement of charge transport, a dispersive regime is reached in which variation in the hopping rate causes a charge packet to be spread out or disperse during transit through the material.

2.7 Dispersive and Non-Dispersive Transport

The concept of dispersive transport was first addressed in a methodological manner by Scher and Montroll who developed a model to differentiate between dispersive and non-dispersive transport. Their model can be used to describe the nature of transport based on the transient photocurrent. Before and after the transit time, the following asymptotes may be fitted to the photocurrent on a log-log scale

$$I \propto t^{-(1-\alpha_i)} \qquad t < t_{tr} \qquad 2.14$$

$$I \propto t^{-(1+\alpha_f)} \qquad t > t_{tr} \qquad 2.15$$

where α is a disorder or dispersion parameter. In the case of a large α, charge transport is considered to be less dispersive and smaller α corresponds to highly dispersive transport (Scher & Montroll 1975; Santos *et al.* 2007).

Further information may be obtained by considering the field dependence of the dispersion parameter. That is, hopping in an exponential distribution of states is indicated by a field independent dispersion parameter, whereas, in a Gaussian distribution of states, the dispersion parameter is predicted to be field dependent (Santos *et al.* 2007).

An alternative means of qualifying the degree of dispersion by Schein is from analysis of the transit time and its decay. In this case, a tail broadening parameter describes the dispersion in the spread of a charge sheet with a relative width w, given by

$$w = \frac{t_{1/2} - t_0}{t_{1/2}} \qquad 2.16$$

where t_0 is the transit time at the inflection point and $t_{1/2}$ is the time for the current to decrease to half the value at the inflection point (Schein 1992). Hence, a large w means the charge sheet is wide and transport may be described as dispersive, otherwise, a small w means the charge sheet is narrower and less dispersive.

2.8 Models of Charge Carrier Transport

The Gaussian Disorder Model (GDM) draws together several underlying aspects to model charge carrier transport. The most essential aspect is Gaussian densities of energetic and positional states. The model combines this with charge carrier hopping rates described by the Miller-Abrahams formalism, field-dependent mobility according to Poole-Frenkel behaviour and the zero-field temperature dependence of mobility. These aspects form the basis of the model to provide a general and comprehensive description of the field and temperature dependence of mobility.

The GDM is based on the assumption that charge carrier hopping is through sites that are distributed around the HOMO or LUMO with a Gaussian density of states (DOS), $g(\epsilon)$, of width σ (the energetic disorder) and at an energy, ε, relative to the centre of the DOS:

$$g(\epsilon) = \frac{1}{(2\pi\sigma^2)^{1/2}} \exp\left(-\frac{\epsilon^2}{2\sigma^2}\right). \qquad 2.17$$

Bässler *et al.* (Bässler 1993) used the simpler Miller-Abrahams approach for calculating the hopping rate $v_{i\to j}$ between sites i and j rather than the Marcus theory discussed earlier. The hopping rates are therefore given by

$$\upsilon_{i\to j} = \upsilon_0 e^{-2\gamma r_{ij}} e^{-\frac{(E_j - E_i)}{kT}}, \qquad E_j > E_i \tag{2.18}$$

$$\upsilon_{i\to j} = \upsilon_0 e^{-2\gamma r_{ij}}, \qquad E_i > E_j \tag{2.19}$$

where υ_0 is the maximum hopping rate (attempt-to-escape frequency), r_{ij} is the jump distance between sites i and j and γ is the inverse localisation radius (that is, the inverse of the decay length of the wavefunction) (Miller & Abrahams 1960; Borsenberger *et al.* 1991).

The Boltzmann term ($e^{-(E_j - E_i)/kT}$) describes the thermal activation, such that if the final state energy E_j is greater than the initial state energy E_i (an upward hop), hopping is reduced. Whereas in the opposite case (a downward hop), the term is replaced with unity indicating downward hops are energetically favoured.

Compared to Marcus theory, intermolecular interactions are ignored and instead an approximated attempt-to-escape frequency is put in its place. Furthermore, only site energies are considered rather than a reorganisation energy. Despite the simplified nature of the Miller-Abrahams approach, both yield similar results. One of the main alternatives to the Miller-Abrahams model is Mott's variable range hopping model in which states are distributed throughout the energy gap (Mott & Davis 2012; Tessler *et al.* 2009).

The calculation of the hopping rate, enables the calculation of the velocity, υ, by an estimate of the number of jumps through a specified length and therefore leads to the determination of the charge carrier mobility μ when the driving force is an electric field, F:

$$\upsilon = \mu F. \tag{2.20}$$

Monte Carlo simulation of charges undergoing a random walk through a Gaussian distribution of states under the influence of an applied field performed by Borsenberger & Bässler led to the following expression for the charge carrier mobility

$$\mu(F,T) = \mu_0 \exp\left[-\left(\frac{2\sigma}{3kT}\right)^2\right] \exp\left[C\sqrt{F}\left(\left(\frac{\sigma}{kT}\right)^2 - \Sigma^2\right)\right] \tag{2.21}$$

where Σ is the width of a Gaussian distribution related to the configurational disorder or positional disorder from variation in intermolecular distances and the relative orientations of molecules. This is also referred to as off-diagonal disorder when energetic disorder is referred to as diagonal disorder.

The model leads to several observations regarding charge transport by considering a charge carrier injected or generated in the DOS with a random energy, which we refer to as the occupied DOS

(ODOS). Firstly, the centre of the ODOS relaxes towards the thermal equilibrium energy such that the ODOS is at an energy $\frac{\sigma^2}{kT}$ below the centre of the density of states.

As the temperature is reduced, the centre of the ODOS is lowered relative to the centre of the DOS such that the ODOS lies at the tail of the DOS (Fig. 2.13). The charge transport level is close to the centre of the DOS; hence, the charge carrier requires an activation energy to promote the ODOS to the transport level. This results in a strong temperature dependence of charge transport and at lower temperatures, there is less energy for activation to the energy at which charge transport occurs. The temperature dependence of the mobility is then of the form

$$ln\,\mu \propto 1/T^2 \qquad 2.22$$

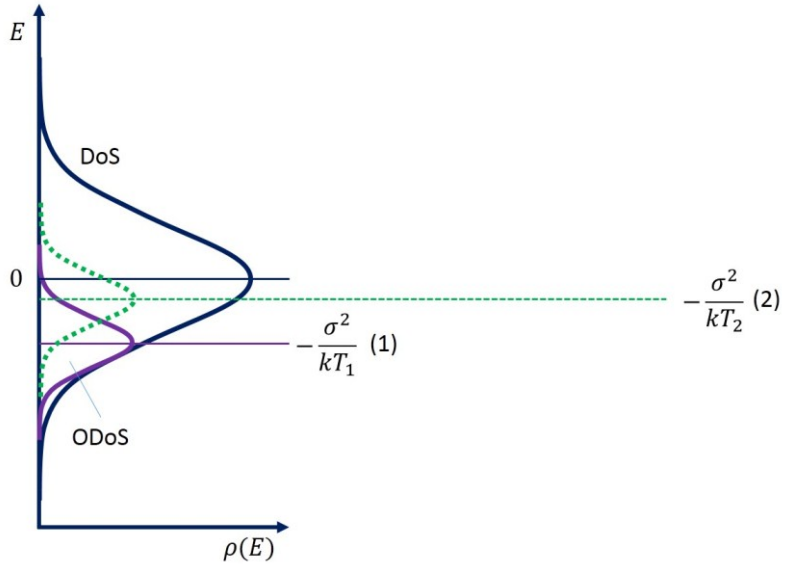

Fig. 2.13 The Gaussian Density and States (DoS) and the Occupied Density of States (ODoS) at temperatures $T_1 < T_2$. An injected charge carrier relaxes to thermal equilibrium by hopping to lower energy states in the ODoS (1). Hopping transport is more likely to occur when the charge is promoted closer to the transport energy near the centre of the DoS (2) at higher temperatures.

The second observation regarding charge transport that emerges from the model is the electric field dependence. If we consider a charge at a local energy minimum in an electric field, F, in order for electron hopping to reach the next local energy minimum an activation energy E_a is required. The electric field tilts the DOS in the direction of the field such that E_a is reduced by an amount $\beta\sqrt{F}$ (where $\beta = \sqrt{q^3/\pi\epsilon_0\epsilon_r}$, q is the electric charge, ϵ_0 and ϵ_r are the vacuum permittivity and relative permittivity, respectively) (Fig. 2.14). This leads to the characteristic Poole-Frenkel field dependence of the mobility of the form:

$$log\mu \propto \beta\sqrt{F}. \qquad 2.23$$

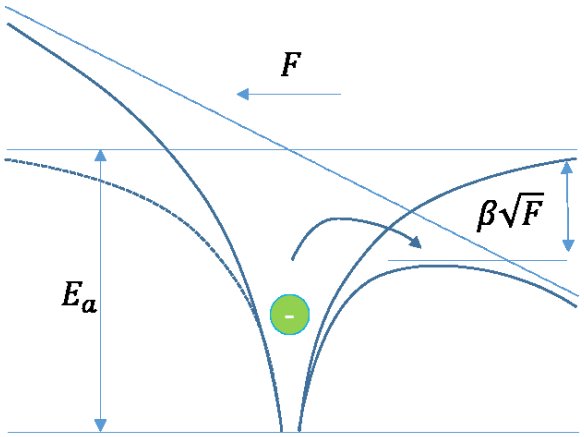

Fig. 2.14 Schematic of the Poole-Frenkel effect by which the barrier to hopping is reduced by the application of an electrical field.

The GDM expression for the mobility in equation 2.23 is only valid for temperatures above a critical temperature that is lower than the glass transition temperature. Below this temperature, time of flight photocurrent transients show dispersive transport and there is a break in the $\ln \mu \propto {}^{1}/_{T^2}$ relationship of the temperature dependence (Bässler & Borsenberger 1993).

The GDM is subject to several limitations, for example, it has been shown to be invalid at low electric fields and polaronic effects of transport are ignored, which have been accounted for in later extensions of the model. Despite these limitations, it has been shown that it successfully models charge transport in disordered materials especially at low charge carrier densities. In relation to experiments, the energetic disorder parameter σ is particularly useful for comparing similar materials or the effects of processing steps such as annealing and the mobility pre-factor, μ_0, which is the theoretical mobility at zero-field and infinite temperature, provides an insight into the theoretical maximum mobility if the effects of energetic disorder are not present.

2.9 Charge Trapping

In a broad DOS, sites of a certain energy may be defined as charge traps in which de-trapping from the trap site takes longer than the time for the trap to become occupied. The origin of charge traps may be related to chemical or physical defects or the presence of oxygen and water in the case of electron traps. According to descriptions of charge transport based on charge hopping, such as the GDM, sites at a lower energy than neighbouring sites require an activation energy to hop upwards in energy. Hence, traps may be further classified as deep or shallow, where shallow traps are those sites energetically closer to the sites where charge transport occurs and deep traps are at significantly lower energies.

The energy states at the tails of the DOS are characterised as being trap states, themselves having a Gaussian distribution. In the case of shallow traps, de-trapping may be possible at slightly elevated temperatures, when the trap depth is of the order of kT.

The presence of charge traps has implications for the charge carrier density dependence of mobility. In view of the Marcus theory, at high charge carrier densities, the filling of deep traps decreases the variation in ΔE (that is, energetic disorder) and the average hopping rate increases, which leads to a higher mobility of the mobile charge carriers.

Another view is to consider the position of the Fermi level, corresponding to the energy of the highest occupied state, relative to the "transport energy" as in the Vissenberg-Matters model, which is a further development of variable range hopping (Vissenberg & Matters 1998). The concept of the transport energy is the energy level within the distribution of energy levels that represents the optimum energy level for charge hopping; hence, the hopping rate at this level determines the mobility. This model takes into account charge carriers occupying localised states and approximates states in the tail of a Gaussian DOS as an exponential DOS.

As the separation between the Fermi level and the transport energy level increases, the rate of charge transport by charge hopping decreases. At a high charge carrier density, the Fermi level is closer to the transport energy level, which increases the rate of charge transport and hence the mobility. In effect, the high charge carrier density has filled traps and raised the Fermi level to closer proximity to the transport energy level.

The mobility is therefore strongly dependent on charge carrier density and this must be taken into account when comparing the mobility obtained by different techniques. For example, ToF measurements are conducted with carrier densities kept as low as possible yielding mobilities that can be several orders of magnitude lower than FET measurements performed at significantly higher carrier densities. In the absence of traps, ToF and FET mobilities should become comparable, and when they agree closely, this may signify charge transport in a trap free material.

2.10 Charge Carrier Injection

Charge carrier injection into a molecular material from a metallic contact is determined by the energy barrier between the contact and the HOMO or LUMO level for hole or electron injection, respectively. If the energy barrier is small enough to not limit the flow of charge and therefore behaves as an effective infinite reservoir of charges, then the contact is ohmic (Rose 1955).

In the case of such an ohmic contact, charge transport may be limited by the bulk properties such as trap states and the morphology of the active layer. In the absence of traps, the injected charge will be space charge limited (SCL) where an ohmic contact may supply more charge carriers per unit time

than may be transported through the dielectric. The SCL current density is given by (Barth *et al.* 1999)

$$J_{SCLC} = \frac{9}{8}\epsilon\epsilon_0\mu\frac{V^2}{d^3}. \qquad 2.24$$

Injection limited transport arises when the contact limits the flow of charge and arises from an injection barrier between the electrode and polymer based on the injection barrier height, the electronic properties of the injecting contact, and the effects of interfacial doping or the morphology of the polymer at the interface.

Two of the most important models for charge injection are the Fowler-Nordheim (FN) model for quantum tunnelling and the Richardson-Schottky (RS) model for thermionic emission. In the case of FN tunnelling, the current I is predicted to follow the relationship of

$$I \propto F^2 \exp\left(-\frac{\kappa}{F}\right) \qquad 2.25$$

where F is the electric field strength and κ is a parameter that describes the barrier shape, typically modelled as a triangular barrier. FN tunnelling ignores image-charge effects and is temperature independent (Fowler & Nordheim 1928; Simmons 1963; Parker 1994).

In the case of the RS model of thermionic emission, tunnelling is ignored and image-charge effects are accounted for in the lowering of the energy barrier ϕ when an electric field is applied. The injected current is given by

$$J_{RS} = A^*T^2 \exp\left(\left[-\phi + \left(\frac{e^3}{4\pi\epsilon\epsilon_0}\right)^{\frac{1}{2}} F^{\frac{1}{2}}\right] \Big/ k_B T\right) \qquad 2.26$$

where A^* is the Richardson constant (Barth *et al.* 1999; Santos *et al.* 2007).

Both of these models were developed for band type semiconductors, hence, experimental data for carrier injection from a metal into disordered organic material shows better agreement with a model based on a distribution of hopping sites (Barth *et al.* 1999).

In the preceding discussion, we have described charge transport through a Gaussian distribution of energy states. Accordingly, charge injection may be considered to follow the same principle of charge hopping into a distribution of states in polymer materials that occurs by thermally activated hopping and tunnelling (Abkowitz *et al.* 1995) and field assisted tunnelling.

Injection in such a system may be limited by interfacial disorder at the interface that may result in broadening of the width of the energetic disorder at the interface from interface dipoles and the image potential of injected charges, which have an inhomogeneous distribution according to the morphology

at the interface (Baldo & Forrest 2001). Fig. 2.15 illustrates a model that includes the spatial dependence of the width of the energetic disorder.

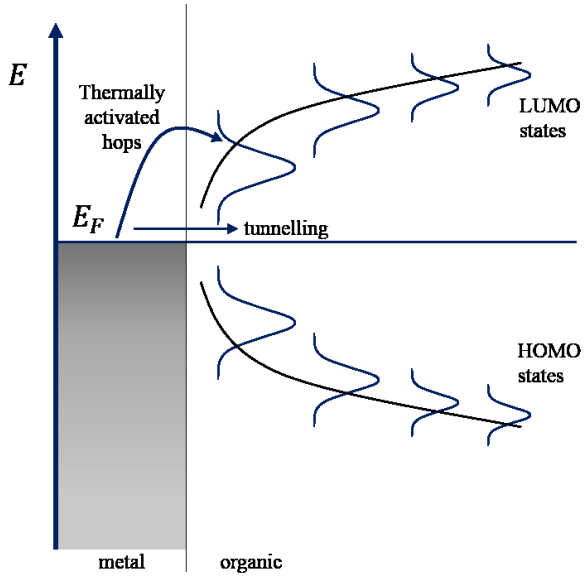

Fig. 2.15 Illustration of a spatial dependence of the width of the energetic disorder, adapted from (Limketkai & Baldo 2005).

2.11 Domains of Charge Carrier Transport

We have already mentioned that charge transport occurs by intrachain drift/diffusion and interchain hopping. Measurements at different time-scales illustrate these different domains of charge carrier transport in terms of time and geometric scale. Devizis *et al.* (2010), used time-resolved electric field second harmonic generation (TREFISH) on the sub-picosecond scale together with time-of-flight techniques to resolve these domains.

On a time-scale of a few hundred femtoseconds, transport takes place by intrachain processes, such as charge transfer within conjugated segments and along the π-conjugated backbone of a polymer. On a time-scale of nanoseconds, transport is between chains, that is, interchain and finally, at longer timescales, charge transport is in the macroscopic domain through the bulk of the material in regions of different order, such as over grain boundaries or between disordered amorphous regions and ordered polycrystalline regions, which determines the overall charge-carrier mobility, which represents a macroscopic parameter.

Consequently, the former microscopic domain of mobility may be considered to represent the intrinsic mobility of a particular polymer and overcoming the factors that limit extrinsic mobilities to be lower by many orders of magnitude has been the subject of many research investigations. Amongst the factors that have been investigated are chemical structure, molecular packing, conformation, disorder (torsional, chain bending and coiling), impurities, morphology, chain alignment, side chains (length, structure and sequence), and molecular weight and size (Coropceanu *et al.* 2007).

2.12 Organic Semiconductor Devices

An optically pumped polymer laser consists of a polymer semiconductor as the optical gain medium within a resonant structure that provides multiple passes (feedback) of light through the gain medium. Examples of optical feedback structures include the Fabry-Perot cavity where the polymer is between two mirror surfaces or distributed feedback (DFB) structures such as distributed Bragg reflectors (DBR).

In order to understand the challenges towards electrically pumped polymer lasers, we briefly discuss the operating principles of the most significant organic semiconductor devices that already exist to show how the devices physics required for lasers diverges and requires the unification of physical processes that may be mutually exclusive in the operation of existing devices.

The most widespread form of organic photovoltaic (OPV) device is based on the bulk-heterojunction system because of the advantage this system offers of more effective charge separation of excitons. In such an OPV device, light conversion begins with absorption of light to form an exciton, which diffuses to a donor-acceptor heterojunction where charge separation of excitons into electron and hole polarons may occur. The final stage is charge transport of the charge carriers to their respective electrodes and charge collection. The design of OPV devices must contend with various losses in each of these steps and is posed with significant optimisation problems to balance the competing processes to maximise the device efficiency.

The operating principles and challenges associated with OPVs are discussed in numerous reviews (Brabec *et al.* 2001) and we mention a few of these challenges here. For example, absorption must be matched to the solar spectrum and thicker layers are preferred to maximise absorption, however, thicker layers require charge carriers to be transported further to the collection electrodes, which therefore increases the probability of charges recombining. Efficient charge separation requires intermixing of the donor and acceptor materials in a way that maximises the interfacial area between them and hence the likelihood of an exciton encountering a heterojunction. Losses may also occur by partial separation into geminate pairs of electrons and holes.

Separated charges must then be transported to their respective electrodes. This process is facilitated by a high mobility for both carriers, however, a high mobility increases the rate of the competing process of non-geminate recombination in which separated charges recombine to form another exciton. In the case of an unbalanced mobility, a space charge region may form, which may limit the photocurrent that may be extracted (Choulis *et al.* 2003).

Organic light emitting diodes, in their simplest form, combine an active light emitting polymer layer between hole and electron injection electrodes aligned to the HOMO and LUMO energy levels of the

polymer, respectively. The key processes in the device physics of OLEDs are summarised as charge injection, ambipolar charge transport, exciton formation, radiative decay of excitons and light out-coupling.

When the device is operated in a forward bias, holes and electrons are injected which recombine to form excitons. As we mentioned, the probability of generating non-radiative triplet excitons compared to singlet excitons is three times higher, which represents one of the most significant loss mechanisms in OLEDs, although this problem may be mitigated in devices that use spin-orbit coupling of heavy metals to enhance inter-system crossing or where there is a singlet-triplet splitting of the order of kT.

More recently, very high internal quantum efficiencies have been obtained by the use of triplet harvesting by thermally activated delayed fluorescence (TADF) which has been demonstrated in small molecule donor-acceptor systems (Endo *et al.* 2009; Endo *et al.* 2011; Nakagawa *et al.* 2012; Zhang *et al.* 2012; Dias *et al.* 2013; Park *et al.* 2013). Such TADF materials are designed to minimise the singlet-triplet energy gap.

Although organic light emitting diodes are the most well researched devices for light emission using organic semiconductors, they are far removed from being suitable for electrically pumped lasing since they operate at very low charge carrier densities and do not provide optical gain or include a resonant cavity for feedback of stimulated emission.

The operation and device physics of organic field effect transistors (OFETs) are discussed in detail later in this chapter as they are used as experimental devices for charge transport measurements in this thesis. In brief, OFETs are three terminal devices with source, drain and gate electrodes with an organic semiconductor thin film deposited in the channel between the source and drain and a dielectric layer between the gate and semiconductor. Charges are injected from the source electrode depending on the polarity of the bias applied to the gate electrode and accumulate at the semiconductor/insulator interface. From this point, an OFET operates in different regimes depending on the source-drain bias, which are described later in this chapter.

These latter two device types have been combined in the form of the organic light-emitting transistor (OLET) or light-emitting field effect transistors (LEFET), which has attracted significant interest over the past few years for its light emission capabilities and as a possible precursor towards an electrically pumped organic laser. In particular, because of its resemblance to field-effect transistors in terms of device structure and, therefore, its high charge carrier density in the operating regime.

As with an ordinary field-effect transistor, an OLET is a three terminal device with source, drain and gate electrodes, except it is designed to enhance exciton generation by electron and hole

recombination in the channel. Recent reviews discuss their properties including prospects for electrically pumped lasing (Muccini *et al.* 2012; Wakayama *et al.* 2014).

In an OLET, causes of exciton quenching, such as interaction with charge carriers, the externally applied electric field and injecting electrodes, may be avoided based on device structure, which may result in a higher electroluminescence quantum efficiency. Other benefits include the ability to balance electron and hole currents and an effective separation of the exciton population and charge carriers.

Importantly, OLETs operate in the very high current density regime, which is necessary for electrically pumped lasing. For this reason, and the opportunity to integrate waveguiding and optical resonators alongside the planar geometry of the active layer, these devices have prompted an optimistic outlook as possible antecedent devices to electrically pumped lasers.

Several structures of OLET exist in the literature; the most basic is the unipolar thin film OLET that has a single active layer in the channel and equivalent source and drain electrodes. This structure requires a compromise between emission efficiency and channel length that arises because of enhanced injection of electrons by higher electric fields in shorter channels close to the drain electrode, which can also result in excessive exciton quenching if the channel length is too short.

An improvement of the previous scheme, where a single charge dominates transport such that the EL is confined to the region opposite to the electrode of the dominant carrier, is to use an ambipolar material with appropriately tuned electrodes for hole and electron injection to the HOMO and LUMO levels of the organic material, respectively. This structure also has the advantage of control over the EL emission region by varying the gate-source and drain-source voltages. The external quantum efficiency (EQE) of a single layer device of this type was estimated to be ~0.8% (Zaumseil *et al.* 2008).

Using a trilayer device composed of an HTL, ETL and emission layer showed that the EQE could be improved to 5% (Capelli *et al.* 2010). This was found to be more than twice as efficient as an OLED with the same set of optimised layers. In a trilayer device, charge percolation occurs to the central recombination region by the transverse electric field generated by hole and electron accumulation in the surrounding charge transport layers. Quenching by exciton-polaron interaction is reduced because the charge carrier accumulation and high exciton density regions are separated in the different layers.

OLETs have also been demonstrated that implement feedback. For example, both 1D and 2D DFB gratings can be incorporated into the device. (Namdas *et al.* 2009) showed that this was possible by nano-imprint lithography of the polymer, which has been cast on the gate dielectric. Alternatively, a DFB waveguide may be integrated into the channel with light coupled from the recombination zone

into the resonant mode of the DFB waveguide (Gwinner *et al.* 2009). In this case, the confinement provided by the DFB waveguide was used for confinement of the optical mode away from the electrodes to eliminate losses by electrode absorption. It was shown that light intensity did increase with increasing current, however, there was no indication of lasing. Optical excitation, on the other hand, did show lasing at a certain threshold in pump energy.

In a more recent work, the same group demonstrated that certain optimisations could produce an even higher EQE of ~8% from a single layer ambipolar device. In particular, the use of zinc oxide as the source electrode to enhance injection in to the LUMO of F8BT, and a 100nm layer of silver as the gate electrode to reduce absorption losses. In addition to this, the thickness of the gate dielectric, PMMA, was tuned to optimise the EQE. One explanation for the high EQE obtained from F8BT is that the fraction of singlet excitons generated may be much greater than 0.25 (Gwinner *et al.* 2012).

A major disadvantage of all the OLETs discussed so far is the high operating voltage (>80V), which significantly reduces the power efficiency of these devices. However, this may be addressed with optimised gate dielectrics, injection electrodes and device geometries.

2.13 Challenges towards Electrically Pumped Polymer Lasing

From this brief review of the key mechanisms behind existing device types, we see that the development of polymer lasers requires optimisation across multiple seemingly mutually exclusive processes. For example, they must combine simultaneously high charge carrier mobility with high luminescence efficiency and high charge carrier densities without exciton quenching.

The challenges for electrically pumped lasers are numerous and may be considered on several levels. First, the underlying physical phenomena relating to charge transport and energy transfer, secondly the challenge to design materials that exhibit high charge carrier mobility and luminescence efficiency, combined with the requirement of suitable electrical contacts to inject sufficient charge carriers into these materials to reach the lasing threshold exciton density. The final level is that of device architectures required to provide optical feedback with minimal optical losses.

It has already been mentioned that electrical injection can lead to the formation of non-radiative triplet excitons with a higher yield than singlet excitons that can decay radiatively. The formation of triplet excitons can also proceed via an intersystem crossing from the first singlet state to the first triplet state (T_1). Decay from a triplet is non-radiative and occurs on a significantly longer timescale resulting in accumulation of the triplet state. This hinders stimulated emission because of an efficient T_1 to T_2 triplet-triplet absorption or by non-radiative energy transfer between a singlet and triplet (singlet-triplet annihilation) (Chénais & Forget 2012).

Other mechanisms hinder stimulated emission such as exciton quenching by annihilation. Four of the main singlet annihilation processes that are detrimental at high current densities are singlet-singlet, singlet-triplet, singlet-polaron and singlet-heat annihilation (Hayashi *et al.* 2015).

In singlet-singlet annihilation, a singlet exciton is annihilated by energy transfer to a second singlet, which obtains a higher excited state followed by relaxation to the first excited state or a triplet state. Singlet-triplet annihilation occurs when a triplet is excited to a higher state in the annihilation of the singlet, which then relaxes to the first triplet state, which has a non-radiative transition.

Charge carriers injected into organic materials form polarons and bipolarons, which are the charge transport species in organic materials. These give rise to their own sub-band-gap energy levels between the HOMO and LUMO levels and thus new optical transitions. The combination of an electron and hole polaron results in the formation of a singlet exciton, however, a polaron or bipolaron can quench a singlet exciton and adopt a higher lying charge state. Several other annihilation processes also exist (Gärtner *et al.* 2007). Exciton quenching may also occur at chemical defect sites or impurities, and excitons may be subject to dissociation in high electric fields.

These effects lead to several challenges for the design of materials that may mitigate their losses. The requirements for an organic lasing material can be summarised as follows from the perspective of their optical properties.

The material should have a high photoluminescence quantum yield in the solid state, a low ASE threshold and high optical gain. A compromise must be struck in the size of the Stokes shift, which should be large enough to avoid self-absorption at the laser wavelength yet narrow enough to reduce the fraction of energy lost by non-radiative channels. Finally, it should have a low intersystem crossing rate and low spectral overlap with the triplet absorption cross section (Chénais & Forget 2012).

In addition to the above, the thin film morphology should favour dense chain packing to increase the refractive index for optical confinement of the lasing mode. As for the charge transport properties of the material, it should have a high electron and hole mobility, preferably ambipolar, to maximise exciton generation. High mobility is required for injected charges to reach the charge density required for the lasing threshold exciton density. The high mobility is further required in order to exceed the intrinsic losses discussed earlier and extrinsic losses arising from the resonator and electrodes. Finally, a high ionisation potential (deep HOMO-level, >5.4eV) is favourable for stability against oxygen.

As discussed earlier, these two properties of high luminescence and high charge carrier mobility have often been found to be mutually exclusive, however there may be exceptions to this rule or optimisations that favour both, as has been shown in the work of Yap *et al.* (2008).

It has been the case for most material systems that efficient emission has not been obtainable at the same time as high charge carrier mobility. This is a consequence of the different mechanisms for energy transfer and charge transport in organic semiconductors. Improved interchain interaction required for hopping transport has the effect of providing pathways for excitons to quenching sites and other mechanisms of non-radiative decay.

Thus, for the improvement of luminescence, bulky substituent groups or side-chains are preferred to ensure separation between neighbouring polymer chains whereas close proximity is preferred in the case of high mobility polymers.

Energy transfer of excitons can take place by one of three processes; trivial transfer, Förster transfer or Dexter transfer. Between chains, Förster transfer is the main mechanism for interchain energy transfer. This relies on coulombic interaction of the dipoles of the donor molecule in an excited state and the acceptor molecule, which results in the promotion of an electron in the acceptor if the oscillating dipole is coupled strongly in resonance with an electron in the acceptor molecule.

Since dipoles are oriented along conjugated sections of polymer chains and thus weakly coupled (Brédas *et al.* 2004), intrachain energy transfer cannot occur by the Förster mechanism. It was thus shown by Nguyen *et al.* (2000), using chains of MEH-PPV embedded in nanoscale channels, that intrachain energy migration takes place on a time scale of a few hundred picoseconds compared to interchain transfer, which takes place in a few picoseconds.

The reverse is true for interchain charge transfer. One-dimensional charge carrier mobility measurements of isolated chains of MEH-PPV by Hoofman *et al.* (1998) using time-resolved microwave conductivity showed mobilities several orders of magnitude higher than that measured in the bulk by the time-of-flight technique. Hence, enhanced interchain charge hopping to improve mobility may have the drawback of more rapid interchain energy transfer for quenching sites.

In the work of Yap *et al.* (2008), the authors demonstrated that an alteration of a fraction of the solubilising substituent groups of poly(9,9-dioctylfluorene) can enhance hole mobility by two orders of magnitude without compromising luminescence efficiency or optical gain. This increase is expected to be because of the introduction of sites at which charge hopping between chains is favoured by closer chain proximity, together with a fraction of β-phase segment formation.

This “structured heterogeneity” should enhance mobility without detrimental effects to the luminescence efficiency of the original chemical structure of the polymer. This is the key concept that has motivated the research investigation in chapter six on a novel series of copolymers. We briefly summarise the key results of this study and related research conducted to this date.

The two copolymers derived from poly(9,9-dioctylfluorene) (PFO) were produced from new monomers containing two fluorene moieties one of which was substituted with linear octyl side chains (F8) and the other with a shorter, branched side group (F5). It was found that a ratio of 80:20 of F8:F5 could improve hole mobility of ordinary PFO by two orders of magnitude to $3 – 6 \times 10^{-2}$ cm^2/Vs. Furthermore, an improvement in optical confinement because of a higher refractive index achieved by denser polymer chain packing in thin-film waveguides led to improved gain in ASE measurements. Excellent lasing performance on 1D distributed feedback gratings was also achieved.

This publication was later followed by Kim *et al.* (2010) who investigated a similar theme to the work of Yap *et al.* (2008) based on blue emitting indenofluorene-phenanthrene copolymers. According to their experiments, the authors demonstrated high optical gain and high charge carrier mobility from one of the structures containing a pair of C8-alkyl side chains and a pair of aryl units on a single indenofluorene moiety. This structure had a reported hole mobility of $\sim 10^{-2}$ cm^2/Vs and showed higher optical gain compared to a structure in which the aryl substituents had further linear alkyl-oxy groups attached and to a fully arylated indenofluorene homopolymer.

Most recently, S. Foster *et al.* (unpublished) found that the effect of removing β-phase in PFO thick films improves time-of-flight hole mobility from $\sim 10^{-4}$ cm^2/Vs. to $\sim 10^{-2}$ cm^2/Vs, which is discussed in further detail in chapter four.

The final challenge towards electrically pumped polymer lasers is addressing the requirements of device architecture. Some of these problems are being addressed with work on optically pumped organic lasers where there is a similar requirement for optimising lasing structures for low losses and thus low-thresholds. However, in the case of electrical pumping, there are significantly greater losses from quenching mechanisms and charge induced absorption, as discussed, alongside the additional losses incurred by interaction of the optical field with the injecting contacts. Consequently, an optimised structure for optical pumping is not expected to bear a direct resemblance to a structure for electrical pumping; however, optical pumping is the key way of testing the lasing performance of novel polymers.

In waveguide-based resonators, there may be leakage of the guided mode as it is absorbed by the metal electrodes. This interaction with the electrodes can be reduced to some extent by placing contacts at a distance corresponding to a higher order guided mode or by using thicker charge transport layers to keep the mode away from the electrode (Chénais & Forget 2012). This latter alteration has the drawback of reducing the recombination rate of electrons and holes and displacing the recombination region towards the electron injecting electrode because of unequal hole and electron mobility. Losses associated with electrodes may also be reduced by using transparent conductive oxides such as molybdenum oxide and zinc oxide for hole and electron injection, respectively.

There have been several attempts at estimating the requirements for lasing in terms of charge density for a particular lasing threshold. For example, Samuel *et al.* (2009) show that a lasing threshold of 84 μJcm^{-2} theoretically requires a current density of 10^5 Acm^{-2}, assuming perfect efficiency of the device, neglecting electrode losses and exciton annihilation. Elsewhere, a threshold current density for ASE of 3.84 kA/cm^2 has been estimated in the presence of transparent electrodes (Yamamoto *et al.* 2004). Recently, a maximum current density of 2.8 kA/cm^2 has been demonstrated under pulsed operation (with a pulse width of 5 μs) in a patterned OLED structure designed to suppress singlet-heat annihilation (Hayashi *et al.* 2015).

Wallikewitz *et al.* (2010) implemented a resonator and electrodes in an ordinary sandwich type OLED to fabricate an organic light-emitting diode that lases with optical pumping. They showed that even a low current density of 7 $mAcm^{-2}$ increases the laser threshold by 15% from 4.8 to 5.6 μJcm^{-2}, with an accompanied reduction in slope efficiency.

Perhaps one major step towards an electrically pumped organic laser is the demonstration of a device that incorporates single pass gain alone without the optical feedback required for a laser. This device would provide optical gain along a waveguide to generate ASE by electrical pumping. Such devices known as a "super-luminescent light emitting diodes" (SLEDs) with emission in the blue region ~420 nm have only recently been demonstrated using inorganic III-nitride semiconductor technology (Feltin *et al.* 2009). If such a device could be realised with organic materials, there would be direct access to a significantly broader part of the spectrum.

Reports of electrically excited spectral narrowing or ASE from organic semiconductors have been reported (Bisri *et al.* 2009) as well as reports of a superlinear dependence on emission intensity with current density (Yokoyama *et al.* 2008). However, the former results have been criticised by Samuel *et al.* (2009) because of the wide linewidth of the supposed ASE spectra of over 60nm and the absence of energy or power dependence showing a superlinear increase in intensity expected at the onset of ASE.

2.14 Charge Transport Measurement Techniques

Plastic electronic materials have a very low concentration of intrinsic free charges such that measuring charge transport requires generation of the charge carrier species of interest from an external source. This may be by direct electrical injection or photogeneration as in the techniques outlined here.

Other means of charge carrier generation are also possible such as pulse-radiolysis time-resolved microwave conductivity (PR-TRMC), which is an electrodeless technique using high energy (3 MeV) electron pulses to generate carriers by inducing ionisation in a sample held in a microwave

conductivity cell. This technique probes very short lengths as charges are transferred along a single polymer chain in the oscillating microwave field (Grozema & Siebbeles 2011), whereas here we are interested in techniques that measure the bulk mobility. In the following pages, we discuss the theoretical basis for the techniques used in this thesis and the experimental methods are described in Chapter 3.

2.15 Time-of-Flight (ToF)

The Time-of-Flight (ToF) technique is amongst the most widely established techniques and the only method that directly measures the bulk mobility of charge carriers because of an unambiguous arrival time of the photogenerated charge carriers at the counter-electrode that is apparent in the transient photocurrent signal when transport is non-dispersive. The ToF technique was first used in organic solids as a pulse photoconductivity technique to measure the electron and hole mobility in anthracene (LeBlanc Jr 1960; Kepler 1960).

The material of interest (thickness d) is deposited between two electrodes of which one is semi-transparent (typically ITO). Pulsed laser light is shone through this transparent electrode, which generates excitons in the material under investigation within a short distance of the electrode, depending on the absorption depth of the material. A voltage is applied to the device such that the photogenerated excitons are separated into electron and holes in the applied field. Depending on the applied bias, the charge carriers of interest are transported to the counter electrode.

The time required for the charge carriers to reach the counter electrode is the carrier transit time, t_{tr} (Fig. 2.16). The polarity of the field determines whether electrons or holes are transported through the sample. For example, for measurements of the hole mobility, the counter electrode is negatively biased. As the charge packet of holes drifts across the sample, they generate a constant displacement current which is measured through a resistance, R. This photocurrent appears as a plateau in the current transient, if transport is non-dispersive, followed by an inflection point ("the signature of the carrier transit time" (Hertel *et al.* 1999)) after which the current begins to decrease monotonically.

The charge carrier mobility can be determined using the following relationship,

$$\mu = {d^2}/{t_{tr}V} \qquad 2.27$$

where μ is the mobility, d is the sample thickness, t_{tr} is the transit time given by the inflection point of the transient photocurrent and V is the applied voltage. Alternatively, the half-current time $t_{1/2}$ may be used instead of the inflection point.

The residual current tail is typically extended much more for dispersive transport, to the extent that plateau and tail cannot be readily distinguished (Fig. 2.16) on a linear scale but may be seen more

clearly in a log-log plot of the transient. The physical reasons for this are discussed earlier in this chapter and are related to the charges not reaching thermal equilibrium within the transit time as a result of the distribution of charge trapping sites of different energies and trapping times (Bässler & Borsenberger 1993; Borsenberger *et al.* 1992).

The requirements of the measurement are that the RC time of the circuit must be shorter than the transit time so that the latter is not concealed by the RC response. For high mobility materials, thicker films are preferred. In general, thicknesses need to be several microns. The penetration depth of the laser pulse must be substantially less than the sample thickness, hence the laser wavelength is selected where the material investigated is known to have a high absorption coefficient, α.

$$d \gg \frac{ln10}{\alpha}. \qquad 2.28$$

Ideally, the laser wavelength is chosen to match the peak absorption such that charge carriers are generated within ~100nm of the interface (absorption coefficients are typically ~10^5 cm^{-1}).

The duration of the laser pulse should be shorter than the transit time and its intensity should be low enough that the number of charges generated is significantly smaller (≤ 10 %) than the charge stored in the effective capacitance of the sample such that a uniform electric field, with no space-charge effects, is maintained in the bulk (and the photogenerated charge is a minor perturbation). Finally, the dielectric relaxation time, τ_σ, that is, the time for the dielectric to polarise in response to the presence of the photogenerated charges, must be longer than the transit time (Hertel & Bässler 2008).

$$\tau_\sigma = \frac{\epsilon\epsilon_0}{\sigma} \qquad 2.29$$

where σ is the conductivity of the material (Lampert & Mark 1970). The TOF measurement may be performed using a very large resistor (1MΩ) in the circuit to increase the transit time beyond the RC time constant, in which case the measurement is being performed in "integral mode". We, however, do not make use of the integral mode in this thesis. The measured integral mode signal is the total charge accumulated at the counter electrode and the transit time can be approximated as the time it takes for the current to reach half of its maximum (Campbell *et al.* 2001a).

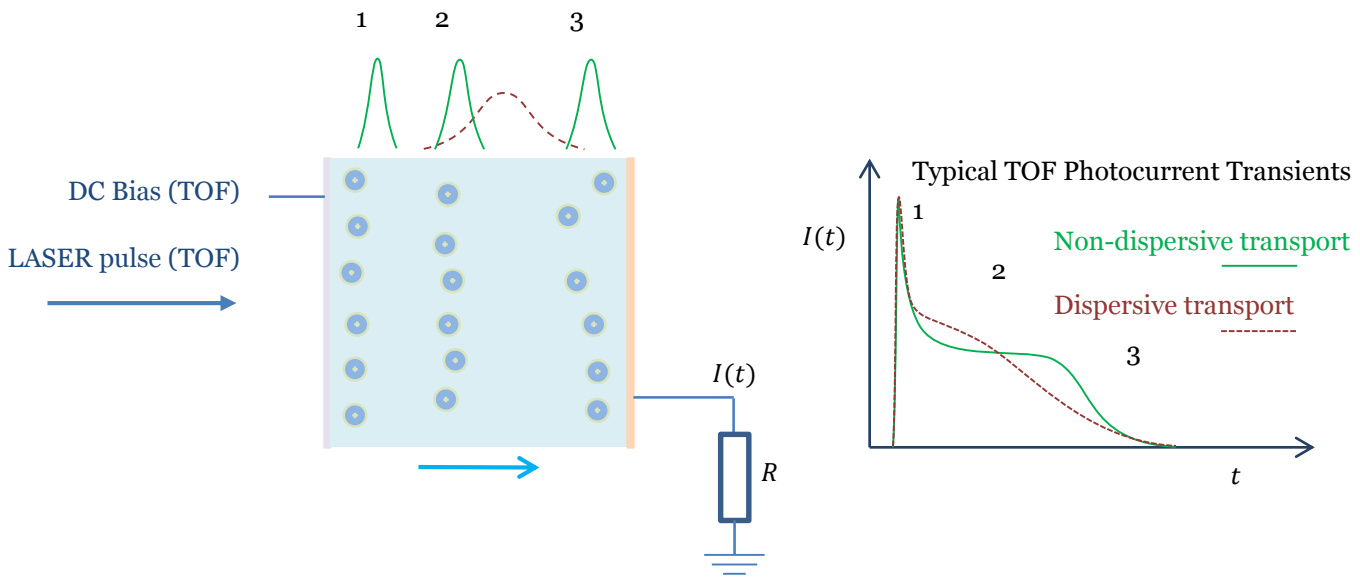

Fig. 2.16 Illustration of the ToF technique. A laser excitation at a semi-transparent, non-injecting electrode (ITO) is used to photo-generate charge carriers in the material. Characteristic dispersive and non-dispersive transients are shown on the right.

Variations of the ToF technique exist such as the charge generation layer technique (CGL-ToF), which may be used when the material of interest has a low absorption at the laser wavelength. Instead of generating charges in the polymer film, an additional thin layer with a peak absorption matching the laser wavelength is used for photogeneration of charges, which are transferred to the main layer by alignment of the HOMO or LUMO levels.

Charge retraction TOF is based on electrical injection of charges that accumulate at a blocking layer. After charge accumulation, the applied voltage is reversed such that the accumulated charge is swept back through the device as a charge packet similar to the photogenerated charge in an ordinary ToF experiment, yielding a transient current subject to the same analysis as ToF (Wallace 2009).

2.16 Dark Injection Space Charge Limited Current (DI-SCLC)

The Dark Injection Space Charge Limited Current (DI-SCLC) technique involves the application of a voltage pulse (a step function) at one of the electrodes for charge injection (rather than the laser pulse excitation used in ToF).

If the injecting electrode fulfils the condition of forming an ohmic contact with the polymer layer, to act as an effectively unlimited reservoir of charge, the induced current will be bulk limited. By monitoring the transient dark current, several features related to charge carrier movement through the bulk sample may then be observed.

In the case of space charge limited bulk conduction, the most significant feature for mobility measurements is the observation of a cusp in the DI transient, which is measured across an external

resistor (Fig. 2.17). The time at which this occurs corresponds to the arrival of the first carriers at the counter electrode given by t_{DI}, and is related to the TOF transit time by the following relationship (Many & Rakavy 1962),

$$t_{DI} = 2\left(1 - e^{-\frac{1}{2}}\right) = 0.786 t_{tr}. \qquad 2.30$$

The mobility can then be calculated from equation 2.27. The constant of proportionality between t_{DI} and t_{tr} is based on several assumptions, for example, a one-dimensional charge carrier packet, a constant mobility and negligible carrier diffusion. Later studies have attempted to better understand variations in this ratio, for example, as a consequence of the field dependence of the mobility (Goldie 1999).

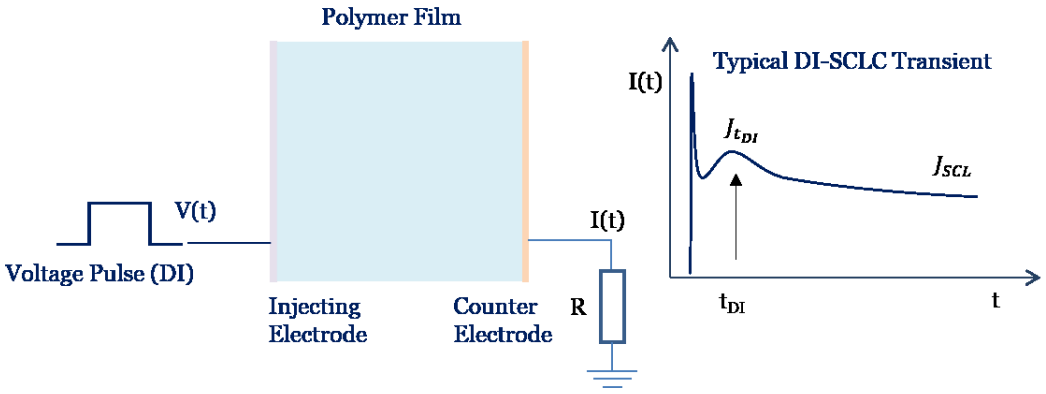

Fig. 2.17 Illustration of the DI-SCLC technique. A voltage pulse is applied at the injecting electrode and injected charges drift through the device to the counter electrode. The transient dark current is measured using an oscilloscope and a characteristic DI-SCLC transient is shown on the right highlighting the dark injection transit time (t_{DI}), the peak current ($J_{t_{DI}}$) and the steady state current (J_{SCL}).

As the injected charges progress through the film to the counter electrode, the distance between the leading edge of the charge carrier packet and the counter electrode decreases. Hence, the electric field between the leading sheet of carriers and the counter electrode is continually increasing with time as the carriers get closer to the counter electrode and the pull of this field is the reason why the space charge limited transit time, t_{DI}, is supposed to be shorter than the space charge free transit time, t_{tr}.

This increasing electric field enables the injection of more charge such that the current density rises beyond the steady-state value to a peak current density (the peak of the cusp), given by $J_{t_{DI}}$, at the time of arrival of carriers at the counter electrode. After this point, the current density tends towards the steady-state space-charge limited current, J_{SCL} (Fig. 2.17). The ratio of $J_{t_{DI}}/J_{SCL}$ in the ideal trap free SCLC case, with ohmic contacts is ≈ 1.21 (Lampert & Mark 1970).

The mobility obtained by this method shows a close correspondence to TOF mobility measurements (Poplavskyy & Nelson 2003), with the advantage that the electrodes do not have to be transparent and

the measurement can be done on thin polymer films since a minimum thickness for absorption of the laser light pulse no longer needs to be considered. The initial spike in the DI transient is related to the RC time constant where C is the sample capacitance and R is the value of the series resistance.

The final feature expected in an ideal DI transient is the decay to a steady state current density, however, for some materials the current density continues to decrease beyond J_{SCL} because of the effects of charge trapping. The reasons for this have been studied by Poplavskyy (2003) by the simulation of DI current transients with different trapping times and a single trap level.

For trapping times longer than the transit time, most of the charge carriers transit across the device without being trapped and the current density reduces following the peak until it reaches the steady state value. When the trapping time is on the same time scale as the transit time, a higher proportion of charge carriers are trapped before transporting through the device such that the maximum current is not reached and no cusp is observed in the transient. A more recent work by Harding *et al.* (2010) discusses how interfacial traps affect the DI transient and how interfacial and bulk traps may be differentiated by the use of steady-state and transient measurements.

2.17 Current-Density-Voltage Measurements

The previous two techniques are based on transient measurements, however, mobility may also be estimated by steady-state current-density-voltage measurements in the space–charge-limited regime.

One of the key requirements for the measurement of current-density vs. voltage is ohmic injection to ensure that measurements correspond to the bulk characteristics of the device, otherwise an injection-limited current is observed (Rose 1955). Hence, injecting electrodes are selected to minimise the energetic barrier to injection for electrons or holes to the LUMO or HOMO, respectively.

The relation between space-charge limited current density and voltage for a perfect insulator at zero temperature such that the background density of free charge, n_0, from impurities or defects is negligible, is given by Child's Law (known as the steady-state TFSCLC Mott-Gurney equation for a field-independent mobility):

$$J_{TFSCL} = \frac{9}{8}\epsilon_r\epsilon_0\mu\frac{V^2}{d^3} \qquad 2.31$$

where ϵ_r is the relative permittivity, ϵ_0 is the vacuum permittivity and d is the thickness of the sample. At low applied voltages where the injected carrier density is much lower than the background density (i.e. $n_{inj} << n_0$) the current density follows Ohm's Law and is given by:

$$J = en_0\mu\left(\frac{V}{d}\right). \qquad 2.32$$

As the voltage is increased further, Child's Law (equation 2.31) is observed, which describes the trap-free space charge limited (TFSCLC) regime. Intrinsic traps in organic semiconductors reduce the current density, however, at a certain voltage, the majority of traps will be filled, and the trap free space-charge limited current density will be observed.

In the case of amorphous organic materials, transport is assumed to be trap free and the mobility is found to have a strong field and temperature dependence according to the Poole-Frenkel relationship:

$$\mu = \mu_0 \exp(\beta\sqrt{E}) \qquad 2.33$$

where μ_0 and β are temperature dependent parameters discussed earlier in this chapter and E is the electric field. The equation for the steady-state TFSCLC for a field dependent μ is given by the Murgatroyd equation as follows (Murgatroyd 1970),

$$J_{TFSCLC} = \frac{9}{8}\epsilon_r\epsilon_0\mu_0 \exp\left(0.89\beta\sqrt{\frac{V}{d}}\right)\left(\frac{V^2}{d^3}\right). \qquad 2.34$$

For a device in the SCL regime, there is a non-uniform distribution of space charge and therefore a non-uniform electric field. The space-charge limited current is thus given as a function of V rather than the field, E (Poplavskyy (2003)).

Deviations from the trap-free model can be used to determine whether a contact is ohmic and a figure of merit can be calculated for the injection efficiency, $\chi(F)$ (Abkowitz *et al.* 1998; Campbell *et al.* 2001b):

$$\chi(F) = \frac{J_{Measured}(F)}{J_{TFSCLC}(F)}. \qquad 2.35$$

2.18 Organic Field-Effect Transistor Measurements

Measurement of the characteristics of field-effect transistors provides another perspective on charge transport in semiconducting polymers, which is charge transport parallel to the interface, compared to measurements of bulk mobility obtained from TOF and DI-SCLC measurements, which occurs in the perpendicular direction.

The charge carrier mobility is extracted from I-V expressions derived for inorganic FETs based on the gradual channel approximation. The essential components of a FET are source and drain electrodes of width W, separated by a distance L. Between the source and drain is the channel that contains the semiconducting polymer, which is a thin film of spin-coated polymer. Between the gate, and the polymer is an insulating dielectric layer.

A number of configurations are possible, for example top-contact bottom-gate or bottom-contact top-gate (Fig. 2.18 and Fig. 2.19).

Fig. 2.18 Schematic of a top-contact bottom gate (TCBG) OFET with a thermally evaporated MoO_3 interlayer

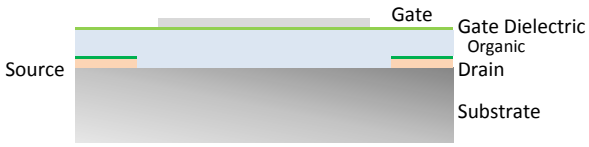

Fig. 2.19 Schematic of a bottom-contact top-gate (BCTG) OFET

The choice of structure may be based on the requirements of the materials involved. For example, the relative surface energies that a polymer solution requires to wet a substrate or dielectric layer and the need for orthogonal solvents in the case of a top gate structure where the dielectric layer is spin coated on top of the semiconducting polymer.

In addition to this, it is necessary to consider additional layers such as self-assembled monolayers (SAMs), which may be used to modify work functions by introducing an interface dipole, to modify surface energy, for the passivation of silanol and other OH-groups, or as the dielectric itself.

The basic operation of an FET, explanations of the operating regimes and the derivation of equations using the gradual channel approximation are described in numerous sources (Zaumseil & Sirringhaus 2007).

The key equations for current-voltage characteristics in the linear ($V_{DS} << V_{GS} - V_T$) and saturation ($V_{DS} >> V_{GS} - V_T$) regimes are

$$I_{DS,lin} = \frac{W}{L}\mu C_i(V_{GS} - V_T)V_{DS} \qquad 2.36$$

$$I_{DS,sat} = \frac{W}{2L}\mu C_i(V_{GS} - V_T)^2. \qquad 2.37$$

The field effect mobility, μ_{FET}, in the linear regime is calculated from the slope of the measured transfer characteristics (I_{DS} vs. V_{GS}) using

$$\mu_{lin} = \frac{\partial I_{DS}}{\partial V_{GS}}\left(\frac{L}{WC_i V_{DS}}\right). \quad 2.38$$

The mobility in the saturation regime is then given by

$$\mu_{sat} = \frac{\partial^2 I_{DS,sat}}{\partial V_{GS}^2}\left(\frac{L}{WC_i}\right). \quad 2.39$$

For polymers with an aligned microstructure, the measured FET mobility is highly dependent on the alignment of the polymer in the channel and since the measurement direction is perpendicular to that of the ToF technique, the charge carrier mobility measured may be orders of magnitude different in the two techniques in some circumstances. In addition, the charge densities are very different, such that trap filling occurs for FET measurements, which results in higher mobility values than ToF.

In OFETs, transport may be affected by structural defects in the organic layer and by the presence of traps at the interface. This structural and energetic disorder along the interface results in "percolation motion" and rate limiting of transport (Sirringhaus *et al.* 2010).

Dynamic disorder caused by fluctuations in intermolecular packing on the timescale of carrier motion may hinder charge transfer as the molecular configuration alternates between states where charge transfer is favourable and unfavourable (Sirringhaus *et al.* 2010; Brédas *et al.* 2002). It is therefore important to reduce these effects by selection of appropriate gate dielectrics.

2.19 Gate Dielectrics

The selection of gate dielectric is guided by compatibility with other processing steps and the need to avoid the deleterious effects to charge transport of a poorly chosen dielectric. A poor choice of dielectric may make it difficult to identify problems elsewhere with the FET configuration, such as injection limited contacts and may result in underestimating the potential of a particular polymer.

As mentioned previously, surface wetting and solvent orthogonality are essential considerations. The insulating dielectric, which is the substrate in TCBG FETs, may affect the morphology of the polymer when spin coated or drop cast. For example, greater physical roughness of the interface inhibits the growth of crystal domains (Veres *et al.* 2004) and affects charge transport because of differences in molecular orientation at the dielectric interface. Such inhomogeneity would present an "energy landscape" to charges hopping through the channel at the interface.(So *et al.* 2011)

There are many inorganic and organic dielectrics available, many of which are discussed in detail in several reviews (Veres *et al.* 2003; Veres *et al.* 2004). Organics dielectrics typically contain less trap states from "dangling bonds" or -OH group functionalisation that affects bare inorganic dielectric

substrates such as silicon dioxide. Additional treatment is therefore required such as oxygen plasma exposure and complementary self-assembled monolayers (SAMs) such as octadecyltrichlorosilane (OTS) or hexamethyldisilazane (HMDS), which passivate these groups. In the top-contact bottom-gate FETs fabricated in this work, OTS is used for this purpose.

For the insulating dielectric in bottom-contact top-gate structures in this work, a fluoropolymer, CYTOP™ (Kalb *et al.* 2007), is used which is dissolved in a fluorinated solvent known as CT-SOLV 180™ and is selected based on the requirement of solvent orthogonality with the polymer layer.

2.20 Discussion on Charge Transport Measurement Techniques

Measurements using the FET technique can often obscure the intrinsic nature of charge transport in a material for several reasons. For example, the use of a gate dielectric may introduces interface states and possibly impurities that reduce mobility. Other important differences, which relate to fundamental device physics must also be considered, in particular, how the derivation of mobility from source drain I-V measurements of FETs relates to the bulk mobility of TOF and DI measurements, especially since charge transport is parallel to the interface for FETs and perpendicular for TOF and DI.

The main differences and limitations are discussed by Rawcliffe *et al.* (2003). The first issue is whether the FET equations derived from inorganic semiconductor theory are applicable for organic FETs especially since key principles such as the depletion and inversion regimes are essentially meaningless in the latter because of the negligible intrinsic and extrinsic carrier densities. Furthermore, the injection barrier required for the accumulation of carriers requires a different interpretation of the turn-on voltage. Despite these problems, the source-drain I-V characteristics are very similar to inorganic FETs and the equations are widely considered a valid approximation.

The second issue discussed is the fact that mobility may be affected by the high carrier densities in the conduction channel of an FET when compared to TOF measurements where the carrier density is kept as low as possible to avoid space-charge effects. This may alter the effective level of energetic disorder by filling of deep traps. However, there may be better agreement of FET mobility with the DI-SCLC mobility since in this case the carrier density is also maximised. The three measurements combined therefore provide a useful cross-reference for mobility in different regimes of charge carrier density.

Thirdly, there may be significant differences in the morphology of the thick films used for TOF and the thin films used for FETs. The DI-SCLC is again a useful validation since both types of film can be studied and all techniques combined may allow for a more detailed study of intrachain and interchain charge transport. Finally, TOF measurements where transport is dispersive result in a vaguer interpretation of the mobility and it remains unclear how it relates to mobility from FET and DI

measurements. Hence, we will consider each of these issues throughout this thesis using charge transport measurements and attempt to make comparisons between the techniques wherever possible.

CHAPTER 3

3 EXPERIMENTAL METHODS

This section provides detailed information of the experimental procedures used throughout this thesis and the routines adhered to for sample preparation.

3.1 Device Fabrication for Charge Transport Measurements

The basic TOF and DI device structure is illustrated in Fig. 3.1 and consists of ITO on quartz substrates onto which the polymer is spin coated followed by evaporation of counter electrodes.

A standard cleaning procedure is followed to clean the ITO on quartz substrates involving removal of photoresist with acetone followed by ultrasonication, first in acetone and then in IPA at least twice. The substrates are removed from their holder, given a final rinse in IPA and dried individually with N_2. Prior to spin coating, the ITO is subjected to O_2 plasma treatment. The spin coating parameters are tuned according to the solution concentration, its viscosity and the desired film thickness.

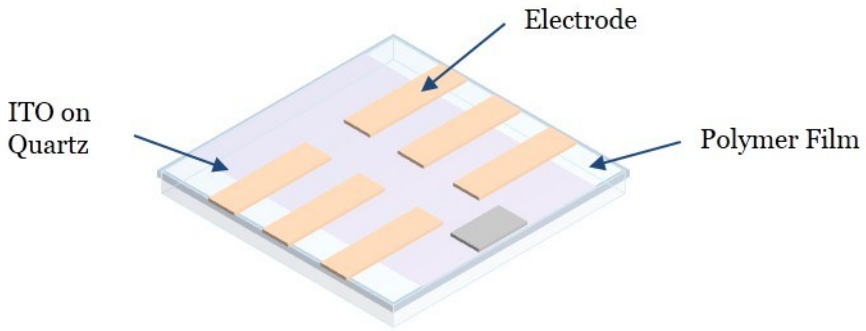

Fig. 3.1 ITO on quartz device strucutre used for TOF, DI and J-V measurements with thermally evaporated contacts.

As discussed, the most important requirement to reach the space charge limited current regime for DI measurements is to use an injecting electrode that can inject sufficient charge carriers, in this case holes, into the HOMO level of the polymer being studied by having as small an energy barrier as possible. Such an electrode is known as an ohmic contact. The simulations of Poplavskyy (2003) showed that a barrier for hole injection of up to 0.35eV is still able to provide enough charge to reach space charge limited current, although the current amplitude is around half of that in the case of true ohmic contact. A useful definition proposed in the work is therefore that an ohmic contact is any contact that is capable of providing an injection current equal to the maximum space charge limited current or within a factor of two.

Despite this small degree of flexibility in requirements to reach SCLC and the definition of ohmic injection, it is still a significant challenge to find suitable contacts for the class of blue-emitting, wide-band gap copolymers under investigation in this work because of they have HOMO levels of ~5.84eV.

The work functions of common electrodes are summarised in Table 3.1 where it is clear that even cleaned platinum is only just suitable as an electrode for injection into these polymers.

Table 3.1 Work functions of typical hole injection electrodes (Hwang et al. 2009)

	Work function, Φ (eV)
Aluminium	4.06 to 4.26
ITO	4.4
PEDOT:PSS interlayer	5.2±0.1
Gold	4.7 (contaminated), 5 (ozone treated) to 5.4 (clean)
Platinum	5.1 to ~5.5 (clean)

Despite the hole injection barrier between PEDOT:PSS and the HOMO of PFO at ~5.8eV, it has been demonstrated that it can be used for ohmic injection by an electrical conditioning procedure (Poplavskyy *et al.* 2003). The conditioning results in the formation of an interfacial dipole layer that reduces the barrier for injection such that it becomes ohmic, which is confirmed by DI-SCLC measurements. However, it is noted that the conditioning is non-uniform.

One advantage of PEDOT:PSS is that it provides passivation of surface defects and presents a smoother surface than ITO for the subsequent layer, however, it is not ideal in a number of other ways, such as the fact that it degrades under UV illumination (Cattin *et al.* 2009). It is dissolved in water, which could get into the active layer requiring baking at ~120°C to remove the water thus making it unsuitable for device structures where the layer cannot be prepared outside a glovebox.

Recent work on transition metal oxides has shown they may be used with polymers with deep-lying HOMO levels for ohmic hole injection (Nicolai et al. 2010).

3.2 Time-of-Flight Photocurrent

Following on from the theoretical basis of the ToF experiment, we describe the experimental method here. In the case of room temperature measurements, a sample with a configuration as shown as in Fig. 3.1 is inserted into a sample chamber flushed with nitrogen gas, which is placed facing towards the laser in the beam path. For temperature dependent measurements, the sample is placed in an Oxford Instruments Optistat cryostat with a quartz glass optical window for optical access by the laser. The temperature in this case is controlled by an Oxford Instruments ITC503 Temperature Controller unit.

A DC bias voltage is applied to the device from a Keithley 237 source-meter and the light pulse generated by a frequency tripled Quantel Nd:YAG pulsed laser with a wavelength of 355 nm and pulse width of approximately 6 ns. The photocurrent signal is measured across a resistor in series with the sample and is displayed on a 500 MHz Tektronix TDS 3052 oscilloscope and data captured via LabView. The value of the series resistor is chosen to keep the RC response of the circuit as low as possible yet large enough to ensure the signal-to-noise ratio is sufficient to observe the features in the transient photocurrent.

The laser intensity is modulated by a neutral density filter in the beam path to ensure the generated charge density does not disturb the uniformity of the applied electric field. The total charge collected Q may be obtained by integrating the area under the transient current and is kept at less than ten percent of the sample capacitance charge given by $Q_0 = CV$ where C is the device capacitance and V is the applied voltage.

3.3 Current-Density Voltage Measurement of Space-Charge Limited Current

The method for current-density voltage measurements is very straightforward as it only requires a voltage sweep and current measurement at each voltage, however, finding optimum contacts for ohmic injection presents many challenges as discussed.

The measurements are conducted in the dark using a Keithley 237 source-measure unit, which applies a steady-state voltage in steps for a given time and measures the current simultaneously. The data is captured via a LabView application.

3.4 Dark-Injection Space-Charge Limited Current

The DI-SCLC technique is conducted with the same sample configuration and chamber as the ToF experiment. Instead of a laser pulse, a pulse generator, in this case an HP 8114A with a rise time of less than 10 ns, is used to apply a voltage step to the sample. The sample chamber window is covered to ensure no light reaches the sample. A time-varying current is detected by an oscilloscope (a 500

MHz Tektronix TDS 3052) connected across a series resistor, which has the same requirement as in ToF of being low enough to keep the RC response of the circuit shorter than the dark injection transit time, that is, where the cusp occurs in the transient current.

3.5 Field Effect Transistor Measurements | FET Device Preparation

For top-contact bottom gate FETs, highly doped silicon substrates were selected as a common gate electrode with a thermally grown SiO_2 insulating layer onto which a monolayer of OTS was prepared by Jeremy Smith according to a standard procedure of immersion of the substrate in a toluene solution for over 20 minutes at 60°C. Polymers solutions were spin-coated at 2000 rpm from toluene in initial samples and then from chloroform to improve wetting of the surface. This was followed by evaporation of a thin MoO_3 interlayer capped with a layer of gold through a shadow mask with a range of device geometries of source and drain electrodes.

In the case of bottom-contact, top-gate FETs, Au and the MoO_3 interlayer were evaporated on to Schott Borofloat glass. The polymers were spin coated from toluene solutions and dried at 80°C before spin coating of a 900 nm layer of the CYTOP dielectric, which was dried at 100°C before deposition of Al gate electrodes.

3.6 Optical Measurements

UV-Vis absorption and photoluminescence measurements are essential tools for characterising material systems. Absorption measurements, for example, may be use to approximate the optical band gap and the LUMO level if the HOMO level has already been measured. In addition, it can be a useful, non-destructive tool for estimating film thickness from the Beer-Lambert relation and for comparing the quality of the polymer-substrate interface by the observation of Fabry-Perot oscillations.

Absorption and PL spectra can reveal the presence of defects and impurities, for example, oxidation of the polymer (keto defects) that are photo-induced or from aging and can be seen as emission in the green band (Keivanidis *et al.* 2005). Different morphologies of polymers also exhibit different photophysics and spectral fingerprints such as the β-phase of PFO (Rothe *et al.* 2004).

Furthermore, knowing the absorption of a material is useful for estimating the absorbed pump energy in ASE measurements and the absorption depth of photogenerated carriers in TOF measurements.

3.7 Sample Preparation for Optical Measurements

The film preparation for absorption and photoluminescence measurements is identical to that of the preparation for ASE and optical gain measurements, which require polymer waveguides; hence, we describe the preparation of the polymer waveguides that are used for all of these optical techniques.

3.8 Polymer Waveguide Preparation

Samples are prepared in a cleanroom environment to minimise the number of particles from the air that may be large enough to cause optical defects in thin films.

Solutions of the polymers are prepared in toluene for spin coating on fused silica substrates. The solution concentration is variable according to the molecular weight of the polymer in order to achieve a particular film thickness. Solutions are stirred using magnetic stirrers for several hours at 70°C.

The substrates are Spectrosil 2000 fused silica with a low refractive index of 1.47 at 400 nm. The cleaning procedure involves immersion in an ultrasonic bath, first with acetone, then IPA. The cleaning solution is blown away with nitrogen gas then placed on a hot plate at 100°C. Finally, the substrates are exposed to oxygen plasma before proceeding with spin-coating the solutions.

The main parameters for spin-coating polymer films include the acceleration, spin speed, the choice of solvent and concentration, and the ambient temperature and humidity. In most cases, the spin speed is 2000 rpm in order to achieve the required film thickness to achieve confinement of the light in an asymmetric planar waveguide structure. This thickness is typically ~100 nm for the polymers investigated in this thesis, which is below the cut-off thickness for the bound propagation mode of these polymers. The film thickness is measured using an alpha-step surface profilometer

Finally, the uncoated side of the substrate is cleaned to remove any polymer residue and samples are stored in a desiccator between measurements.

3.9 Optical Absorption in the UV and Visible Regions (UV-Vis)

UV-Vis absorption is measured using a Shimadzu UV-2550 UV-Vis spectrophotometer, which has two lamps to cover wavelengths from 190 nm to 900 nm. Light is converged into a beam and passed through a monochromator and then through the sample.

The transmission through the sample at discrete wavelength steps is measured. The transmittance, defined as $T = {}^{I}/_{I_o}$, where I_0 and I are the intensities of the incident and transmitted light, is used to calculate the absorbance by:

$$A = -\log_{10}\left(\frac{I}{I_o}\right). \quad 3.1$$

The absorbance of the film is corrected for with the absorption of a reference substrate and given by:

$$A_{film} = -\log_{10}\left(\frac{T_{film\ \&\ substrate}}{T_{substrate}}\right) \quad 3.2$$
$$= -OD$$

where OD is the optical density. The absorption coefficient, α, is thus calculated by the Beer-Lambert relation:

$$I = I_0 e^{-\alpha d} \quad 3.3$$

$$\alpha = \left(\frac{A}{d}\right) \ln 10$$

with

$$\alpha = \left(\frac{A}{d}\right) \ln 10 \quad 3.4$$

where d is the film thickness measured by surface profilometry with an Alpha-Step 200 surface profilometer.

The substrates used are 12 x 12 mm fused Silica Spectrosil 2000 substrates, which according to the manufacturer's specifications have optical transmission over 90 % from 200 nm to 2000 nm and a refractive index of 1.47 at 400 nm. The transmittance is shown in Fig. 3.2.

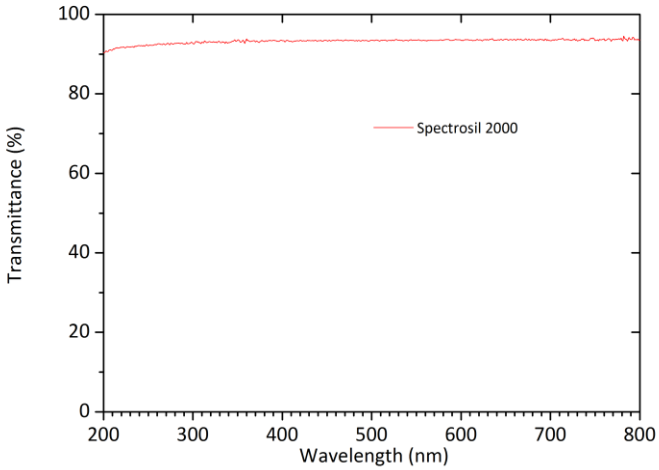

Fig. 3.2 Transmittance of a Spectrosil 2000 substrate

Reflection from substrates is estimated by:

$$R = \frac{(n_1 - n_{sub})}{(n_1 + n_{sub})} \quad 3.5$$

where n_1 is the refractive index of the film and n_{sub} is the refractive index of the substrate. In the case of PFO with n of 1.78 at 384 nm, the reflection from the substrate is up to 9.5 % and for high refractive index polymers such as SC005, a PFO F8F5 copolymer, n is 1.96 at 381 nm and the reflection from the substrate is 14.2 %.

Reflection is therefore an important consideration for UV-Vis measurements of high mobility polymers that are believed to have improved charge transport by dense chain packing, which can be characterised by refractive index measurements.

3.10 Photoluminescence (PL) and Photoluminescence Quantum Efficiency (PLQE)

Photoluminescence (PL) spectra is measured using a Jobin Yvon Horiba Spex Fluoromax 3 spectrofluorometer with a 150W xenon arc lamp that provides continuous light output. The excitation wavelength is selected by a monochromator and approximately 8 % of the light output is directed to a reference detector, which monitors the output intensity as a function of time and wavelength for correcting recorded data.

Parameters of the measurement, such as excitation wavelength, slit widths and integration time, are controlled and recorded using Datamax spectroscopy software. The excitation wavelength is set at the peak absorption of the material. The width of the entrance slit of the excitation spectrometer controls the intensity of the light incident on the sample and the width of the exit slit of the emission spectrometer controls the measured intensity of the emission. Wider slit widths increase the magnitude of the detected signal as well as the noise so narrower slit widths are preferred for better spectral resolution.

PLQE is measured and analysed using the integrating sphere technique proposed by de Mello *et al.* (1997). The PLQE of a material is defined as the ratio of the number of emitted and absorbed photons. The sample is placed in an integrating sphere made from $BaSO_4$, which provides a highly reflective and diffusive surface for photons to be captured by the detector and three measurements are taken:

a) Empty sphere
b) Sample in the sphere where it does not intersect the beam
c) Sample mounted in the sphere so that it intersects the path of the excitation beam

The emission spectrum shows a distinct peak, corresponding to the excitation beam, and a broad emission region when the sample is in the sphere.

In each case, the intensity of the excitation beam varies with the sample in its different positions such that the integral of the peak corresponds to the fraction of light not absorbed by the sample. Similarly, the area under the emission region curve corresponds to the amount of light emitted by the sample when in different positions in the sphere (after correcting for the sphere absorption). The integrated areas of the excitation peak are denoted L_a, L_b and L_c and the areas from the emission region are labelled P_b and P_c.

The PLQE is thus given by:

$$\eta = \frac{(P_c - (1 - A)P_b)}{L_a A} \qquad 3.6$$

where $A = 1 - (\frac{L_c}{L_b})$. We assume the integrating sphere has a uniform response and, for reference, we obtained PLQEs of 79 % and 75 % for PFO and F8BT, respectively, using this technique with an error range of ±15 %.

3.11 Amplified Spontaneous Emission (ASE)

Amplified spontaneous emission measurements provide an indication of the potential of a material for lasing by using stimulated emission to observe the amplification of spontaneously emitted photons without the optical feedback required for lasing, hence it is also known as “mirror-less lasing”.

ASE is measured using thin films of the polymer spin coated on fused silica substrates to make asymmetric planar waveguides. A stripe-shaped excitation is applied near the edge of the sample and the emission of light at the edge is observed. At a sufficient incident energy density, the amplified spontaneous emission becomes apparent and is waveguided along the stripe to the edge (Fig. 3.3).

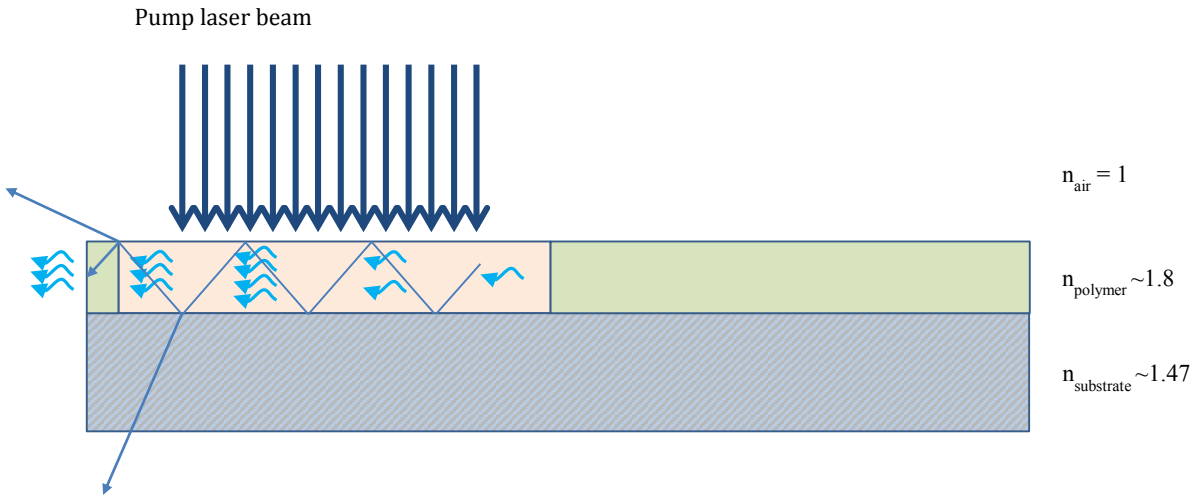

Fig. 3.3 Schematic of an asymmetric planar waveguide used for measuring ASE showing an incident laser beam with a flat-top intensity profile and light emission being waveguided through the polymer film to its edge.

Since the refractive index of the polymer thin film is higher than the air and the substrate, the incident light is confined and waveguided to the edge where a microscope objectives and an optical light-guide direct the light to a detector.

The ASE spectra appears as a narrowing of the emission spectrum as the PL collapses to a peak in the emission corresponding to the 0-1 energy level transition, with an associated increase in intensity as the pump energy is increased beyond a certain threshold. The requirements of the measurement are a homogeneous pump intensity distribution and a stripe shaped excitation, which needs to have an intensity profile that is as flat as possible.

The polymer film thickness for ASE measurements is dictated by the cut-off thickness of a single optical mode. The cut-off thickness for transverse electric (TE) modes in an asymmetric planar waveguide is given by:

$$d_{cut-off,TE} = \frac{\lambda_{ASE}}{2\pi\sqrt{n^2 - n_{sub}}}\left[\tan^{-1}\left(\frac{\sqrt{n^2 - n_{air}}}{\sqrt{n^2 + n_{sub}}}\right) + m\pi\right] \quad 3.7$$

where m is the mode number and λ_{ASE} is the wavelength of the ASE (M. Campoy-Quiles *et al.* 2005; Azuma *et al.* 2007).

For PFO, which has a refractive index of 1.78 and λ_{ASE} of 451 nm, the cut-off thicknesses for the zero order and first order TE modes are 58.7 nm and 283 nm, respectively. Higher refractive index polymers such as the F8F5 copolymers with $n = 1.96$ have cut-off thicknesses for the zero order and first order TE modes of 38.4 nm and 212 nm respectively.

The refractive indices of these polymers can be used as reasonable approximations for polymer films in this study and the thickness of spin-coated films is therefore between these two extremes.

3.12 Experimental Configuration for ASE Measurements

The basic experimental set-up includes a pump laser, which passes through an array of optics to create a narrow stripe shaped beam. The main components are illustrated in (Fig. 3.4). A Mechanical aperture is used to control the dimensions of the beam and a translation stage to position the stripe on the sample.

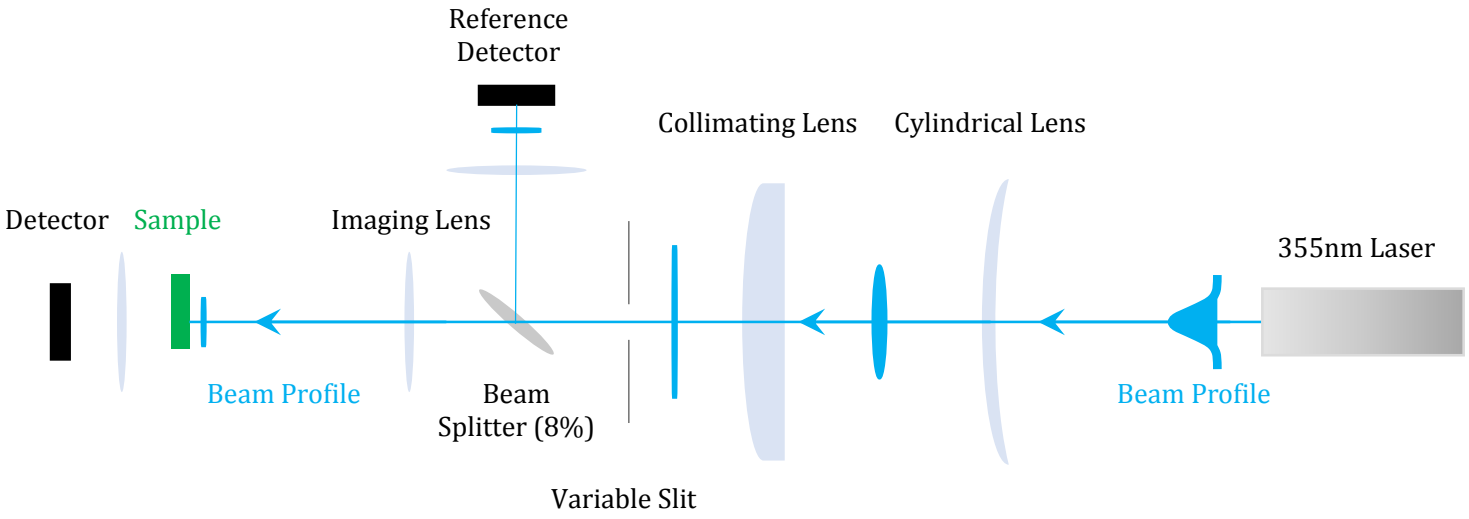

Fig. 3.4 Schematic of the experimental configuration for ASE measurements.

The laser beam is provided by a CrystaLaser LC model QL355-100-X diode laser pulsed at 10Hz with a pulse width of ~10 ns and a wavelength of 355nm. Experiments are performed with and without the presence of a polariser in the path of the laser beam, although this is not expected to affect the emission from the polymer because of the isotropic distribution of polymer chains in the film.

The energy incident on the sample is controlled by a computer controlled neutral density filter wheel. When there is no sample in the path of laser beam, a detector measures the beam energy directly, when the sample is present, a beam splitter in the path of the laser directs a fraction (8 %) of the incident beam to a reference detector such that the energy of each pulse striking the sample is recorded.

The array of optics used to create the narrow striped shape excitation requires meticulous alignment to achieve a flat top intensity profile. The optical elements in the light path are a cylindrical lens, a collimating lens and an imaging lens to pass the image of the beam at the slit onto the sample.

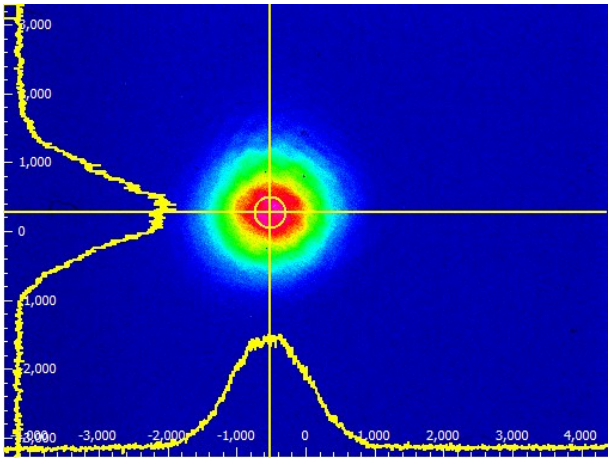

Fig. 3.5 Beam profile image showing the Gaussian intensity of the laser beam before re-shaping.

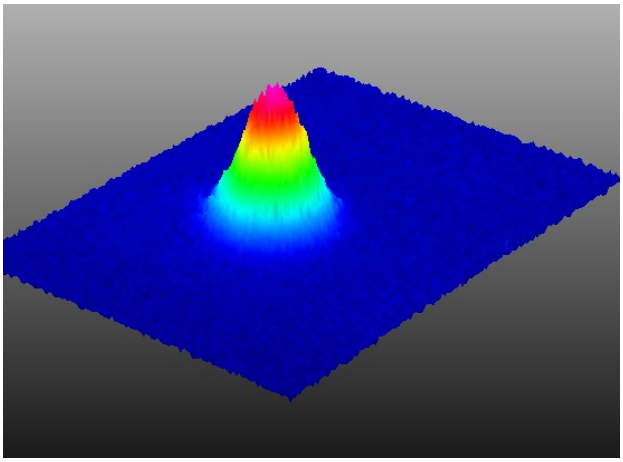

Fig. 3.6 Isometric projection of the laser beam profile showing its Gaussian intensity before re-shaping.

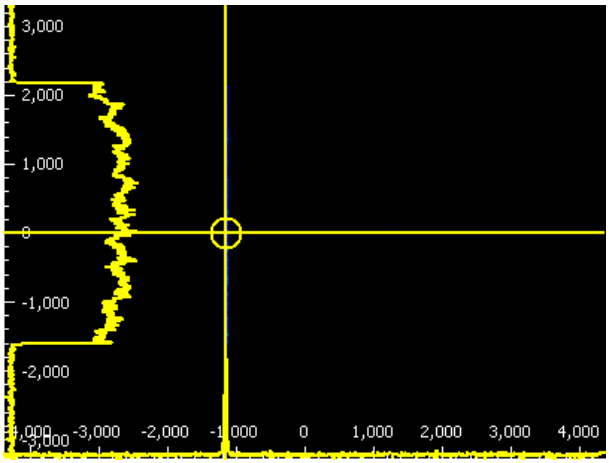

Fig. 3.7 Laser beam intensity profile after passing through optics to achieve a flat-top intensity profile.

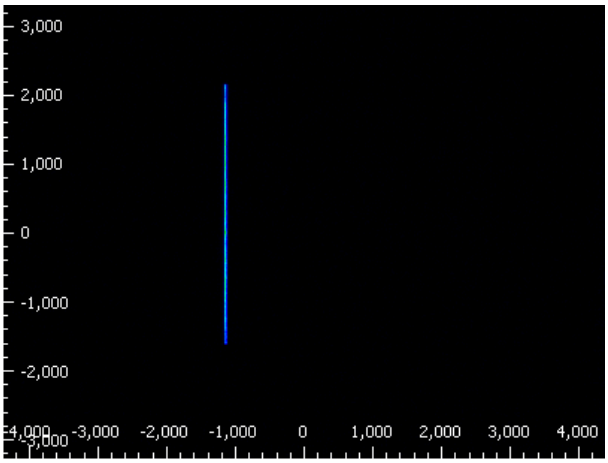

Fig. 3.8 Beam profile image of the laser stripe used for ASE and optical gain measurements.

The main consideration regarding the excitation stripe is that it has a flat intensity profile flat in both dimensions and the width should be sufficiently narrow to approximate a one-dimensional stripe as required by the model for optical gain described. The Gaussian shape of the laser excitation is shown in Fig. 3.5 and the re-shaped laser stripe that is incident on the sample for ASE measurements is shown in Fig. 3.7 and Fig. 3.8.

The Gaussian profile of the pump beam can cause variation in the intensity profile of the stripe and the consequent inhomogeneity in the pump beam intensity may result in some areas being focussed to higher intensities that may damage the polymer. Such hot spots have been avoided by alignment of the optics in the path of the laser and the stripe has a uniformity of over 90 % from edge to edge.

The emission is waveguided along the stripe and the output from the edge of the sample is focussed into an optical fibre using a microscope objective lens, which guides the light to a Princeton Instruments Acton SpectraPro 2300i spectrometer and Princeton Instruments Pixis 400 charge-

coupled device (CCD). An isotropic PL emission is also emitted from the edge, which is filtered by alignment of the microscope objective and a TE polariser before the optical waveguide.

3.13 Optical Gain Measurements

The use of asymmetric waveguides for measuring gains yields the modal gain since we observe the gain of an optical mode propagating through the wave-guiding structure rather than the material gain, which is the optical gain in a free medium.

In order to extract the net modal gain, the ASE signal intensity I_{ASE} in the small signal regime, that is when the ASE signal is less than the saturation intensity, is fitted to the following expression (Cerdán *et al.* 2010)

$$I_{ASE}(L) = \frac{\Omega}{g}(e^{gL} - 1) \tag{3.8}$$

where L is the stripe length Ω is the spontaneous emission parameter and g is the net modal gain. At short pump lengths or low pump intensities, that is when $gL \ll 1$, fluorescence dominates over ASE and 3.8 may be approximated by

$$I_F(L) \approx \Omega L \tag{3.9}$$

which shows that before threshold the fluorescence intensity increases linearly with stripe length. After threshold, ASE output intensity becomes twice the fluorescence intensity such that

$$I_{ASE}(L_{th}) \approx 2I_F(L_{th}). \tag{3.10}$$

The optical gain may be evaluated by the variable stripe length technique introduced by Shaklee in 1971 in their study of semiconductor crystals (Shaklee 1971) or by the variable pump intensity technique. In the former, the sample is irradiated with a stripe shaped excitation and the emission from the edge is collected, as described earlier. Increasing the length of the stripe, leads to a superlinear increase in emission intensity after threshold and the optical gain is obtained by fitting the ASE intensity I_{ASE} as a function of L for a particular pump energy density.

The alternative technique is the variable pump intensity technique in which I_{ASE} is measured as a function of E_{pump} at a fixed stripe length.

Here the system is configured such that the data for both techniques is obtained simultaneously and the gain parameters from both techniques may be obtained and compared.

CHAPTER 4

4 CHARGE CARRIER INJECTION AND TRANSPORT IN THE POLYFLUORENE HOMOPOLYMER POLY(9,9-DIOCTYLFLUORENE) (PFO)

The charge transport of PFO is revisited in this chapter, based on developments in the use of transition metal oxides as hole injecting electrodes which have enabled the use of Dark Injection Space Charge Limited Current (DI-SCLC) and field effect transistor (FET) techniques for investigating hole transport in particular.

The challenge of finding suitable injecting electrodes has precluded the use of these two techniques for measuring the hole mobility of polymers with highest occupied molecular orbital (HOMO) levels more than 5.6eV below the vacuum level, of which PFO is a prominent example, with a HOMO level of ~5.8eV,

The use of Molybdenum (VI) Oxide (MoO_3), as an ohmic contact for hole injection has thus made it possible to investigate hole mobilities using DI-SCLC and FET measurements to complement ToF measurements, which have been utilised alone extensively in many prior studies of charge transport in PFO. These techniques span several orders of magnitude in charge carrier density which provides an additional perspective on charge transport in PFO and materials with similar energy levels. This chapter also provides a background for charge transport measurements on the copolymers introduced in subsequent chapters.

4.1 Introduction

Recent studies of charge transport in polymer semiconducting materials have typically been conducted by measurements of organic field-effect transistors (OFETs). The polymer of interest is used as the active layer in the channel of the FET and the charge carrier mobility may be obtained from source-drain current voltage characteristics.

This has particularly been the case for studies of novel high mobility polymers, which have been investigated in the FET configuration almost exclusively. In order to produce a functional field-effect transistor, several design considerations are involved, such as the choice of the contact electrodes, the gate dielectric, the substrate and the overall layout of the device, including the dimensions of the active channel.

It has been demonstrated that all of these parameters have an effect on the performance of a field-effect transistor such that the FET mobility may not represent an intrinsic property of the material under investigation. Nevertheless, FET mobility has become the standard for comparing materials and highlighting milestones in the development of semiconducting polymers. Amongst the highest recorded OFET hole mobilities to date is that of a macroscopically aligned polymer, with $\mu = 23.7\ cm^2/Vs$ (Tseng *et al.* 2014).

Other techniques to investigate charge transport include transient Time of Flight photocurrent and Dark Injection Space Charge Limited Current measurements. The former has already been used extensively to study poly(9,9-dioctylfluorene) and many other materials. It has been shown the PFO has non-dispersive hole transport and a mobility of ~10^{-4} cm^2/Vs (Redecker *et al.* 1998). It has also been demonstrated by ToF measurements that its hole mobility may be enhanced in aligned glassy nematic films to 8.5 x 10^{-3} cm^2/Vs (Redecker, D. D. C. Bradley, *et al.* 1999).

The DI-SCLC measurement is conducted on a device that resembles a typical polymer light-emitting diode and requires an injecting electrode with ohmic contact for injection of the charge carrier of interest. An interlayer of PEDOT:PSS, with a work function of ~5.2 eV, may be used to provide ohmic contact with PFO, despite its IP of 5.8 eV, using an indirect method of electrical conditioning (Poplavskyy *et al.* 2003). In this case, a hole mobility of ~10^{-4} cm^2/Vs was measured.

More recently, ohmic contact with PFO has been achieved in SCLC measurements using a molybdenum trioxide interlayer (Nicolai *et al.* 2010) and has consequently opened the way towards functional devices using plastic electronic materials with deep HOMO levels and also charge transport studies that include measurements from a wider range of techniques.

Here we present the results of charge carrier mobility measurements of PFO FETs as well as the results of dark injection SCLC measurements, which have been obtained directly without prior

electrical conditioning. The results herein thus contribute to an extensive collection of literature on PFO and updates the record of data on PFO with measurements of its FET hole mobility, directly obtained DI-SCLC hole mobility and in addition contains the results from measurements by the photo-generated charge extraction by linear increase in voltage (Photo-CELIV) technique.

4.2 PFO Background

One of the key aspects of the significant interest in poly(9,9-dioctylfluorene) has been its wide range of phase behaviours such as isotropic, liquid crystalline, crystalline and a phase particular to itself known as the beta-phase. Here we briefly review the morphological characteristics of PFO in order discuss their implications for charge carrier transport and mobility.

PFO is similar to the class of hairy rod polymers with a semi-rigid backbone although the side chains lie perpendicular to the plane of the aromatic rings instead of being coplanar as is typical of this class of polymer (M. Grell *et al.* 1999).

It is known to be semi-crystalline with a key crystalline phase (α) and a modified form of this phase (α') with differences in molecular packing and co-planarity of backbones (S. H. Chen *et al.* 2005). It has a melting temperature of ~170°C above which it enters a glassy nematic LC phase, then at 270°C to 280°C it becomes isotropic (Grell *et al.* 1997). Spin-coated films are found to have a mixture of these phases, where the majority component is a glassy matrix and crystallinity may be induced by thermal annealing. The beta-phase is also present to some degree without specific procedures to control its formation.

Beta-phase was first identified as a form of very high intra-chain order or in other words, extended conformation, of a polymer chain in PFO. It may be induced by processes that cause stress within the polymer film such as casting from a poor solvent or a solvent mixture, processing with different temperature cycles or solvent vapour exposure. X-ray measurements have shown that the beta-phase has a "planar zigzag" structure or 2_1 helical conformation (i.e. two monomer units per turn of the helix), which is structurally similar to LPPPs with a fully planar backbone conformation. The intrachain correlation length of beta-phase varies according to different procedures however, it is typically around 22 nm (26 monomer units) compared to the alpha phase, which has a length of approximately 15 nm (18 monomer units) (Grell *et al.* 1998; M. Grell *et al.* 1999).

Da Como *et al.* found that under toluene exposure, the beta-phase is preferentially formed in extended polymer chains by re-ordering of torsional angles between monomers of single chains unlike the rearrangement of multiple polymer chains involved in the formation of crystalline phases (Da Como *et al.* 2007). Furthermore, the process of beta-phase formation by toluene exposure was not found to induce further chain extension.

Beta-phase is a feature particular to PFO, although in the series of poly(9,9-di-alkyl-fluorenes) with linear alkyl side chain of length six to ten carbon atoms (PF6, PF7, PFO/PF8, PF9 and PF10) it has been observed in solution in PF7, PF8 and PF9 (Bright *et al.* 2009).

4.3 Polyfluorene Charge Transport

Charge transport in PFO has been investigated at several scales from the individual backbone using time-resolved microwave conductivity (TRMC) to the scale of mobility as a bulk property by ToF photocurrent. The former is able to probe intramolecular charge transport and arguably yields an intrinsic mobility free of the effects of charge trapping (Saeki *et al.* 2011), whilst the latter represents the overall mobility as a combination of intrachain and interchain transport.

There are therefore large differences between the charge carrier mobility measured by these two techniques, and TRMC in particular, highlights the significant limits on the bulk mobility imposed by disorder and interchain hopping transport. For example, it has been shown by TRMC measurements of PFO that the mobility of an ordered chain may be as high as 45 cm^2/Vs compared to 1 cm^2/Vs on a disordered non-planar chain (Prins *et al.* 2007).

Based on results such as this, a strategy of enhancing long-range order has been attempted and found to be particularly effective in various polymer systems such as those based on thiophenes and bi-thiophenes. The most prominent example of which is P3HT, which has a large degree of torsional freedom along its backbone such that control of its alkyl groups can lead to self-organisation into morphologies that favour strong intermolecular interactions. In this case, it would seem that enhancing interchain packing is more effective than intrachain optimisation for high mobility applications; however, this type of packing is detrimental to high luminescence applications, in particular, polymer lasers where both high mobility and luminescence are required simultaneously, since intermolecular interactions lead to quenching of luminescence.

As we have mentioned, both of these qualities may be combined in PFO and its copolymers hence we briefly review the charge transport studies of PFO that have led to a different strategy from the above for enhancing charge transport in this polymer system. Most charge transport studies of PFO have been based on ToF because of its high IP of 5.8eV, which has prevented measurements by DI-SCLC and by field-effect transistors because of injection-limited behaviour.

The first study of charge transport by ToF obtained a hole mobility of $4 \times 10^{-4} cm^2/Vs$ (at a field of 5×10^5 V/cm) (Redecker *et al.* 1998). This was followed by a report of its mobility in polymer films aligned on a polyimide alignment layer of $9 \times 10^{-3} cm^2/Vs$ (at a field of 4×10^4 V/cm) (Redecker, D. D. C. Bradley, *et al.* 1999), which illustrated the role of intrachain transport in the polyfluorene series. This was supported in later studies of oligofluorenes (fluorene oligomers) which were studied as

amorphous, aligned glassy nematic and homeotropically aligned LC-glass films. In the first two cases, hole mobilities of 1.9 x 10^{-3} cm^2/Vs (at fields of 1.6 – 7.1 x 10^5 V/cm) and 2 x 10^{-2} cm^2/Vs (at fields of 1 - 3 x 10^5 V/cm) were found, respectively. In the latter, where the chains are aligned parallel to the charge transport direction, the hole mobility reached 1 x 10^{-1} cm^2/Vs (at fields of 0.8 – 2.3 x 10^5 V/cm) (L.-Y. Chen *et al.* 2005; Chen *et al.* 2007). These results demonstrate the potential for improving charge carrier transport by enhancing intrachain transport and that interchain hopping transport is a significant limiting factor

Such intrachain enhancement is part of the explanation of the results in the case of the F8:F5 statistical copolymer in the study by Yap *et al.* where charge carrier mobility was enhanced by two orders of magnitude compared to the homopolymer (Yap *et al.* 2008). Specifically, that the shorter extension from the backbone of the branched side-chains in the F8:F5 polymer introduced preferential interchain hopping sites that are more likely to be encountered by charges being transported in intrachain segments.

From these results, it would seem that the extended chain conformation of the beta phase with long segments of high intrachain transport would be beneficial in enhancing bulk mobility. Indeed, it has been shown in TRMC measurements of beta-phase segments that there is a higher charge carrier mobility in a PFO film with beta-phase compared to a polyfluorene film with branched side-chains where beta-phase formation is hindered (Prins *et al.* 2006). However, the authors noted that the ratio between the mobility in beta-phase and non-beta-phase regions could not be determined because the fraction of PFO with beta-phase was unknown in the study.

However, more recent work by Foster *et al.* has interpreted the role of beta-phase in PFO differently as we will discuss in the following section and has led to a new understanding about obtaining high mobility in glassy isotropic films.

4.4 Effects of the PFO Beta-Phase Conformation on Charge Carrier Mobility

Foster *et al.* have recently measured a ToF hole mobility of PFO of 3 x 10^{-2} cm^2/Vs at room temperature by control of phase formation leading to a new understanding that the beta-phase embedded in glassy PFO acts as a hole trap that reduces mobility by two orders of magnitude (Foster 2013). For this reason, earlier reports in which no techniques for control of phase formation were used, such as those already cited, found the mobility of PFO to be ~10^{-4} cm^2/Vs. The work of Foster *et al.* therefore shows the effect of a specific conformational defect on charge transport and further aids in explaining why the hole mobility is enhanced in the F8:F5 statistical copolymer of Yap *et al.* compared to the homopolymer. In this case, the branched side groups prevent the formation of beta phase, which eliminates this hole trap and significantly enhances the hole mobility.

The study of Foster *et al.* also illustrates the effect of crystallinity in polyfluorenes. Samples that have a degree of crystallinity introduced by thermal annealing have a hole mobility of ~10^{-3} cm^2/Vs, which lies midway between the higher mobility of fully glassy films and lower mobility beta-phase films.

From these results, it may be deduced that charge transport properties are limited by structural traps present as a minority population of states which could be in the form of ordered crystalline regions or conformational defects. It is thus proposed that the typical approach to optimising charge transport of improving chain ordering and crystallinity or the conformation length of chains may not be as effective as optimisation in the opposite direction for certain systems, that is, to decrease the concentration of ordered regions or eliminate them to improve charge transport and mobility. Where the former strategy only leads to improved intra-chain transport by extended conjugation that is obtained with greater planarity and the latter simultaneously improves inter-chain transport by enabling closer chain interaction.

Other works have also shown that high mobilities may be obtained in other polymer systems with disordered morphologies, such as a FET mobility of ~$10^{-1}cm^2/Vs$ in films of a benzothiadiazole (BTZ) and cyclopentadithiophene (CDT) copolymer with no signs of macroscopic order (Zhang *et al.* 2007). Furthermore, indacenodithiophene polymers have been designed to suppress crystallisation and yield a high mobility of ~$1cm^2/Vs$ (Zhang *et al.* 2010).

4.5 Effect of the Keto Defect on Charge Transport in PFO

The presence of keto defect in PFO has been the subject of many studies, in particular to establish its connection to the green band emission observed in PFO contaminated with the defect. More recently, Kuik *et al.* investigated its effects on charge transport in PFO, based on the use of MoO_3 for ohmic hole contact and is therefore of interest in this chapter and briefly reviewed here.

The authors used MoO_3 for ohmic hole contact in diodes of PFO and fluorenone contaminated PFO (designated PFO-F) and found the J-V characteristics of PFO to be space charge limited whereas PFO-F showed signs of trap-limited transport. In their analysis, the J-V characteristics of hole and electron only devices were fitted to a drift-diffusion model in which the number of traps and their energy levels could be calculated and compared to energy levels obtained by cyclic voltammetry.

EL measurements showed the effect of trap filling by the relative intensities of green and blue emission at increasing voltages where the green band of PFO-F decreased to a lower intensity at higher voltages relative to the blue emission. Blue light was attributed to recombination of free electrons and holes and green light from trapped charges that then recombine. Since the number of traps is fixed at the defect sites, when fully filled, the proportion of free carrier recombination is increased leading to the higher relative intensity of the blue emission.

This effect was not observed in PL measurement, as there is no electric field to drive charges to trapping sites making excitons less likely to encounter traps compared to EL measurements, hence the PL spectra of PFO and PFO-F appeared almost identical in their report.

In fitting the JV characteristics of electron only devices of PFO-F, it was required to introduce a trap level that the authors attributed to the keto defect. This trap level was used to account for electron and hole trapping via the fluorenone defect and calculated to have a LUMO level of 3.06 eV and HOMO level of 5.62 eV, that is, between the HOMO-LUMO gap of PFO itself and close to CV measurements of the fluorenone moiety (Kuik *et al.* 2011).

However, as we have discussed, the beta-phase represents a significant source of hole trapping and has its own shift in the HOMO and LUMO levels with respect to the glassy phase (Prins *et al.* 2006). Hence, the single-level trap model used by Kuik *et al.* may not represent a complete description of charge trapping in PFO.

4.6 Improved Charge Carrier Injection in Polyfluorenes

The ability to use MoO_3 for ohmic hole injection in PFO represents the fulfilment of a significant prerequisite for further studies of charge carrier transport such as those in the prior study on the effect of the keto defect on charge carrier transport in PFO and such as the present investigation of charge transport in this chapter. Hence, we briefly review prior attempts to improve charge carrier injection in PFO before it was known that MoO_3 might be used as an injection interlayer for holes, followed by a brief review of the initial report on the use of MoO_3 for SCLC measurements of PFO and its connection to the present study.

The HOMO level of 5.8eV of PFO has been a significant barrier for efficient hole injection since there has not been a convenient (easily deposited) electrode with a work function close enough to the HOMO of PFO to provide ohmic injection of holes. The work functions of common electrodes are summarised in Table 3.1, which highlights the limitation of typical materials for hole injection, where the closest alignment (clean platinum at 5.5eV) is still over 0.3eV from the HOMO level of PFO.

Numerous approaches have been used to solve this problem, which are summarised by Grimsdale & Müllen (2008). For example, hole injecting layers and blends with charge-transporting materials, which have the problem of phase separation (Sainova *et al.* 2000). Alternatively, incorporating charge-transporting units into the polymer backbone or side-chains can bring the HOMO closer to the vacuum level so that typical electrodes can be used, such as in the case of alternating copolymers of dialkylfluorenes and hole-transporting triphenylamines (Bernius *et al.* 2000) or tri-block polymers containing emissive units and hole and electron transporting units (Chen *et al.* 1999). This, however,

may have the drawback of significantly altering the charge transport and optical properties. There have also been attempts at end-capping with hole transporting moieties (Miteva *et al.* 2001).

All of these approaches require a modification of the PFO chemical structure in some way, yet it has been shown that ohmic injection can be achieved via PEDOT:PSS despite the hole injection barrier of ~0.6 eV with the HOMO of PFO based on an electrical conditioning procedure (Poplavskyy *et al.* 2003). The conditioning results in the formation of an interfacial dipole layer that reduces the barrier for injection such that it becomes ohmic, confirmed by DI-SCLC measurements. However, there are certain drawbacks to this technique, such as non-uniformity and the requirement for electron injection to fill electron traps and form an interfacial charge layer, which is subject to de-trapping over time.

One advantage of PEDOT:PSS is that it provides passivation of surface defects and presents a smoother surface than ITO for the subsequent layer, however, it is not ideal in a number of other ways, such as the fact that it degrades under UV illumination (Cattin *et al.* 2009). It is dissolved in water, any residues of which could get into the active layer thereby requiring baking at ~120°C to ensure full removal of the water thus making it unsuitable for device structures where the layer cannot be prepared outside a glovebox.

A significant step has been made more recently by Nicolai *et al.* to resolve this problem of hole injection in PFO by the use of transition metal oxides. In this case, the authors showed space-charge limited hole currents in PFO diodes by direct hole injection from an MoO_3 interlayer. The hole mobility was found to be ~1.3 x 10^{-5} cm^2/Vs based on fitting the experimentally obtained JV characteristics to the Mott-Gurney square law (Nicolai *et al.* 2010)**.** This report of the use of a MoO_3 interlayer for ohmic hole injection in PFO has enabled the measurements by DI-SCLC and OFET techniques in this chapter and we briefly discuss a few aspects of the theoretical basis of these two techniques for studying charge carrier transport.

4.7 DI-SCLC and OFET Techniques for Charge Transport Studies

The transient Dark Injection technique involves electrical injection of charge carriers by application of a voltage pulse to an ohmic contact that is able to inject sufficient charge to reach the maximum, space charge limited current through the sample.

In the case of ohmic contact and no charge carrier trapping, the current transient shows a cusp at the time of arrival of the first charge carriers at the counter electrode. This time corresponds to the space-charge free transit time obtained from time-of-flight photocurrent measurements by the following relationship:

$$t_{DI} = 2\left(1 - e^{-\frac{1}{2}}\right) = 0.786\, t_{tr}. \qquad 4.1$$

The time-varying electric field between the leading edge of the charge carriers and the counter electrode results in charges being drawn across faster than in the non- space-charge limited case resulting in a shorter transit time. The cusp in the transient current density measurement, from which we deduce the arrival time, is a result of a higher average electric field before arrival of carriers at the counter electrode compared to the steady-state current density. (Poplavskyy & Nelson 2003) (Tsoi *et al.* 2008) (Lampert & Mark 1970)

The DI-SCLC technique is therefore similar to ToF in that it leads to the observation of a transient signal that is correlated with the transit time of charge carriers by which the charge carrier mobility may be determined directly. In the case of OFET measurements, the mobility is obtained from a model of the device in steady-state operation. The operation and device physics of solution processed organic field effect transistors are discussed in chapter three. Here we highlight several aspects of OFET device configuration that may reduce the overall performance of an OFET and therefore affect the deduced field effect mobility.

First, if injection is limited at the source electrode, the contact resistance must be taken into account when analysing device characteristics. In short channels, contact resistance may be comparable to the channel resistance requiring a higher voltage to reach the operating threshold. Contact resistance increases with injection barrier and decreases with a higher charge carrier mobility. In low mobility materials, the formation of a space-charge region close to the injecting electrode further reduces injection.

Charge transport in an OFET is affected by being parallel to and in close proximity to an interface with a gate dielectric such that the choice of dielectric will have a significant effect on the field-effect mobility. Surface roughness, charge traps and impurities at this interface also affect device stability and can lead to hysteresis in transfer characteristics (Veres *et al.* 2004). Trapped charges may also screen the gate field resulting in a gate voltage dependent contact resistance and will all together reduce the charge carrier mobility. (Liu *et al.* 2013)

When comparing charge carrier mobility obtained by different techniques an often-overlooked parameter of the measurement is the charge carrier density regime in which the measurement takes place. In diode devices such as the configurations of ToF and DI devices, the charge carrier density is of the order of 10^{13} to 10^{15} cm^{-3}. The ToF measurement in particular is conducted while ensuring photogenerated charge carriers do not exceed more than 10 % of the maximum space charge to avoid inhomogeneity in the electric field distribution throughout the bulk. The charge carrier density regime

of FETs may be higher than 10^{19} cm^{-3}, thus these three techniques together span several orders of magnitude in charge carrier density and provide an insight into its effects on mobility.

The dependence of hole mobility on charge carrier density has been addressed in the case of OC_1C_{10}-PPV and P3HT in diodes and field-effect transistors. It was found that the hole mobility of OC_1C_{10}-PPV increased from ~10^{-6} to ~10^{-4} cm^2/Vs with an increase in hole density from 10^{17} to 10^{19} cm^{-3} which was a trend found to be in agreement with a variable rate hopping model. The field effect mobility of P3HT increased by an order of magnitude in the same range of carrier densities and the hole mobility of both materials began to converge to a similar value at the highest charge carrier densities measured (Tanase *et al.* 2003).

Since it has been demonstrated that it is possible to form an ohmic contact with PFO using a molybdenum trioxide injection electrode, we are now able to experimentally consider the relationship between hole mobility and charge carrier density in PFO using MoO_3 as the injection layer for DI and FET measurements.

4.8 Charge Injection and Transport Measurements of PFO

In order to perform the DI-SCLC measurements, devices were prepared with an interlayer of molybdenum trioxide in the configurations ITO/PEDOT:PSS/PFO/MoO_3/Au and ITO/MoO_3/PFO/Au. In both cases, an approximately 7 nm interlayer of molybdenum trioxide and ~70 nm layer of gold were thermally evaporated and the polymer was spin-coated from solution in toluene. In the former case, the additional layer of PEDOT:PSS between the ITO and PFO was spin coated to serve as an electron blocking layer for ToF measurements. Measurements were performed in a nitrogen gas filled sample chamber.

For the DI measurements, a step voltage with a positive bias was applied to the MoO_3 as the hole injecting electrode and the transient current was measured across a resistor that was selected to minimise the RC response time and maximise the measured signal.

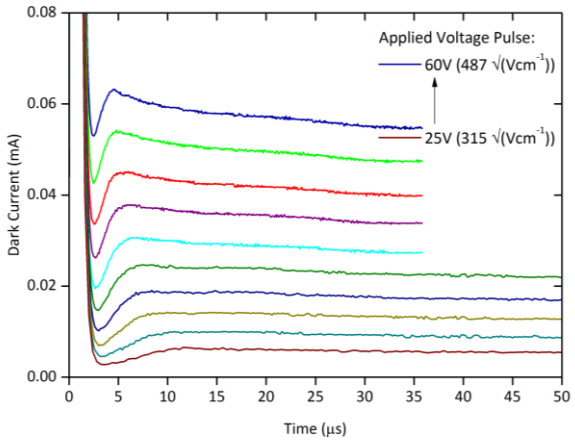

Fig. 4.1 Dark injection transients for a 2.53 µm thickness PFO film in an ITO/MoO_3/PFO/Au structure measured at fields from 315 to 487 $(Vcm^{-1})^{1/2}$

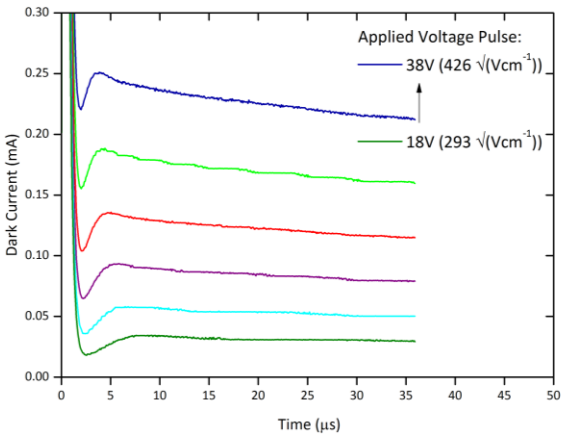

Fig. 4.2 Dark injection transients for a 2.10 µm thickness PFO film in an ITO/PEDOT:PSS/PFO/MoO_3/Au structure, measured at fields from 293 to 426 $(Vcm^{-1})^{1/2}$

We find that the cusp in the DI transient signal is clearly visible for both device configurations, which provides strong evidence of ohmic injection of holes via the MoO_3 interlayer. The peak of the cusp is used to determine the DI transit time t_{tr} and hence the hole mobilities are calculated to be 2.36 x 10^{-4} cm^2/Vs and 1.66 x 10^{-4} cm^2/Vs at ~378 $\sqrt{Vcm^{-1}}$ for the MoO_3 on PFO and PFO on MoO_3 devices, respectively.

The hole mobility of these spin-coated PFO samples is comparable to values in the literature by TOF measurements (Redecker *et al.* 1998) and previous DI measurements where electrical conditioning of the device was used to enable injection (Poplavskyy *et al.* 2003).

The inverted device configuration also permits ToF measurements to be conducted on the sample since the PEDOT:PSS layer acts to block hole injection at the anode in the region where charge carriers are photo-generated. This device configuration has the advantage of allowing evaporation of the MoO_3 interlayer and the metal electrode without breaking the vacuum of the evaporator, avoiding exposure to residual moisture. Additionally, it has been suggested that it allows the formation of an intermixed region of the MoO_3 interlayer and the polymer, which may improve injection further (Gwinner *et al.* 2011).

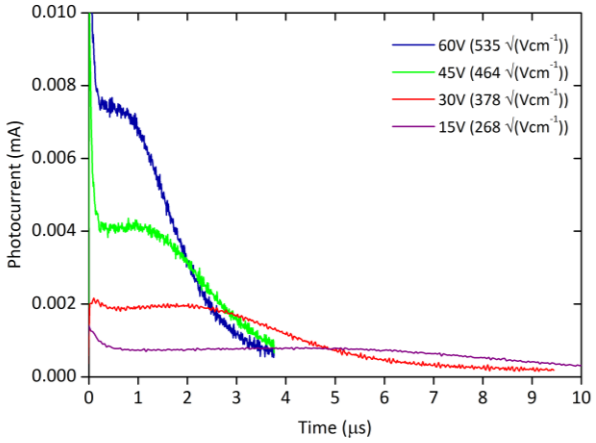

Fig. 4.3 ToF transients of a 2.10µm thickness PFO film in an ITO/PEDOT:PSS/PFO/MoO_3/Au structure, measured at fields from 268 to 535 $(Vcm^{-1})^{1/2}$

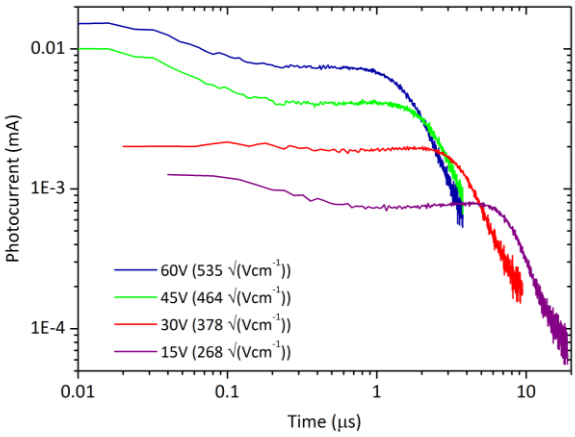

Fig. 4.4 log-log plot of ToF transients of a 2.10µm thickness PFO film in an ITO/PEDOT:PSS/PFO/MoO_3/Au structure, measured at fields from 268 to 535 $(Vcm^{-1})^{1/2}$

The results from TOF measurements are presented on a linear scale in Fig. 4.3 which shows the shortening length of the plateau as the applied field increases and the clearly distinguishable inflection point which is characteristic of non-dispersive transport. This is illustrated more clearly in the log-log plot in Fig. 4.4.

With careful choice of the measurement resistance to reduce to the RC response and maximise the photocurrent, it was possible to measure over a very wide field range from 10^3 Vcm^{-1} to 10^5 Vcm^{-1}. The hole mobility of 4.83 x 10^{-4} cm^2/Vs at ~378 $\sqrt{Vcm^{-1}}$ is approximately twice that of the DI measurement for this sample, which is a discrepancy typical for previous studies of other polymers (Campbell *et al.* 2000).

In the intermediate field range, a very shallow cusp at the inflection point is observed that seems to become less prominent at higher fields. This cusp in the TOF photocurrent may be explained by considering the charge transport variation with the electric field or because of a space charge layer near the charge-collecting electrode (Tse *et al.* 2006).

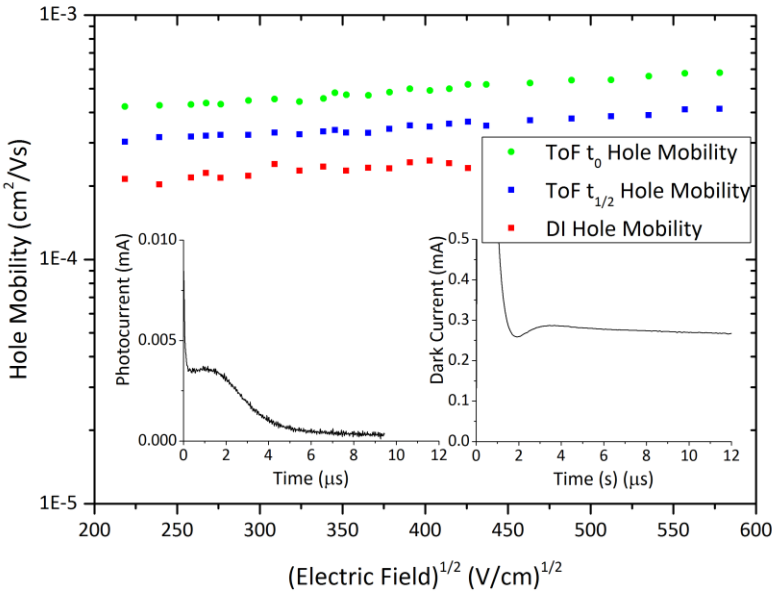

Fig. 4.5 Field dependence of DI hole mobility (using $t_{DI}=0.787t_{tr}$) and ToF hole mobility evaluated at t_0 and $t_{1/2}$ for a 2.10µm thickness PFO film in an ITO/PEDOT:PSS/PFO/MoO_3/Au structure

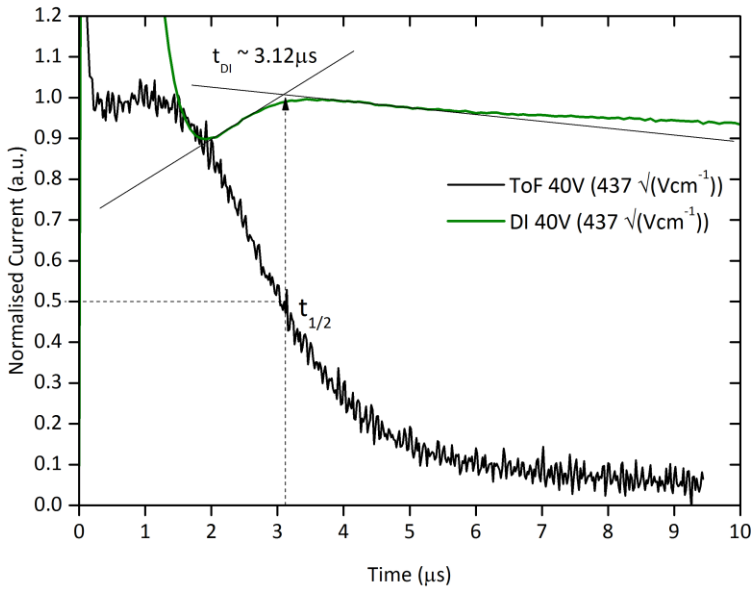

Fig. 4.6 Comparison of DI and ToF transients showing the approximate correspodence of t_{DI} and $t_{1/2}$ for a 2.10µm thickness PFO film in an ITO/PEDOT:PSS/PFO/MoO3/Au structure

The $t_{1/2}$ transit time is an alternative method for determining the mobility from TOF transients. The field dependence of the hole mobility from t_{DI}, t_0 and $t_{1/2}$ times of ToF measurements is shown in Fig. 4.5. The hole mobility in all cases exhibits a similar (weak) electric field dependence and, as with previous reports, the $t_{1/2}$ mobility is in closer agreement with the DI mobility.

The shape of DI transients is subject to variation based on a number of factors and observed in the following features of the transient current. First, the rise time to the cusp, whether it is a sharply defined peak or smooth and undefined and the decay from the peak of the cusp. The correspondence between the inflection point from ToF and the cusp position from DI is illustrated in Fig. 4.6 at the same applied field with the ToF transient normalised to the plateau position and the DI transient to the cusp. The peak of the rising DI cusp occurs reasonably close to the point at which the ToF transient has decayed to half of the photocurrent at the plateau, that is, the $t_{1/2}$ time.

The DI cusp in these results spans several microseconds, which is an amount of time that is significant in relation to the transit time, whereas the peak of the cusp in the theoretical DI transients of Many and Rakavy are highly defined. In the theoretical case, the defined peak is explained to be an artefact arising from the assumption that the leading front of the charge is unaffected by diffusive spreading and sharply defined (Many & Rakavy 1962; Lampert & Mark 1970). Therefore, the smooth and rounded nature of the cusps found in these experimental transients may be accounted for by considering a degree of spread of the leading edge of carriers.

Hence, for experimental data, t_{DI} may be determined from the exact time of the peak of the current where the cusp touches its maximum value or from the point of inflection at the rising edge of the cusp. Here we have favoured using the latter, as the visibility of the exact peak position is limited by the time resolution of the experimental data in most cases.

Based on the theoretical ratio for the DI time compared to the ToF transit time, where,

$$t_{DI} = 2\left(1 - e^{-\frac{1}{2}}\right) t_{tr} \tag{4.2}$$

$$t_{DI} = 0.787 t_{tr} \tag{4.3}$$

we see that the effective transit time used to calculate the DI mobility is predicted to occur earlier than the experimentally obtained TOF transit time at the inflection point, whereas the experimentally obtained transient shows t_{DI} is after the ToF inflection and the experimental ratio between t_{tr} and t_{DI} shown in Fig. 4.7 has a mean value of ~1.38. That is, the theoretical ratio, when applied to the experimental data, results in a longer time for the t_{DI} used to calculate the DI mobility, which is therefore found to be lower than the TOF mobility. This discrepancy between the theory and experiment accounts for the above finding of the DI mobility being less than the TOF mobility.

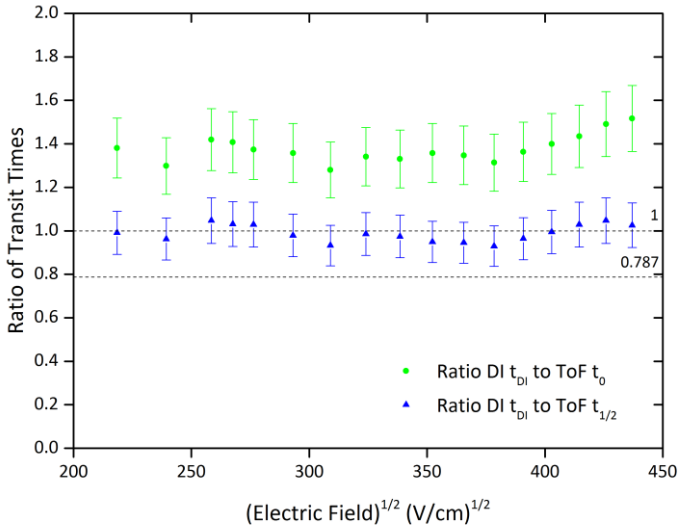

Fig. 4.7 Field dependence of the ratios of t_{DI} to t_0 and $t_{1/2}$ for a 2.10μm thickness PFO film in a ITO/PEDOT:PSS/PFO/MoO3/Au structure.

The ratio of our experimental t_{DI} to the $t_{1/2}$ transit time from TOF across the field range measured is also shown in Fig. 4.7 and has a mean ratio of ~0.99. This still implies an underestimation of the DI mobility when using the ratio of 0.787 in equation 4.3 compared to the ToF mobility from $t_{1/2}$.

A similar relationship between the TOF and DI transients was observed by Goldie (1999) in the case of molecularly doped polymers. Numerical modelling showed that the time of the peak might shift in association with variations in the ratio between the peak current density and the steady-state current density with increasing field dependence or diffusion. The author thus attempted to include the field dependence and diffusion into a model of the transient current response of molecularly doped polymers under space charge limited conditions (Goldie 1999).

The peak time according to this model, is found to be variable between 0.632 and 0.787 compared to the aforementioned ratio of $t_{DI} = 0.787 t_{tr}$. This analysis updates the fixed mobility of the original work by Many and Rakavy with a field dependent mobility described as follows,

$$\mu_m(F) = \mu_0 \left(\frac{F}{F_0}\right)^m \qquad 4.4$$

where $m \gg 0$ and F_0 is a normalising field, hence a modified differential equation at the collection electrode ($F_{x=L(t)}$) is obtained with the field dependent mobility. The solution to this equation shows the location of the current peak, t_P, may be determined by:

$$\frac{t_P}{t_o} = \frac{m+2}{m+1}\left[1 - \exp\left(-\frac{(m+1)}{(m+2)}\right)\right]. \qquad 4.5$$

For the case of a field-independent mobility, $m = 0$, and $\frac{t_p}{t_0} = 0.787$, as in the original papers on transient dark injection. However, in the case of a field-dependent mobility, where mobility is marginally enhanced at higher fields, $m \to \infty$, and $\frac{t_p}{t_0}$ tends towards $\frac{e-1}{e} = 0.632$. Which means the DI peak position is expected to be at a shorter time than the ToF transit time.

The explanation for this reduction in the peak time is that the drift velocity of the leading edge of charges becomes progressively faster leading to a shorter arrival time. However, as discussed, the results of the model still appear contradictory to the experimental results in this study where the DI peak time is after the ToF transit time.

In the work of Goldie, experiments were conducted in addition to the theoretical analysis, in which the discrepancies related to the peak time found in the present measurements were observed as well. The author suggested that it may be related to the method of defining the average carrier transit time, which our results support by showing the correspondence of $t_{1/2}$ from ToF with the dark injection peak time rather than with the inflection point in the ToF signal.

More recently, Li *et al.* have used Monte Carlo simulations of ToF and DI transients and have drawn a connection between the ratio of the DI peak time to the ToF transit time and the energetic disorder. That is, the ratio of Many and Rakavy is only valid when energetic disorder is small or at high temperatures. Otherwise, the ratio deviates because of the high charge carrier density in the space-charge-limited regime and the inhomogeneous field distribution (Li, Duan, Zhang, Dong, *et al.* 2014). However, their analysis still predicts a ratio of less than one and anticipates a higher mobility at the charge carrier density of the DI-SCLC measurements compared to ToF, which is contrary to our experimental results.

Experimental data from measurements by the DI-SCLC technique may be subject to analysis that yields further information about the nature of charge transport than the mobility. For example, by examining dark-injection transients, we may obtain information about the nature of charge trapping in long and short time-scales by comparing the peak (J_{peak}) and steady state (J_{SS}) current densities.

We consider this in more detail with reference to the theory and physics underlying the understanding of these measurements, which are based on the works by Many and Rakavy (1962), Lampert and Mark (1970) and more recent publications.

Based on the theory of transient injection currents in the trap-free case described by Many and Rakavy, the maximum current overshoots the steady-state current by a factor of ~1.21, that is,

$$J_{peak} = 1.21 J_{TFSCLC}. \quad 4.6$$

The reason J_{peak} may be lower than expected compared to J_{TFSCLC} is that the amount of charge contributing to the transient current before the transit time is less than $Q_{SCLC} = 1.5C(V - V_{bi})$. This may occur because of bulk traps, for example where the trapping time is shorter than the transit time $t < t_{tr}$ and the release is longer than the transit time $t \gg t_{tr}$. Such traps are characteristic of dispersive charge transport. Since the current before t_{DI} is reduced in this case, the cusp which is characteristic of DI-SCLC transients is less pronounced.

If trapping occurs at a significantly shorter time than the transit time, $t \ll t_{tr}$, then a clear DI transient may still be observed. The short length of this time would correspond to the moment of injection $t = 0$. That is, the charge would be trapped at a very close distance to the injection interface, blocking charge from flowing into the device and effectively reducing the surface area of the injecting interface.

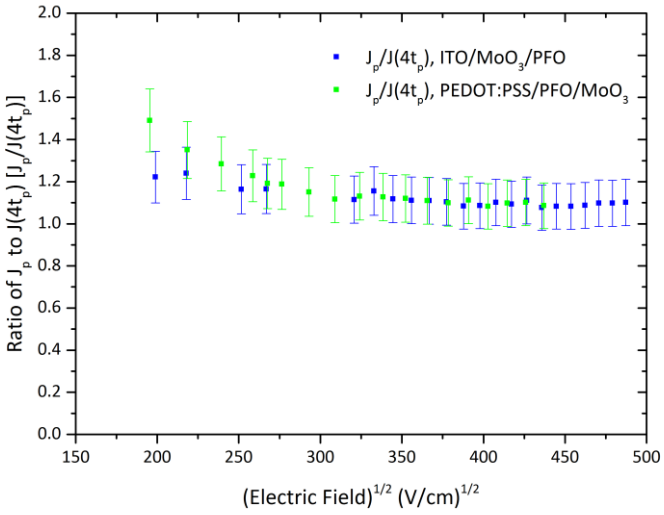

Fig. 4.8 Field dependence of the ratio of J_p to $J(4t_p)$. Blue squares correspond to ITO/MoO₃/PFO/Au data. Green squares correspond to ITO/PEDOT:PSS/PFO/MoO₃/Au data

We have evaluated the steady-state current density at $4t_{DI}$, which is limited by the duration of the DI transients measured. Other authors have used $3t_{DI}$ (Goldie 1999) and $10t_{DI}$ (Campbell *et al.* 2000). The ratios of J_{peak} to $J(4t_{DI})$ across a range of fields for both the ITO/PEDOT:PSS/PFO/MoO₃/Au and ITO/MoO₃/PFO/Au structures are shown in Fig. 4.8. By comparing the two device configurations, we may have further insight into the effect of the preparation method of the hole injection interlayer.

The ratio of J_{peak} to $J(4t_{DI})$ for both device configurations is found to be in good agreement at higher fields, with both tending to ~1.09. However, at low fields, the ITO/PEDOT:PSS/PFO/MoO₃/Au

structure has a higher ratio that decreases monotonically from 1.5 as the field is increased. This is an indication of traps close to the interface that are filled at a time-scale much shorter than the transit time ($t \ll t_{tr}$) that consequently partially blocks charge injection into the bulk. The ratio may have reduced as the field increased because of the effect it has on de-trapping charges trapped at the interface.

We may estimate the concentration of these traps (n_t) based on the assumption that all traps are filled at the electric field that marks the transition (E_{tr}) to the lower ratio:

$$n_t \sim \frac{CE_{tr}}{A} = \frac{\epsilon\epsilon_0 E_{tr}}{d} \qquad 4.7$$

where C is the device capacitance, A is the device area and d is the thickness (Poplavskyy *et al.* 2005). From Fig. 4.8, this occurs at a field of 9.55 x 10^4 V/cm, which yields a trap concentration of ~ 1 x 10^{16} cm^{-3}.

At higher fields, the presence of both a clearly resolved cusp in the transient and the ratio falling below the predicted trap-free ratio of 1.21 is typical of SCLC in the presence of bulk traps. The fact that the ratio tends towards the same value of ~1.09 for both device configurations implies that the trap species behaves in the same way and is an indication that the traps are intrinsic to as spin-coated PFO.

In the analysis of Goldie, where the field dependence of the mobility is considered, the ratio between the peak and steady-state current density is determined to be:

$$\frac{J_p}{J_{ss}} = e^1 \left[\frac{m+3}{m+2}\right]^{-(m+2)}. \qquad 4.8$$

For a field independent mobility, $m = 0$, and the equations for typical SCLC behaviour are recovered with a $\frac{J_p}{J_{ss}}$ ratio of 1.21. For the case of $m \to \infty$, $\frac{J_p}{J_{ss}} \to 1$. Based on this analysis, the field dependence of the mobility may also account for the ratio we measured of ~1.09. The hole mobility of PFO has a weak field dependence, as we have seen in the earlier ToF data and in previous studies of PFO.

4.9 Injection Limited Hole Currents in PFO Using a Solution Processed Hole Injection Layer

In the case of PFO on MoO_3 devices, the MoO_3 interlayer we have used for hole injection has been prepared by thermal evaporation and subsequent spin-coating of the active layer within a glovebox. We have encountered a degree of sensitivity to ambient conditions, in particular moisture, which eventually degrades the injection efficiency to the point the contact becomes a hole blocking layer. Indeed, it has been shown that air exposure and water are responsible for energetic changes in MoO_3

that are detrimental to hole injection, in particular by adsorption of species such as water that decrease the IP (Kröger *et al.* 2009; Meyer & Kahn 2011).

At present, the usefulness of the excellent hole injection characteristics into PFO we have observed from MoO_3 may therefore be limited to experimental devices and studies, although there has been great interest in preparing an effective injection layer by solution processing (Murase & Yang 2012; Liang *et al.* 2014). Encapsulation would be helpful in overcoming this problem, especially for MoO_3 on PFO structures, which could be encapsulated before the device is brought into ambient conditions. An inert atmosphere would, however, still be required for preparation of the layers, which is not attractive with respect to costs, hence, other injection layer materials are therefore of interest.

Here, we briefly present results from copper(I)thiocyanate (CuSCN) which is another p-type semiconductor and a hole injection interlayer that may be processed from solution. The IP of CuSCN has been reported to be 5.53 eV and a hole mobility of $\mu \approx 0.01$ to 0.1 x 10^{-4} cm^2/Vs has been determined (Pattanasattayavong *et al.* 2013).

Hole only devices with a CuSCN injection layer were prepared on ITO substrates. The CuSCN solution provided by Ajay Perumal was spin coated at 2000 rpm for 60s, which yields a 45 nm film. This layer was annealed at 120°C for approximately 10 minutes before spin coating the next layer. Since the CuSCN layer is deposited from solution onto the substrate followed by the polymer (PFO), we were able to thermally evaporate the MoO_3/Au counter electrode to directly compare hole injection for the same polymer film.

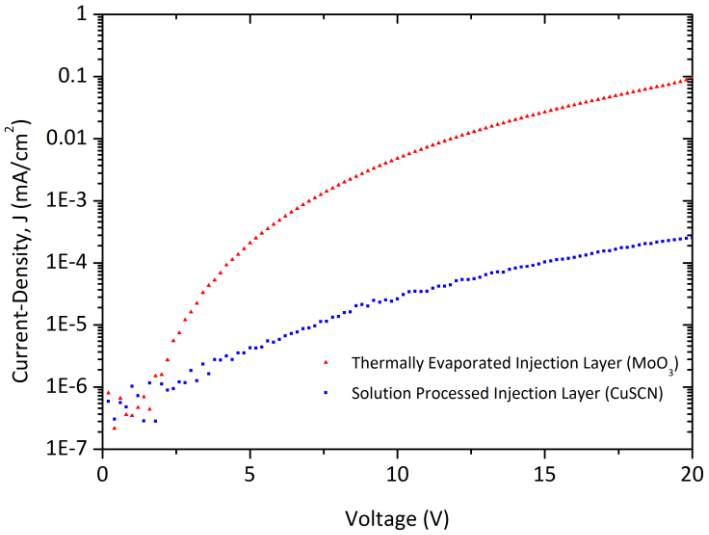

Fig. 4.9 Comparison of hole injection into PFO from solution processed CuSCN and thermally evaporated MoO_3

Current-density-voltage measurements are presented in Fig. 4.9 from both the CuSCN and MoO_3 layers, which show a severely injection limited hole current-density for the CuSCN layer, whereas the

MoO_3 current-density is several orders of magnitude higher. Ohmic injection was further verified for MoO_3 in this sample by DI-SCLC measurements that showed a clear cusp in the transient current. In contrast, there was no DI cusp when the positive voltage pulse was applied to the CuSCN layer.

4.10 PFO Field-Effect Transistors

As previously mentioned, ohmic injection from MoO_3 leads to the possibility of viable FET devices, which for our purposes enables us to measure the hole mobility of PFO in the high charge carrier density regime.

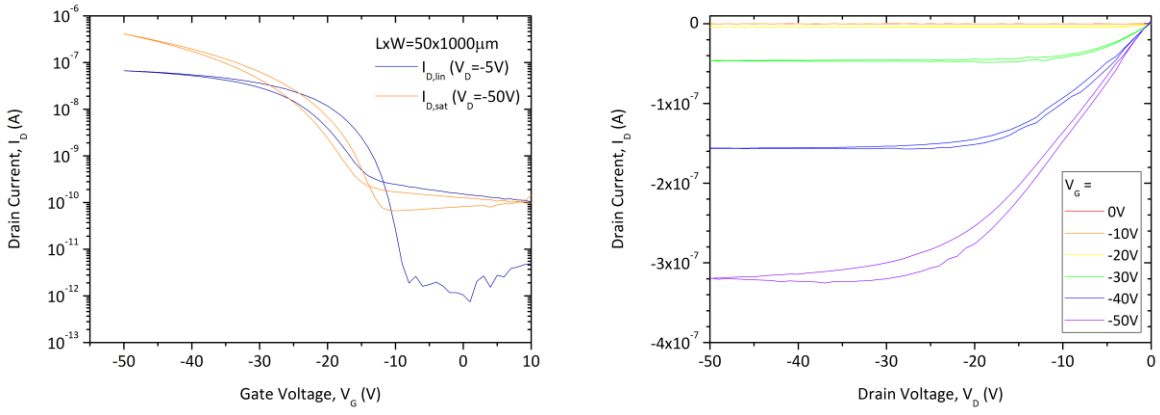

Fig. 4.10 Transfer characteristics of a BGTC PFO/F8 OFET (left) output characteristics (right).

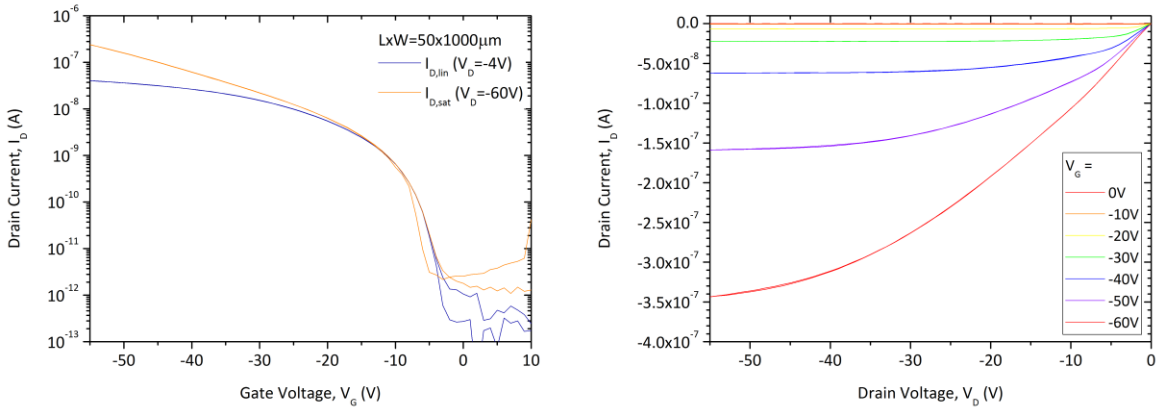

Fig. 4.11 Transfer characteristics of a BCTG PFO/F8 OFET (left) output characteristics (right).

FET devices were prepared in the bottom gate, top-contact (BGTC) and bottom-contact, top-gate (BCTG) configurations; the description of the device fabrication may be found in chapter three. Typical FET transfer characteristics were obtained in the initial configuration of BGTC FETs as shown in Fig. 4.10. The hole mobility in the linear and saturation regions (μ_{lin} and μ_{sat}) were calculated to be $(2.7\pm0.1)\times10^{-3}$cm^2/Vs and $(5.9\pm0.3)\times10^{-3}$cm^2/Vs, respectively. The threshold voltage of -16 ± 2V is significantly better than previous attempts at PFO FETs in the literature, which did not produce functional devices (Babel & Jenekhe 2003; Yasuda *et al.* 2005; Sonar *et al.* 2007). We note that an

electron mobility of PFO FETs of 5 x 10^{-3}cm^2/Vs has been reported using calcium electrodes for ohmic electron injection (Chua *et al.* 2005).

In order to investigate whether the high threshold is related to the gate dielectric in these devices or an injection limitation from the MoO_3, FETs were also fabricated in the BCTG configuration. The transfer characteristics in Fig. 4.11 show a lower threshold of ≈5V. Furthermore, the minor hysteresis is eliminated and the linear mobility, μ_{lin}, is found to be twice as high at 6x10^{-3}cm^2/Vs and μ_{sat} is 1.5 x 10^{-2} cm^2/Vs.

4.11 Carrier Extraction by Linearly Increasing Voltage Measurements of PFO

A relatively recent technique for measurements of charge carrier mobility is Charge Extraction by Linearly Increasing Voltage (CELIV). In this technique, two triangular voltage pulses are applied in sequence to a sample between two non-injecting contacts. The current rise observed following the first voltage pulse is due to the capacitance of the sample (Fig. 4.12). The slope of the current following the second voltage pulse is related to the bulk conductivity so that the time at which the current is at a maximum allows a determination of the mobility of intrinsic carriers (Hertel & Bässler 2008). In the case of materials with a very low concentration of intrinsic carriers, irradiation of a short laser pulse may be used to photo-generate charge carriers to increase the carrier concentration, which is known as Photo-CELIV.

CELIV measures charge carriers in equilibrium rather than the drift of photogenerated charges in ToF, which makes it insensitive to any redistribution of the electric field in the sample because of an injected carrier concentration. CELIV has been claimed to have a few advantages compared to ToF, including that it may be used on thin film samples and to obtain the mobility of materials in which the dielectric relaxation time is shorter than the transit time of a carrier.

The mobility is estimated according to

$$\mu = \frac{2d^2}{3At_{max}^2}\left[1 + 0.36\frac{\Delta j}{j(0)}\right]^{-1} \qquad 4.9$$

where Δj is the extraction current and A is the slope of the linearly increasing voltage, U (Juscaronka et al. 2002):

$$A = \frac{U}{t_{pulse}}. \qquad 4.10$$

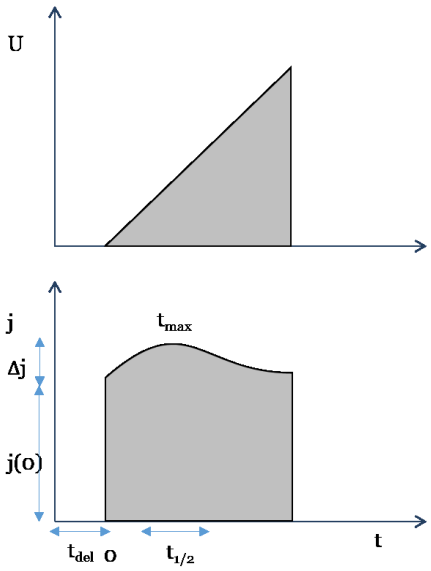

Fig. 4.12 Schematic of a CELIV voltage pulse (top) and typical transient current response (bottom) annotated to show the time the extraction current (Δj) reaches its maximum (t_{max})

In the case where $\frac{\Delta j}{j(0)} \leq 7$, the mobility may be defined more precisely by the following numerical solution to the equations for the transient current (Bange *et al.* 2010; Kokil *et al.* 2012):

$$\mu = \frac{2d^2}{At_{max}^2}\left[0.329e^{-0.180\frac{\Delta j}{j(0)}} + 0.005e^{0.253\frac{\Delta j}{j(0)}}\right]. \qquad 4.11$$

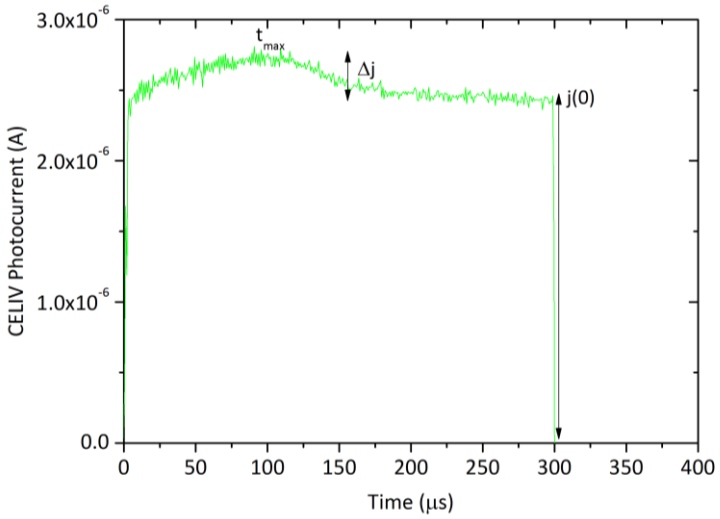

Fig. 4.13 Photo-CELIV measurements of PFO

The Photo-CELIV technique was applied to a 3.39 μm thickness PFO film sample in a configuration of ITO/PEDOT:PSS/PFO/MoO_3/Au structure with typical CELIV transient data shown in Fig. 4.13. The charge carrier mobility is estimated to be 3.12 x 10^{-4} cm^2/Vs at room temperature, which is in excellent agreement with mobility measurements using other techniques.

4.12 Discussion

Ohmic injection of holes into PFO using molybdenum trioxide has been confirmed using the transient DI measurement technique in accordance with an earlier report of the observation of steady-state space-charge limited current in PFO hole only diodes (Nicolai *et al.* 2010).

The hole mobility obtained by DI of ~ 2 x 10^{-4} cm^2/Vs in the present measurements is highly consistent with an earlier report which used an electrical conditioning technique to enhance injection from PEDOT:PSS. The conditioning technique requires the use of bipolar devices that relies on electron injection from the cathode to fill traps resulting in an interface dipole at the anode interface that lowers the barrier for hole injection. Here, the use of a unipolar architectures means that no interfacial effects are expected to occur because of negligible electron injection from the Au electrode, providing further certainty that the MoO_3 interlayer has enabled direct ohmic injection of holes without the disadvantages of the electrical conditioning technique.

The TOF hole mobility we have measured also corresponds well with both approximations of the space-charge free transit time (t_0 and $t_{1/2}$). Further agreement with prior charge transport measurements of PFO has also been found in the fact that both $\mu(t_0)$ and $\mu(t_{1/2})$ are higher than $\mu(t_{DI})$ (Poplavskyy *et al.* 2003), which has also been the case in TOF and DI measurements of polyfluorene copolymers (Campbell *et al.* 2000).

However, this slight difference between the mobility values obtained from ToF and DI seems to go against descriptions of charge carrier mobility that consider the effect of charge-carrier density on mobility (Tanase *et al.* 2003; Pasveer *et al.* 2005), where it is found that charge carrier mobility should increase in higher charge carrier density regimes. However, it is possible that the charge carrier density may still be low enough in the DI measurement for the mobility to be in a density independent regime in which other factors set the limit of the charge carrier mobility such as morphology and charge trapping.

This discrepancy is even more apparent in the case, of the hole mobility obtained from steady-state SCLC measurements by Nicolai *et al.* that was found to be an order of magnitude lower than typical ToF measurements at 1.3x10^{-5} cm^2/Vs (Nicolai *et al.* 2010). In this case, the authors mention that this lower mobility could be related to the morphology and various phases of PFO (Cadby *et al.* 2000; Martin Grell *et al.* 1999). A key difference between this study and most other charge transport studies of PFO, including the work in the present chapter, is that the measurements of Nicolai *et al.* were performed on thin films of several hundred nanometres compared to the thick films of several micrometres typically used in ToF measurements.

FET device measurements are also performed on thin films, although charge transport takes place in a region within a few nanometres of the interface and is in a direction parallel to the interface, unlike the aforementioned techniques, which yield a bulk mobility and are perpendicular to the interface. Since FET device operation occurs in the very high charge carrier density regime, we have been able to investigate the effect of a high charge carrier density on hole mobility by the successful fabrication of FET devices enabled by ohmic injection using MoO_3.

An earlier attempt at PFO FET devices found that the PFO FET hole mobility could not be measured directly because of injection limited contacts and relied on extrapolating results from similar polymers to estimate the mobility, which was found to be around 6-10 x 10^{-4}cm^2/Vs (Babel & Jenekhe 2003). Similarly, another study involving PFO FETs found the linear mobility to be $7x10^{-5}$cm^2/Vs because of non-ohmic injection (Sonar *et al.* 2007).

The highest PFO FET hole mobility reported was achieved using a rubbed polyimide alignment layer to find a hole mobility of $5.8x10^{-3}$cm^2/Vs parallel to the rubbing direction and $2.2x10^{-4}$cm^2/Vs perpendicular to it (Yasuda *et al.* 2005). The output and transfer characteristics were not shown for PFO and it is unlikely that ohmic injection was achieved since gold source and drain electrodes were used, which are not known to form an ohmic contact with PFO. Furthermore, the threshold voltage was found to be -43V for another material in the study, a dodecafluorene, with a similar HOMO level to PFO.

The threshold voltage, of ~5V for the BCTG devices presented here, is thus a significant improvement and the measured transfer and output characteristics are more faithful to the ideal characteristics required by the FET equations for obtaining the mobility. As for the higher threshold and lower mobility in both linear and saturation of the BGTC device, this is likely to be related to a slightly injection limited contact, as we have noted in the DI-SCLC measurements of ITO/PFO/MoO_3 devices which we determined to have traps at the injection interface by analysis of the DI current transients. Such traps result in contact resistance, an increased voltage threshold and hysteresis in the case of FET devices.

The highest hole mobility obtained for the BCTG FET device is two orders of magnitude higher than the TOF mobility (μ_{sat} of 1.5 x 10^{-2} cm^2/Vs) and approaches the hole mobility of the F8:F5 statistical copolymer with octyl and branched substituent groups (Yap *et al.* 2008).

This higher FET hole mobility is likely to be a result of the charge carrier density dependence of mobility. The higher charge carrier densities in a FET channel predominates over the density of traps typical of PFO, in particular, the trap states introduced by the beta phase and ketone defects. We note that PL spectra measured for these devices (not shown) do not show the green band emission

characteristic of ketone defects yet we do observe a red shifted peak in (0-0) emission, typical of samples with beta phase.

Hence, we may be certain that there is a population of beta-phase related charge traps in the films and we suggest that the high charge carrier density injected into the active channel has filled these traps and others to leave a charge transport energy level that is not hindered by trapping. Since transport is no longer hindered by charge traps in this case, the mobility reaches the level of the two previous cases of ToF measurements of poly(fluorene) films where the beta-phase is not present (Yap et al. 2008; Foster 2013).

FET and ToF measurements have previously been compared for the liquid crystalline polymer pBTTT-C_{12} (poly(2,5-bis(3-dodecylthiophen-2-yl)thieno[3,2-b]thiophene), in order to investigate its bulk charge transport properties since most studies had been focused on its characteristics in FET devices. The ToF hole mobility was found to be three orders of magnitude lower than the FET mobility. This was explained by the out-of-plane alignment of polymer chains compared to the direction of transport in ToF resulting in a large interchain separation compared to the in-plane alignment that provides π-π stacking for efficient charge hopping in FET measurements (Baklar *et al.* 2010). Trapping effects may have also played a role in these measurements.

4.13 Conclusions

The use of molybdenum trioxide for ohmic injection into PFO has enabled the preparation of viable hole only PFO FETs and devices for measuring transient dark injection. Together with time-of-flight measurements, an experimental investigation of charge transport and injection into PFO has been possible that spans several orders of magnitude of charge carrier density and shows measurements of charge carrier mobility vary widely depending on the technique used. We have shown, in particular, that the FET hole mobility of PFO can be two orders of magnitude higher than the mobility typically obtained by measurements of the bulk charge transport properties.

In the case of FET measurements, this mobility is of the order of ~10^{-2} compared to ~10^{-4} cm^2/Vs from three different techniques, namely, ToF, DI-SCLC and CELIV. In the case of FET measurements, a mobility that is at least one order of magnitude higher than the bulk techniques is obtained in an un-optimised device configuration and up to two orders of magnitude higher in a device with an optimum choice of dielectric. Hence, FET mobilities may underestimate the potential of many materials if the FET device is not optimised in all areas, from injecting electrodes, choice of dielectric or device geometry. If the device is optimised, the high charge current density may conversely obscure many features of charge transport such as the nature of charge trapping in the polymer film itself.

CHAPTER 5

5 BLUE POLYMERS

5.1 Introduction

This chapter presents the results form charge transport and optical characterisation studies of a novel series of blue emitting fluorene based copolymers.

The first pair of polymers shown in Fig. 5.1 and Fig. 5.2 consists of a homopolymer based on the poly(fluorene) (PF) backbone with each of the fluorene units 9,9-di-substituted with hexyloxyphenyl groups (PFHOP) and the other, S50F8:50FHOP, is a 50:50 copolymer of this structure and 9,9-dioctylfluorene.

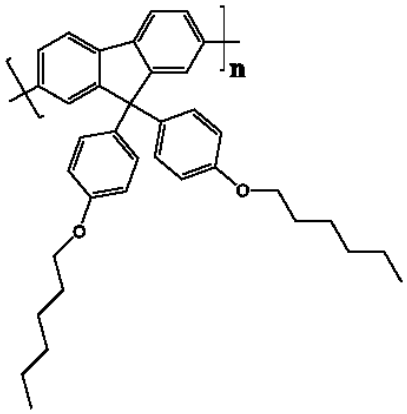

Fig. 5.1 poly(9,9-di(4-hexyloxyphenyl)fluorene) (PFHOP)

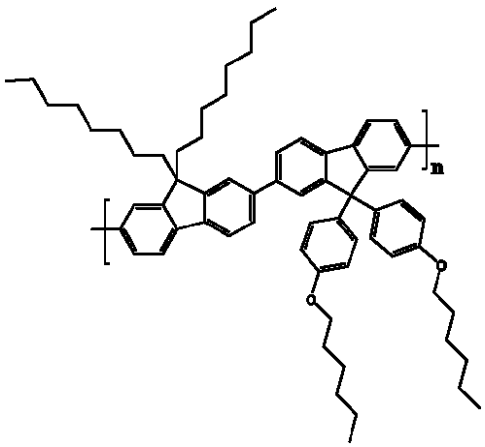

Fig. 5.2 poly(9,9-di(4-hexyloxyphenyl)fluorene-alt-*9,9-dioctylfluorene) (S50F8:50FHOP)*

The second set, shown in Fig. 5.3 and Fig. 5.4, is based on the inclusion of a triarylamine derived phenyloxazole (POZ) unit in the backbone, first in an alternating copolymer arrangement with 9,9-dioctylfluorene and second in a statistical terpolymer structure comprising the POZ unit, the 9,9-disubstituted hexyloxyphenyl fluorene and 9,9-dioctylfluorene in a 10:40:50 ratio.

In the first set, the phenyl ring substituents are likely to be rotated out-of-plane with the backbone because of steric effects and are therefore not likely to be conjugated to the backbone. Hence, the backbone is decoupled from any slight electron withdrawing effect of oxygen atoms in the hexyloxy substitution compared to alkyl side chains because of the higher electronegativity of oxygen atoms compared to carbon, which could otherwise lead to a small reduction in the ionisation potential.

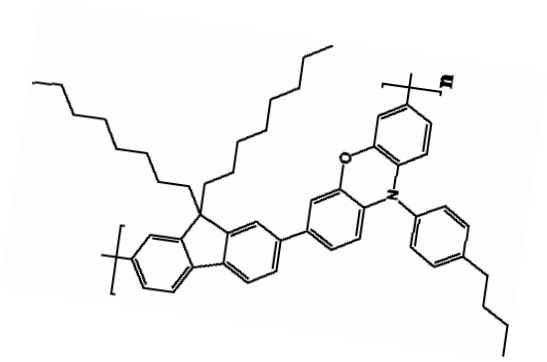

Fig. 5.3 poly(9,9-dioctylfluorene)-co-*(phenyloxazole*-alt-*9,9-dioctylfluorene) (S50F8:50BPPX)*

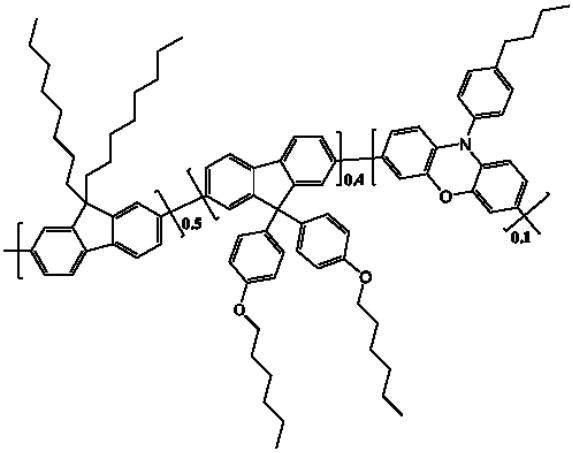

Fig. 5.4 poly((9,9-di(4-hexyloxyphenyl)fluorene-alt-*9,9-dioctylfluorene)$_{0.8}$* -co- *(phenyloxazole*-alt-*9,9-dioctylfluorene)$_{0.2}$) (S50F8:40FHOP:10BPPX)*

An alkoxyphenyl substituted polyfluorene has previously been presented by Lee & Hwang (Lee & Hwang 2003) with linear octyloxy side chains attached to the pendant phenyl groups, instead of the linear hexyloxy chains used in this work, the aim of using the alkoxyphenyl substituents was to suppress long-wavelength green-band emission. The origin of this emission was still subject to differing views at the time of publication and the authors tended towards the view that the emission is related to the formation of aggregates and hence excimers. The use of aryl substituent groups was hoped to suppress aggregate formation and the undesirable emission in this case. However, as discussed in the previous chapter, the green emission from poly(fluorene) is more likely to be related to emission from ketone defect sites and the increased interchain interaction in aggregates has the role of facilitating exciton migration to the defect sites.

In either case, the authors showed that whilst introduction of alkoxyphenyl groups to the 9-position of the fluorene has almost no effect on the absorption characteristics compared to PFO, it does stabilise the PL emission remaining similar to pristine PFO, even after thermal annealing. Furthermore, FT-IR spectra confirmed a degree of resistance towards oxidation after thermal annealing at 180°C by absence of evidence of the carbonyl peak associated with the formation of keto-defects.

Octyloxyphenyl substituted polyfluorene was also synthesised by Ahn *et al.* (Ahn *et al.* 2007) where it was blended with an electron transporting material. In this case, the blended films were found to produce significantly less long-wavelength green-band emission.

The bulky hexyloxyphenyl substituents of PFHOP in this study are therefore expected to aid also in the suppression of aggregate formation and emission, and lend more resistance to the formation of ketone defects as in the case of the octyloxyphenyl substituted polymers discussed above. In addition, these side groups are expected to disrupt the complex phase behaviour associated with the di-octyl substituted fluorene polymer such as the formation of the PFO beta-phase, which is now known to

have a deleterious effect on the hole mobility by acting as a trap. The disruption of beta-phase formation should also be likely to apply to the alternating copolymer, S50F8:50FHOP, as the effective conjugation length (or intrachain correlation length) of beta phase of at least 18 (Tsoi *et al.* 2008) to 26 9,9-dioctylfluorene monomer units (M. Grell *et al.* 1999) will be prevented by the alternation of the two backbone units.

The charge transport and injection properties have not been reported previously for the aforementioned polymer structures and are therefore the subject of investigation in this chapter. It is expected that the hexyloxyphenyl substituents will have a slightly higher mobility than the octyloxy substituted polymer of Lee and Hwang because of the shorter chain length in this series, which permits closer interchain interaction, although no measurements are available in the literature for comparison.

The hexyloxyphenyl side chains are slightly longer in length compared to the linear side chains of di-octyl poly(fluorene) because of the phenyl ring, although the two C-O bonds are slightly shorter than the C-C bond of the linear alkyl chains. Shorter interchain hopping distance and suppression of the beta-phase by the bulky substituents may lead to a higher hole mobility in the case of PFHOP compared to as spun PFO. The alternating units in S50F8:50FHOP may yield further improvements to the hole mobility because of suppression of the beta-phase acting as a hole trap and a distribution of hopping distances that is intermediate between PFO and PFHOP.

The chemical structures of the second set of polymers to be characterised in this chapter are given in Fig. 5.3 and Fig. 5.4. As mentioned, the structure S50F8:50BPPX is a copolymer of (9,9-dioctylfluorene) and a *N*-(4-*n*-butylphenyl)phenoxazine) (BPPX) unit derived from more familiar triarylamine structures by bridging two benzene rings with an additional oxygen atom. This fused tricyclic structure leads to a more rigid backbone and the oxygen bridging the benzene rings in the structures results in greater backbone planarity for BPPX compared to earlier triarylamine based structures although PPX has been shown to have a degree of non-planarity that prevents excimer formation (Yang *et al.* 2006).

The phenoxazine unit has been investigated in several previous reports of polymers and copolymers with different substituent groups compared to those in this work. For example, Zhu *et al.* (2005) investigated a series with linear hexyl substituents including a homopolymer (poly(10-hexylphenoxazine-3,7-diyl)), and fluorene copolymers (poly((10-hexylphenoxazine-3,7-diyl-*alt*-9,9-dihexyl-2,7-fluorene)) in the ratios 25:75, 50:50 and 75:25.

The phenoxazine homopolymer was found to have poor solubility in organic solvents compared to the copolymers because of its rigid backbone. DSC measurements showed the alternating copolymer has a glass transition temperature (T_g) of 168°C, which increases in the copolymers with a higher fraction

of the phenoxazine unit. The HOMO levels were found to be between -4.8 eV and -4.9 eV and the optical gap was found to increase as the fraction of fluorene increases, for example, the optical gap of the homopolymer was 2.44 eV and for the alternating copolymer it was 2.61 eV.

The FET hole mobility of the homopolymer was 2 x 10^{-6} cm^2/Vs, which was attributed to its low molecular weight and poor-film forming ability because of its poor solubility, whereas the alternating copolymer had the highest FET hole mobility of 3 x 10^{-4} cm^2/Vs. (Zhu *et al.* 2005)

Another study of a series of copolymers with linear substituents by Yang *et al.* (2006) used quantum-chemical techniques to study a linear methyl substituted phenoxazine (poly(10-methylphenoxazine-3,7-diyl) (PPOZ)) and a fluorene copolymer (poly[(10-methylphenoxazine-3,7-diyl)-*alt*-2,7-(9,9-dimethyl-fluorene)] (PFPOZ)). Their investigation showed the phenoxazine ring in the ground state unit has a non-planar conformation that impedes π-stacking and excimer formation, which prevents keto defect emission (Yang *et al.* 2006).

Yuanfu at al. (2007) synthesised and characterised the same butylphenyl substituted unit as in our study (BPPX) and copolymerised it with 9,9-di-*n*-butylfluorene (DBF) in a range of fractions from 0 to 42 %. The authors note that phenoxazines usually have high PLQE values and that they are used as efficient laser dyes. The absorption maximum shifted to longer wavelengths with increasing PPX, from 367 nm with 0% PPX to 402 nm with 42% PPX and a similar red shift was observed in the PL spectra as the fraction of PPX was increased.

Time-of-flight hole mobility increased from 2.6 x 10^{-6} cm^2/Vs to 3.7 x 10^{-5} cm^2/Vs from 0% PPX to 42% PPX, showing its effectiveness as a hole transporting unit (Yuanfu *et al.* 2007).

As we mentioned, BPPX has some resemblance to triarylamine although the fused backbone is expected to be more rigid and planar, which therefore leads to the expectation of different charge transport characteristics. However, the fluorene-triarylamine copolymers represent a relevant and interesting reference point for comparative analysis of the charge transport characteristics of the structures in this report.

The charge transport properties of fluorene-triarylamine polymers have been studied extensively in previous reports, in particular, the room temperature hole mobility of the most closely related alternating copolymer TFB[1] has been found to be of the order of 10^{-3} cm^2/Vs (Redecker, Donal D.C. Bradley, *et al.* 1999; Khan *et al.* 2007).

[1] Poly(9,9-dioctylfluorene-*co*-*N*-(4-butylphenyl) diphenylamine)

From previous work on fluorene-triarylamine copolymers, it has been found that increasing the proportion of the triarylamine unit relative to the fluorene moiety in the backbone to 2:1 (the PFB[2] copolymer) results in a slightly lower mobility of around 10^{-4} cm^2/Vs compared to the 10^{-3} cm^2/Vs value for TFB. Increasing the weight percentage of the triarylamine component in the backbone also has the added effect of reducing the ionisation potential from 5.8eV in the case of PFO to 5.30eV and 5.09eV in the cases of TFB and PFB respectively (Redecker, Donal D.C. Bradley, *et al.* 1999).

The final structure characterised in this chapter, S50F8:40FHOP:10BPPX, combines all of the aforementioned moieties in a ter-polymer configuration of the BPPX unit, the hexyloxyphenyl substituted fluorene and 9,9-dioctylfluorene in a 10:40:50 ratio.

5.2 Optical Characterisation

The UV and visible absorption coefficients of thin films of the PFHOP and S50F8:50FHOP polymers is given in Fig. 5.5 and shown alongside the absorption spectrum of PFO as a reference. As with the previous report on the octyloxypheyl substituted polymer (Lee & Hwang 2003), both of these hexyloxyphenyl substituted polymers have very similar absorption spectra to PFO with a peak at 383 nm. Notably, there is no indication of a morphology resembling the beta-phase in these films, which is usually identified with the appearance of a characteristic absorption peak around 430 nm.

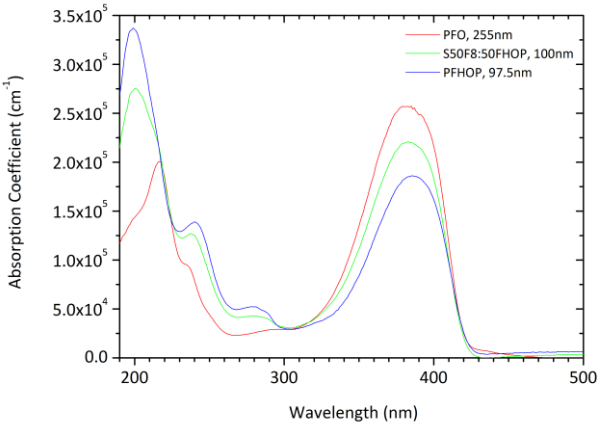

Fig. 5.5 Absorption coefficient of PFHOP and S50F8:50FHOP compared to PFO.

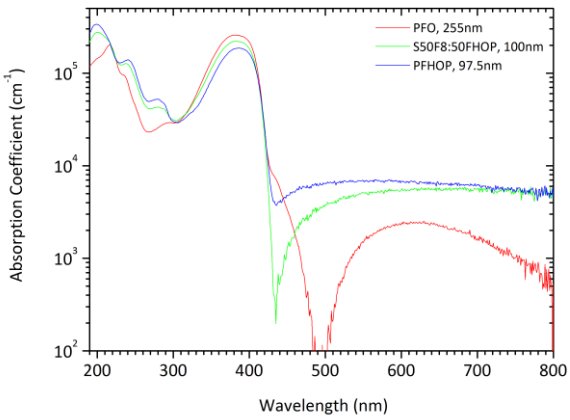

Fig. 5.6 Absorption coefficient of PFHOP and S50F8:50FHOP compared to PFO plotted on a log scale.

The peak absorption coefficient is observed to decrease evenly from PFO to S50F8:50FHOP to PFHOP, which illustrates the dilution effect of the bulky phenyl substituents. The main difference in the spectra of the unprocessed films compared to PFO is the higher ratio of the peak at ~210nm, which corresponds to the absorption of the electron density of the additional benzene rings in the side

[2] Poly(9,9-dioctylfluorene-*co*-bis-*N*,*N*-)4-butylphenyl(-bis-*N*,*N*-phenyl-1,4-phenylenediamine)

groups. The evolution of this peak is illustrated in Fig. 5.5 and its shift to a shorter wavelength of ~200 nm since the additional benzene content in PFHOP is not conjugated to the backbone.

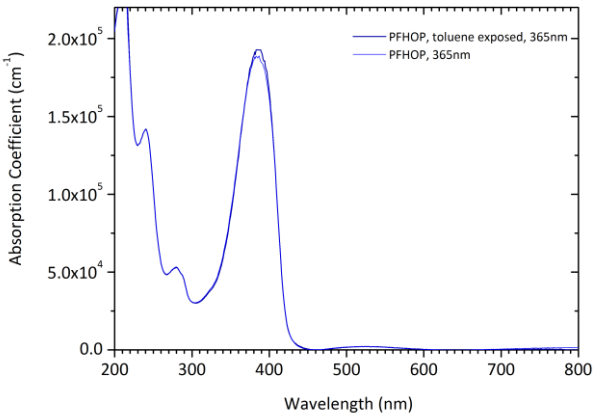

Fig. 5.7 Absorption spectrum of toluene exposed thin film of PFHOP.

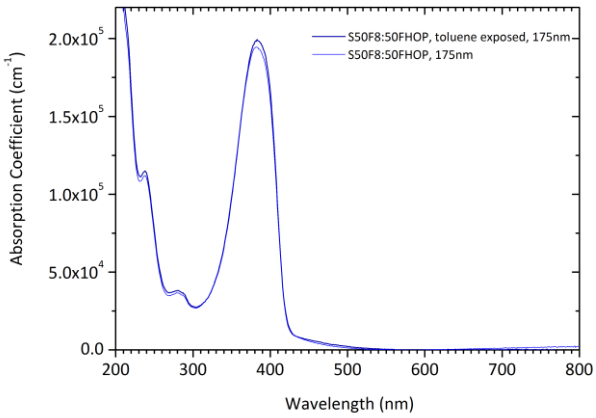

Fig. 5.8 Absorption spectrum of toluene exposed thin film of S50F8:50FHOP.

The films were exposed to toluene vapour, first for ten minutes, and then for an extended period, to investigate whether any morphological changes may be induced in films of these polymers by the technique of vapour annealing. Absorption spectra in Fig. 5.7 and Fig. 5.8 for PFHOP and S50F8:50FHOP, respectively, remain very similar to the as cast films.

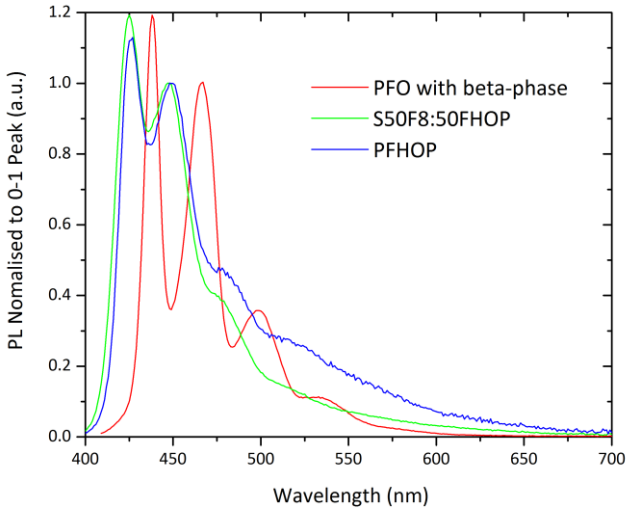

Fig. 5.9 PL of PFHOP and S50F8:50FHOP thin films and PL of a PFO thin film with beta-phase for comparison.

The PL spectra shown in Fig. 5.9 shows well resolved vibronic structure in both PFHOP and S50F8:50FHOP. The spectra, which have been normalised to the 0-1 peak positions, shows the PL is shifted towards higher energy compared to the PL of PFO thin film with a small fraction of beta-

phase. The peak positions are at approximately the same positions for both polymers with the 0-0 peak at 425nm for S50F8:50FHOP and 426nm for PFHOP. The 0-1 peaks are at 448nm for S50F8:50FHOP and 449nm for PFHOP. These are blue-shifted compared to the PFO film with beta-phase, for which they are at 438nm and 466nm, respectively. Both polymers have a greater Stoke's shift compared to PFO and therefore a higher degree of self-absorption, which is preferably as low as possible for prototype lasing materials.

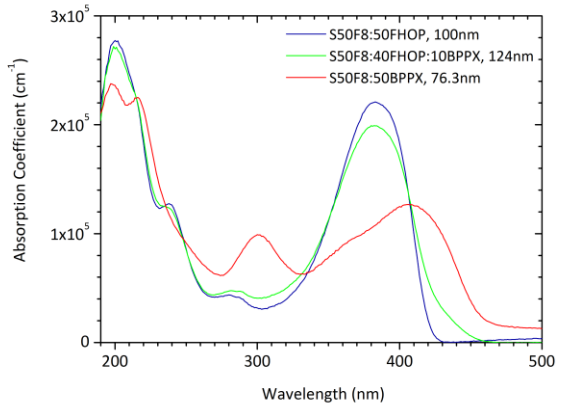

Fig. 5.10 Absorption spectra of S50F8:50BPPX and S50F8:40FHOP:10BPPX compared to the alternating copolymer, S50F8:50FHOP

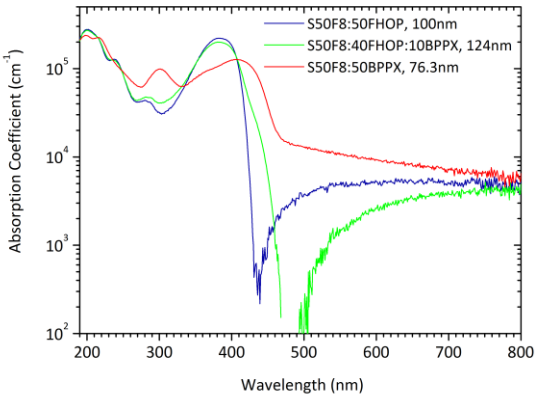

Fig. 5.11 Absorption spectra of S50F8:50BPPX and S50F8:40FHOP:10BPPX compared to the alternating copolymer, S50F8:50FHOP plotted on a log scale

The absorption spectrum of S50F8:50BPPX given in Fig. 5.10 shows that the BPPX moiety produces notable differences in absorption compared to PFO and the FHOP copolymers. First, the longest wavelength absorption peak is broader and red-shifted to 407nm. Second, there is a distinct shoulder at ~363nm and finally there is another prominent absorption peak at 300 nm.

We may contrast this with the spectrum of S50F8:40FHOP:10BPPX also shown in Fig. 5.10 which is very similar to the alternating copolymer, with an absorption peak at 382nm, although the peak absorption coefficient is slightly lower. This shows that, as expected, the inclusion of a small quantity of the PPX moiety in the polymer backbone does not have a significant effect on the overall absorption.

A similar result was observed by Lu *et al.* (Lu *et al.* 2012) in a 99:1 blend of an aryl substituted polyfluorene and TFB (Aryl-F8:TFB) where the absorption spectra did not vary significantly compared to the homopolymer thin film.

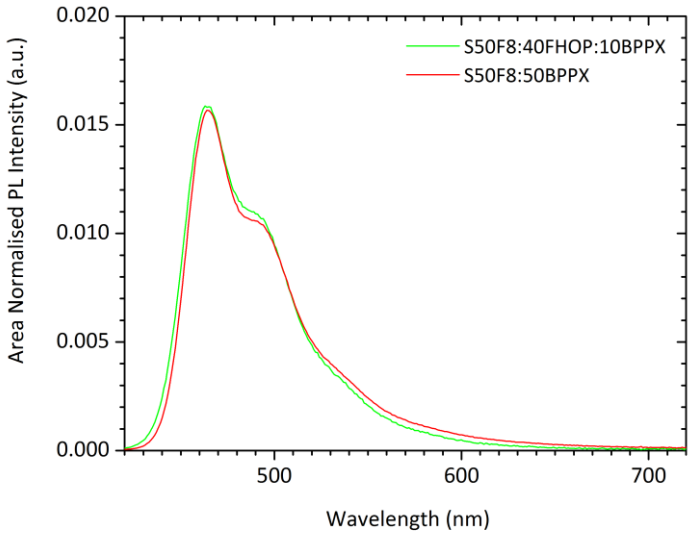

Fig. 5.12 Area normalised PL spectra of S50F8:50BPPX and S50F8:40FHOP:10BPPX

However, as we observe in the PL spectra of S50F8:40FHOP:10BPPX in Fig. 5.12, the minority POZ component is present in a sufficient amount to dominate the emission spectrum. This results from energy transfer to the lowest energy sites. Thus we observe an emission peak at 465nm compared to PFO at ~425nm, the spectrum matches that of S50F8:50BPPX when the POZ moiety is present in equal proportion to the fluorene moiety as an alternating copolymer structure (Fig. 5.12).

Table 5.1 PLQE values of the copolymers

	PLQE (%)
PFHOP (RT spin-coated)	65.7
S50F8:50FHOP (RT spin-coated)	52
S50F8:50BPPX (RT spin-coated)	2.3-6.6
S50F8:40FHOP:10BPPX (RT spin-coated)	15.8
S50F8:40FHOP:10BPPX (RT spin-coated, annealed at 80°C)	31
S50F8:40FHOP:10BPPX (RT spin-coated, annealed at 130°C)	26.6
S50F8:40FHOP:10BPPX (70°C-80°C spin-coated)	32

The effect of the POZ moiety on the PL emission spectrum is most pronounced in the reduction of the photoluminescence quantum efficiency compared to the other polymers in this series as shown in Table 5.1. That is, the lowest PLQE is obtained in the alternating copolymer, S50F8:50BPPX where it is most abundant. In the case of the terpolymer, S50F8:40FHOP:10BPPX, where a small fraction is present, the PLQE is reduced to approximately half that of the PFHOP homopolymer and slightly lower than S50F8:50FHOP.

5.3 Charge Transport and Injection

We have observed in the optical characterisation of this series of polymers that the substitution of hexyloxyphenyl groups to the fluorene backbone does not significantly alter the absorption or emission spectral characteristics of the conjugated system. Hence, in the case of PFHOP and S50F8:50FHOP, the optical characteristics of the poly(fluorene) structure which are desirable for investigations of lasing materials are retained, such as a sufficient Stoke's shift, clear vibronic structure and good luminescence. However, the bulkier substituents result in a lower density of chain packing and further separation of the backbones of polymer chains, as is evident in the reduction of absorption coefficients with an increase in FHOP content.

We therefore proceed to investigate the charge transport and injection characteristics of this series and how they vary in relation to the different combinations of substituents and backbone structures.

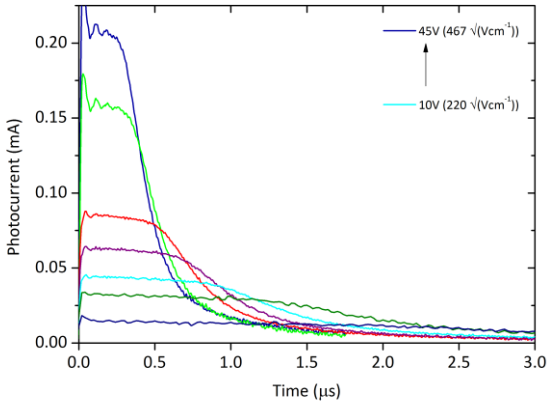

Fig. 5.13 ToF transients of PFHOP (2.06 µm film) at increasing fields

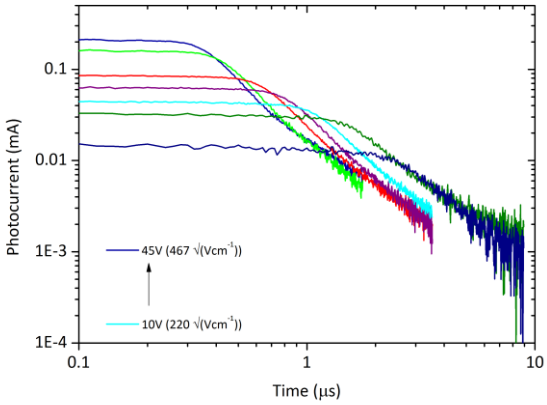

Fig. 5.14 ToF transients of PFHOP (2.06 µm film) on a log-log-plot

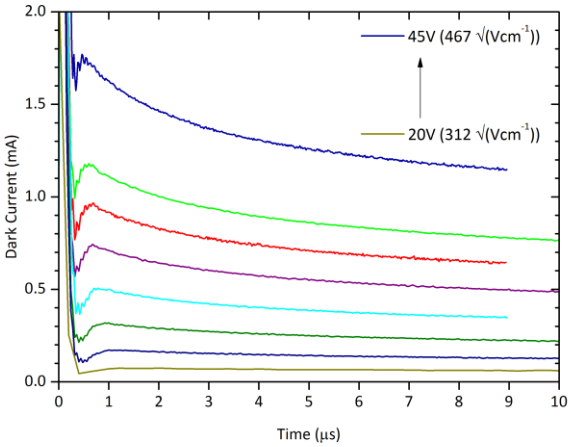

Fig. 5.15 DI-SCLC tranients of PFHOP at increasing fields

Time of flight hole mobility measurements of PFHOP films (of 2.06 µm thickness) show characteristics of non-dispersive transport as indicated by a clearly visible plateau region, followed by a cusp and decay in the measured photocurrent transient signal. Data are shown in **Error! Reference source not found.** at several applied fields in the range of 10^5 V/cm.

Ohmic hole injection was achieved for this device using a MoO_3 interlayer which enabled measurement by the DI-SCLC technique. The transient dark current shown in Fig. 5.15 shows the characteristic cusp at the DI arrival time, followed by decay towards a steady state current, which is evidence of the high injection efficiency. Several attempts were made with an MoO_3 interlayer to achieve ohmic injection, however, most samples showed injection limited behaviour despite similar device fabrication procedures.

We note, at this point, the relatively high ratio ($R = J(t_p)/J(t)$) between the peak current and the current after several multiples of the transit time. At $5t_p$ the ratio falls in the range 1.2 to 1.26 and at $10t_p$ the range is 1.34 to 1.42 This is much higher than the theoretical ratio of $J_p \approx 1.21J_{ss}$ discussed in the literature and reviewed in the previous chapter (Many & Rakavy 1962; Lampert & Mark 1970; Goldie 1999). This feature of the transient signal and what may be inferred from it regarding the nature of trap states will be examined in detail below.

The ToF hole mobility deduced from the transit time at the inflection point is found to be slightly higher than the DI mobility at the same applied bias, for example, at 1.46 x 10^5 V/cm the hole mobility from ToF is 2.36 x 10^{-3} cm^2/Vs (at the inflection point t_0) and from DI is 1.27 x 10^{-3} cm^2/Vs. The ToF mobility evaluated from the $t_{1/2}$ time at the field is 1.77 x 10^{-3} cm^2/Vs.

ToF transients show that the charge transport varies from being dispersive at low fields of ~10^4V/cm to non-dispersive at fields above 10^5V/cm, hence the $t_{1/2}$ time is estimated as the time at half the photocurrent at the inflection at low fields and the time at half the plateau photocurrent at high fields.

The difference in mobility from the $t_0, t_{1/2}$ and t_{DI} times is consistent with results presented elsewhere (Campbell et al. 2000) and in chapter four. The field dependence of the mobility is weak as shown in Fig. 5.16, which also shows there is close agreement in the field dependence of the hole mobility from ToF and DI.

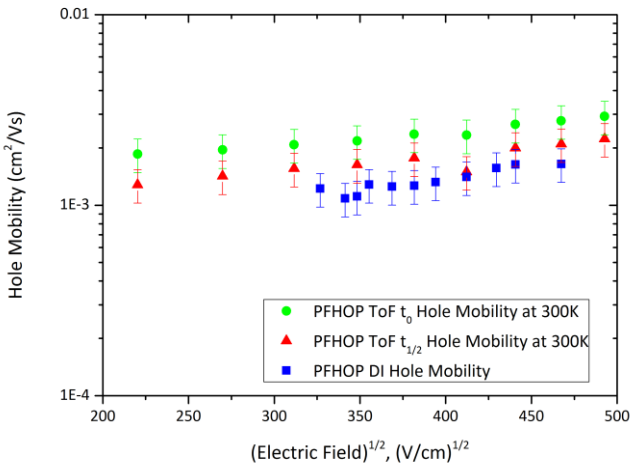

Fig. 5.16 Field dependence of hole mobility for PFHOP

The hole mobility of this polymer is approximately an order of magnitude higher than PFO films produced by spin coating at RT, which have a mobility of ~10^{-4} cm^2/Vs. In the case of PFO, this has been attributed to a small fraction of beta-phase which acts as a hole trap. With this morphology minimised or removed, the mobility may reach 10^{-2} cm^2/Vs (Foster 2013).

In addition, these films are seemingly free of the ketone defect that is detrimental to charge transport in polyfluorenes by acting as a trap for electrons and possibly for holes (Kuik *et al.* 2011) and also degrades desirable deep blue emission to include a green emission component.

One possible reason which may explain why the hole mobility is lower than beta-phase free PFO yet higher than as cast films of PFO is that the length of the hexyloxyphenyl side chains may have increased the relative interchain distance and resulted in a reduction in the charge hopping rate and therefore, the charge carrier mobility. This is consistent with the lower absorption coefficient measured for PFHOP compared to PFO (Fig. 5.6), which is evidence that the conjugated segments of PFHOP are less dense than in PFO because of the bulkier hexyloxyphenyl side chains.

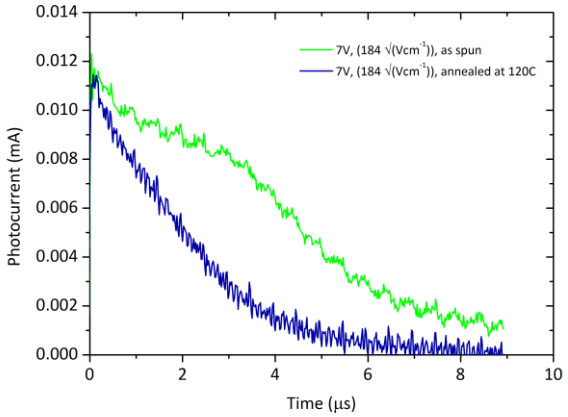

Fig. 5.17 ToF transients of PFHOP, as spun and annealed films showing dispersive characteristics of the annealed film.

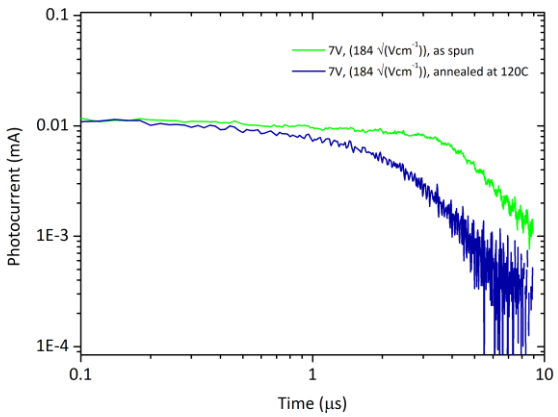

Fig. 5.18 ToF transients of PFHOP, as spun and annealed films showing dispersive characteristics of the annealed film on a log-log plot.

Thermal annealing is a rudimentary technique to try to alter the microstructure in a polymer film and thus examine whether charge transport is structurally limited. Hence, the sample was annealed at 120°C an oxygen and ambient moisture controlled glovebox followed by a repeated ToF measurement, with the measured transients shown in Fig. 5.17. The annealing temperature of 120°C was chosen in correspondence to measurements of PFO in the literature and in the absence of DSC data at the time. This is slightly higher than for an octyloxyphenyl di-substituted fluorene for which the glass transition was found to be approximately 108°C (Lee & Hwang 2003).

Here, it is quite apparent that thermal annealing has caused a transition from relatively non-dispersive to dispersive character. There is seemingly a slight increase in the hole mobility from the 1.62 x 10^{-3} cm^2/Vs to 4.1 x 10^{-3} cm^2/Vs evaluated at the inflection point (t_0). We do not compare the $t_{1/2}$ transit time in this case because of the highly dispersive nature of the transient from the annealed device.

As discussed in the previous chapter, dispersive transport occurs in the case of ToF, when the photo-generated sheet of carriers spreads out in to a broad distribution as they transit through the film with a range of drift velocities. Charge transport of this nature is associated with material systems with a high degree of energetic disorder, in particular, possessing energy states that behave as charge traps on a range of time scales.

Temperature and field dependent measurements fitted to the Gaussian disorder model (GDM) were used to provide an insight into the degree of energetic disorder in spin cast films of this polymer. The full range of measurements was only conducted on the un-annealed sample as the annealed sample already shows dispersive transport at room temperature. As the temperature is lowered, the time required for charge carriers to attain the dynamic equilibrium of non-dispersive transport increases more than the transit time. Consequently, transients tend towards dispersive character strongly as the

temperature is lowered, obscuring the visibility of an inflection point with which to determine the transit time (Borsenberger *et al.* 1992; Bässler & Borsenberger 1993; Tsoi *et al.* 2008; Faria *et al.* 2011). Since the inflection point is already obscured at room temperature for the annealed sample, obtaining a full range of ToF measurements at different temperatures would not be possible.

The temperature and field dependence of the hole mobility of the un-annealed sample of PFHOP is shown in Fig. 5.19, which shows how the field dependence of the mobility decreases with increasing temperature and the scaling of the mobility from ~10^{-5} cm^2/Vs to ~10^{-3} cm^2/Vs over the range 200 < T < 340 K. The energetic disorder from the gradient of Fig. 5.20 is calculated to be 89.6meV and the zero field mobility, μ_0, at the intercept is 0.28 cm^2/Vs. If only the higher temperature points from 280 to 340 K are fitted, the energetic disorder is 94.3 meV and μ_0 is 0.49 cm^2/Vs.

The energetic disorder therefore falls approximately in the middle of the range of values obtained from as spin coated PFO, which is reported to have an energetic disorder of between 82 and 95 meV (Kreouzis *et al.* 2006) and μ_0 of 0.005 to 0.019 cm^2/Vs, respectively.

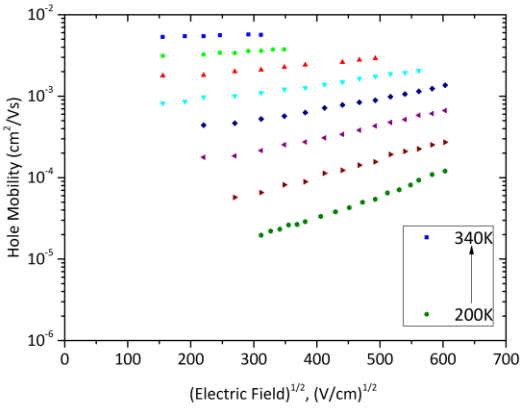

Fig. 5.19 Temperature and field dependence of the hole mobility of PFHOP

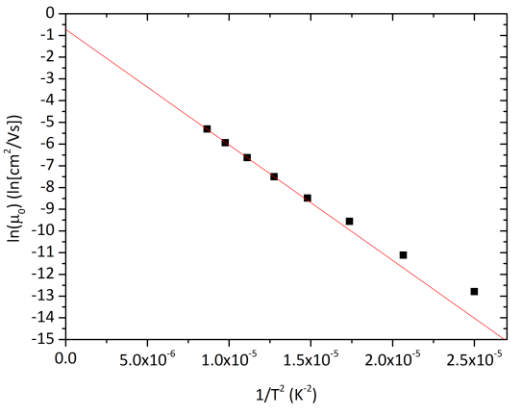

Fig. 5.20 Temperature Dependence of the zero field mobility of PFHOP

In the case of PFO, annealing at 120°C is expected change the microstructure by an increase in crystallinity resulting in closer packing and enhanced planarity of polymer chains. The effect on charge transport is to convert a film showing dispersive characteristics to non-dispersive and leads to a reduction in the energetic disorder (Kreouzis *et al.* 2006). Based on the observation that the transients of PFHOP are indicative of dispersive transport when annealed, we would expect the energetic disorder to have increased as well. These effects of thermal annealing on the hole transport have also been observed in ToF measurements of MEH-PPV (Lee *et al.* 2006).

As discussed earlier in this chapter, the optical characteristics of the polyfluorene unit have been maintained after di-substitution of hexyloxyphenyl side groups. Reintroduction of the dialkylfluorene

unit to the homopolymer, PFHOP, in the copolymer configuration of S50F8:50FHOP may also have the favourable effect, with respect to charge carrier transport, of preventing the formation of beta-phase while permitting closer chain interaction than achieved with the homopolymer. This latter advantage of closer chain interaction seems to have been confirmed according to the peak absorption coefficient reported earlier, which is between that of PFHOP and PFO (Fig. 5.5).

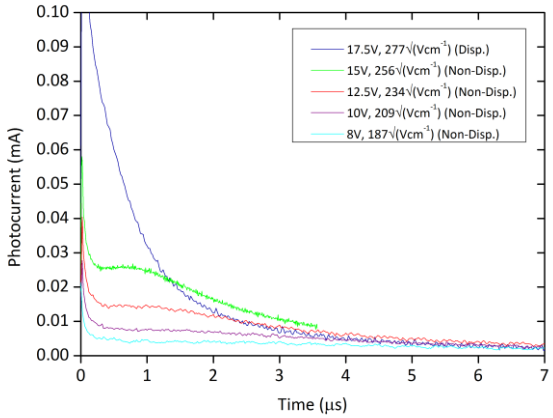

Fig. 5.21 ToF transients of S50F8:50FHOP

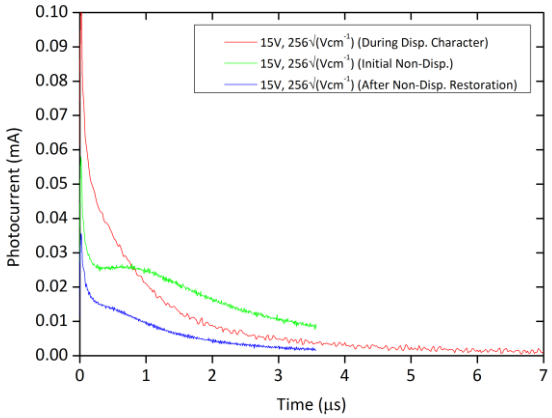

Fig. 5.22 ToF transients of S50F8:50FHOP before and after application of a negative bias

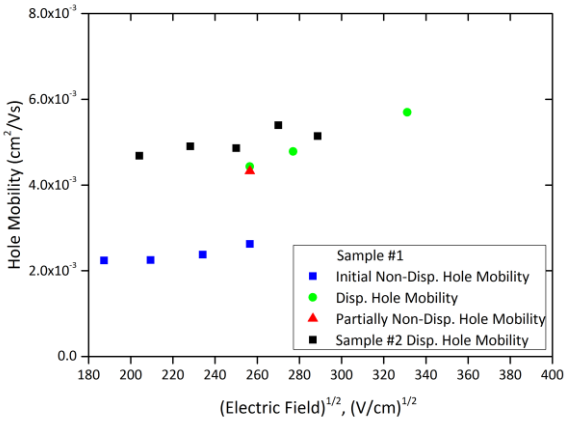

Fig. 5.23 Field dependent hole mobility of S50F8:50FHOP

Initial transient photocurrent signals from ToF measurements are given in Fig. 5.21, which show that charge transport for this sample (#1) was non-dispersive at low fields. However, as the applied field was increased, the transient signal became indicative of dispersive transport by the smearing out of the plateau and inflection point. This dispersive character remained when repeating measurements at low fields. It was found that after application of a negative bias of -15V for ten minutes, the plateau was partially restored (Fig. 5.22). The hole mobility was also observed to vary from ~2 x 10^{-3} cm^2/Vs to ~4 x 10^{-3} cm^2/Vs from the initial non-dispersive state to the dispersive state and remained at the higher level after the reversed bias was applied (Fig. 5.23).

We note that J-V measurements were conducted on this sample just prior to these ToF measurements. Hence, a possible explanation for the behaviour of this particular sample is filling of deep charge traps by charge injection from the MoO_3 electrode that remained filled at the time of the ToF measurements. The application of a negative bias therefore "reconditions" the device by injecting charges that fill traps. We note, that the typical behaviour from other samples of S50F8:50FHOP is dispersive transport with a comparable mobility to sample #1 in the dispersive charge transport stage (Fig. 5.23).

Charge transport measurements from PFHOP earlier in this chapter showed that its transport became dispersive after annealing. In the case of S50F8:50FHOP, there is no discernible difference in the character of ToF transients after annealing at 120°C, which remained dispersive (not shown) although an increase in hole mobility is observed from 5.14 x 10^{-3} to 9.29 x 10^{-3} cm^2/Vs at a field of 8.33 x 10^5 V/cm.

This indicates annealing may not have resulted in a reduction in energetic disorder as expected from temperature and field measurements of PFO in prior works (Kreouzis *et al.* 2006). However, some degree of polymer chain re-ordering must have occurred within the sample morphology to account for the improvement in hole mobility.

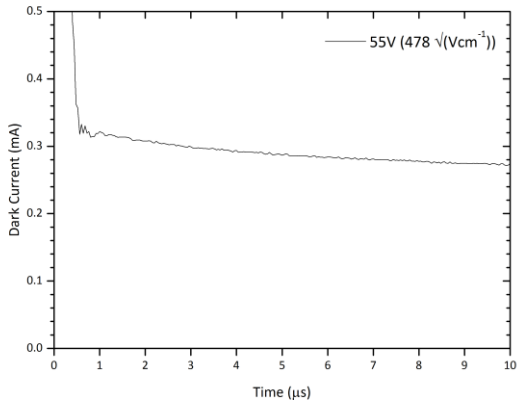

Fig. 5.24 Tranient dark current of S50F8:50FHOP from an MoO_3 injection layer

DI-SCLC measurements were attempted on S50F8:50FHOP samples, however, no cusp was observed in dark injection transients as shown in a typical plot in Fig. 5.24. This may be because the film is too thin and the transit time too quick for the cusp to appear outside the RC response of the sample device. This is a likely explanation for the absence of the cusp because comparison of the RC decay times with transit times from ToF measurements indicate that the ToF transit time is within the RC response. For example, at a field of 1.46 x 10^5 V/cm the ToF transit time is 0.22 µs, meaning the DI cusp is expected to occur at 0.17 µs (based on $t_{di} = 0.786 t_{tr}$), which is within the RC response of

0.55 µs. Attempting to reduce the RC response using a smaller resistor increased ringing in the dark current transient.

These measurements for PFHOP and S50F8:50FHOP show an enhancement of the hole mobility in general compared to PFO, with the usual effects of energetic disorder, charge trapping and injection limitations also evident.

With the chemical structure of S50F8:50BPPX, we consider the effect on charge transport and injection of incorporating POZ units that specifically target improved hole transport in an alternating copolymer structure with (9,9-dioctylfluorene).

The transient dark injection SCLC and steady state JV measurements both give a clear indication of ohmic injection by the visibility of a cusp at progressively shorter times with an increasing applied field (Fig. 5.25) in the former and an increase in current-density with voltage that corresponds to an SCL current (Fig. 5.26) in the latter. The JV measurements are fitted to the field-dependent Murgatroyd equation for SCLC in Fig. 5.26 and shows an excellent fit to the experimental current density.

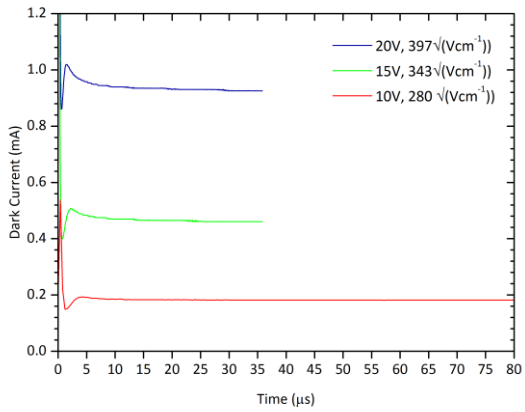

Fig. 5.25 DI tranients of S50F8:50BPPX using an MoO_3 injection layer.

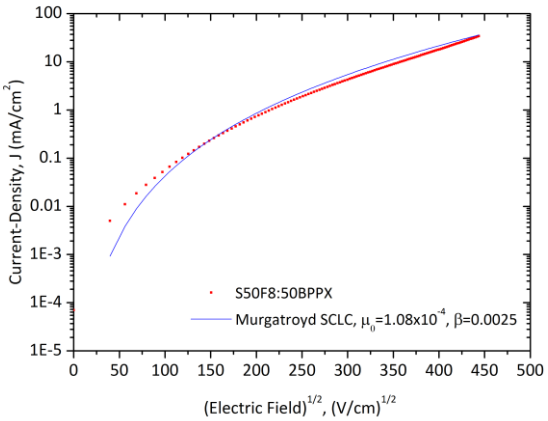

Fig. 5.26 JV of S50F8:50BPPX from an MoO_3 injection layer including field-dependent theoretical fits.

The hole mobility from the DI measurements of S50F8:50BPPX is found to be 3.6 x 10^{-4} cm^2/Vs at 10^5 V/cm and Fig. 5.27 shows the field dependence of the hole mobility compared to PFHOP, the latter has an approximately twice as high mobility but shows a very similar field dependence.

For comparison, the highest hole mobility obtained for a fluorene-triarylamine copolymer, TFB[3], with the same di-octyl substituents on the fluorene unit was found to be ~10^{-2} cm^2/Vs from ToF measurements at RT and at a comparable field (Fong *et al.* 2006; Fong *et al.* 2009). This value is higher than had previously been reported for nominally the same TFB polymer and other related

[3] poly(9,9'-dioctylfluorene-*co*-*N*-(4-butylphenyl)diphenylamine)

fluorene-arylamine copolymers such as PFMO[4] and BFB[5] in a much earlier report where the hole mobilities were found to be ~10^{-3} cm^2/Vs (Redecker, Donal D.C. Bradley, *et al.* 1999).

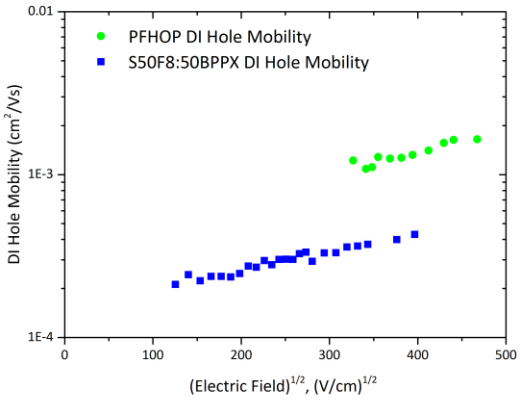

Fig. 5.27 Field dependence of the hole mobility for S50F8:50BPPX compared to PFHOP.

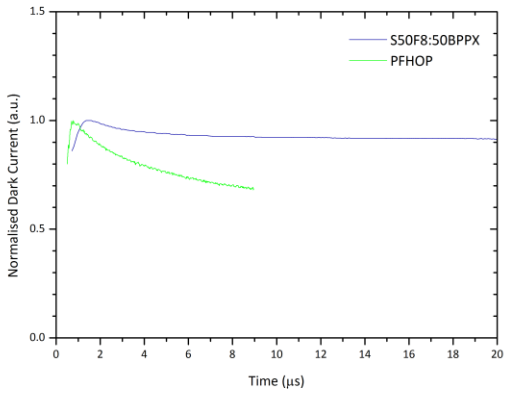

Fig. 5.28 Normalised DI transients from PFHOP and S50F8:50BPPX

A key feature to note in the DI transients of S50F8:50BPPX compared to measurements of other materials in this thesis discussed so far is the short time in which the current approaches the steady state level relative to the transit time. This is illustrated in Fig. 5.28 where the transient DI signals from PFHOP and S50F8:50BPPX are shown normalised to their peak currents (the peak of the cusp). The transient of S50F8:50BPPX quickly reaches an equilibrium level whereas the transient of PFHOP decreases asymptotically over several multiples of the DI transit time. A large ratio between the peak current and steady state currents has been previously connected with the presence of charge traps at the interface or in the bulk (Harding *et al.* 2010).

For S50F8:50BPPX, the ratio of $J(t_p)$ to the current density at ten times the peak time, $J(10t_p)$, is found to vary between 1.08 and 1.10 in the measured field range. This compares to a ratio of ~1.4 for PFHOP (Fig. 5.40). This difference in transient behaviour and its connection with charge traps will be discussed later in this chapter in view of the expected theoretical maximum ratio of ~1.21 (Lampert & Mark 1970).

It is also possible to achieve ohmic hole injection from ITO into S50F8:50BPPX, which showed the same magnitude of current density as the MoO3/Au HIL (not shown). This result is expected, considering HOMO level of hexylphenoxazine polymers has been measured to be between -4.8 eV and -4.9 eV (Zhu *et al.* 2005). Hence, ohmic hole injection from ITO is possible in S50F8:50BPPX since the difference between its HOMO and the work function of ITO at ~ 4.4 to 4.6 eV is close to the approximate requirement for ohmic injection of a barrier that is less than 0.35 eV. ITO is hole

[4] poly(9,9-dioctylfluorene-*co*-bis-*N*,*N*'-(4-methoxyphenyl)-bis-*N*,*N*'-phenyl-1,4-phenylenediamine)
[5] poly(9,9'-dioctylfluorene-*co*-bis-*N*,*N*'-(4-butylphenyl)-bis-*N*,*N'*-phenylbenzidine)

blocking for PFO and the fluorene based polymers, PFHOP and S50F8:50FHOP, discussed in this chapter since their HOMO level is ~5.8 eV.

This ability to achieve ohmic injection from low work-function contacts such as ITO prevented reliable ToF measurements from being conducted because the requirement of a counter electrode that blocks hole injection has not been fulfilled in the case of these sample devices of S50F8:50BPPX.

In the results presented thus far, we have seen how charge transport and injection may be systematically enhanced by novel copolymer combinations of new backbone units. The final structure characterised in this chapter combines all of the moieties discussed above in a ter-polymer configuration of (9,9-dioctylfluorene), the hexyloxyphenyl substituted fluorene (PFHOP) and the BPPX unit (in S50F8:50BPPX) in the ratio 50:40:10.

The chemical structure of this polymer is therefore closest in resemblance to S50F8:50FHOP with the alternation of the dioctylfluorene and hexyloxyphenyl moieties. The addition of 10% of the BPPX unit is expected to lead to improved hole injection by modification of the HOMO level although we have already seen in the optical characterisation that this proportion of the unit reduces the PLQE from 37.5% for S50F8:50FHOP to 32% for S50F8:40FHOP:10BPPX.

ToF transients show clear signs of non-dispersive transport with a distinct plateau and inflection point. The hole mobility (from t_0) is found to be the lowest of this series by approximately two orders of magnitude and is between 2 x 10^{-6} and 7 x 10^{-6} cm^2/Vs at ~10^5 V/cm. The temperature and field dependence of the as spin-coated sample is shown in Fig. 5.29, which shows the mobility increasing from around 10^{-7} cm^2/Vs to 10^{-5} cm^2/Vs as the temperature is increased from 200K to 340K.

Temperature and field dependence measurements were also performed on the sample after it was annealed at 80°C, then at 130°C. The ToF transients show transport to be non-dispersive after all annealing stages when measured at room temperature, unlike PFHOP which was discussed earlier, for which transport became dispersive after the sample was annealed.

The wide range of the temperature and field dependence measurements in terms of the temperature and field range provides a particularly interesting experimental insight into the nature of charge transport in polymer systems. The inverse-squared temperature dependence of the zero-field mobility is given in Fig. 5.30 from which the energetic disorder and the mobility pre-factor (which is a theoretical limit of the mobility at zero field and infinite temperature) of the Gaussian Disorder Model may be extracted from the gradient and intercept, respectively (Kreouzis *et al.* 2006).

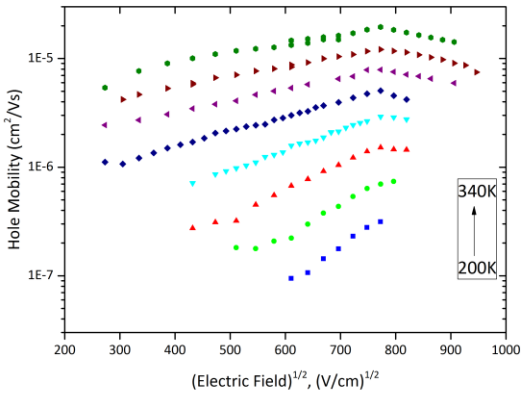

Fig. 5.29 Temperature and field dependence of the ToF hole mobility of S50F8:40FHOP:10BPPX

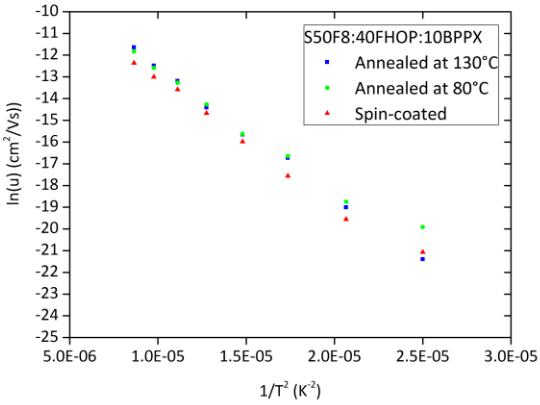

Fig. 5.30 Temperature dependence of the zero field hole mobility of S50F8:40FHOP:10BPPX

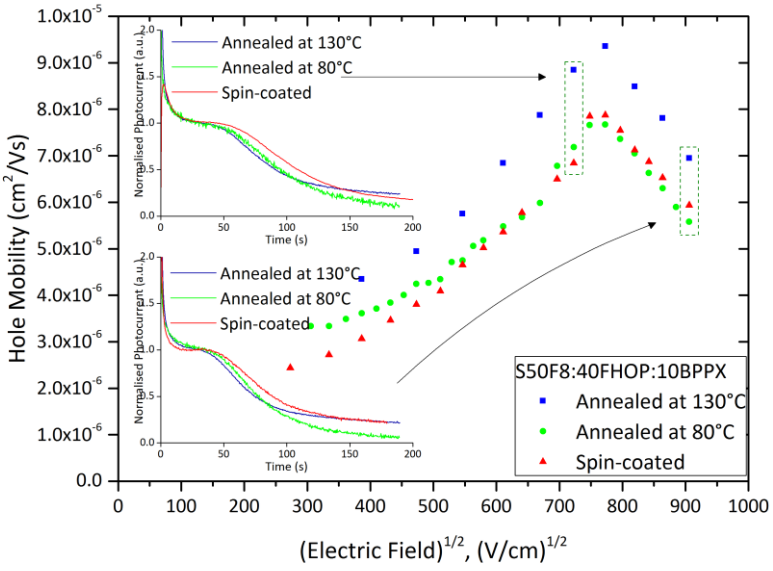

Fig. 5.31 Temperature and field dependence of the ToF hole mobility of S50F8:40FHOP:10BPPX annealed films with insets of ToF transients normalised to the plateau.

The calculated energetic disorder values given in Table 5.2 do not vary significantly after each annealing step, however there is a slight increase in the hole mobility and mobility pre-factor. The temperature dependence of the charge transport follows the familiar pattern of a transition from dispersive to non-dispersive as the temperature is increased according to the shape of the transient signal, in which the plateau becomes apparent as temperature increases.

Table 5.2 Summary of energetic disorder and mobility pre-factor values obtained for S50F8:40FHOP:10BPPX RT spin-coated and annealed films obtained from temperature and field dependent ToF measurements.

S50F8:40FHOP:10BPPX	**σ, Energetic disorder (meV)**	**μ_0, Mobility Pre-factor (cm^2/Vs)**
RT Spin-coated	100.6	8.88×10^{-4}
Annealed at 80°C	97.4	9.08×10^{-4}
Annealed at 130°C	100	1.36×10^{-3}

If we consider only the field dependence at any particular temperature, as in Fig. 5.31, we observe several features of note. First, there is a small degree of non-linearity in the field dependence of the hole mobility from the low field range until 6×10^5 V/cm, where the hole mobility reaches its highest level of 7×10^{-6} cm^2/Vs. Following this peak, the mobility begins to decrease in proportion to further increases in the applied field. These trends are also observed when the mobility is calculated using $t_{1/2}$.

The decrease in hole mobility at increasing electric fields, in which the field dependence departs from Poole-Frenkel type behaviour $ln\ \mu\ \propto SE^{1/2}$ by a reversal of the sign of S, is a well-known effect attributed to strong electric fields locking charging hopping to the direction of the electric field rather than facilitating charge hopping to the most efficient pathways, typically where interchain distances are shortest (Peled & Schein 1988; Tsoi *et al.* 2008).

5.4 The Cusp in ToF Transients

The dependence of the mobility on the applied field is further reflected in the shape of the ToF transients shown in Fig. 5.32 (bottom), which have been normalised to the photocurrent of the plateau region, before the inflection point. Here we observe a pronounced cusp at the inflection point of the transient that is gradually reduced at higher fields until it is almost completely eliminated.

Furthermore, we find that this cusp may be reduced by annealing Fig. 5.32 (top) which shows restoration of a steady plateau after the sample is annealed at 130°C.

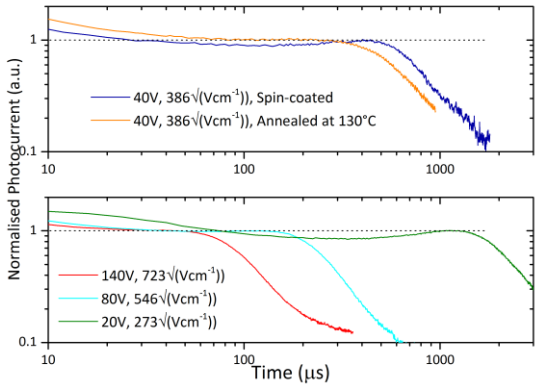

Fig. 5.32 ToF transients of S50F8:40FHOP:10BPPX at different applied fields on log-log plots.

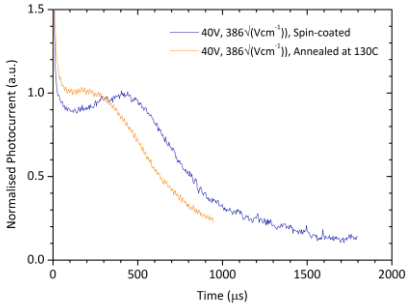

Fig. 5.33 Linear plot corresponding to top-left

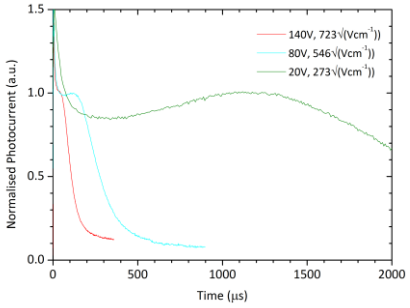

Fig. 5.34 Linear plot corresponding to bottom-left

Tyutnev et al. (2012) discuss the existence of this cusp in detail in the case of molecularly doped polymers and they propose a model that involves a two-layer structure of a thin surface layer and the bulk of the polymer, which have different trap concentrations.

The authors use three variations of the ToF technique and computational models to investigate the temperature and field dependence of ToF transients. First, the technique used in this study, involving photogeneration close to the interface, secondly, a technique based on bulk generation using an electron gun for uniform generation of charge carriers and finally, by controlled variation of the width of the generation zone. (Tsoi *et al.* 2008)

In the case of measurements using an electron gun, the authors show that a higher electron energy increases the fraction of carriers generated in the bulk, leading to weaker cusps until a flat plateau appears at a certain electron energy. The appearance of a flat plateau is attributed to the alignment of

currents in the two layers following carrier generation in the respective layers. At even higher energies, their measurements showed the plateau begin to slope downwards. The plateau region sloping downwards is observed in our measurements of S50F8:40FHOP:10BPPX below 280K at high applied fields

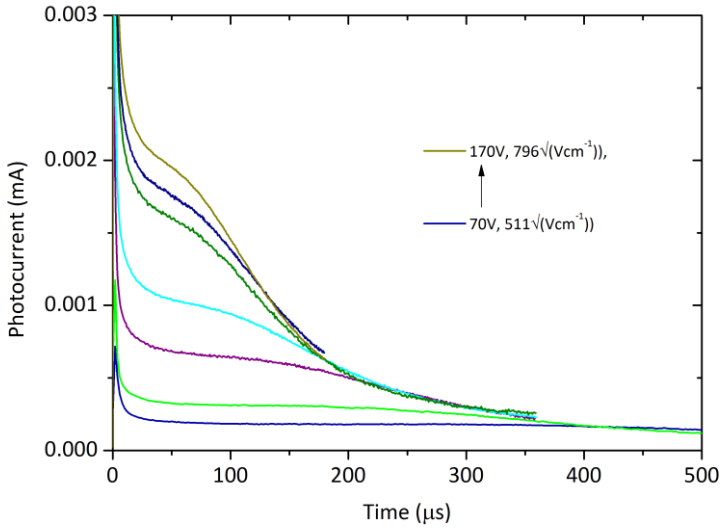

Fig. 5.35 ToF transients of S50F8:40FHOP:10BPPX at different applied fields illustrating the change from a flat plateau region to a downwards-slope

Computational results based on the two layer model show that the visibility of the cusp may be related to the width of the generation zone, which causes the current transient to change from having a distinct cusp, to a flat plateau and finally to a sloping plateau as the width of the generation zone is increased.

Another feature in these measurements, and ToF transients in general, is the anomalously broadened tail which provides evidence that charge transport may in fact be dispersive rather than Gaussian, even with the appearance of a plateau.

Hence, according to the authors, the widely used GDM appears to be inadequate for describing all of the features of the temperature and field dependence of the photocurrent transients in a time-of-flight measurement, which leads the authors to a two layer multiple trapping model with a Gaussian distribution of traps rather than an exponential distribution that is more able to describe the physics of charge carrier transport represented in the shape of current transients such as the formation of the plateau and cusp.

Another view is that the assumption of charge transport in a space-charge-free regime for ToF measurements is incorrect and space-charge-perturbed currents may be more appropriate. In this case, higher laser intensities lead to a more prominent cusp in ToF transients (Li, Duan, Zhang & Qiu

2014). However, in our measurements, the laser intensity is continually adjusted to ensure a low density of photogenerated charge carriers and this would not explain the reduction of the cusp in the ToF transients of the annealed sample.

Dark injection measurements were possible with this material in the polymer-on-HIL device configuration (Fig. 5.36), using a procedure of high temperature spin coating at 70°C instead of room temperature spin coating. In this case, we find the DI hole mobility to be around 10^{-5} cm^2/Vs (Fig. 5.37).

This is higher than the ToF device described above, which showed injection limited behaviour that prevented DI measurements. The ToF device was in the HIL-on-polymer configuration and spin-coated at room temperature.

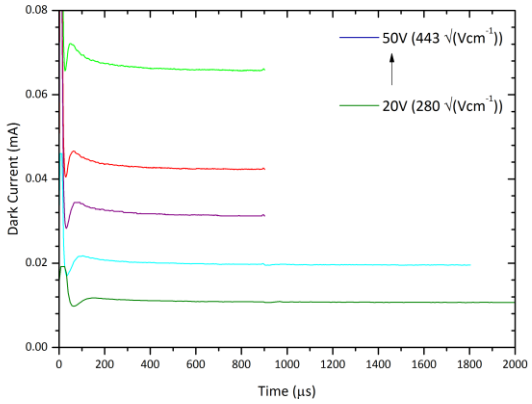

Fig. 5.36 DI-SCLC transients of an ITO/MoO_3/ S50F8:40FHOP:10BPPX/Au device

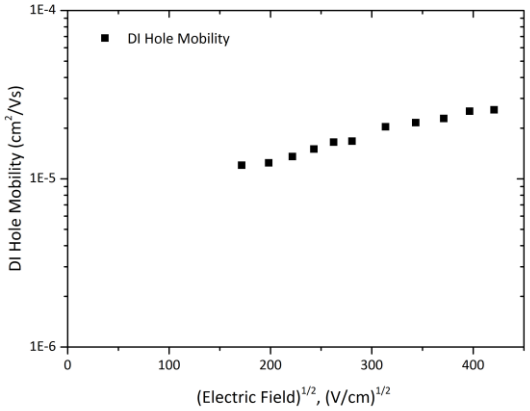

Fig. 5.37 Field dependence of the DI hole mobility for S50F8:40FHOP:10BPPX

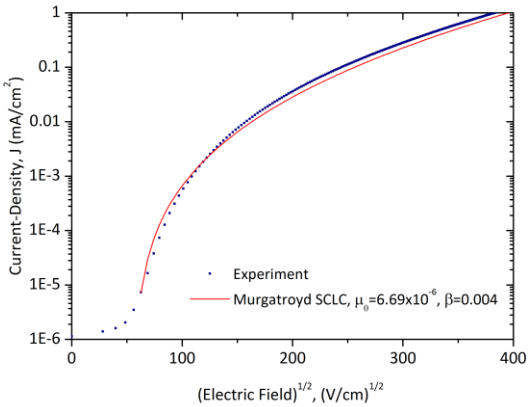

Fig. 5.38 JV characteristics of S50F8:40FHOP:10BPPX including field-dependent theoretical fits using parameters derived from DI measurements.

This difference in mobility is unusual as the ToF mobility tends to be slightly higher, as discussed earlier in this thesis. However, this is when both ToF and DI measurements are performed on the same sample. Hence this difference in mobility and the fact that ohmic injection has been possible in this latter device may be because of a difference in film morphology between the sample used for DI measurements and the ToF sample that has arisen from spin coating at 70°C.

Steady state current density measurements are shown Fig. 5.38 including the field-dependent Murgatroyd fit using μ_0 and β parameters derived from DI-SCLC, showing excellent correspondence between theory and experiment as was the case with S50F8:50BPPX discussed earlier.

5.5 Dark Injection Transients and Charge Traps

In the discussion on the measurements on S50F8:50BPPX samples, we mentioned features seen in DI transients that give an indication of charge traps at either the injection contact interface or in the bulk. Here we draw together the results from the three polymers for which DI transients were obtained and PFO from the previous chapter to investigate the role of charge trapping in the different polymers.

DI transients of as spin-coated films of S50F8:40FHOP:10BPPX, PFHOP and S50F8:50BPPX and PFO are shown in Fig. 5.39 normalised to their peak currents (the peak of the cusp at the DI transit time) from measurements at similar fields of ~396 $\sqrt{Vcm^{-1}}$ apart from PFO, which is at a slightly lower applied field of 364 $\sqrt{Vcm^{-1}}$. The occurrence of the cusps at different times is indicative of the range of hole mobilities for these polymers.

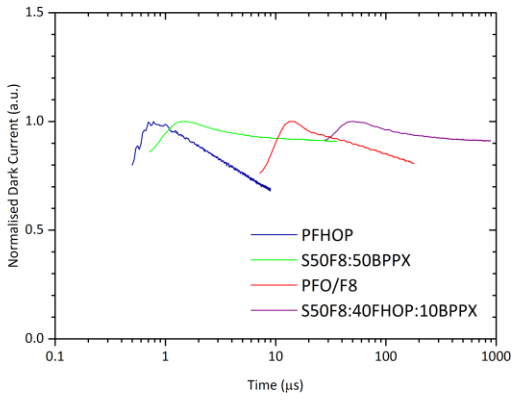

Fig. 5.39 DI-SCLC transients of polymers in this chapter normalised to the peak dark current values including a DI transient of PFO/F8.

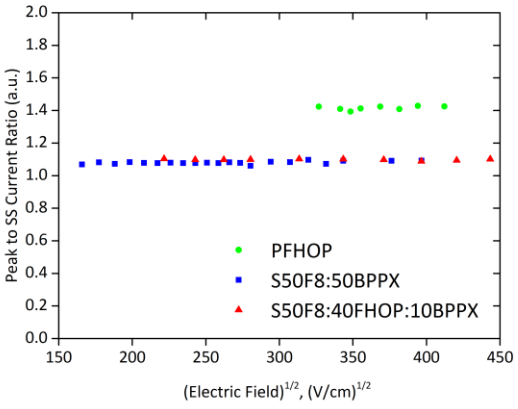

Fig. 5.40 Field dependent ratios of peak to steady-state current densities.

The transients for S50F8:40FHOP:10BPPX and S50F8:50BPPX are found to reach an equilibrium level shortly after the transit time whereas the transients for PFHOP and PFO continue to fall for several multiples of the DI transit time.

Comparing the ratio of J_p to the current density at ten times the peak time, $J(10t_p)$, for the polymers shows a ratio of 1.08 to 1.10 for S50F8:40FHOP:10BPPX and S50F8:50BPPX in the measured field range, whereas the ratio is ~1.4 for PFHOP (Fig. 5.40). It is clear from the transients in Fig. *5.39* that PFHOP and PFO have not yet reached a steady state current density at ten times the peak time ($10t_p$).

According to the main theoretical model of dark injection transients, the maximum ratio of J_P to the trap free space charge limited current density (J_{TFSCLC}) should be 1.21 (Lampert & Mark 1970).

Here we have compared J_p to the current density after $10t_p$ instead of using the experimental steady state values. This provides for consistency across datasets and experiments and is based on the length of the transients recorded.

From the DI transients we see that S50F8:40FHOP:10BPPX and S50F8:50BPPX have reached a steady current density at $J(10t_p)$ that we may approximate to the steady state current density (J_{SS}) such that $J(10t_p) \approx J_{SS}$. The ratio for these two polymers is less than that of the theoretical model, whereas PFHOP, for which the current density is still decreasing at $J(10t_p)$, has a ratio that has already exceeded the theoretical ratio of ~1.21 and is continuing to increase.

According to the theoretical understanding of DI measurements, a high ratio between the peak and steady state current density, such as the long decaying tail observed in the case of PFHOP, is an indication of space charge limited current in the presence of traps, in particular interfacial traps that have trapped charges very close to the moment of injection. In the case of a shallow cusp ($J_p/J_{SS} <$ 1.21), this may be accounted for by bulk traps that trap charge on a timescale shorter than the transit time and release them after a much longer time (Harding *et al.* 2010).

5.6 ASE and Optical Gain

We complete our investigation of this series of polymers with the presentation of results from ASE and optical gain measurements of PFHOP and S50F8:50FHOP, which are the only polymers found to exhibit ASE in the experimental configuration described in chapter three. We are therefore able to compare directly the effects on optical gain in the alternating copolymer compared to the homopolymer.

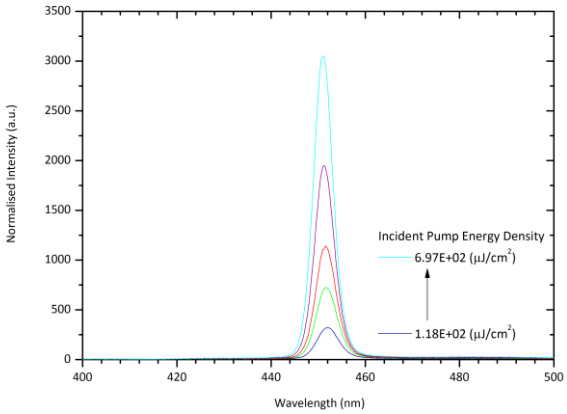

Fig. 5.41 ASE spectra of PFHOP (97.5 nm film)

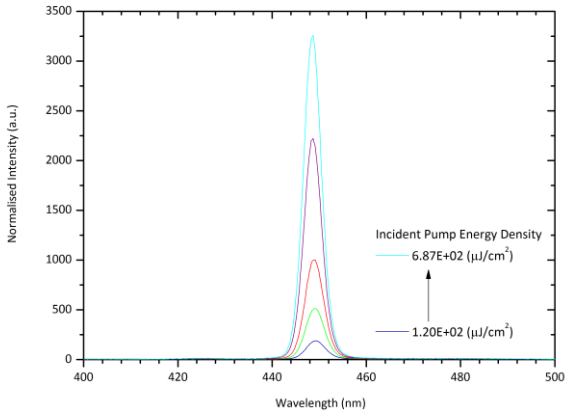

Fig. 5.42 ASE spectra of S50F8:50FHOP (100 nm film)

The sample is pumped with a 355 nm stripe shaped laser excitation with a width of 50 μm and variable length up to 4 mm. The edge emission is collected through a microscope objective and TE polariser to an optical waveguide connected to a spectrometer.

The ASE spectra for a PFHOP (97.5 nm film) and S50F8:50FHOP (100 nm film) are shown in Fig. 5.41 and Fig. 5.42, which show how the peak intensity grows with an increasing incident pump energy density. The ASE peak wavelengths are 451.4 nm and 448.9 nm, respectively and the full-width half-maximum in both cases is approximately 5 nm. There is a slight shift in wavelength of the peak position at increasing incident pump energy densities as the emission narrows into the ASE wavelength and the energy dependence plots of the ASE for PFHOP in Fig. 5.43 and S50F8:50FHOP in Fig. 5.44 are based on the intensities at these wavelengths, which are the maximum gain positions.

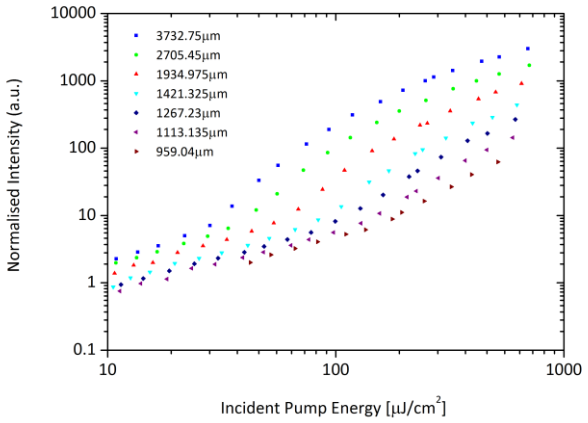

Fig. 5.43 Energy dependence of the ASE intensity of PFHOP

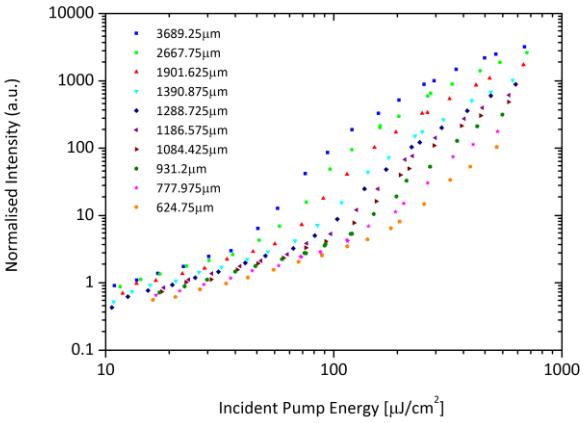

Fig. 5.44 Energy dependence of the ASE intensity of S50F8:50FHOP

At the longest stripe length of 3.7 mm, the ASE threshold is 29 μJ/cm^2 for PFHOP, which is identical to the threshold reported for PFO by Heliotis *et al.* (Heliotis *et al.* 2002), and the threshold for S50F8:50FHOP is 41 μJ/cm^2. Both polymers show a smooth roll-off in ASE intensity as the gain begins to saturate instead of a well-defined saturation threshold.

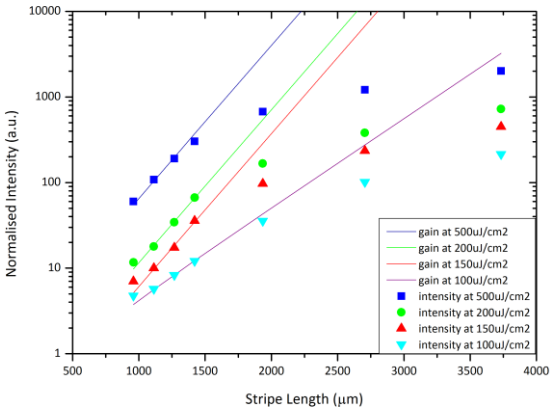

Fig. 5.45 Stripe length dependence of the ASE intensity of PFHOP and fitted optical gain.

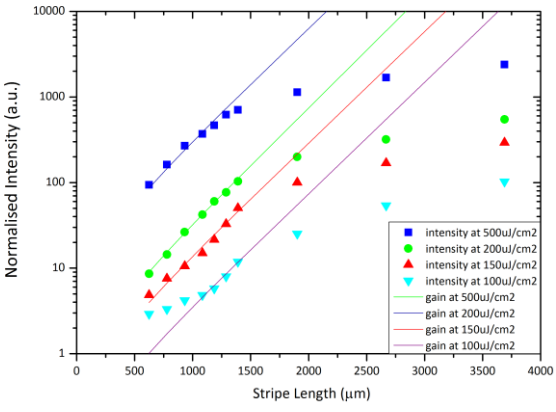

Fig. 5.46 Stripe length dependence of the ASE intensity of S50F8:50FHOP and fitted optical gain.

The optical gain is determined using the one-dimensional gain equation,

$$I(\lambda) = \frac{AI_p}{g(\lambda)}\left(e^{g(\lambda)l} - 1\right) \qquad 5.1$$

to obtain the wavelength dependent gain coefficient $g(\lambda_{ASE})$ in units of cm^{-1}, where AI_p is the term corresponding to the spontaneous emission and l is the length of the stripe shaped excitation (McGehee *et al.* 1998; Laquai *et al.* 2008).

The length dependence of the ASE intensity plots for PFHOP and S50F8:50FHOP are shown in Fig. 5.45 and Fig. 5.46, respectively. The ASE intensities are plotted at several pump energy densities as well as fits of equation 5.1 at each energy. We observe gain saturation after ~1.5 mm, hence the gain is fitted to the measurements at stripe lengths shorter than 1.5 mm. The gain values at each energy are summarised in Table 5.3.

Table 5.3 Optical gain at different pump energy densities.

Pump Energy Density ($\mu J/cm^2$)	**Optical Gain, PFHOP (cm^{-1})**	**Optical Gain, S50F8:50FHOP (cm^{-1})**
100	24	30
150	41	30
200	41	30
500	41	30

PFHOP and S50F8:50FHOP exhibit maximum gains of 41 cm^{-1} and 30 cm^{-1} at energy densities above 150 $\mu J/cm^2$. The gain drops to 24 cm^{-1} for PFHOP at 100 $\mu J/cm^2$ since this represents the region of sub-threshold emission at short stripe lengths.

At 150 $\mu J/cm^2$, S50F8:50FHOP appears to show a change of slope. This is because the measurements at the shortest three stripe lengths are in the sub-threshold region. Fitting only the four points between 1 mm and 1.5 mm yields a gain of 40 cm^{-1}.

These gain values are lower than the literature value for PFO of 74 cm^{-1} (Heliotis *et al.* 2002). However, this was achieved using a 300 μm stripe width compared to the 50 μm stripe used here. A wider stripe results in a larger amplification area through which light is waveguided, which may inflate gain values.

ASE was not observed for S50F8:50BPPX or S50F8:40FHOP:10BPPX. This is not unexpected for S50F8:50BPPX considering the low PLQE for this polymer of 6.6%. However, S50F8:40FHOP:10BPPX has a PLQE that is only slightly lower than S50F8:50FHOP yet no ASE is observed, which we attribute to the presence of a fraction of BPPX units and highlights the significant effect this unit has on luminescence. ASE may be possible at much higher thresholds than are accessible in the existing ASE measurement system.

This leaves the question of why the gain is lower for the alternating copolymer compared to the homopolymer. We attribute this to a marginally higher density in S50F8:50FHOP (based on the higher absorption coefficient) leading to shorter interchain separation distances, which enhance energy transfer to quenching sites.

5.7 Summary

The series of blue emitting fluorene based polymers in this chapter follows the pattern of substituent group modification, backbone modification and a combination of both.

In the first case, this is by the use of substituent groups that are not conjugated to the backbone by the use of hexyloxyphenyl substituents instead of linear alkyl side chains used in poly(fluorene) in the homopolymer PFHOP and the alternating copolymer S50F8:50FHOP. The second case is based on including a phenoxazine moiety in the backbone in S50F8:50BPPX and finally both features are combined in S50F8:40FHOP:10BPPX.

The use of 9,9-di-substituted hexyloxyphenyl groups in PFHOP and S50F8:50FHOP have been successful in suppressing aggregate formation and the beta-phase according to PL measurements. Charge transport of unprocessed, as spin-coated films of PFHOP has improved compared to its antecedent, PFO, by a slight increase in hole mobility with non-dispersive characteristics. This is despite the fact that it has a lower chain packing density according to its lower absorption coefficient.

The alternating copolymer has been shown to have an intermediate chain packing density between PFO and PFHOP with an absorption coefficient that is almost exactly between the two, however, the typical charge transport characteristics are dispersive yet the hole mobility is very similar to PFHOP. The dispersive character may be attributed to the presence of hole traps based on the observation of non-dispersive ToF transients after the application of an injected charge carrier density which may have filled these traps.

DI-SCLC measurements showed the hole mobility of PFHOP to be in close agreement to the ToF mobility and further showed that it is also affected by charge traps, which in its case are interfacial traps that block charges from being injected, causing the injected current to reach an equilibrium level after many times the transit time.

The hole transporting BPPX unit in S50F8:50BPPX remedies the problem of interfacial traps as indicated by transient injection currents that reach a steady state level very shortly after the transit time. It also appears to have a low concentration of bulk traps according to a low ratio of peak to steady-state current density and steady-state currents which are very close to theoretical trap free injection currents. The key drawbacks are a significant decrease in PLQE and the hole mobility is an order of magnitude less than PFHOP (~$10^{-4}$$cm^2$/Vs compared to ~$10^{-3}$$cm^2$/Vs, respectively). However,

its mobility is higher than a similar copolymer in the literature with a ToF hole mobility of 3.7 x $10^{-5}$$cm^2$/Vs (Yuanfu *et al.* 2007) and identical to the FET hole mobility of a copolymer with same backbone structure with linear hexyl side chains (Zhu *et al.* 2005).

Reducing the BPPX content to only 10% in S50F8:40FHOP:10BPPX restores the PLQE to a value close to S50F8:50FHOP and transient dark injection currents give the same indications of a low density of charge traps in the bulk and not at the interface. It also shows a range of interesting charge transport features in temperature and field dependent ToF measurements such as a change in Poole-Frenkel type behaviour, the visibility of a cusp and a change in slope of the plateau.

The hole mobility of S50F8:40FHOP:10BPPX is the lowest in this series at ~$10^{-6}$$cm^2$/Vs, however, we have shown that it may be improved to ~$10^{-5}$$cm^2$/Vs with additional processing steps during sample preparation.

Finally, and of central importance to the overall theme of this thesis, is the fact that optical gain was only observed in PFHOP and S50F8:50FHOP, where the former is found to be a more effective gain medium based on higher optical gain values.

CHAPTER 6

6 POLY(INDENOFLUORENE-FLUORENE) (P(IF-F)) COPOLYMERS

6.1 Introduction

The investigation in the previous chapter had as its primary focus the effects of combining different chemical units in the polymer backbone on charge transport, injection and optical properties.

This chapter introduces a second novel series of copolymers, namely, poly(indenofluorene-fluorene)s (P(IF-F)), in which we consider the role of increased backbone rigidity compared to polyfluorene and the variation of side chain length and structure on charge transport and optical properties.

In the latter part of the chapter, a further modification of the indenofluorene-fluorene paradigm is introduced in the form of a series of novel indenopyrazine-fluorene co-polymers and an indenopyrazine-triarylamine co-polymer with the aim of achieving a more balanced charge transport for holes and electrons in polymers with good optical gain characteristics.

6.2 Poly(indenofluorene-fluorene) Background

The indenofluorene structural unit has an early origin in the literature (Ebel & Deuschel 1956; Chardonnens & Salamin 1968) and has become a building block in the more recent synthesis of conjugated polymers. For example, (poly(3,9-di-*tert*-butylindeno[1,2-*b*]fluorene)), in which indeno[1,2-*b*]fluorene units were fitted together at the 6- and 12-positions, was synthesised by Reisch *et al.*. Quantum chemical calculations examined the indeno[1,2-*b*]fluorene with C_6H_5 side chains at the 6- and 12-positions as a "quinoid subunit" and led to a predicted HOMO/LUMO energy gap of 2.28 eV (Reisch *et al.* 1996).

This was later followed by the synthesis of poly(tetra-alkyl-indenofluorene) by Setayesh *et al.* (2000) as used in the copolymers in this chapter with two pairs of side chains connected to the backbone. With its three planarised phenylene rings, the indenofluorene unit finds itself structurally intermediate between the poly(di-alkyl-fluorene) series and ladder-type poly(para-phenylene) (LPPP), with the advantage of the high fluorescence quantum yield of the former and avoiding the tendency towards aggregation and excimer emission of the latter.

The authors produced both octyl and ethyl-hexyl substituted variants, which were found to have an emission band between PF and LPPP, indicating its enhanced conjugation compared to PF. The effective conjugation length was determined by absorption and emission maxima of oligomers to be 6

to 7 indenofluorene units (three benzene rings per unit) for absorption and 5 to 6 units for emission (Setayesh *et al.* 2000), which is at the lower range of that found for beta-phase PFO of at least 18 benzene rings (Tsoi *et al.* 2008).

Silva *et al.* (2000) performed femtosecond transient absorption measurements on poly(indenofluorene) derivatives with ethyl-hexyl and octyl side groups, which showed significant differences in their PL spectra, although both polymers were found to have the same transient absorption spectra. This early attempt at synthesis of the tetra-octyl PIF showed an undesirable green emission band at ~550 nm in the solid state, similar to that observed from the keto defect emission of poly(9,9-dialkylfluorene), however, the ethyl-hexyl polymer showed blue emission with clear vibronic structure.

Preliminary AFM images of the authors films showed a high degree of texture on the scale of ~20 nm for the octyl PIF, hence the low energy feature was speculated to be related to excimer emission (Silva *et al.* 2000), which was in accordance with the dominant theory at the time regarding PFO. Further AFM based studies appeared to confirm that the green emission was correlated with π-stacking in long ordered structures apparent from AFM images (Grimsdale *et al.* 2002)

In order to counter-act this aggregation, the copolymer poly-2,8-(indenofluorene-*co*-anthracene) was designed with a small proportion of a bulky 9,10-dibromoanthracene units to avoid the excimer formation perceived to be the cause of the green emission of the octyl-PIF (Marsitzky *et al.* 2001). The octyl-PIF films did show a significantly broader absorption and red shift in the PL spectra compared to in solution whereas the PIF-co-Anthracene polymer showed little change in absorption and PL. Hence, the explanation connecting the green emission to aggregation seemed plausible because the presence of bulkier moieties such as ethyl-hexyl or anthracene reduced interchain interactions and hence non-radiative decay pathways.

The force of this explanation spread to interpretations of other measurements, for example, EL measurements showed that ethyl-hexyl PIF had an initial blue emission that was followed by a rapid decay in luminance and a red shift in its emission, which was thus attributed to reordering under electrical driving (Grimsdale *et al.* 2002).

However, as with PF, an alternative explanation for the sub-gap green emission became apparent, which is that the emission is from a population of fluorenone or keto defect sites and determined by the exciton diffusion or charge trapping at these defect sites (List *et al.* 2002; Lupton 2002).

With this new perspective on the origin of the green emission from PF and PIF polymers, Keivanidis *et al.* presented a new synthetic approach for the indenofluorene unit towards reducing the probability of keto formation by attempting to obtain complete alkylation of the bridgehead carbon atoms. They

thus investigated the minimum keto concentration that affects the photo-physical properties of a series of PIF polymers. In their study, octyl and ethyl-hexyl substituted poly(indenofluorene)s were investigated as well as a novel poly(tetra-aryl-indenofluorene) in which full arylation was achieved compared to the alkyl-PIF variants.

By the use of a mono-indenofluorene with the ketone defect (Fig. 6.1) in photoluminescence quenching experiments, the authors were able to investigate the effect of this impurity and energy transfer to keto sites such that the green emission band was confirmed to be related to defect emission in PIF polymers (Keivanidis *et al.* 2005).

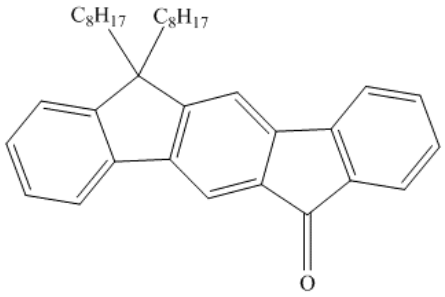

Fig. 6.1 Chemical structure of mono-indenofluorene with a ketone defect (Keivanidis et al. 2005; Grimsdale & Müllen 2008)

In the course of the study, the authors noted higher regularity in chain packing of octyl-PIF compared to ethyl-hexyl-PIF according to PL and WAXS measurements such that close chain packing is possible. Whereas in the latter, the branched side chains surround the backbone as though they are a cylindrical shell which minimises interchain interactions (Neher 2001), which is a formation that is particularly relevant to our interest in polymeric structures that are between the two morphologies for simultaneously high interchain charge transport and luminescence.

The P(IF-F) series of copolymers in this study are thus designed to investigate whether this balance may be achieved by combining different side chain groups across the backbone of the indenofluorene and fluorene units of the backbone in order to improve interchain interactions for improved charge carrier hopping without introducing pathways for exciton quenching.

From this brief background summary of research on the indenofluorene structure, we have found that it has predominantly been the subject of investigations regarding its photophysical properties with few reports on its charge transport properties, compared to the PF series in particular, which has been investigated in depth. Amongst these few reports is that of Kim *et al.* on an indenofluorene-phenanthrene copolymer, which will be discussed later in this chapter. The bulk of this chapter will therefore discuss the novel P(IF-F) series with experiments based on hole transport and injection in connection with optical properties that may be favourable as a step towards materials suitable for electrically pumped polymer lasing.

Finally, other studies in the literature on the indenofluorene unit have included, for example, an investigation of its morphological properties in oligoindenofluorenes (Elmahdy *et al.* 2006), studies of dispirofluorene–indenofluorene derivatives (Poriel *et al.* 2007) and alternating copolymers (Xia *et al.* 2012) for blue OLEDs, and as part of copolymers of blue, red and green moieties of tetra-octyl-indenofluorene (IF), 2,1,3-benzothiadiazole (BT) and 4,7-bis(2-thienyl)-2,1,3-benzothiadiazole (DBT) for white light emission (Jeong *et al.* 2009). A brief review of poly(indenofluorene)s has also been published (Grimsdale & Müllen 2008).

6.3 Poly(Indenofluorene)-Fluorene Copolymers

The three copolymers in the series shown in Fig. 6.2 are differentiated by their substituent groups following a similar pattern of chemical structure modifications to the work of Yap et al. (2008).

S50F8:50IF8

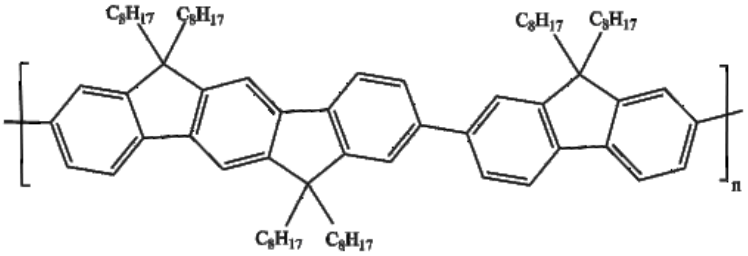

S50F3:50IF8

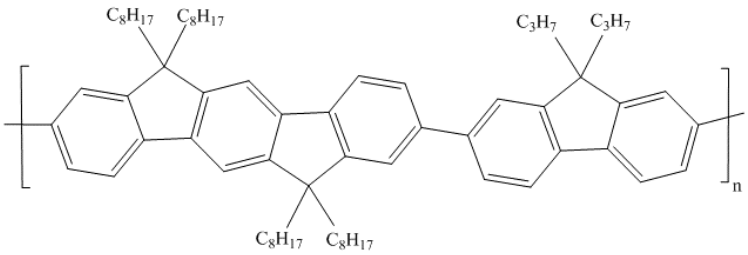

S50F8:50IF1,4

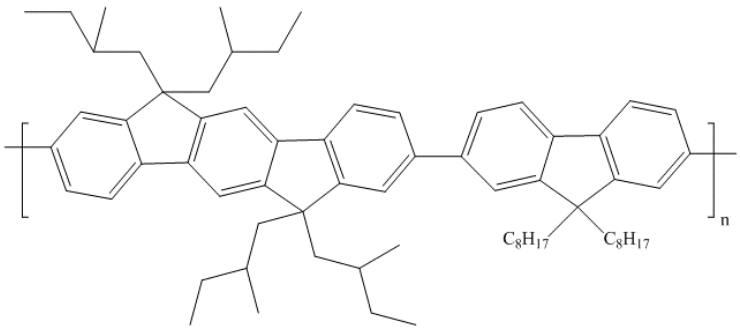

Fig. 6.2 Chemical structure of the three P(IF-F) copolymers studied. Polymers were synthesised by Suzuki-coupling leading to an alternating IF-F structure.

The indenofluorene moiety consists of three benzene rings and holds two pairs of side chains for every three rings, which are located on opposite sides where the benzene rings link. This results in an increase in side chain density compared to a poly(9,9-dialkylfluorene) homopolymer with one pair of side chains at the 9-position where its two benzene rings are linked.

First, the additional benzene ring of IF adds greater planarity compared to F, potentially resulting in a longer conjugation length along the backbone. The single bond that joins the IF and F units on the backbone permits a degree of rotational freedom around the bond axis which should allow chains to adopt relaxed conformations in the solid state between which there can be improved interchain interactions leading to a fraction of preferential hopping sites.

Secondly, the marginal increase in side chain density lends the copolymer structure a greater degree of solubility in typical solvents that are used in this work, such as toluene, and has thus allowed a reduction in the length of selected side chains for the S50F3:50IF8 variant, with linear C8 alkyl chains on the indeno section and linear C3 chains on the fluorene. This should simultaneously reduce steric hindrance of side chains along the backbone enabling slightly more extended conformations for intrachain transport and closer interchain interactions where the alkyl chain lengths are shorter, that is, "preferred hopping sites".

The other two structures are S50F8:50IF8, with linear C8 alkyl chains on both the IF and F moieties, and S50F8:50IF1,4, with branched chains on the IF unit and linear chains on the F unit. As noted earlier, the branched side chains are expected to prevent aggregation.

6.4 Optical Properties of P(IF-F) | Absorption, Photoluminescence and ASE

The absorption, photoluminescence and ASE spectra of each of the P(IF-F) co-polymers are shown in Fig. 6.3. The absorption spectra of thin films of the copolymers is similar in all three cases with a single broad absorption centred around 396 nm , 395 nm and 388 nm for S50F8:50IF8, S50F3:50IF8 and S50F8:50IF1,4, respectively. S50F8:50IF8, in particular, shows a partial resolution of vibronic structure manifest as a splitting of the peak into two with the maximum absorption at ~403 nm. This feature is also observed in S50F3:50IF8, although in that case there is only a very minor trough in the peak centre.

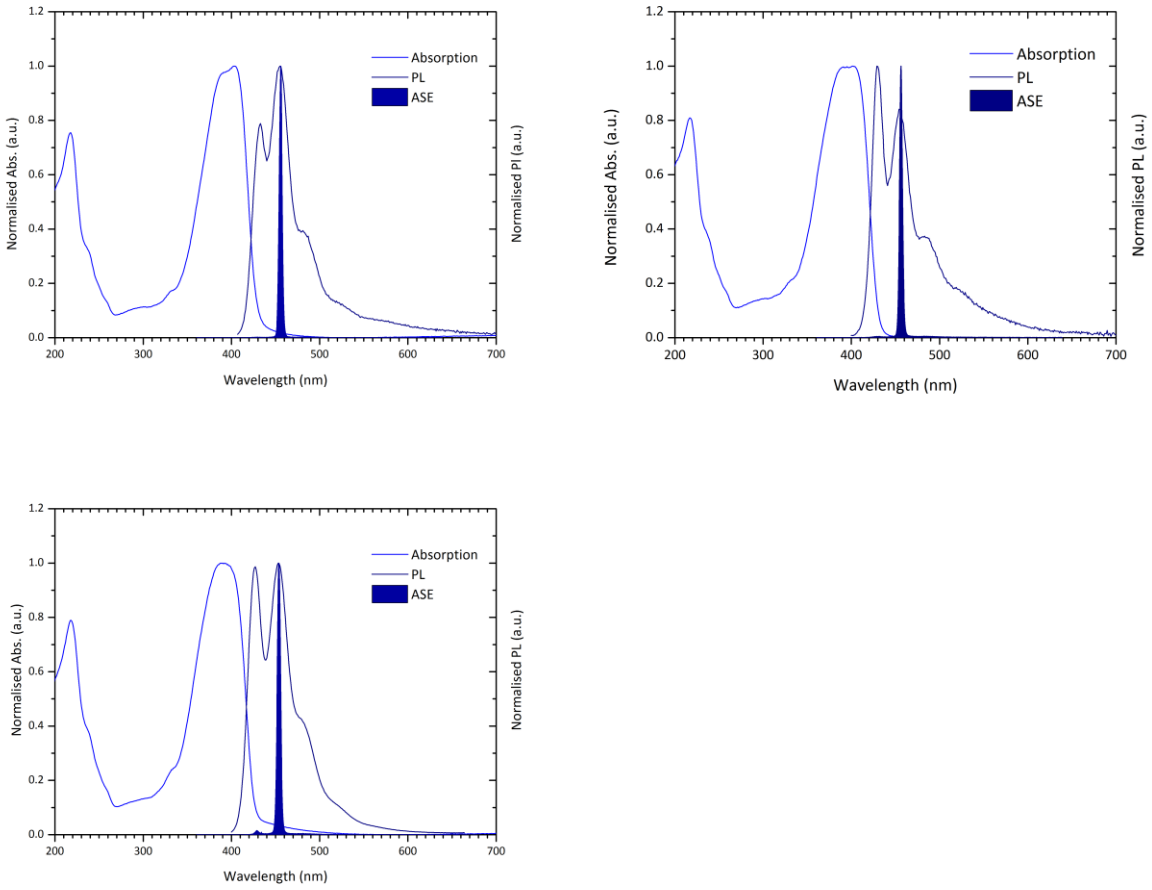

Fig. 6.3 Absorption, Photoluminescence and ASE spectra for P(IF-F) co- polymers, S50F8:50IF8 (top left), S50F3:50IF8 (top right) and S50F8:50IF1,4 (bottom).

S50F8:50IF1,4 is different in this respect as it only has a single featureless absorption peak at ~388 nm, which is 4-5 nm blue-shift relative to the linear alkyl substituted variants. This slight blue shift for S50F8:50IF1,4 is a possible indication of a lower degree of conjugation along the backbone. None of the polymers shows any indication of morphologies such as the beta-phase of PFO. All of the polymers have similar absorption coefficients of ~2.25 ± 0.05 x $10^5 cm^{-1}$ at their peak wavelengths, which indicates that they are likely to have comparable chain packing densities.

We also note that the peak at 210 nm corresponding to the localised π-π* transition of the phenyl rings and is dependent on their number. The coincidence of the positon of the peaks at 210 nm with similar absorption coefficients of ~1.7 x $10^5 cm^{-1}$ is consistent with similar packing densities since the number of phenyl rings per unit is the same in each copolymer.

PL spectra, also shown in Fig. 6.3 and normalised to the 0-1 vibronic peak, all show clear vibronic features and a small overlap between absorption and emission, a useful property to mitigate self-absorption losses. The 0-1 peak occurs at approximately 454 nm in all cases. The emission collapses into a single narrow ASE peak at ~456 nm for the linear alkyl variants and ~ 454 nm for

S50F8:50IF1,4 when asymmetric slab waveguide structures comprising films on Spectrosil 2000 substrates are pumped with a striped shaped laser excitation beam.

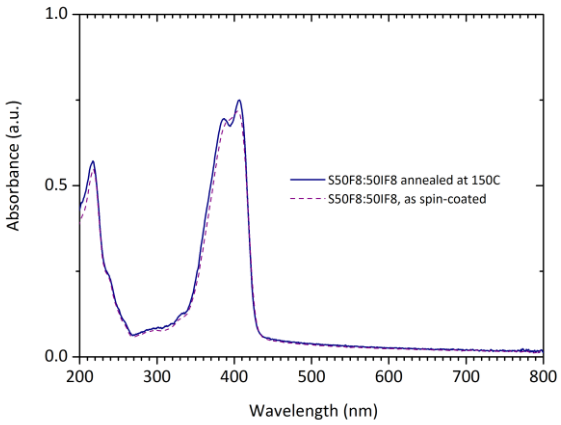

Fig. 6.4 Change in absorption spectrum of thin film of S50F8:50IF8 before and after annealing at 150°C.

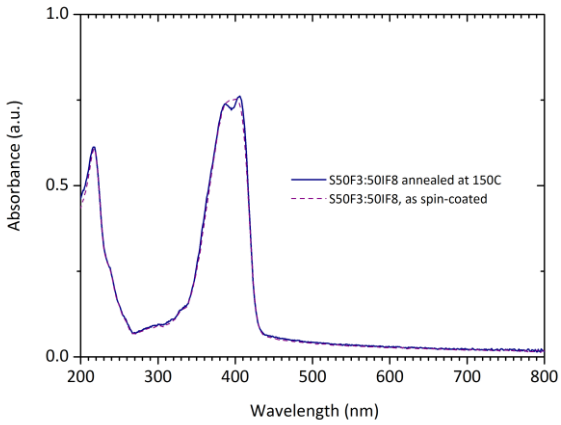

Fig. 6.5 Change in absorption spectrum of thin film of S50F3:50IF8 before and after annealing at 150°C.

Earlier we mentioned the presence of a minor split in the centre of the peak of S50F8:50IF8. We find that annealing thin films at 150°C significantly enhances the splitting of the main absorption peak into two peaks at 386 nm and 406 nm (Fig. 6.4). The absorption peak at 406 nm (the lower energy peak) has a slightly higher intensity. Furthermore, we find that annealing S50F3:50IF8 at 150°C also results in two pronounced peaks at the same wavelengths (Fig. 6.5) where only a minor trough was visible in the absorption of the as-spin-coated thin film. PL of both polymers remains similar after annealing (not shown), although the 0-1 vibronic peak of S50F8:50IF8 is shifted to 452 nm. The reason for the appearance of this structure in the absorption peak after annealing may be related to a higher degree of ordering in the films after annealing.

Table 6.1 summarises the PLQE of as spin-coated and annealed films of the copolymers. The highest PLQE is achieved in as spin-coated S50F8:50IF8 at 61.5% compared to S50F3:50IF8, which is 48.7%. The values of the PLQE of annealed films are drawn closer together at 58.4% and 54.1%, respectively. That is, it has reduced for S50F8:50IF8 and increased for S50F3:50IF8 after annealing.

Table 6.1 PLQE of P(IF-F) copolymers

	PLQE (%)
S50F8:50IF8 *As spin-coated*	61.5
S50F8:50IF8 *Film annealed at 150°C*	58.4
S50F3:50IF8 *As spin-coated*	48.7
S50F3:50IF8 *Film annealed at 150°C*	54.1
S50F8:50IF1,4 *As spin-coated*	30.9

In summary, the optical properties, comprising absorption, PL and stimulated emission spectra are very similar for all three copolymers. The absorption and PL of S50F8:50IF1,4 are slightly shifted to lower wavelengths, which is likely to be due to steric hindrance imposed by its branched side chains.

It is important to note from the absorption spectra that we do not observe any signs of the intrachain order that results in extended chain conformations such as (the β-phase of PFO). We also do not see any sign of a green band component in the PL emission spectra arising from the presence of keto defect sites.

We may estimate the optical gap from the long wavelength tail of the peak absorption to be ~2.9eV for the linear alkyl substituted P(IF-F) copolymers. The onset of absorption at low energy corresponds to the lowest energy transition from the ground state to the excited state, which may be approximated to the HOMO/LUMO gap of the longest conjugated polymer segments. Hence, we may estimate the LUMO levels of the polymers based on a HOMO level of -5.84eV determined by CV. The inferred LUMO is therefore estimated to be -2.94eV for the linear alkyl copolymer. For S50F8:50IF1,4 the LUMO level is estimated to be slightly deeper at -2.96eV relative to the vacuum level. We note however, that there are potential inaccuracies in estimating the electron affinity from the optical gap, even if the HOMO has been obtained by CV (Janietz *et al.* 1998).

6.5 Charge Transport and Injection

Earlier in this chapter, we discussed the research into the P(IF-F) series of polymers regarding their optical properties and the origin of the green band emission. Despite the interest in this series of polymers as an intermediate form between poly(fluorene)s and ladder-type PPPs, there have been relatively few reports characterising their charge carrier mobility. Hence, the subject of this section is

to investigate whether the copolymer system of P(IF-F) leads to enhanced mobility without detriment to optical properties since this is of key importance in seeking to make progress towards materials that may be candidates for electrically pumped polymer lasers.

We begin with discussing ToF experiments on films of S50F8:50IF8 of 1.7 µm deposited on ITO substrates with MoO_3 and/or gold or aluminium counter electrodes. ToF transients representative of the photocurrent response at room temperature are given in for S50F8:50IF8. In the field range of the measurement, the hole mobility was found to be ~ 1 x 10^{-2} cm^2/Vs and the complete temperature and field dependence of the hole mobility is shown in Fig. 6.8. We observe the transients to be characteristic of non-dispersive transport for measurements around and above room temperature in the field range of just below ~ 10^5 V/cm, which is indicated by a clear plateau region and inflection point.

As anticipated by typical models for charge carrier transport, the transport tends towards dispersive character at lower temperature as less energy is available for the photogenerated charge carriers transiting through the device to reach a dynamic equilibrium associated with the plateau for non-dispersive signals. We do however note that at lower fields, the plateau region is not clear and the photocurrent is slightly decreasing with time, which may be indicative of a population of trap states.

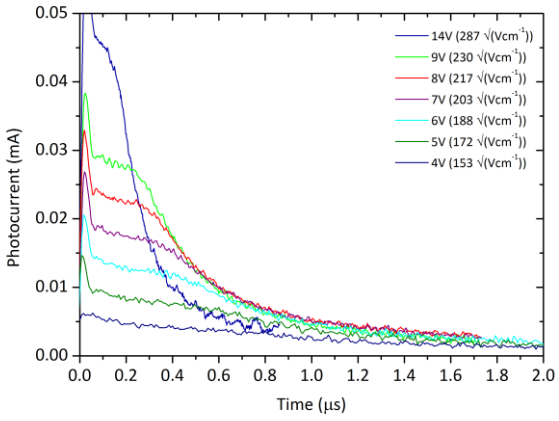

Fig. 6.6 Transient photocurrent data for a S50F8:50IF8 film of thickness 1.7 µm. Data are shown for a sequence of bias voltages from 4 to 14 V at 300K

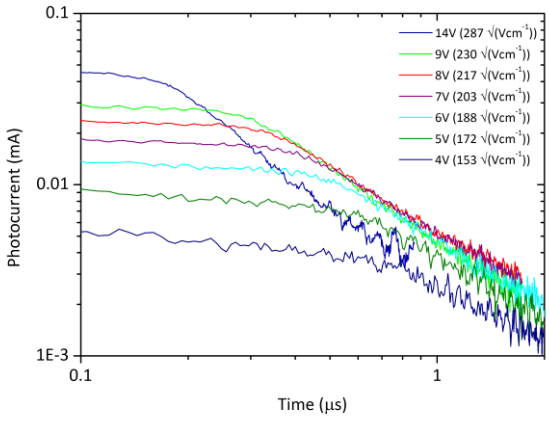

Fig. 6.7 Transient photocurrent data for a S50F8:50IF8 film of thickness 1.7 µm. Data are shown for a sequence of bias voltages from 4 to 14 V at 300K on a log-log plot.

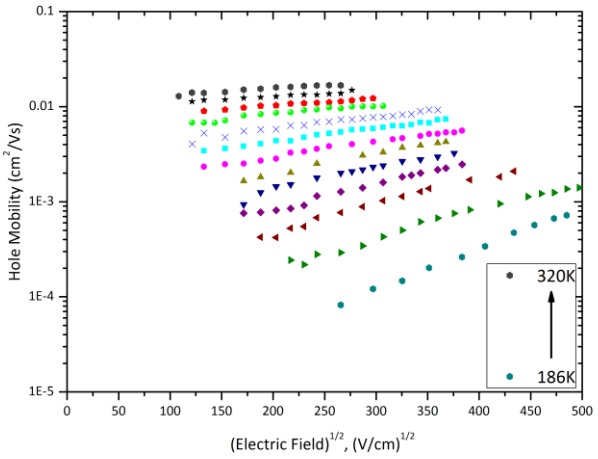

Fig. 6.8 S50F8:50IF8 ToF hole mobility data as a function of $E^{1/2}$, parametric in temperatures from 186 to 320 K.

The ToF transients for 3.03 µm films of S50F3:50IF8 in show similar behaviour, that is, the change in the slope of the plateau region as the applied field is increased and the clearly defined inflection points. The hole mobility also reaches ~ 1 x 10^{-2} cm^2/Vs, although at a slightly higher field of 325 $(V/cm)^{1/2}$ compared to 242 $(V/cm)^{1/2}$.

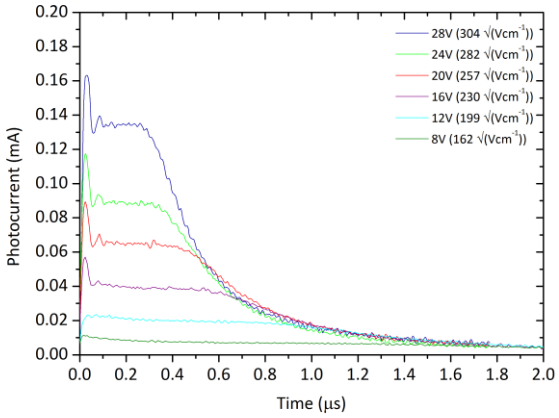

Fig. 6.9 Transient photocurrent data for a S50F3:50IF8 film of thickness 3.03 µm. Data are shown for a sequence of bias voltages from 8 to 28 V.

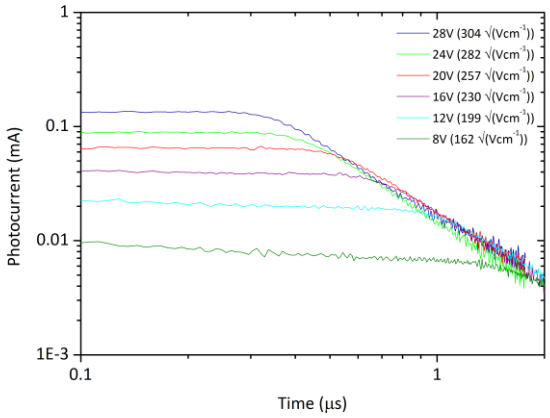

Fig. 6.10 Transient photocurrent data for a S50F3:50IF8 film of thickness 3.03 µm. Data are shown for a sequence of bias voltages from 8 to 28 V on a log-log plot.

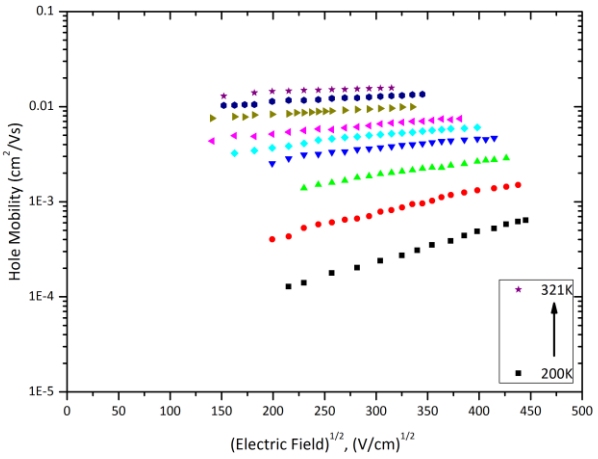

Fig. 6.11 S50F3:50IF8 ToF hole mobility data as a function of $E^{1/2}$, parametric in temperatures from 200 to 321 K.

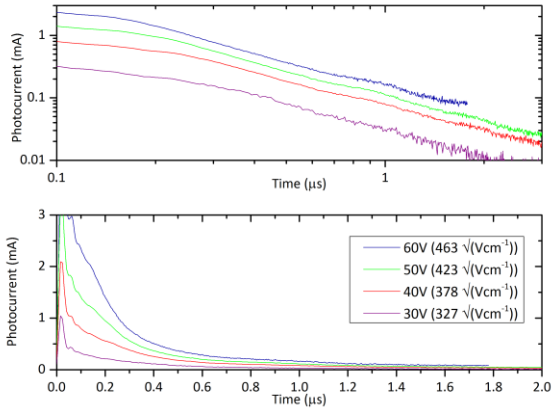

Fig. 6.12 Transient photocurrent data for a S50F8:50IF1,4 film of thickness 1.65 µm. Data are shown on linear and log-log plots for a sequence of bias voltages from 30 to 60 V.

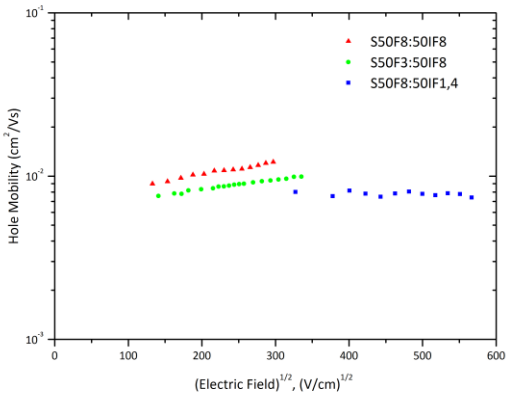

Fig. 6.13 Field dependence of the hole mobility of S50F8:50IF1,4 compared to linear-alkyl P(IF-F) copolymers.

ToF measurements on the branched chain substituted S50F8:50IF1,4 show significantly different charge transport characteristics compared to the linear alkyl substituted P(IF-F) copolymers. The transient photocurrent signals measured at room temperature (see Fig. 6.12) show that charge transport is dispersive since there is no clear plateau or inflection point. This is even more evident in the linear plot in which we see a slight shoulder corresponding approximately to the transit time.

Despite the dispersive nature of the hole mobility, we calculate the mobility to be just below ~ 8 x 10^{-3} cm^2/Vs, although we note the higher field range of the measurements for this polymer compared to the linear alkyl substituted variants. This is illustrated in Fig. 6.13 with the room temperature field dependence of the mobility for all three materials. The mobility at low fields of the linear alkyl-P(IF-F) polymers matches the mobilities for S50F8:50IF1,4 across the full field range for which it was

measured. We further notice that S50F8:50IF1,4 shows almost no field dependence, whereas the other two polymers show a weak field dependence. This may be because of the different field regimes of the measurements such that the high field is already constraining charge hopping to align with the electric field direction.

We also notice a second inflection point that is visible in the log-log plot in Fig. 6.12, which may correspond to the transit time of a secondary packet of charge arriving at the counter electrode with a mobility of 8.3 x 10^{-4} to 1.28 x 10^{-3} cm^2/Vs. Two distinct arrival times have previously been observed by Barard *et al.* in thin films of polytriarylamine with a bimodal distribution of chain lengths where it was suggested that there are two conduction paths that arise from phase segregation of polymer chains of different lengths (Barard *et al.* 2009). This seems unlikely as an explanation here since the IF1,4 and F8 moieties are connected in an alternating chain and the polymer batch has a low PDI of 1.7.

The dispersive nature of the ToF transients has meant that it has not been possible to obtain a full range of temperature and field measurements for this copolymer because the inflection point becomes even more obscure as the temperature is lowered and more charges are trapped.

Table 6.2 Summary of charge transport parameters for this series of P(IF-F) copolymers.

	Room Temperature Hole Mobility (μ, cm^2/Vs)	**Square-root Electric Field $(V/cm)^{1/2}$ for RT hole mobility (left)**	**GDM Energetic Disorder (σ, meV)**	**Mobility Pre-factor (μ_0, cm^2/Vs)**	**C $(cm/V)^{1/2}$**	**Σ**
S50F8:50IF8 *As-spun*	$1x10^{-2}$ (non-dispersive)	242	80.5	0.517	$4.87x10^{-4}$	2.42
S50F8:50IF8 *Film annealed at 150°C*	$6.03x10^{-3}$ (dispersive)	282	73.7	0.120	$3.38x10^{-4}$	1.26
S50F8:50IF8 *Film annealed at 270°C*	$4.2x10^{-3}$ (dispersive)	436	-	-		
S50F3:50IF8 *As-spun*	$8.3x10^{-3}$ - $1x10^{-2}$ (non-dispersive)	200 – 325	81.5	0.598	$4.89x10^{-4}$	2.70
S50F3:50IF8 *Film annealed at 150°C*	$8.27x10^{-3}$ (non-dispersive)	217	71.7	0.218	$4.82x10^{-4}$	2.61
S50F8:50IF1,4 *As-spun*	$7.82x10^{-3}$ (dispersive)	462	-	-	-	-
S50F8:50IF1,4 *Device annealed at 120°C*	$1.01x10^{-2}$ (dispersive)	462	-	-	-	-

The GDM parameters for the other two polymers are summarised in Table 6.2 where we find that the energetic disorder for both alkyl-P(IF-F) polymers to be very similar at 80.5 meV for S50F8:50IF8 and 81.5 meV for S50F3:50IF8. This is very similar to reported non-annealed PFO samples with an energetic disorder of 82 meV (Kreouzis *et al.* 2006).

The mobility pre-factor, μ_0, which is a theoretical mobility at zero field and infinite temperature is found to be slightly higher for S50F3:50IF8 at 0.598 cm^2/Vs compared to 0.517 cm^2/Vs for S50F8:50IF8. These values are up to two orders of magnitude higher than μ_0 obtained for as-spin-coated PFO, for which the value is between 0.005 to 0.019 cm^2/Vs in different samples (Kreouzis *et al.* 2006).

We also investigated the effect of annealing for all of the materials as it has previously been shown that annealing may recover non-dispersive transients in the case of PFO (Kreouzis *et al.* 2006) and thus may have an effect on the nature of transport for S50F8:50IF1,4. DSC data for S50F8:50IF1,4 did not show any transitions, hence the first annealing of this polymer was at a low temperature of 70°C in order to remove the presence of any residual solvent used in spin-coating which may result in dispersive characteristics. Following this, annealing of this polymer was in steps of 50°C.

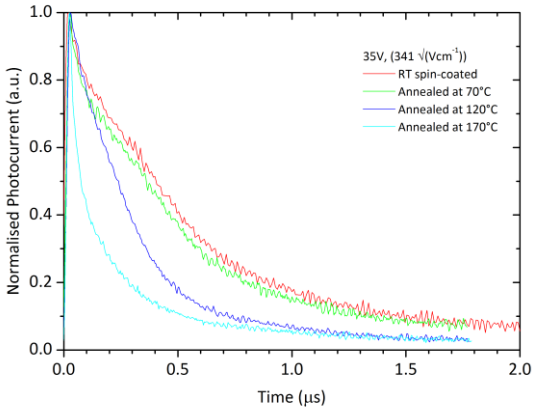

Fig. 6.14 Transient photocurrent data for annealed films of S50F8:50IF1,4. Data are shown for a bias voltage of 35 V.

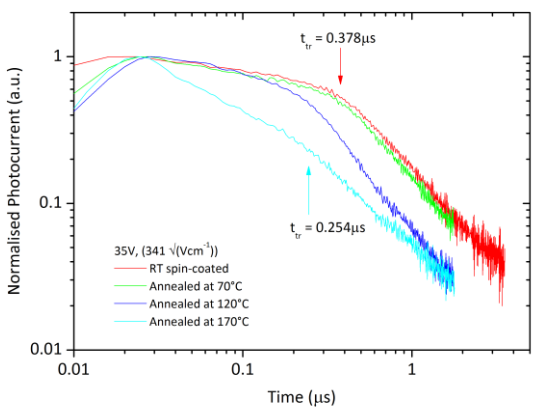

Fig. 6.15 Transient photocurrent data for annealed films of S50F8:50IF1,4. Data are shown for a bias voltage of 35 V on a log-log plot.

ToF transients after the several stages of annealing in glovebox conditions of a S50F8:50IF1,4 sample are shown in Fig. 6.14 and Fig. 6.15 in linear and log-log plots, respectively. The transients show significant differences, although there is a clear trend for the transients towards more dispersive character, contrary to the typical effects of annealing that result in morphological changes that reduce the amount of energetic disorder.

Annealing beyond 120°C resulted in a significant change in the transport by reducing the transit time and further annealing at 170°C resulted in an undesirable smearing out of the plateau and inflection

point that were just about discernible in the log-log plot without any further decrease in the transit time. The mobility after annealing at 120°C is ~1 x 10^{-2} cm^2/Vs, which is in the same range as the as-spin-coated linear alkyl-P(IF-F) copolymers.

Annealing of the linear alkyl polymers at 150°C resulted in a slight decrease in mobility in both cases (Table 6.2), in contrast to the increased mobility obtained for S50F8:50IF1,4. However, the GDM energetic disorder did reduce in both copolymers by approximately 10 meV. Despite this apparent reduction in the energetic disorder, the transport characteristics of S50F8:50IF8 became more dispersive after annealing. For S50F3:50IF8 they remained the same. The reduction in mobility after annealing may be related to less intrachain order from the P(IF) and P(F) units twisting out-of-plane as discussed in the changes to absorption of thin films annealed at the same temperature.

In summary, we have found that as spin-coated films of the linear alkyl-P(IF-F) copolymers behave in a very similar way with a hole mobility of ~10^{-2} cm^2/Vs that is high with respect to similar glassy fluorene based copolymers. Annealing films of S50F8:50IF8 led to more dispersive transport. In the case of S50F3:50IF8, the short length of the fluorene side chains may not present the same level of steric hindrance and hence annealing had less of an effect on the charge transport.

The charge transport of the branched chain P(IF-F) copolymer has been found to be dispersive with a slightly lower mobility than the linear alkyl-P(IF-F) copolymers, across a range of batches and molecular weights (data not shown). PL measurements of thin films and thick ToF films did not reveal any signs of green band emission from keto defects before and after annealing. Furthermore, preliminary FTIR measurements did not reveal the presence of bands related to C=O functional groups of the keto defect.

This does not however preclude the existence of a small quantity of the keto defect since old samples of S50F3:50IF8 left in ambient conditions for over a year show signs of a green band in their PL spectra. However, it is not certain that the presence of the keto defect will affect hole transport since the main paper in which it is described as both an electron and hole trap (Kuik *et al.* 2011) does not account for the presence of the beta-phase, which has been determined to be a cause of hole trapping in PFO (Foster 2013). Hence, we do not attribute charge trapping to the keto defect, however we also note that there is no evidence in the optical characterisation of a morphology known to behave as a charge trap such as the beta phase of PFO.

The charge transport properties will be discussed further below with reference to the characterisation by Kim *et al.* of indenofluorene-phenanthrene copolymers after discussion of our attempts to investigate hole injection in the P(IF-F) series.

6.6 Charge Injection

Steady state current density-voltage and transient DI-SCLC measurements were conducted using molybdenum trioxide as a hole injection layer in hole only devices. We found highly injection limited behaviour for the as spin-coated films of all of the copolymers. However, for S50F3:50IF8 annealed at 150°C we observe temperature dependent current densities in the steady state that appear to follow a power law of $J \propto V^2$, which is indicative of SCL currents as shown in Fig. 6.16.

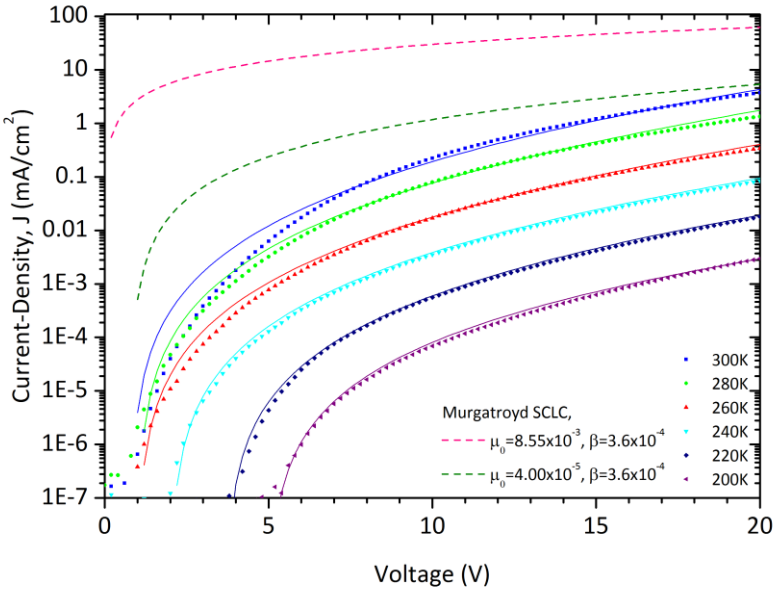

Fig. 6.16 Temperature dependent JV measurements of a 1.08 µm S50F3:50IF8 device annealed at 150°C. $E^{1/2}$ is 430 $(V/cm)^{1/2}$ at 20 V.

Fits to the data using the Murgatroyd field dependent trap-free SCLC equation are also shown in Fig. 6.16. Using parameters for μ_0 and β that have been derived from temperature and field dependent ToF measurements, we find that the current densities are injection limited here as well since the experimental current density (at 300K) is approximately two orders of magnitude lower than the theoretical model at the highest field measured.

Table 6.3 Parameters used for field dependent fits to experimental JV data in Fig. 6.16.

	β (cm/V)$^{1/2}$	μ_0 (cm^2/Vs)
ToF parameters at 300K	3.60 x 10^{-4}	8.55 x 10^{-3}
ToF β at 300K, fit of μ_0	3.60 x 10^{-4}	4.00 x 10^{-5}
Fitted Parameters at 300K	1.42 x 10^{-2}	1.80 x 10^{-7}
Fitted Parameters at 280K	1.40 x 10^{-2}	0.82 x 10^{-7}
Fitted Parameters at 260K	1.40 x 10^{-2}	0.19 x 10^{-7}
Fitted Parameters at 240K	1.30 x 10^{-2}	0.82 x 10^{-8}
Fitted Parameters at 220K	1.20 x 10^{-2}	0.36 x 10^{-8}
Fitted Parameters at 200K	1.00 x 10^{-2}	0.15 x 10^{-8}

Closer approximations to the experimental data are obtained using the parameters in Table 6.3, however, the values of μ_0 and β differ greatly from those obtained experimentally by ToF measurements. That is, μ_0 is orders of magnitude lower and β is overestimated. Fixing β to the experimental value produces a close fit at higher fields with μ_0 estimated to be 4.00 x 10^{-5} cm^2/Vs.

Fits to the data using the Murgatroyd field dependent trap-free SCLC equation are also shown in Fig. 6.16. Using parameters for μ_0 and β that have been derived from temperature and field dependent ToF measurements we find that the current densities are injection limited here as well since the experimental current density (at 300K) is approximately two orders of magnitude lower than the theoretical model at the highest field measured.

DI-SCLC measurements of S50F3:50IF8 did not show any signs of a cusp, which is further evidence of non-ohmic injection. DI-SCLC measurements of S50F8:50IF1,4 (with a thickness of 1.65 μm) show signs of a cusp in Fig. 6.17, however, the peak appears convoluted in the RC response and is affected by ringing oscillations. The hole mobility is estimated to be 6 – 7 x 10^{-4} cm^2/Vs, which is an order of magnitude lower than the hole mobility from ToF measurements, although this may be underestimated because of the obscurity of the exact peak location.

The ratio of the approximate peak magnitude to the current density at ten-times the peak $\left(J(t_p)/J(10t_p)\right)$ is ~1.2 and continues to increase at higher multiples of the transit time. As we discussed in chapter four and five, this may be related to interfacial traps that become filled and effectively decrease the surface area of the injection interface.

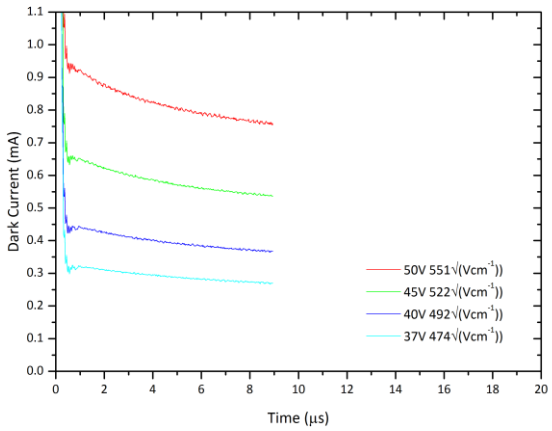

Fig. 6.17 DI-SCLC transients of S50F8:50IF1,4 showing signs of a cusp corresponding to a DI transit time.

6.7 ASE and Optical Gain

The final part of our investigation of this series of polymers is a detailed study of their ASE and optical gain properties since the demonstration of optical gain is an essential requirement for potential lasing materials. Hence, in this section, the optical gain of the polymers is investigated using the variable stripe-length technique discussed in Chapter 3.

The results are presented through numerous plots of the measured data that are required for the final plot of the intensity against stripe length (at a particular incident pump energy density) which is fitted according to the one-dimensional gain equation,

$$I(\lambda) = \frac{AI_p}{g(\lambda)}\left(e^{g(\lambda)l} - 1\right) \qquad 6.1$$

to obtain the wavelength dependent gain coefficient $g(\lambda_{ASE})$ in units of cm^{-1}, where AI_p is the term corresponding to the spontaneous emission and l is the length of the stripe shaped excitation (Laquai *et al.* 2008).

Earlier in this chapter we discussed the ASE spectra of the P(IF-F) copolymers in connection to absorption and photoluminescence to show the wavelength of ASE is centred at ~456 nm for the linear alkyl substituted polymers and slightly lower at ~ 454 nm for S50F8:50IF1,4. Representative emission data above threshold showing the narrow linewidth of the stimulated emission and its superlinear increase with pump intensity are shown in Fig. 6.18, for the specific case of S50F3:50IF8.

Fig. 6.19 plots the peak intensity of the stimulated emission peak detected at the edge of the sample with increasing incident pump energy density and for a range of stripe lengths. These plots follow a characteristic sigmoidal shape, with spontaneous emission below threshold at low pump energy

density followed by a superlinear increase in intensity at the onset of ASE, which persists until saturation occurs at high pump energy densities.

An alternative technique of observing the threshold for ASE is to observe the variation of the full-width half-maximum (FWHM) of the emission peak as the incident energy density is increased. An example of this is shown in Fig. 6.20 alongside the points corresponding to the energy dependence of the peak intensity. As the incident energy increases, the FWHM collapses from over 20 nm to ~3 nm to 4 nm at a certain threshold, that is approximately the same incident energy as that for the superlinear increase in intensity.

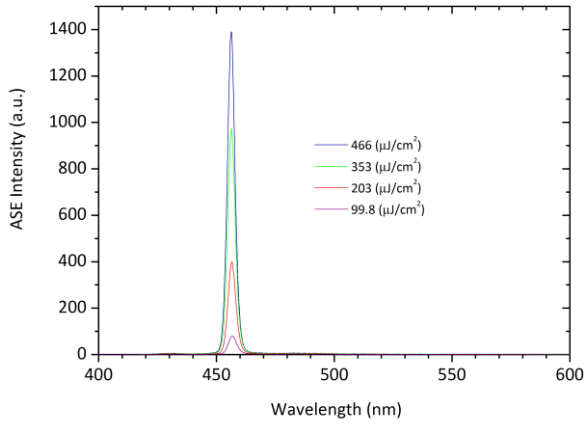

Fig. 6.18 ASE spectra of S50F3:50IF8 at increasing pump energy densities using a 355 nm laser excitation with a pulse duration of 10 ns stripe dimensions of 3.69 mm x 50 μm.

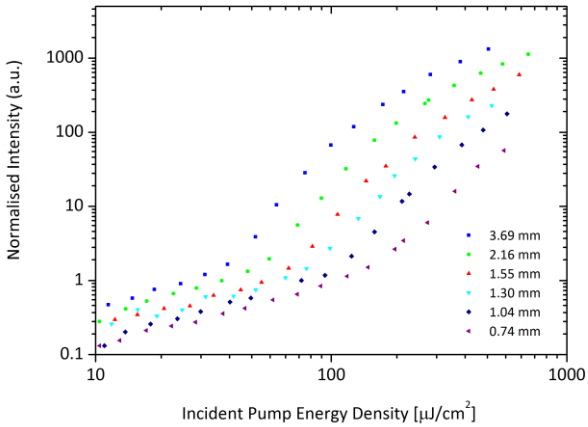

Fig. 6.19 Energy dependence of ASE intensity of S50F3:50IF8 at increasing stripe lengths.

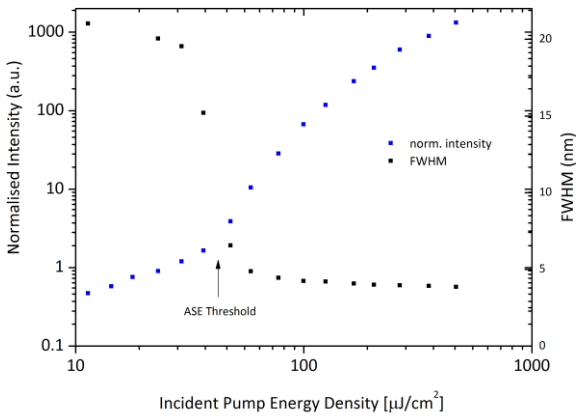

Fig. 6.20 Comparison of energy dependence of ASE intensity and FWHM of S50F3:50IF8.

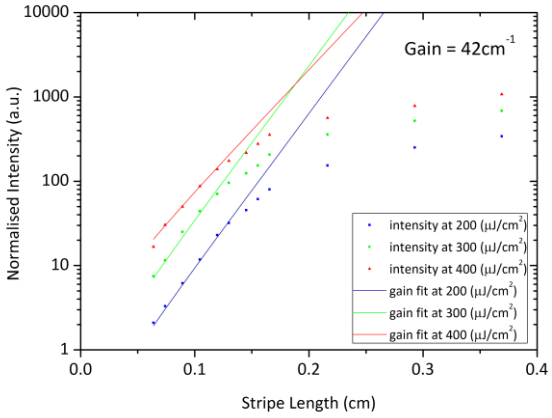

Fig. 6.21 Stripe length dependence of ASE intensity of S50F3:50IF8 at different pump energy densities including fits for optical gain extraction.

Finally, the intensities at particular incident energy densities are plotted against stripe length, as in Fig. 6.21 for S50F3:50IF8, which shows the optical gain of the polymer in an asymmetric waveguide configuration. This gain data is fitted according to the one-dimensional gain equation to extract the gain coefficient, g, The set of energies to which we have chosen to fit the gain equation are after threshold at 200, 300 and 400 μJ/cm^2. At a certain stripe length, we observe saturation of the gain so we have fitted the data in the region before this occurs.

The measured gains for the three polymers are 42 cm^{-1} for S50F3:50IF8 (Fig. 6.21), 43 cm^{-1} for S50F8:50IF8 (Fig. 6.23) and 33 cm^{-1} for S50F8:50IF1,4 (Fig. 6.25). The ASE thresholds were found to be 40.7, 28 and 64 μJ/cm^2, respectively. These values for the gain were consistent at all energy densities for the linear alkyl P(IF-F) polymers, however, at lower energies, the gain of S50F8:50IF1,4 is slightly lower at 28 cm^{-1}. The gain and threshold results are summarised in Table 6.4.

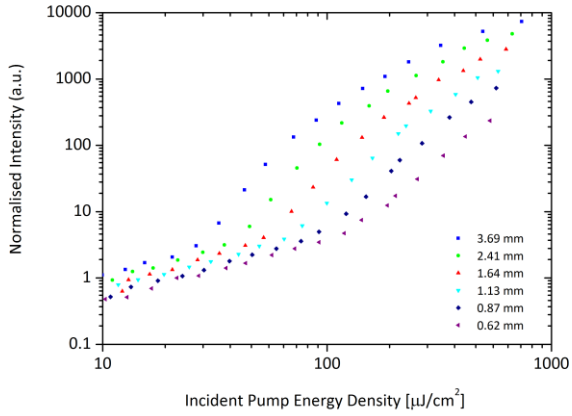

Fig. 6.22 ASE spectra of S50F8:50IF8 at increasing pump energy densities.

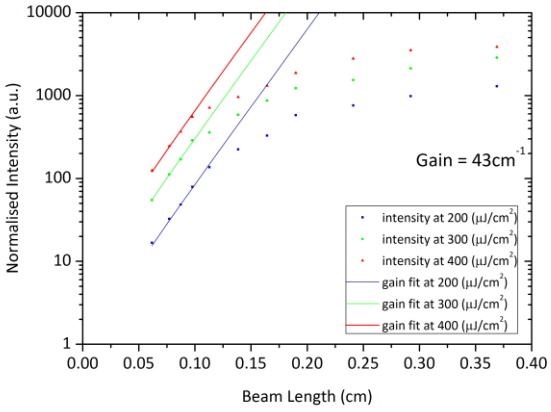

Fig. 6.23 Stripe length dependence of ASE intensity of S50F8:50IF8 at different pump energy densities including fits for optical gain extraction.

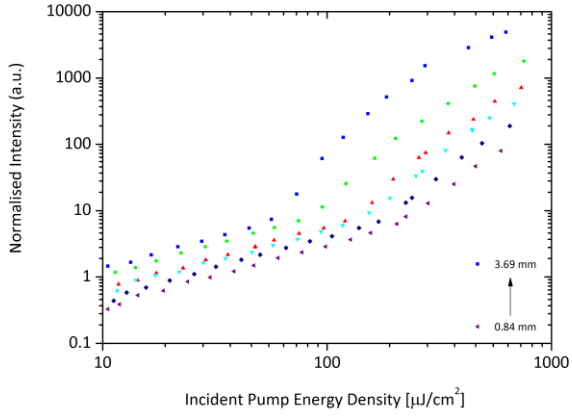

Fig. 6.24 ASE spectra of S50F8:50IF1,4 at increasing pump energy densities.

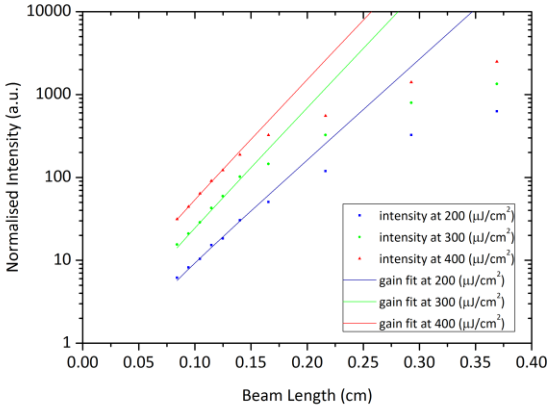

Fig. 6.25 Stripe length dependence of ASE intensity of S50F8:50IF1,4 at different pump energy densities including fits for optical gain extraction.

The optical gain obtained for the two linear alkyl polymers is almost identical. The lower threshold of the S50F3:50IF8 copolymer might be, in principle, from two reasons. First, it might be because of a difference in the refractive index of the polymers, with better confinement of light in the waveguide structure of higher index. Alternatively, it may be related to closer chain interactions leading to more efficient energy transfer to quenching sites. In relation to the former reason, we would expect a higher density of conjugated units for the S50F3:50IF8 copolymer and consequently a higher refractive index, although this is not consistent with the observed higher threshold. However, the shorter propyl side chains would be consistent with the latter reason.

For reference, the highest gain deduced for the blue polymers in the previous chapter (using the same experimental configuration) was found to be 36 cm^{-1} and the threshold 30.9 μJ/cm^2. The S50F8:50IF8 data are better for both of these performance parameters, confirming the suitability of the indenofluorene-fluorene copolymer architecture.

Table 6.4 ASE threshold of P(IF-F) copolymers and extracted optical gain values.

	ASE Threshold (μJ/cm^2) (at stripe length $l = 3.7\ mm$)	**Modal Gain (cm^{-1})** (at 200 μJ/cm^2)	**Modal Gain (cm^{-1})** (at 300 μJ/cm^2)	**Modal Gain (cm^{-1})** (at 400 μJ/cm^2)
S50F8:50IF8	28	43	43	43
S50F3:50IF8	41	42	42	33
S50F8:50IF1,4	64	28	33	33

We may consider these results in comparison to reports in the literature, in particular, the study of Kim *et al.* on indenofluorene-phenanthrene copolymers, which is purported to have yielded the highest optical gain of any conjugated polymer of 154 cm^{-1}. This result is double that of the optical gain of 87 cm^{-1} for the statistical copolymer, Y80F8:20F5, obtained by Yap *et al.* (2008). The results from the former mentioned study are summarised in Table 6.5.

In the former work, a variable stripe length of up to 8 mm and fixed width of 1 mm was used to pump the samples. The experimental data points used to fit the gain on the plot of ASE intensity against stripe length were the points corresponding to stripe lengths of less than 0.5 mm.

That is, the gain data has been fitted to stripe lengths that are shorter than the width of the stripe itself of 1 mm, which represents a significant departure from the requirement of a one-dimensional stripe inherent in the gain equation used to obtain the gain coefficient. We note that the strongest gain in the copolymers in this study is observed at stripe lengths of between 0.5 to 1.5 mm with a fixed width of 50 μm.

We therefore conclude that the authors may have obtained ASE from the sample edge that has been waveguided in an off-axis direction from the stripe width, which is aligned parallel to the sample edge. Consequently, their results may be a result of a systematic error within their experimental method in which the effective stripe length is miscalculated, leading to an exaggerated optical gain.

Table 6.5 ASE and optical gain parameters reported for indenofluorene-phenanthrene copolymers (Kim et al. 2010)

	ASE Threshold ($\mu J/cm^2$)	**Optical Gain (cm^{-1})**	**SSA Threshold ($\mu J/cm^2$)**
Aryl-PIF	2.8 ± 1.0	22 ± 4	~ 20
BLUE-1	17.5 ± 1.0	154 ± 4	~ 100
BLUE-2	4.5 ± 1.1	59 ± 4	~ 100

In the measurements on indenofluorene based copolymers reported by Kim *et al.* in Table 6.5, we also notice that the material with the lowest threshold for ASE has the lowest gain and the material with the highest threshold has the highest gain. We would, however, expect a low threshold to correlate with higher gain. The lowest ASE threshold is reported for aryl-PIF, of 2.8 $\mu J/cm^2$, which is ten times lower than the lowest threshold for the present series of P(IF-F) polymers, namely 28 $\mu J/cm^2$ in the case of S50F8:50IF8.

It has previously been demonstrated that the ASE threshold increases as the number of bridged phenyl rings of the monomer unit is increased from three to five in the example of a series of polymers from fully arylated poly(ladder-type indenofluorene) (or aryl-PIF, as above) to poly(ladder-type pentaphenylene) (Laquai *et al.* 2008). Hence, one would expect the threshold of our P(IF-F) polymers to be comparable or lower based on their structure with an alternation of three and two phenyl rings in the indenofluorene and fluorene moieties, respectively. It may be that the lower threshold for aryl-PIF is because of the bulky aryl substituents reducing the rate of interchain energy transfer to quenching sites. We note further that no beam dimensions are quoted for the ASE thresholds reported by Kim *et al.*, which limits comparison of the results since ASE thresholds are substantively dependent on the beam length. The dependence on the stripe length of the ASE threshold is illustrated in Fig. 6.26 for S50F3:50IF8, which shows how the threshold decreases as beam stripe length increases.

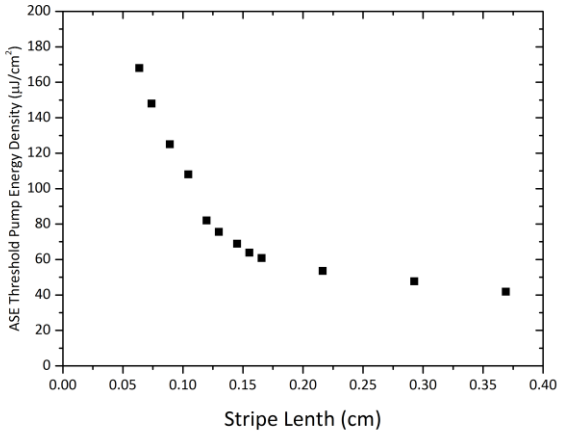

Fig. 6.26 Threshold energy density for ASE in S50F3:50IF8 plotted as a function of stripe length for a fixed stripe width of 50 μm.

6.8 Indenopyrazine-Fluorene Copolymers

The poly(indenofluorene-fluorene) series has demonstrated highly promising characteristics with respect to charge transport and optical gain, which makes it an excellent series for further studies in the field of polymer lasing. In particular, we have observed simultaneously high hole mobilities, luminescence efficiencies and optical gain from this series. However, a key requirement for electrically pumped polymer lasing is balanced electron and hole mobility in order to maximise exciton generation efficiency and minimise long-lived polaron formation.

This section therefore discusses the properties of a novel series of poly(indenopyrazine-fluorene) P(IP-F) copolymers designed for enhanced electron transport that are directly analogous to the P(IF-F) series apart from a modification to the benzene ring at the core of the indeno unit, which is replaced with a pyrazine ring that contains two symmetrically arranged nitrogen atoms in the 1,4- position. The incorporation of nitrogen atoms on the backbone is known to increase the electron affinity and lower the LUMO level because of their higher electronegativity (Grimsdale *et al.* 1997), which enables the use of more stable electron injecting layers and may improve electron transport.

At this stage, we are particularly interested in the effect on the luminescence and optical properties of the pyrazine unit in comparison to the characteristics of the P(IF-F) series. As mentioned, the structures in this series, shown in Table 6.6, are analogous to the P(IF-F) copolymers in the former part of this chapter with different combinations of linear and branched alkyl side chains on the indenofluorene and fluorene units. In this case, one further structure, P(IP(C1C4)-F(C3)), with branched C1C4 chains and linear C3 chains on the indenopyrazine and fluorene units, respectively, has been synthesised. We also present results from the indenopyrazine homopolymer to consider the nature of its interaction with the fluorene unit in the copolymer.

One of the first applications of the indenopyrazine unit was as a new core structure in a series of deep-blue emitting small molecules (Park *et al.* 2008), although the first report of its synthesis was in 1956 (Ebel & Deuschel 1956). The optical properties of the indenopyrazine monomer have previously been presented in comparison to indenofluorene by Lee *et al.* (Lee *et al.* 2010). Their interest in the polymer extended to its use in devices such as OFETs and LEDs. The absorption maximum was found to be red shifted by 25 nm compared to indenofluorene and a computational study based on time-dependent density functional theory showed that the nitrogen atoms induce this spectral shift. More specifically, indenopyrazine was calculated to have a smaller HOMO-LUMO gap than indenofluorene because of a 0.6 eV stabilisation of the LUMO level.

The results in this chapter section represent the first report on the optical properties of indenopyrazine copolymers together with a brief charge transport and injection study of an indenopyrazine-triarylamine copolymer that has been synthesised with the aim of balanced electron and hole transport and efficient hole and electron injection.

Table 6.6 Chemical structures of the indenopyrazine-fluorene copolymers.

S50F8:50IP8	Mw: 24000 PDI: 1.7	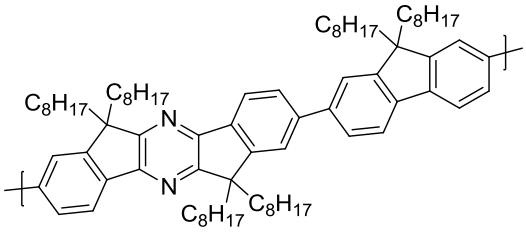
S50F3:50IP8	Mw: 82000 PDI: 1.6	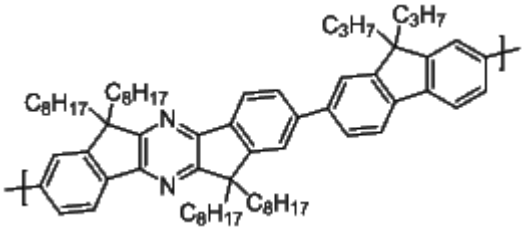
S50F8:50IP1,4	Mw: 24000 PDI: 1.7	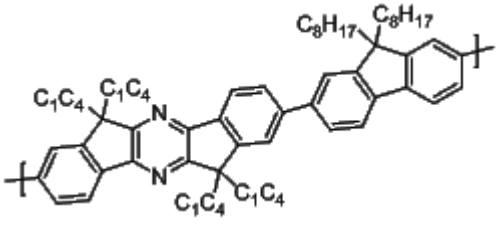
S50F3:50IP1,4	Mw: 26000 PDI: 1.5	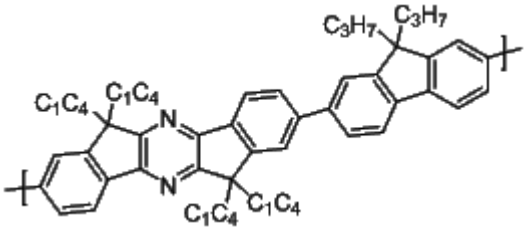

PIP8

Mw: 82000
PDI: 2.2

HOMO:
5.97 eV
LUMO:
3.35 eV

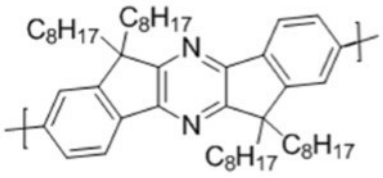

We proceed with a comparison of the absorption and photoluminescence spectra of the S50F8:50IP8, in relation to S50F8:50IF8 (reported in the earlier part of this chapter). The UV/Vis absorption and PL spectra from both polymers are plotted together in Fig. 6.27 in order to directly compare the effect of an indenopyrazine unit relative to indenofluorene with the same linear octyl substituents.

First, the main absorption peak is red shifted from 404 nm to 434 nm. This agrees with a reduction in the optical gap associated with a lowering of the LUMO level of S50F8:50IP8 compared to S50F8:50IF8. The PL spectrum shows clear vibronic structure with 25 nm and 27 nm peak shifts for the 0-0 and 0-1 vibronic levels, respectively.

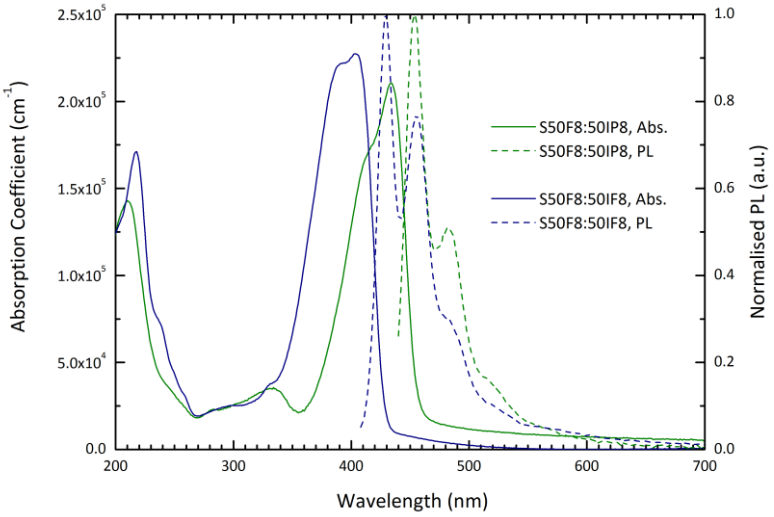

Fig. 6.27 Absorption and PL of S50F8:50IP8 thin film compared to S50F8:50IF8.

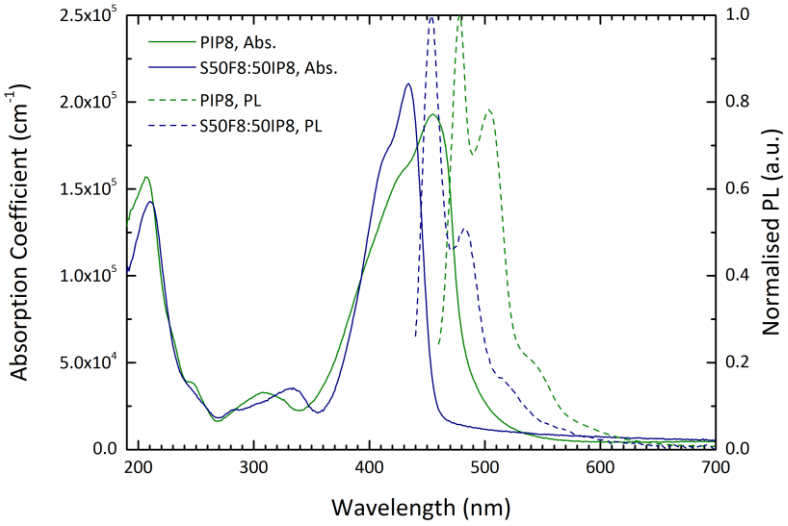

Fig. 6.28 Absorption and PL of alternating copolymer S50F8:50IP8 thin film compared to the PIP homopolymer..

The absorption and PL spectra for the PIP8 homopolymer in Fig. 6.28 are both further red shifted by ~23 nm from the main peaks of S50F8:50IP8. This shows that the indenopyrazine and fluorene moieties are both significant in determining the optical characteristics of the copolymer and that mixing between IP and F units has led to raising of the LUMO compared to PIP8. The spectra for the copolymer are sharper than the homopolymer and we note that in the emission spectra, the 0-0 emission of the copolymer is more dominant. The main absorption peak of the PIP8 homopolymer is weaker than the copolymer, which is an indication that the fluorene unit, with only one pair of side chains, increases the optical density.

The homopolymer has a molecular weight and PDI that are higher than the copolymer (Table 6.6), which may lead to a greater degree of inhomogeneity in the thin film with small regions of crystallinity within a matrix of amorphous, entangled chains.

A significant drawback of the indenopyrazine series is that there is much more overlap between the absorption and emission, which may lead to self-absorption of stimulated emission and thus an increase in the threshold for stimulated emission. A particularly useful feature of the pyrazine unit is that absorption may be tuned over a range of ~100 nm by oxidation of the N-atoms, which may be observed as a change in the colour of the materials from yellow to orange-red (Grimsdale *et al.* 1997).

The PLQE for each of the P(IP-F) copolymers and the PIP8 homopolymer are given in Table 6.7, which shows that all of the P(IP-F) copolymers have low quantum yields of at most 11.1% for S50F8:50IP1,4, which is approximately three times lower than in the P(IF-F) series. However, it does not seem as though we can attribute this directly to the indenopyrazine unit since the PIP homopolymer has a much higher PLQE of 18.7%.

The slightly higher PLQE of S50F8:50IP1,4 compared to the rest of the series may be because of its bulkier side groups. However, there does not seem to be a clear correlation between the side chain length and PLQE since the copolymers with the shortest and longest side chains, S50F3:50IP1,4 and PIP(C8)-F(C8), respectively, have approximately the same PLQE of ~8%. It is more likely that other factors such as impurities, which quench emission or the bounds of experimental errors are more significant in determining the PLQE in this case since the differences are only several percent.

Table 6.7 PLQE values for the indenopyrazine-fluorene polymers.

S50F8:50IP8	**S50F3:50IP8**	**S50F8:50IP1,4**	**S50F3:50IP1,4**	**PIP8**
8.1%	9.9%	11.1%	8.2%	18.7%

The side chain dependence of the optical characteristics is further investigated in Fig. 6.29 to Fig. 6.32, which also shows the results of ASE measurements. ASE was observed for all of the copolymers apart from S50F3:50IP1,4. The wavelength of the ASE peak is at 485 nm for S50F8:50IP8 (Fig. 6.32) and slightly red shifted to ~488 nm for S50F8:50IP1,4 and S50F3:50IP8 (Fig. 6.30 and Fig. 6.31, respectively). The appearance of stimulated emission from this series is highly promising and may be considered a successful development of the P(IF-F) series with respect to combined charge transport and luminescence properties because of its lower LUMO, which may enable balanced charge transport of electrons and holes.

We do note, however, that the ASE was observed at high pump energy densities since the emission was too weak to be recorded at low energy densities. We were therefore unable to ascertain the ASE threshold; however, we expect that it may be up to an order of magnitude higher than in the P(IF-F) series. The unpolarised emission is shown in all cases apart from S50F8:50IP8, for which both the polarised and unpolarised emission is shown in Fig. 6.33. The fact that the emission has not fully collapsed into one narrow peak for all of the copolymers, despite the high pump energy densities used for these measurements, is an indication of the high ASE threshold for these copolymers. The polarised emission of S50F8:50IP8 in Fig. 6.33 also shows a residual emission at around ~520 nm, which may be an indication of the existence of keto defects in this first batch of copolymers.

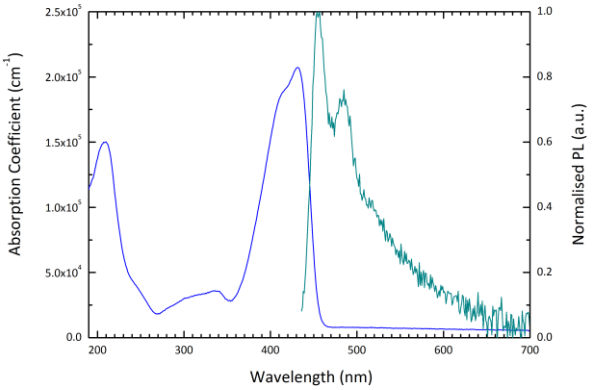

Fig. 6.29 Absorption and PL of S50F3:50IP1,4 (101 nm film, excitation for PL at peak absorption). PL spectra shows noise because of the low emission intensity and integration time of 1 s used for measurements of the entire series.

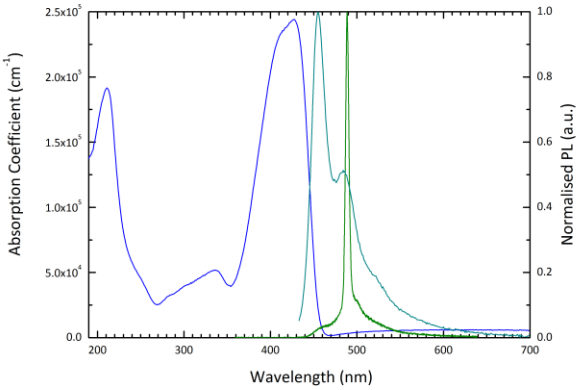

Fig. 6.30 Absorption, PL and ASE of S50F8:50IP1,4 (111 nm film, excitation for PL at peak absorption)

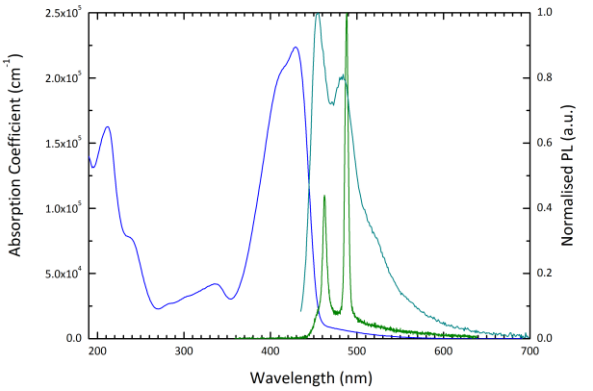

Fig. 6.31 Absorption, PL and ASE of S50F3:50IP8 (208 nm film, excitation for PL at peak absorption)

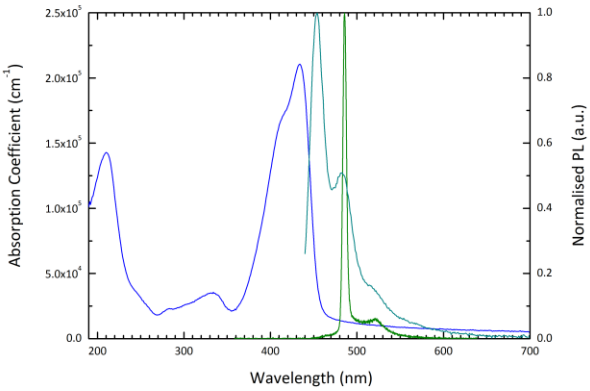

Fig. 6.32 Absorption, PL and ASE of S50F8:50IP8 (80 nm film, excitation for PL at peak absorption)

We note one additional feature of S50F3:50IP8 in Fig. 6.31, which is a narrowed emission peak at 462 nm, which is a few nanometres red-shifted from the position of the PL from the 0-0 vibronic transition. The reasons for this competing emission are unclear, however it may relate to the slightly greater thickness of the film at 208 nm, which may be able to support wave guiding of an additional mode at this wavelength.

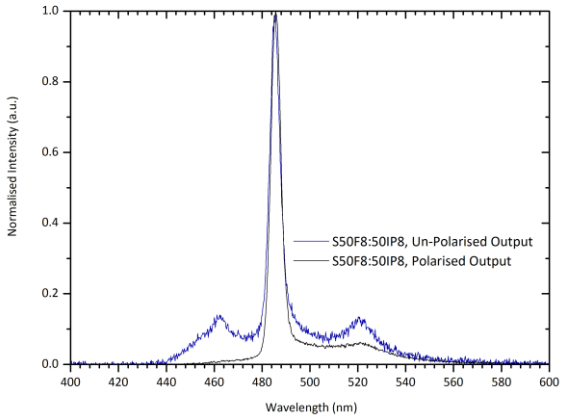

Fig. 6.33 TE polarised and unpolarised edge emission from a S50F8:50IP8 thin film using polarising lens before the optical waveguide leading to the detector.

ToF measurements were attempted in order to determine the charge carrier mobility, however, the technique could not be implemented successfully because the strongest absorption of these copolymers occurs directly between the laser wavelengths available for photoexcitation at 355 nm and 532 nm. Hence, the photoexcitation is absorbed deep into the film and not as a confined packet close to one interface as required by the technique. In all cases, the transient photocurrent response resembled those from highly dispersive materials and no clear plateau or inflection point could be discerned.

Finally, initial attempts at charge injection of holes and electrons by MoO_3 and Ca/Al injection layers, respectively, were unsuccessful preventing analysis of charge transport by the JV and DI-SCLC techniques.

This leads us to report briefly on one further indenopyrazine copolymer with triarylamine, a well-known hole-transporting unit that has been shown to yield mobilities of up to 0.01 cm^2/Vs as a copolymer with polyfluorene (Fong *et al.* 2006) and improved hole injection by modification of the HOMO level (Fong *et al.* 2009). The structure of this novel indenopyrazine-triarylamine copolymer is shown in Fig. 6.34. The HOMO level, measured by CV, is at 5.49 eV, which is 0.48 eV closer to the vacuum level compared to the indenopyrazine homopolymer. The optical gap determined from the absorption spectra in Fig. 6.35 is 2.62 eV, hence the LUMO level is at approximately 2.87 eV, which is similar to the LUMO of PFO at 2.85 eV obtained by the same method (Chen *et al.* 2008), although other techniques find it to be shallower at 2.12 eV (Janietz *et al.* 1998).

The PL spectrum in Fig. 6.35 is not as well resolved as in the formerly discussed P(IP-F) copolymers and the PLQE was measured to be very low at 3.3%. Indeed, this is reflected in the fact that no amplified spontaneous emission was observed from thin films of 80 nm in asymmetric waveguides when pumped at high energy densities.

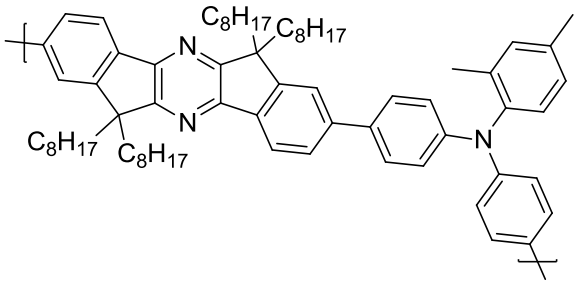

Fig. 6.34 Poly(indenopyrazine-co-triarylamine) (P(IP-TAA))

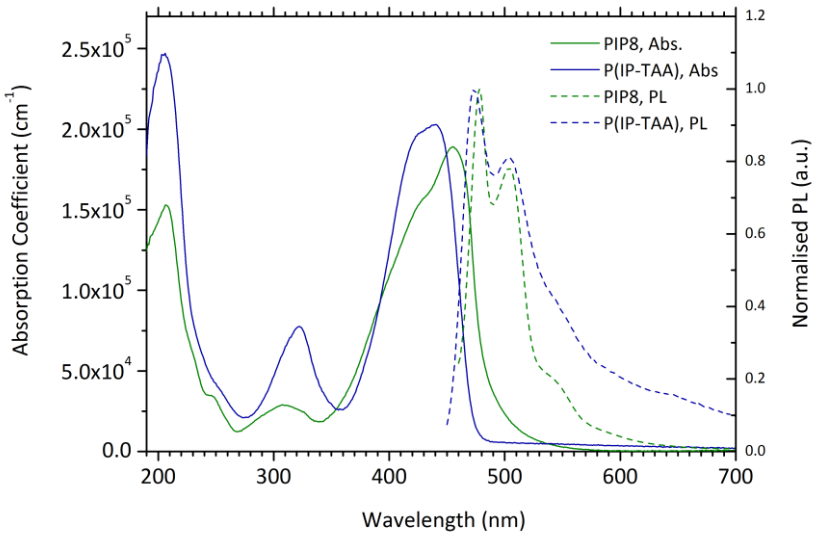

Fig. 6.35 UV/Vis absorption and PL of 80 nm thin film of P(IP-TAA)

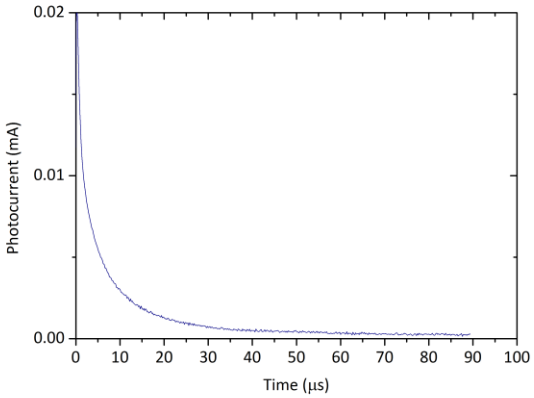

Fig. 6.36 ToF transient of 1.01 µm thick film of P(IP-TAA) on a linear scale.

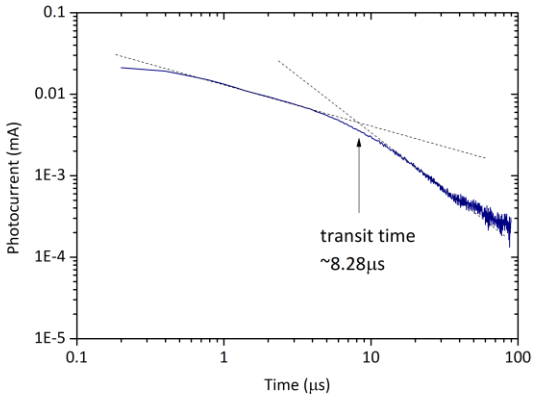

Fig. 6.37 ToF transient of 1.01 µm thick film of P(IP-TAA) on a log-log plot.

In order to investigate the hole mobility, time-of-flight measurements and transient dark injection SCLC measurements were conducted with slightly greater success than the P(IP-F) polymers, although with significant limitations, in particular, because of the severely dispersive character of the photocurrent transient shown in Fig. 6.36. This limits the resolution of a clear inflection point corresponding to the transit time but the log-log plot of Fig. 6.37 shows a plausible transit time of ~8.28 μs. This would correspond to a very low hole mobility of ~6.16 x 10^{-5} cm^2/Vs at a field of 2 x 10^5 V/cm (i.e. 445 $(V/cm)^{1/2}$). The dispersive nature of the transport further limits the possibility of measurements across a range of fields because of the obscurity of a clear inflection point.

The reason for dispersive characteristics may be the low absorption coefficient at the ToF laser wavelength of 355 nm. The distribution the photogenerated charge carriers would therefore extend deep within the film instead of a packet of charge close to the interface, in the same way that the charge packet is diffusively spread when charge transport is dispersive.

The raising of the HOMO level achieved by incorporation of a TAA unit permits facile hole injection using a MoO_3 hole injection interlayer such that the DI-SCLC technique could be used to measure the mobility. The dark injection transients of Fig. 6.38 show clear cusps corresponding to the DI transit time, which shift to earlier times as the applied field is increased as expected. The hole mobility was found to be ~4.58 x 10^{-5} cm^2/Vs at 445 $(V/cm)^{1/2}$, slightly lower than the mobility from the ToF measurement. This is as typically observed (see chapter four), and supports the ToF photocurrent measured mobility.

The field dependence of the hole mobility from the DI measurements is shown in Fig. 6.39. The mobility reaches 2 x 10^{-4} cm^2/Vs at 700 $(V/cm)^{1/2}$. This is significantly lower than for typical fluorene-triarylamine copolymers such as TFB (Redecker, Donal D.C. Bradley, *et al.* 1999; Fong *et al.* 2006).

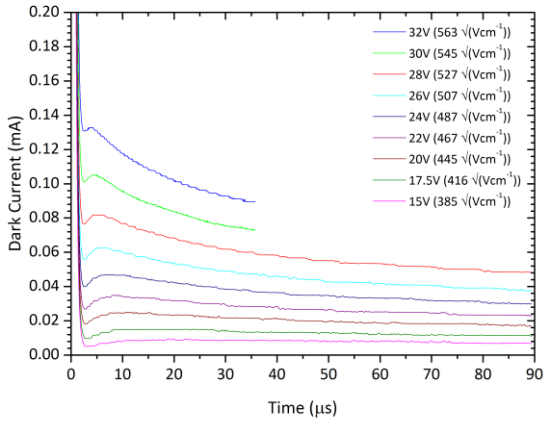

Fig. 6.38 DI-SCLC transients of 1.01 μm film of P(IP-TAA) at increasing applied electric fields.

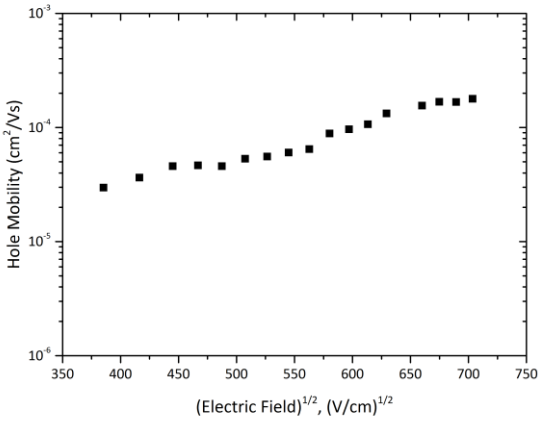

Fig. 6.39 Field dependence of the DI-SCLC hole mobility of 1.01 μm film of P(IP-TAA)

The first integral method ToF measurements of the hole mobility for TFB gave μ_h ~10^{-3} cm^2/Vs (Redecker, Donal D.C. Bradley, *et al.* 1999), with significant dispersion. Several years later, a further study on the hole mobility determined a value of ~10^{-2} cm^2/Vs via standard ToF measurements, with clearer non-dispersive characteristics (Fong *et al.* 2006). This change in behaviour was attributed to improvements in synthesis that led to a higher purity less disordered material. We may consider that the hole mobility measured here for the P(IP-TAA) copolymer is likely to be the result of charge traps that originate from impurities or defects in the initial synthesis of this new copolymer.

This is supported by the fact the ToF transients are highly dispersive, which is an indication of charge trapping. Furthermore, by measuring the ratio of the peak of the cusp in the DI transients to the current at ten times the DI transit time (10 x t_{DI}), we find a ratio in the range 1.41 (445 √(V/cm)) to 1.51 (704 √(V/cm)). These ratios are already much greater than the theoretical ratio of the magnitude of the cusp to the steady state current density of ~1.21, an observation that again is characteristic of SCLC in the presence of traps. Therefore, it would be desirable to re-synthesise these polymers for a future study with the aim of enhancing their chemical purity and reducing the presence of defects.

6.9 Summary

This chapter may be divided into two parts, the first concerning the novel copolymer structure combining alternating indenofluorene and fluorene moieties. The combination of the three planarised phenylene rings of the indenofluorene moiety with fluorene offers the potential of an extended conjugation without the tendency to form the beta-phase as in polyfluorene, while providing additional positions for side chain substitution. It has been hoped, therefore, that this configuration and the use of different side chains may lead to enhanced intrachain and interchain transport.

Hence, a series of this copolymer was synthesised with linear alkyl and branched substituents of different lengths to explore further the concept of structured heterogeneity, which is proposed to enhance charge transport without affecting luminescence.

We found that hole mobilities greater than 1 x 10^{-2} cm^2/Vs may be achieved with high PLQE over of 61.5% and high optical gain of $43cm^{-1}$ in the case of the S50F8:50IF8 copolymer. The S50F3:50IF8 copolymer was found to trail slightly behind in each property. These results therefore expand the range of polymers now known to be able to exhibit simultaneously high charge carrier mobility and optical gain.

In relation to our interest in the effect of substituent groups, reducing the length of the linear alkyl substituents on the fluorene unit from C8 to C3 has not led to any significant improvement in charge transport and optical properties. We further find that the combination of branched and linear side chains has led to dispersive charge transport and a lower mobility compared to the linear alkyl substituted copolymers. PLQE and optical gain were also found to be the least in the series.

Experiments based on charge injection using MoO_3 were also performed, in which we found injection limited behaviour in all cases despite the copolymers in this series having similar HOMO levels to the PFO and PFHOP polymers, which were shown to have ohmic injection in chapters four and five, respectively.

In the second half of this chapter, we reported on the results of the synthesis of novel copolymers that develop the concept of the P(IF-F) backbone by the introduction of a pyrazine unit at the centre of the indeno moiety for modification of the LUMO level. This new series of indenopyrazine-fluorene copolymers was also synthesised with a range of different side chain configurations.

The key result from experiments of this copolymer show that optical gain is possible when the pyrazine unit is present on the backbone. However, measurements of electron mobility have not been successful at this stage, which has proven difficult to measure in transient measurements of polymer semiconductors in general. Hole mobility could not be measured because the peak absorption of the polymers is between the available excitation laser wavelengths for ToF.

Finally, charge transport was also investigated in an indenopyrazine-triarylamine copolymer in which the fluorene moiety is replaced with a hole transporting triarylamine unit. The TAA unit modifies the HOMO level, enabling charge transport and charge injection measurements, however, the PLQE was significantly reduced to only a few percent.

CHAPTER 7

7 CONCLUSIONS AND FURTHER WORK

The electrically pumped polymer laser remains notably absent from a variety of devices that have already been demonstrated using plastic electronic materials because of challenges in several key areas. These challenges include issues related to fundamental excitations, electrodes for efficient charge injection, device structures for optical feedback and research into novel polymer structures that combine high ambipolar charge carrier mobility, luminescence efficiency and optical gain.

In this thesis, we have focussed our investigation on the challenge of developing suitable polymer materials that exhibit the prerequisite charge transport and optical characteristics necessary for electrically pumped lasing, while maintaining the ability to inject charge carriers efficiently. We have focussed, in particular, on fluorene-based copolymers since the PFO homopolymer is one of the earliest polymers to attract attention as a potential lasing material and closely related copolymers with small changes to side chain structure have exhibited highly promising characteristics (Yap *et al.* 2008).

In the first chapter of experimental results, we investigated hole injection in PFO to show that the use of MoO_3 enables hole injection in to this polymer, which has not been possible with other electrode materials because of the deep-lying HOMO level of PFO. We further studied the effects of the charge-carrier density regime on charge mobility by the combination of FET, space charge limited and space-charge free measurements, where we found that the FET hole mobility is comparable to beta-phase free ToF mobility in a previous study (Foster 2013). The effects of charge trapping on hole injection from MoO_3 were also studied using DI-SCLC measurements.

The two proceeding chapters introduced two different series of copolymers that are developments of the fluorene system and comprise of an investigation into their charge transport and optical properties, including attempts at hole injection. Polymers with the fluorene backbone and hexyloxyphenyl substituents were found to yield a hole mobility of ~10^{-3} cm^2/Vs, high PLQE of 65.7% and optical gain of 41cm^{-1}. DI-SCLC measurements showed the presence of charge traps at the injection interface. Excellent hole injection was achieved in polymers containing 50% and 10% of the BPPX unit, however, ASE was not observed in these copolymers.

Chapter six comprises of a study of polymer materials designed with the concept of "structured heterogeneity" and is divided into two sections, the first related to indenofluorene-fluorene P(IF-F) copolymers and the second related to an analogous series of indenopyrazine-fluorene P(IP-F) copolymers.

This concept follows the demonstration of a copolymer of polyfluorene with a fraction of branched side groups that enhanced hole mobility by two orders of magnitude compared to ordinary PFO (Yap *et al.* 2008). We find a time-of-flight hole mobility of ~10^{-2} cm^2/Vs may be achieved in the P(IF-F) series as well, although in the case of linear alkyl substituents rather than the copolymers of PF which had alternating branched and linear side groups. However, as with that study, this enhancement in mobility was achieved with simultaneously high luminescence (PLQE) and optical gain properties of 61.5% and 43cm^{-1}, respectively.

The second series of P(IP-P) copolymers is based on indenopyrazine, which is a development of the indenofluorene moiety that replaces the central phenyl ring of IF with a pyrazine unit in order to lower the LUMO with respect to the vacuum level. The observation of ASE from copolymers in this series is a key result and illustrates their potential for future investigations as a series of ambipolar charge transport polymers with good optical gain. Attempts at injection of electrons and holes from appropriate electrodes were unsuccessful at this stage, which is likely to be a consequence of insufficient purity in the initial batch investigated here.

Finally, an indenopyrazine-triarylamine copolymer was investigated (the only copolymer in this thesis without the fluorene moiety). We found the hole mobility to be ~10^{-4} cm^2/Vs and analysis of DI-SCLC transients showed characteristics of SCLC in the presence of traps. Further work into the indenopyrazine series in general would involve re-synthesis in order to attempt to investigate electron transport and injection, which was not achieved successfully with the initial batch.

One of the most important areas to address in further work is the limitation imposed by the yield of singlet and triplet excitons by electrical injection. Potential research with the aim of addressing this problem may be to extend recent work on triplet harvesting using fluorescent small molecules by the Adachi group (Kyushu University) to conjugated polymers.

Singlet exciton production efficiency close to 100% has been possible using phosphorescent materials with heavy metal complexes that provide spin-orbit coupling which enables an otherwise forbidden transition from the S1 to the T1 state followed by phosphorescence on radiative decay from the triplet state. Two key mechanisms exist for up-conversion from triplet to singlet excited states which result in delayed fluorescence. First, triplet-triplet annihilation, which involves the collision of two triplet excitons and results in the production one singlet exciton and one ground state. The second process is thermally activated delayed fluorescence (TADF) in which triplet states are up-converted to singlet states by thermal activation. The exciton generating efficiency of these two processes are 37.5% and 75% respectively. Thus, TADF has been of significant interest in several recent works that have shown highly efficient triplet harvesting.

The extent of mixing between singlet and triplet configurations is given in the first-order by the mixing coefficient, λ, which is inversely proportional to the energy gap between S_1 and T_1 levels (ΔE_{ST}):

$$\lambda = \frac{H_{SO}}{\Delta E_{ST}}$$

where H_{SO} is the spin-orbit interaction. TADF is thus maximised by minimising ΔE_{ST}, which enhances T1 to S1 reverse intersystem crossing (Turro 1991; Uoyama *et al.* 2012). ΔE_{ST} can be minimised when the overlap of HOMO and LUMO levels of a molecule is minimised, which can be accomplished when they are localised on electron donor and acceptor groups, respectively.

(Uoyama *et al.* 2012) demonstrated internal fluorescence efficiency of over 90% from a series of carbazolyl dicyanobenzene (CDCB) materials using intramolecular charge transfer states where carbazole is the donor and dicyanobenzene is the electron acceptor and the HOMO and LUMO are localised to each respectively by steric hindrance between the two moieties.

In order to extend this mechanism of triplet harvesting to conjugated polymers it will be necessary to identify donor and acceptor polymers or copolymer materials with highly localised HOMO and LUMO levels. These materials should have a radiative decay rate > $10^6 s^{-1}$ and there should be little change in molecular conformation between ground and excited states to avoid non-radiative decay pathways. The materials should be selected based on their energy levels to ensure the formation and confinement of exciplex states in solid-state blends and to prevent quenching by energy transfer. This will require an acceptor molecule with a large electron affinity (EA) and ionisation potential (IP) and significantly lower EA and IP in the case of the donor. Once these materials have been identified, they may be investigated for their photoluminescence and electroluminescence properties as well as the possibility of obtaining amplified spontaneous emission (ASE) from them.

A study has very recently been published in accordance with the aims outlined above for the case of a small molecule system (Nakanotani *et al.* 2015) to show that triplet excitons may contribute to light amplification.

Bibliography

Abkowitz, M.A., Mizes, H.A. & Facci, J.S., 1995. Emission limited injection by thermally assisted tunneling into a trap-free transport polymer. *Applied Physics Letters*, 66(10), pp.1288–1290. Available at: http://scitation.aip.org/content/aip/journal/apl/66/10/10.1063/1.113272 [Accessed June 5, 2015].

Abkowitz, M., Facci, J.S. & Rehm, J., 1998. Direct evaluation of contact injection efficiency into small molecule based transport layers: Influence of extrinsic factors. *Journal of Applied Physics*, 83(5), pp.2670–2676. Available at: http://scitation.aip.org/content/aip/journal/jap/83/5/10.1063/1.367030 [Accessed August 2, 2015].

Ahn, J.H. et al., 2007. Blue organic light emitting devices with improved colour purity and efficiency through blending of poly(9,9-dioctyl-2,7-fluorene) with an electron transporting material. *Journal of Materials Chemistry*, 17(29), pp.2996–3001. Available at: http://pubs.rsc.org/en/content/articlelanding/2007/jm/b700047b [Accessed January 30, 2015].

Athanasopoulos, S. et al., 2007. Predictive Study of Charge Transport in Disordered Semiconducting Polymers. *Nano Letters*, 7(6), pp.1785–1788. Available at: http://dx.doi.org/10.1021/nl0708718 [Accessed November 1, 2010].

Azuma, H. et al., 2007. Amplified spontaneous emission in [alpha]-phase and [beta]-phase polyfluorene waveguides. *Organic Electronics*, 8(2-3), pp.184–188. Available at: http://www.sciencedirect.com/science/article/B6W6J-4MWGFGV-2/2/ea963c139cb85bda44744f6c3852360b [Accessed May 1, 2011].

Babel, A. & Jenekhe, S.A., 2003. Charge Carrier Mobility in Blends of Poly(9,9-dioctylfluorene) and Poly(3-hexylthiophene). *Macromolecules*, 36(20), pp.7759–7764. Available at: http://dx.doi.org/10.1021/ma034717t [Accessed October 18, 2010].

Baklar, M. et al., 2010. Bulk charge transport in liquid-crystalline polymer semiconductors based on poly(2,5-bis(3-alkylthiophen-2-yl)thieno[3,2-b]thiophene). *Polymer Chemistry*, 1(9), pp.1448–1452. Available at: http://pubs.rsc.org/en/content/articlelanding/2010/py/c0py00056f [Accessed June 6, 2015].

Baldo, M.A. & Forrest, S.R., 2001. Interface-limited injection in amorphous organic semiconductors. *Physical Review B*, 64(8), p.085201. Available at: http://link.aps.org/doi/10.1103/PhysRevB.64.085201 [Accessed June 6, 2015].

Bange, S., Schubert, M. & Neher, D., 2010. Charge mobility determination by current extraction under linear increasing voltages: Case of nonequilibrium charges and field-dependent mobilities. *Physical Review B*, 81(3), p.035209. Available at: http://link.aps.org/doi/10.1103/PhysRevB.81.035209 [Accessed October 28, 2010].

Barard, S. et al., 2009. Separate charge transport pathways determined by the time of flight method in bimodal polytriarylamine. *Journal of Applied Physics*, 105(1), p.013701. Available at: http://scitation.aip.org/content/aip/journal/jap/105/1/10.1063/1.3054180 [Accessed June 16, 2015].

Barth, S. et al., 1999. Current injection from a metal to a disordered hopping system. III. Comparison between experiment and Monte Carlo simulation. *Physical Review B*, 60(12), pp.8791–8797. Available at: http://link.aps.org/doi/10.1103/PhysRevB.60.8791 [Accessed June 12, 2015].

Bässler, H., 1993. Charge transport in disordered organic photoconductors a Monte Carlo simulation study. *physica status solidi (b)*, 175(1), pp.15–56. Available at: http://onlinelibrary.wiley.com/doi/10.1002/pssb.2221750102/abstract [Accessed March 14, 2015].

Bässler, H. & Borsenberger, P.M., 1993. The transition from nondispersive to dispersive charge transport in vapor deposited films of 1-phenyl-3-p-diethylamino-styryl-5-p-diethylphenylpyrazoline (DEASP). *Chemical Physics*, 177(3), pp.763–771. Available at: http://www.sciencedirect.com/science/article/pii/030101049385039B [Accessed October 9, 2014].

Berggren, M. et al., 1997. Light amplification in organic thin films using cascade energy transfer. *Nature*, 389(6650), pp.466–469. Available at: http://www.nature.com/nature/journal/v389/n6650/abs/389466a0.html [Accessed June 1, 2015].

Bernius, M. et al., 2000. Fluorene-based polymers-preparation and applications. *Journal of Materials Science: Materials in Electronics*, 11(2), pp.111–116. Available at: http://link.springer.com/article/10.1023/A%3A1008917128880 [Accessed April 30, 2015].

Bisri, S.Z. et al., 2009. High Mobility and Luminescent Efficiency in Organic Single-Crystal Light-Emitting Transistors. *Advanced Functional Materials*, 19(11), pp.1728–1735. Available at: http://onlinelibrary.wiley.com/doi/10.1002/adfm.200900028/abstract [Accessed June 23, 2012].

Borsenberger, P.M., Pautmeier, L. & Bässler, H., 1991. Charge transport in disordered molecular solids. *The Journal of Chemical Physics*, 94(8), p.5447. Available at: http://scitation.aip.org/content/aip/journal/jcp/94/8/10.1063/1.460506 [Accessed March 14, 2015].

Borsenberger, P.M., Pautmeier, L.T. & Bässler, H., 1992. Nondispersive-to-dispersive charge-transport transition in disordered molecular solids. *Physical Review B*, 46(19), pp.12145–12153. Available at: http://link.aps.org/doi/10.1103/PhysRevB.46.12145 [Accessed February 8, 2015].

Brabec, C.J., Sariciftci, N.S. & Hummelen, J.C., 2001. Plastic Solar Cells. *Advanced Functional Materials*, 11(1), pp.15–26. Available at: http://onlinelibrary.wiley.com/doi/10.1002/1616-3028(200102)11:1%3C15::AID-ADFM15%3E3.0.CO;2-

A/abstract;jsessionid=80D81A08427AEE94EDF657F3CEFEDE09.d03t01 [Accessed October 18, 2010].

Brédas, J.-L. et al., 2004. Charge-Transfer and Energy-Transfer Processes in π-Conjugated Oligomers and Polymers: A Molecular Picture. *Chemical Reviews*, 104(11), pp.4971–5004. Available at: http://dx.doi.org/10.1021/cr040084k [Accessed October 8, 2010].

Brédas, J.L. et al., 2002. Organic semiconductors: A theoretical characterization of the basic parameters governing charge transport. *Proceedings of the National Academy of Sciences of the United States of America*, 99(9), pp.5804 –5809. Available at: http://www.pnas.org/content/99/9/5804.abstract [Accessed October 18, 2010].

Bright, D.W. et al., 2009. The Influence of Alkyl-Chain Length on Beta-Phase Formation in Polyfluorenes. *Advanced Functional Materials*, 19(1), pp.67–73. Available at: http://onlinelibrary.wiley.com/doi/10.1002/adfm.200800313/abstract [Accessed December 10, 2014].

Burroughes, J.H. et al., 1990. Light-emitting diodes based on conjugated polymers. *Nature*, 347(6293), pp.539–541. Available at: http://dx.doi.org/10.1038/347539a0 [Accessed December 1, 2010].

Cadby, A.J. et al., 2000. Film morphology and photophysics of polyfluorene. *Physical Review B*, 62(23), p.15604. Available at: http://link.aps.org/doi/10.1103/PhysRevB.62.15604 [Accessed November 15, 2010].

Campbell, A.J. et al., 2000. Transient and steady-state space-charge-limited currents in polyfluorene copolymer diode structures with ohmic hole injecting contacts. *Applied Physics Letters*, 76(13), p.1734. Available at: http://link.aip.org/link/APPLAB/v76/i13/p1734/s1&Agg=doi [Accessed February 3, 2011].

Campbell, A.J., Bradley, D.D.C. & Antoniadis, H., 2001a. Dispersive electron transport in an electroluminescent polyfluorene copolymer measured by the current integration time-of-flight method. *Applied Physics Letters*, 79(14), p.2133. Available at: http://link.aip.org/link/APPLAB/v79/i14/p2133/s1&Agg=doi [Accessed November 14, 2010].

Campbell, A.J., Bradley, D.D.C. & Antoniadis, H., 2001b. Quantifying the efficiency of electrodes for positive carrier injection into poly(9,9-dioctylfluorene) and representative copolymers. *Journal of Applied Physics*, 89(6), p.3343. Available at: http://link.aip.org/link/JAPIAU/v89/i6/p3343/s1&Agg=doi [Accessed June 14, 2011].

Campoy-Quiles, M. et al., 2005. Ellipsometric Characterization of the Optical Constants of Polyfluorene Gain Media. *Advanced Functional Materials*, 15(6), pp.925–933. Available at: http://onlinelibrary.wiley.com/doi/10.1002/adfm.200400121/abstract [Accessed October 18, 2010].

Capelli, R. et al., 2010. Organic light-emitting transistors with an efficiency that outperforms the equivalent light-emitting diodes. *Nature Materials*, 9(6), pp.496–503. Available

at: http://www.nature.com/nmat/journal/v9/n6/full/nmat2751.html [Accessed June 21, 2012].

Casperson, L.W. & Yariv, A., 1972. Spectral narrowing in high-gain lasers. *IEEE Journal of Quantum Electronics*, 8(2), pp.80–85.

Cattin, L. et al., 2009. MoO[sub 3] surface passivation of the transparent anode in organic solar cells using ultrathin films. *Journal of Applied Physics*, 105(3), p.034507. Available at: http://link.aip.org/link/JAPIAU/v105/i3/p034507/s1&Agg=doi [Accessed July 31, 2011].

Cerdán, L., Costela, A. & García-Moreno, I., 2010. On the characteristic lengths in the variable stripe length method for optical gain measurements. *Journal of the Optical Society of America B*, 27(9), p.1874. Available at: https://www.opticsinfobase.org/josab/fulltext.cfm?uri=josab-27-9-1874&id=205240 [Accessed August 7, 2012].

Chardonnens, L. & Salamin, L., 1968. Fluorénacènes et fluorénaphènes Synthèses dans la série des indéno-fluorènes XI [1]. Trans-Fluorénacène et dérivés méthylés. *Helvetica Chimica Acta*, 51(5), pp.1095–1102. Available at: http://onlinelibrary.wiley.com/doi/10.1002/hlca.19680510511/abstract [Accessed March 17, 2015].

Chénais, S. & Forget, S., 2012. Recent advances in solid-state organic lasers. *Polymer International*, 61(3), pp.390–406. Available at: http://onlinelibrary.wiley.com/doi/10.1002/pi.3173/abstract [Accessed May 23, 2012].

Chen, J.P. et al., 1999. Improved efficiencies of light-emitting diodes through incorporation of charge transporting components in tri-block polymers. *Synthetic Metals*, 107(3), pp.203–207. Available at: http://www.sciencedirect.com/science/article/pii/S037967799900168X [Accessed December 18, 2014].

Chen, L.-Y. et al., 2007. Anisotropic ambipolar carrier transport and high bipolar mobilities up to 0.1cm2V−1s−1 in aligned liquid-crystal glass films of oligofluorene. *Applied Physics Letters*, 91(16), p.163509. Available at: http://scitation.aip.org/content/aip/journal/apl/91/16/10.1063/1.2801360 [Accessed December 11, 2014].

Chen, L.-Y. et al., 2005. Enhancement of bipolar carrier transport in oligofluorene films through alignment in the liquid-crystalline phase. *Applied Physics Letters*, 87(11), p.112103. Available at: http://scitation.aip.org/content/aip/journal/apl/87/11/10.1063/1.2042536 [Accessed December 11, 2014].

Chen, S.-A., Lu, H.-H. & Huang, C.-W., 2008. Polyfluorenes for Device Applications. In U. Scherf & D. Neher, eds. *Polyfluorenes*. Advances in Polymer Science. Springer Berlin Heidelberg, pp. 49–84. Available at: http://link.springer.com/chapter/10.1007/12_2008_144 [Accessed October 8, 2014].

Chen, S.H. et al., 2005. Crystalline Forms and Emission Behavior of Poly(9,9-di-n-octyl-2,7-fluorene). *Macromolecules*, 38(2), pp.379–385. Available at: http://dx.doi.org/10.1021/ma048162t [Accessed March 27, 2011].

Cheung, C., 2010. *Evolution of optical gain properties through three generations of electroluminescent fluorene-based polymers*. Available at: http://hdl.handle.net/10044/1/6058.

Choulis, S.A. et al., 2003. Investigation of transport properties in polymer/fullerene blends using time-of-flight photocurrent measurements. *Applied Physics Letters*, 83(18), pp.3812–3814. Available at: http://scitation.aip.org/content/aip/journal/apl/83/18/10.1063/1.1624636 [Accessed May 26, 2015].

Chua, L.-L. et al., 2005. General observation of n-type field-effect behaviour in organic semiconductors. *Nature*, 434(7030), pp.194–199. Available at: http://dx.doi.org/10.1038/nature03376 [Accessed October 7, 2010].

Da Como, E. et al., 2007. How Strain Controls Electronic Linewidth in Single β-Phase Polyfluorene Nanowires. *Nano Letters*, 7(10), pp.2993–2998. Available at: http://dx.doi.org/10.1021/nl071207u [Accessed December 10, 2014].

Cornil, J. et al., 2001. Interchain Interactions in Organic π-Conjugated Materials: Impact on Electronic Structure, Optical Response, and Charge Transport. *Advanced Materials*, 13(14), pp.1053–1067. Available at: http://onlinelibrary.wiley.com/doi/10.1002/1521-4095(200107)13:14%3C1053::AID-ADMA1053%3E3.0.CO;2-7/abstract [Accessed October 18, 2010].

Coropceanu, V. et al., 2007. Charge Transport in Organic Semiconductors. *Chemical Reviews*, 107(4), pp.926–952. Available at: http://dx.doi.org/10.1021/cr050140x [Accessed October 8, 2010].

Costela, A. et al., 2008. Amplified spontaneous emission and optical gain measurements from pyrromethene 567 ??? doped polymer waveguides and quasi-waveguides. *Optics Express*, 16(10), pp.7023–7036. Available at: http://www.opticsexpress.org/abstract.cfm?URI=oe-16-10-7023 [Accessed August 20, 2011].

Devizis, A. et al., 2010. Hierarchical charge carrier motion in conjugated polymers. *Chemical Physics Letters*, 498(4-6), pp.302–306. Available at: http://www.sciencedirect.com/science/article/B6TFN-50XV9DK-1/2/9b73dde6e964d6b56fee657c4d97e636 [Accessed October 25, 2010].

Dias, F.B. et al., 2013. Triplet Harvesting with 100% Efficiency by Way of Thermally Activated Delayed Fluorescence in Charge Transfer OLED Emitters. *Advanced Materials*, p.n/a–n/a. Available at: http://onlinelibrary.wiley.com/doi/10.1002/adma.201300753/abstract [Accessed May 30, 2013].

Ebel, F. & Deuschel, W., 1956. trans-Fluorenacendion, ein neues, verküpbares Diketon. *Chemische Berichte*, 89(12), pp.2794–2799. Available at:

http://onlinelibrary.wiley.com/doi/10.1002/cber.19560891222/abstract [Accessed March 17, 2015].

Elmahdy, M.M. et al., 2006. Self-Assembly and Molecular Dynamics of Oligoindenofluorenes. *ChemPhysChem*, 7(7), pp.1431–1441. Available at: http://onlinelibrary.wiley.com/doi/10.1002/cphc.200600015/abstract [Accessed February 4, 2011].

Endo, A. et al., 2011. Efficient up-conversion of triplet excitons into a singlet state and its application for organic light emitting diodes. *Applied Physics Letters*, 98(8), pp.083302–083302–3. Available at: http://apl.aip.org/resource/1/applab/v98/i8/p083302_s1 [Accessed July 17, 2013].

Endo, A. et al., 2009. Thermally Activated Delayed Fluorescence from Sn4+–Porphyrin Complexes and Their Application to Organic Light Emitting Diodes — A Novel Mechanism for Electroluminescence. *Advanced Materials*, 21(47), pp.4802–4806. Available at: http://onlinelibrary.wiley.com/doi/10.1002/adma.200900983/abstract [Accessed July 17, 2013].

Faria, G.C. et al., 2011. Temperature Dependence of the Drift Mobility of Poly(9,9′-dioctylfluorene-co-benzothiadiazole)-Based Thin-Film Devices. *The Journal of Physical Chemistry C*, 115(51), pp.25479–25483. Available at: http://dx.doi.org/10.1021/jp204893q [Accessed October 9, 2014].

Feltin, E. et al., 2009. Broadband blue superluminescent light-emitting diodes based on GaN. *Applied Physics Letters*, 95(8), p.081107. Available at: http://link.aip.org/link/APPLAB/v95/i8/p081107/s1&Agg=doi [Accessed June 19, 2012].

Fong, H.H. et al., 2009. Hole Injection in a Model Fluorene–Triarylamine Copolymer. *Advanced Functional Materials*, 19(2), pp.304–310. Available at: http://onlinelibrary.wiley.com/doi/10.1002/adfm.200800738/abstract [Accessed March 18, 2014].

Fong, H.H., Papadimitratos, A. & Malliaras, G.G., 2006. Nondispersive hole transport in a polyfluorene copolymer with a mobility of 0.01cm2V−1s−1. *Applied Physics Letters*, 89(17), p.172116. Available at: http://scitation.aip.org/content/aip/journal/apl/89/17/10.1063/1.2369545 [Accessed March 13, 2015].

Foster, S., 2013. *On the influence of physical and chemical structure on charge transport in disordered semiconducting materials and devices*. Thesis or dissertation. Available at: https://spiral.imperial.ac.uk:8443/handle/10044/1/11143 [Accessed September 12, 2014].

Fowler, R.H. & Nordheim, L., 1928. Electron Emission in Intense Electric Fields. *Proceedings of the Royal Society of London A: Mathematical, Physical and Engineering Sciences*, 119(781), pp.173–181. Available at: http://rspa.royalsocietypublishing.org/content/119/781/173 [Accessed June 12, 2015].

Gärtner, C. et al., 2007. The influence of annihilation processes on the threshold current density of organic laser diodes. *Journal of Applied Physics*, 101(2), pp.023107–023107–9. Available at: http://jap.aip.org/resource/1/japiau/v101/i2/p023107_s1 [Accessed June 25, 2012].

Goldie, D.M., 1999. Transient space-charge-limited current pulse shapes in molecularly doped polymers. *Journal of Physics D: Applied Physics*, 32(23), pp.3058–3067. Available at: http://iopscience.iop.org/0022-3727/32/23/312 [Accessed September 2, 2011].

Grell, M. et al., 1997. A glass-forming conjugated main-chain liquid crystal polymer for polarized electroluminescence applications. *Advanced Materials*, 9(10), pp.798–802. Available at: http://onlinelibrary.wiley.com/doi/10.1002/adma.19970091006/abstract;jsessionid=79F330647E406FCCBED3D36B76DB5C4B.d02t02 [Accessed December 2, 2010].

Grell, M. et al., 1999. Blue Polarized Electroluminescence from a Liquid Crystalline Polyfluorene. *Advanced Materials*, 11(8), pp.671–675. Available at: http://onlinelibrary.wiley.com/doi/10.1002/(SICI)1521-4095(199906)11:8%3C671::AID-ADMA671%3E3.0.CO;2-E/abstract [Accessed December 2, 2010].

Grell, M. et al., 1998. Chain geometry, solution aggregation and enhanced dichroism in the liquidcrystalline conjugated polymer poly(9,9-dioctylfluorene). *Acta Polymerica*, 49(8), pp.439–444. Available at: http://onlinelibrary.wiley.com/doi/10.1002/(SICI)1521-4044(199808)49:8<439::AID-APOL439>3.0.CO;2-A/abstract [Accessed June 19, 2012].

Grell, M. et al., 1999. Interplay of Physical Structure and Photophysics for a Liquid Crystalline Polyfluorene. *Macromolecules*, 32(18), pp.5810–5817. Available at: http://dx.doi.org/10.1021/ma990741o [Accessed October 18, 2010].

Grimsdale, A. c. et al., 2002. Correlation Between Molecular Structure, Microscopic Morphology, and Optical Propertiesof Poly(tetraalkylindenofluorene)s. *Advanced Functional Materials*, 12(10), pp.729–733. Available at: http://onlinelibrary.wiley.com/doi/10.1002/1616-3028(20021016)12:10<729::AID-ADFM729>3.0.CO;2-F/abstract [Accessed December 15, 2014].

Grimsdale, A.C. et al., 1997. Model compounds for novel high electron affinity polymers. *Synthetic Metals*, 85(1–3), pp.1257–1258. Available at: http://www.sciencedirect.com/science/article/pii/S0379677997802299 [Accessed April 13, 2015].

Grimsdale, A.C. & Müllen, K., 2008. Bridged Polyphenylenes – from Polyfluorenes to Ladder Polymers. In U. Scherf & D. Neher, eds. *Polyfluorenes*. Advances in Polymer Science. Springer Berlin Heidelberg, pp. 1–48. Available at: http://link.springer.com/chapter/10.1007/12_2008_137 [Accessed October 8, 2014].

Grozema, F.C. & Siebbeles, L.D.A., 2011. Charge Mobilities in Conjugated Polymers Measured by Pulse Radiolysis Time-Resolved Microwave Conductivity: From Single

Chains to Solids. *The Journal of Physical Chemistry Letters*, 2(23), pp.2951–2958. Available at: http://dx.doi.org/10.1021/jz201229a [Accessed May 28, 2015].

Gwinner, M.C. et al., 2011. Doping of Organic Semiconductors Using Molybdenum Trioxide: a Quantitative Time-Dependent Electrical and Spectroscopic Study. *Advanced Functional Materials*, 21(8), pp.1432–1441. Available at: http://onlinelibrary.wiley.com/doi/10.1002/adfm.201002696/abstract [Accessed August 3, 2011].

Gwinner, M.C. et al., 2012. Highly Efficient Single-Layer Polymer Ambipolar Light-Emitting Field-Effect Transistors. *Advanced Materials*, 24(20), pp.2728–2734. Available at: http://onlinelibrary.wiley.com/doi/10.1002/adma.201104602/abstract [Accessed June 23, 2012].

Gwinner, M.C. et al., 2009. Integration of a Rib Waveguide Distributed Feedback Structure into a Light-Emitting Polymer Field-Effect Transistor. *Advanced Functional Materials*, 19(9), pp.1360–1370. Available at: http://onlinelibrary.wiley.com/doi/10.1002/adfm.200801897/abstract [Accessed October 19, 2010].

Harding, M.J. et al., 2010. Variations in Hole Injection due to Fast and Slow Interfacial Traps in Polymer Light-Emitting Diodes with Interlayers. *Advanced Functional Materials*, 20(1), pp.119–130. Available at: http://onlinelibrary.wiley.com/doi/10.1002/adfm.200900352/abstract [Accessed July 27, 2011].

Hasegawa, T. & Takeya, J., 2009. Organic field-effect transistors using single crystals. *Science and Technology of Advanced Materials*, 10(2), p.024314. Available at: http://iopscience.iop.org/1468-6996/10/2/024314 [Accessed June 7, 2015].

Hayashi, K. et al., 2015. Suppression of roll-off characteristics of organic light-emitting diodes by narrowing current injection/transport area to 50 nm. *Applied Physics Letters*, 106(9), p.093301. Available at: http://scitation.aip.org/content/aip/journal/apl/106/9/10.1063/1.4913461 [Accessed March 5, 2015].

Heliotis, G. et al., 2002. Light amplification and gain in polyfluorene waveguides. *Applied Physics Letters*, 81(3), p.415. Available at: http://link.aip.org/link/APPLAB/v81/i3/p415/s1&Agg=doi [Accessed November 15, 2010].

Hertel, D. et al., 1999. Charge carrier transport in conjugated polymers. *The Journal of Chemical Physics*, 110(18), p.9214. Available at: http://link.aip.org/link/JCPSA6/v110/i18/p9214/s1&Agg=doi [Accessed October 8, 2010].

Hertel, D. & Bässler, H., 2008. Photoconduction in Amorphous Organic Solids. *ChemPhysChem*, 9(5), pp.666–688. Available at: http://onlinelibrary.wiley.com/doi/10.1002/cphc.200700575/abstract [Accessed October 8, 2010].

Hoofman, R.J.O.M. et al., 1998. Highly mobile electrons and holes on isolated chains of the semiconducting polymer poly(phenylene vinylene). *Nature*, 392(6671), pp.54–56. Available at: http://dx.doi.org/10.1038/32118 [Accessed November 18, 2010].

Hwang, J., Wan, A. & Kahn, A., 2009. Energetics of metal-organic interfaces: New experiments and assessment of the field. *Materials Science and Engineering: R: Reports*, 64(1-2), pp.1–31. Available at: http://www.sciencedirect.com/science/article/B6TXH-4VGDNNB-1/2/8b248817f126af00fac9afbb2fd959ae [Accessed January 14, 2011].

Janietz, S. et al., 1998. Electrochemical determination of the ionization potential and electron affinity of poly(9,9-dioctylfluorene). *Applied Physics Letters*, 73(17), pp.2453–2455. Available at: http://scitation.aip.org/content/aip/journal/apl/73/17/10.1063/1.122479 [Accessed March 15, 2015].

Jeong, E. et al., 2009. Synthesis and characterization of indeno[1,2-b]fluorene-based white light-emitting copolymer. *Journal of Polymer Science Part A: Polymer Chemistry*, 47(14), pp.3467–3479. Available at: http://doi.wiley.com/10.1002/pola.23422.

Juscaronka, G. et al., 2002. Charge transport at low electric fields in pi -conjugated polymers. *Physical Review B*, 65(23), p.233208. Available at: http://link.aps.org/doi/10.1103/PhysRevB.65.233208 [Accessed November 6, 2010].

Kalb, W.L. et al., 2007. Organic small molecule field-effect transistors with Cytop^{TM} gate dielectric: Eliminating gate bias stress effects. *Applied Physics Letters*, 90(9), p.092104. Available at: http://link.aip.org/link/APPLAB/v90/i9/p092104/s1&Agg=doi [Accessed August 18, 2011].

Keivanidis, P.E. et al., 2005. Photophysical Characterization of Light-Emitting Poly(indenofluorene)s. *ChemPhysChem*, 6(8), pp.1650–1660. Available at: http://onlinelibrary.wiley.com/doi/10.1002/cphc.200400634/abstract [Accessed January 21, 2011].

Kepler, R.G., 1960. Charge Carrier Production and Mobility in Anthracene Crystals. *Physical Review*, 119(4), pp.1226–1229. Available at: http://link.aps.org/doi/10.1103/PhysRev.119.1226 [Accessed February 6, 2014].

Khan, R.U.A. et al., 2007. Hole mobility within arylamine-containing polyfluorene copolymers: A time-of-flight transient-photocurrent study. *Physical Review B*, 75(3), p.035215. Available at: http://link.aps.org/doi/10.1103/PhysRevB.75.035215 [Accessed November 11, 2010].

Kim, H. et al., 2010. A High Gain and High Charge Carrier Mobility Indenofluorene-phenanthrene Copolymer for Light Amplification and Organic Lasing. *Advanced Materials*, p.n/a–n/a. Available at: http://doi.wiley.com/10.1002/adma.201003797.

Kneubühl, F.K. & Sigrist, M.W., 2005. *Laser* 6, durchges. Aufl. 2005., Wiesbaden: Vieweg+Teubner Verlag.

Köhler, A. & Beljonne, D., 2004. The Singlet–Triplet Exchange Energy in Conjugated Polymers. *Advanced Functional Materials*, 14(1), pp.11–18. Available at:

http://onlinelibrary.wiley.com/doi/10.1002/adfm.200305032/abstract;jsessionid=F89ABA457EC6812CBB65EDC2C8D779F4.d02t02 [Accessed December 20, 2010].

Kokil, A., Yang, K. & Kumar, J., 2012. Techniques for characterization of charge carrier mobility in organic semiconductors. *Journal of Polymer Science Part B: Polymer Physics*, 50(15), pp.1130–1144. Available at: http://onlinelibrary.wiley.com/doi/10.1002/polb.23103/abstract [Accessed October 12, 2014].

Kreouzis, T. et al., 2006. Temperature and field dependence of hole mobility in poly(9,9-dioctylfluorene). *Physical Review B*, 73(23), p.235201. Available at: http://link.aps.org/doi/10.1103/PhysRevB.73.235201 [Accessed October 18, 2010].

Kröger, M. et al., 2009. P-type doping of organic wide band gap materials by transition metal oxides: A case-study on Molybdenum trioxide. *Organic Electronics*, 10(5), pp.932–938. Available at: http://www.sciencedirect.com/science/article/pii/S1566119909001104 [Accessed July 18, 2011].

Kuik, M. et al., 2011. The Effect of Ketone Defects on the Charge Transport and Charge Recombination in Polyfluorenes. *Advanced Functional Materials*, p.n/a. Available at: http://dx.doi.org/10.1002/adfm.201100374.

Lampert, M.A. & Mark, P., 1970. *Current injection in solids*, Academic Press.

Laquai, F. et al., 2008. Amplified Spontaneous Emission of Poly(ladder-type phenylene)s - The Influence of Photophysical Properties on ASE Thresholds. *Advanced Functional Materials*, 18(20), pp.3265–3275. Available at: http://onlinelibrary.wiley.com/doi/10.1002/adfm.200800299/abstract [Accessed October 19, 2010].

LeBlanc Jr, O.H., 1960. Hole and Electron Drift Mobilities in Anthracene. *The Journal of Chemical Physics*, 33(2), pp.626–626. Available at: http://scitation.aip.org/content/aip/journal/jcp/33/2/10.1063/1.1731216 [Accessed August 21, 2014].

Lee, A. et al., 2010. A comparative study on the optical properties of indenofluorene and indenopyrazine. *Computational Materials Science*, 49(4, Supplement 1), pp.S251–S255. Available at: http://www.sciencedirect.com/science/article/pii/S0927025609004297 [Accessed September 7, 2011].

Lee, J.-H. & Hwang, D.-H., 2003. Alkoxyphenyl-substituted polyfluorene: a stable blue-light-emitting polymer with good solution processability. *Chemical Communications*, (22), pp.2836–2837. Available at: http://pubs.rsc.org/en/content/articlelanding/2003/cc/b309006j [Accessed January 28, 2015].

Lee, T.-W., Kim, Y.-M. & Kim, Y.C., 2006. Effect of Thermal Annealing on the Charge Carrier Mobility in a Polymer Electroluminescent Device. *Molecular Crystals and*

Liquid Crystals, 462(1), pp.241–248. Available at: http://dx.doi.org/10.1080/15421400601013387 [Accessed July 7, 2015].

Lezama, I.G. & Morpurgo, A.F., 2013. Progress in organic single-crystal field-effect transistors. *MRS Bulletin*, 38(01), pp.51–56. Available at: http://journals.cambridge.org/article_S0883769412003119 [Accessed June 7, 2015].

Liang, J. et al., 2014. Aqueous solution-processed MoO3 thick films as hole injection and short-circuit barrier layer in large-area organic light-emitting devices. *Applied Physics Express*, 7(11), p.111601. Available at: http://iopscience.iop.org/1882-0786/7/11/111601 [Accessed May 11, 2015].

Li, H., Duan, L., Zhang, D., Dong, G., et al., 2014. Relationship between Mobilities from Time-of-Flight and Dark-Injection Space-Charge-Limited Current Measurements for Organic Semiconductors: A Monte Carlo Study. *The Journal of Physical Chemistry C*, 118(12), pp.6052–6058. Available at: http://dx.doi.org/10.1021/jp411948d [Accessed June 5, 2015].

Li, H., Duan, L., Zhang, D. & Qiu, Y., 2014. Transient space-charge-perturbed currents of N,N′-diphenyl-N,N′-bis(1-naphthyl)-1,1′-biphenyl-4,4′-diamine and N,N′-diphenyl-N,N′-bis(3-methylphenyl)-1,1′-biphenyl-4,4′-diamine in diode structures. *Applied Physics Letters*, 104(18), p.183301. Available at: http://scitation.aip.org/content/aip/journal/apl/104/18/10.1063/1.4875690 [Accessed June 19, 2015].

Li, J. et al., 2012. A stable solution-processed polymer semiconductor with record high-mobility for printed transistors. *Scientific Reports*, 2. Available at: http://www.nature.com/srep/2012/121018/srep00754/full/srep00754.html [Accessed June 7, 2015].

Limketkai, B.N. & Baldo, M.A., 2005. Charge injection into cathode-doped amorphous organic semiconductors. *Physical Review B*, 71(8), p.085207. Available at: http://link.aps.org/doi/10.1103/PhysRevB.71.085207 [Accessed June 6, 2015].

List, E. j. w. et al., 2002. The Effect of Keto Defect Sites on the Emission Properties of Polyfluorene-Type Materials. *Advanced Materials*, 14(5), pp.374–378. Available at: http://onlinelibrary.wiley.com/doi/10.1002/1521-4095(20020304)14:5<374::AID-ADMA374>3.0.CO;2-U/abstract [Accessed January 30, 2015].

Liu, C. et al., 2013. Critical Impact of Gate Dielectric Interfaces on the Contact Resistance of High-Performance Organic Field-Effect Transistors. *The Journal of Physical Chemistry C*, 117(23), pp.12337–12345. Available at: http://dx.doi.org/10.1021/jp4023844 [Accessed November 15, 2013].

Lu, L.-P. et al., 2012. Charge-Carrier Balance and Color Purity in Polyfluorene Polymer Blends for Blue Light-Emitting Diodes. *Advanced Functional Materials*, 22(1), pp.144–150. Available at: http://doi.wiley.com/10.1002/adfm.201101892 [Accessed March 14, 2015].

Lupton, J.M., 2002. On-chain defect emission in conjugated polymers – Comment on 'Exciton dissociation dynamics in a conjugated polymer containing aggregate states'

[A. Haugeneder, U. Lemmer, U. Scherf, Chem. Phys. Lett. 351 (2002) 354]. *Chemical Physics Letters*, 365(3–4), pp.366–368. Available at: http://www.sciencedirect.com/science/article/pii/S0009261402014483 [Accessed March 21, 2015].

Maiman, T.H., 1960. Stimulated Optical Radiation in Ruby. *Nature*, 187(4736), pp.493–494. Available at: http://www.nature.com/nature/journal/v187/n4736/abs/187493a0.html [Accessed June 1, 2015].

Many, A. & Rakavy, G., 1962. Theory of Transient Space-Charge-Limited Currents in Solids in the Presence of Trapping. *Physical Review*, 126(6), p.1980. Available at: http://link.aps.org/doi/10.1103/PhysRev.126.1980 [Accessed August 17, 2011].

Marsitzky, D. et al., 2001. Poly-2,8-(indenofluorene-co-anthracene)—A Colorfast Blue-Light-Emitting Random Copolymer. *Advanced Materials*, 13(14), pp.1096–1099. Available at: http://onlinelibrary.wiley.com/doi/10.1002/1521-4095(200107)13:14%3C1096::AID-ADMA1096%3E3.0.CO;2-I/abstract [Accessed March 17, 2015].

McCulloch, I. et al., 2006. Liquid-crystalline semiconducting polymers with high charge-carrier mobility. *Nat Mater*, 5(4), pp.328–333. Available at: http://dx.doi.org/10.1038/nmat1612 [Accessed October 6, 2010].

McGehee, M.D. et al., 1998. Amplified spontaneous emission from photopumped films of a conjugated polymer. *Physical Review B*, 58(11), pp.7035–7039. Available at: http://link.aps.org/doi/10.1103/PhysRevB.58.7035 [Accessed June 28, 2015].

de Mello, J.C., Wittmann, H.F. & Friend, R.H., 1997. An improved experimental determination of external photoluminescence quantum efficiency. *Advanced Materials*, 9(3), pp.230–232. Available at: http://onlinelibrary.wiley.com/doi/10.1002/adma.19970090308/abstract [Accessed January 22, 2011].

Meyer, J. & Kahn, A., 2011. Electronic structure of molybdenum-oxide films and associated charge injection mechanisms in organic devices. *Journal of Photonics for Energy*, 1(1), p.011109. Available at: http://link.aip.org/link/JPEOBV/v1/i1/p011109/s1&Agg=doi [Accessed August 4, 2011].

Miller, A. & Abrahams, E., 1960. Impurity Conduction at Low Concentrations. *Physical Review*, 120(3), p.745. Available at: http://link.aps.org/doi/10.1103/PhysRev.120.745 [Accessed November 6, 2010].

Miteva, T. et al., 2001. Improving the Performance of Polyfluorene-Based Organic Light-Emitting Diodes via End-capping. *Advanced Materials*, 13(8), pp.565–570. Available at: http://onlinelibrary.wiley.com/doi/10.1002/1521-4095(200104)13:8<565::AID-ADMA565>3.0.CO;2-W/abstract [Accessed December 18, 2014].

Moses, D., 1992. High quantum efficiency luminescence from a conducting polymer in solution: A novel polymer laser dye. *Applied Physics Letters*, 60(26), p.3215.

Available at: http://link.aip.org/link/APPLAB/v60/i26/p3215/s1&Agg=doi [Accessed December 4, 2010].

Mott, N.F. & Davis, E.A., 2012. *Electronic Processes in Non-Crystalline Materials*, Oxford Classic Texts in the Physical Sciences.

Muccini, M., Koopman, W. & Toffanin, S., 2012. The photonic perspective of organic light-emitting transistors. *Laser & Photonics Reviews*, 6(2), pp.258–275. Available at: http://onlinelibrary.wiley.com/doi/10.1002/lpor.201100008/abstract [Accessed June 20, 2012].

Murase, S. & Yang, Y., 2012. Solution Processed MoO3 Interfacial Layer for Organic Photovoltaics Prepared by a Facile Synthesis Method. *Advanced Materials*, 24(18), pp.2459–2462. Available at: http://onlinelibrary.wiley.com/doi/10.1002/adma.201104771/abstract [Accessed May 11, 2015].

Murgatroyd, P.N., 1970. Theory of space-charge-limited current enhanced by Frenkel effect. *Journal of Physics D: Applied Physics*, 3(2), pp.151–156. Available at: http://iopscience.iop.org/0022-3727/3/2/308 [Accessed May 21, 2012].

Nakagawa, T. et al., 2012. Electroluminescence based on thermally activated delayed fluorescence generated by a spirobifluorene donor–acceptor structure. *Chemical Communications*, 48(77), pp.9580–9582. Available at: http://pubs.rsc.org/en/content/articlelanding/2012/cc/c2cc31468a [Accessed July 19, 2013].

Nakanotani, H., Furukawa, T. & Adachi, C., 2015. Light Amplification in an Organic Solid-State Film with the Aid of Triplet-to-Singlet Upconversion. *Advanced Optical Materials*, p.n/a–n/a. Available at: http://onlinelibrary.wiley.com/doi/10.1002/adom.201500236/abstract [Accessed July 20, 2015].

Namdas, E.B. et al., 2009. Low Thresholds in Polymer Lasers on Conductive Substrates by Distributed Feedback Nanoimprinting: Progress Toward Electrically Pumped Plastic Lasers. *Advanced Materials*, 21(7), pp.799–802. Available at: http://onlinelibrary.wiley.com/doi/10.1002/adma.200802436/abstract [Accessed October 19, 2010].

Neher, D., 2001. Polyfluorene Homopolymers: Conjugated Liquid-Crystalline Polymers for Bright Blue Emission and Polarized Electroluminescence. *Macromolecular Rapid Communications*, 22(17), pp.1365–1385. Available at: http://onlinelibrary.wiley.com/doi/10.1002/1521-3927(20011101)22:17<1365::AID-MARC1365>3.0.CO;2-B/abstract [Accessed March 23, 2015].

Nguyen, T.-Q. et al., 2000. Control of Energy Transfer in Oriented Conjugated Polymer-Mesoporous Silica Composites. *Science*, 288(5466), pp.652–656. Available at: http://www.sciencemag.org/cgi/content/abstract/288/5466/652 [Accessed November 13, 2010].

Nicolai, H.T. et al., 2010. Space-charge-limited hole current in poly(9,9-dioctylfluorene) diodes. *Applied Physics Letters*, 96(17), p.172107. Available at: http://link.aip.org/link/APPLAB/v96/i17/p172107/s1&Agg=doi [Accessed June 14, 2011].

Parker, I.D., 1994. Carrier tunneling and device characteristics in polymer light-emitting diodes. *Journal of Applied Physics*, 75(3), pp.1656–1666. Available at: http://scitation.aip.org/content/aip/journal/jap/75/3/10.1063/1.356350 [Accessed June 12, 2015].

Park, Y.-I. et al., 2008. Synthesis and electroluminescence properties of novel deep blue emitting 6,12-dihydro-diindeno[1,2-b;1′,2′-e]pyrazine derivatives. *Chemical Communications*, (18), pp.2143–2145. Available at: http://pubs.rsc.org/en/content/articlelanding/2008/cc/b718873k [Accessed April 13, 2015].

Park, Y.-S., Kim, K.-H. & Kim, J.-J., 2013. Efficient triplet harvesting by fluorescent molecules through exciplexes for high efficiency organic light-emitting diodes. *APL: Organic Electronics and Photonics*, 6(4), pp.66–66. Available at: http://apl-oep.aip.org/resource/1/aploep/v6/i4/p66_s1 [Accessed May 30, 2013].

Pasveer, W.F. et al., 2005. Unified Description of Charge-Carrier Mobilities in Disordered Semiconducting Polymers. *Physical Review Letters*, 94(20), p.206601. Available at: http://link.aps.org/doi/10.1103/PhysRevLett.94.206601 [Accessed December 4, 2011].

Pattanasattayavong, P. et al., 2013. Electric field-induced hole transport in copper(I) thiocyanate (CuSCN) thin-films processed from solution at room temperature. *Chemical Communications*, 49(39), pp.4154–4156. Available at: http://pubs.rsc.org/en/content/articlelanding/2013/cc/c2cc37065d [Accessed May 11, 2015].

Peled, A. & Schein, L.B., 1988. Hole mobilities that decrease with increasing electric fields in a molecularly doped polymer. *Chemical Physics Letters*, 153(5), pp.422–424. Available at: http://www.sciencedirect.com/science/article/pii/0009261488852369 [Accessed February 8, 2015].

Poplavskyy, D., 2003. *HOLE INJECTION AND TRANSPORT IN ORGANIC SEMICONDUCTORS*. Imperial College London. Available at: https://spiral.imperial.ac.uk:8443/handle/10044/1/11261.

Poplavskyy, D. & Nelson, J., 2003. Nondispersive hole transport in amorphous films of methoxy-spirofluorene-arylamine organic compound. *Journal of Applied Physics*, 93(1), p.341. Available at: http://link.aip.org/link/JAPIAU/v93/i1/p341/s1&Agg=doi [Accessed November 27, 2010].

Poplavskyy, D., Nelson, J. & Bradley, D.D.C., 2003. Ohmic hole injection in poly(9,9-dioctylfluorene) polymer light-emitting diodes. *Applied Physics Letters*, 83(4), p.707. Available at: http://link.aip.org/link/APPLAB/v83/i4/p707/s1&Agg=doi [Accessed February 4, 2011].

Poplavskyy, D., Su, W. & So, F., 2005. Bipolar charge transport, injection, and trapping studies in a model green-emitting polyfluorene copolymer. *Journal of Applied Physics*, 98(1), p.014501. Available at: http://scitation.aip.org/content/aip/journal/jap/98/1/10.1063/1.1941482 [Accessed March 21, 2014].

Poriel, C. et al., 2007. Dispirofluorene–Indenofluorene Derivatives as New Building Blocks for Blue Organic Electroluminescent Devices and Electroactive Polymers. *Chemistry – A European Journal*, 13(36), pp.10055–10069. Available at: http://onlinelibrary.wiley.com/doi/10.1002/chem.200701036/abstract [Accessed March 17, 2015].

Prins, P. et al., 2007. Charge Transport along Coiled Conjugated Polymer Chains. *The Journal of Physical Chemistry C*, 111(29), pp.11104–11112. Available at: http://dx.doi.org/10.1021/jp071077d [Accessed October 31, 2010].

Prins, P. et al., 2006. Enhanced charge-carrier mobility in β -phase polyfluorene. *Physical Review B*, 74, p.113203. Available at: http://adsabs.harvard.edu/abs/2006PhRvB..74k3203P [Accessed November 14, 2010].

Rawcliffe, R., Bradley, D.D.C. & Campbell, A.J., 2003. Comparison between bulk and field effect mobility in polyfluorene copolymer field effect transistors. In *Proceedings of SPIE*. Organic Field Effect Transistors II. San Diego, CA, USA, pp. 25–34. Available at: http://spie.org/x648.html?product_id=506038 [Accessed August 3, 2011].

Redecker, M., Bradley, D.D.C., et al., 1999. High Mobility Hole Transport Fluorene-Triarylamine Copolymers. *Advanced Materials*, 11(3), pp.241–246. Available at: http://onlinelibrary.wiley.com/doi/10.1002/(SICI)1521-4095(199903)11:3%3C241::AID-ADMA241%3E3.0.CO;2-J/abstract;jsessionid=550AC1AF108A3BD8116DF05F72AE3E83.d01t02 [Accessed November 29, 2010].

Redecker, M., Bradley, D.D.C., et al., 1999. Mobility enhancement through homogeneous nematic alignment of a liquid-crystalline polyfluorene. *Applied Physics Letters*, 74(10), p.1400. Available at: http://link.aip.org/link/APPLAB/v74/i10/p1400/s1&Agg=doi [Accessed October 7, 2010].

Redecker, M. et al., 1998. Nondispersive hole transport in an electroluminescent polyfluorene. *Applied Physics Letters*, 73(11), p.1565. Available at: http://link.aip.org/link/APPLAB/v73/i11/p1565/s1&Agg=doi [Accessed October 14, 2010].

Reisch, H. et al., 1996. Poly(indenofluorene) (PIF), a Novel Low Band Gap Polyhydrocarbon. *Macromolecules*, 29(25), pp.8204–8210. Available at: http://dx.doi.org/10.1021/ma960877b [Accessed September 7, 2011].

Rose, A., 1955. Space-Charge-Limited Currents in Solids. *Physical Review*, 97(6), pp.1538–1544. Available at: http://link.aps.org/doi/10.1103/PhysRev.97.1538 [Accessed June 8, 2015].

Rothe, C. et al., 2004. Triplet exciton state and related phenomena in the beta -phase of poly(9,9-dioctyl)fluorene. *Physical Review B*, 70(19), p.195213. Available at: http://link.aps.org/doi/10.1103/PhysRevB.70.195213 [Accessed November 15, 2010].

Saeki, A., Fukumatsu, T. & Seki, S., 2011. Intramolecular Charge Carrier Mobility in Fluorene-Thiophene Copolymer Films Studied by Microwave Conductivity. *Macromolecules*, 44(9), pp.3416–3424. Available at: http://dx.doi.org/10.1021/ma2004844 [Accessed July 24, 2011].

Sainova, D. et al., 2000. Control of color and efficiency of light-emitting diodes based on polyfluorenes blended with hole-transporting molecules. *Applied Physics Letters*, 76(14), pp.1810–1812. Available at: http://scitation.aip.org/content/aip/journal/apl/76/14/10.1063/1.126173 [Accessed December 17, 2014].

Santos, L.F. et al., 2007. Transition from dispersive to non-dispersive transport of holes in poly(2-methoxy-5-(2′-ethyl-hexyloxy)-1,4-phenylene vinylene) light-emitting diodes investigated by time of flight measurements. *Thin Solid Films*, 515(20-21), pp.8034–8039. Available at: http://linkinghub.elsevier.com/retrieve/pii/S0040609007003604 [Accessed March 14, 2015].

Schein, L.B., 1992. Comparison of charge transport models in molecularly doped polymers. *Philosophical Magazine Part B*, 65(4), pp.795–810. Available at: http://dx.doi.org/10.1080/13642819208204920 [Accessed May 31, 2015].

Scher, H. & Montroll, E.W., 1975. Anomalous transit-time dispersion in amorphous solids. *Physical Review B*, 12(6), pp.2455–2477. Available at: http://link.aps.org/doi/10.1103/PhysRevB.12.2455 [Accessed March 11, 2013].

Setayesh, S., Marsitzky, D. & Müllen, K., 2000. Bridging the Gap between Polyfluorene and Ladder-Poly-p-phenylene: Synthesis and Characterization of Poly-2,8-indenofluorene. *Macromolecules*, 33(6), pp.2016–2020. Available at: http://dx.doi.org/10.1021/ma9914366 [Accessed March 17, 2015].

Shaklee, K.L., 1971. DIRECT DETERMINATION OF OPTICAL GAIN IN SEMICONDUCTOR CRYSTALS. *Applied Physics Letters*, 18, p.475. Available at: http://link.aip.org/link/?APL/18/475/1&Agg=doi [Accessed September 11, 2011].

Silva, C. et al., 2000. Excited-state absorption in luminescent conjugated polymer thin films: ultrafast studies of processable polyindenofluorene derivatives. *Chemical Physics Letters*, 319(5–6), pp.494–500. Available at: http://www.sciencedirect.com/science/article/pii/S0009261400001299 [Accessed March 17, 2015].

Simmons, J.G., 1963. Generalized Formula for the Electric Tunnel Effect between Similar Electrodes Separated by a Thin Insulating Film. *Journal of Applied Physics*, 34(6), pp.1793–1803. Available at: http://scitation.aip.org/content/aip/journal/jap/34/6/10.1063/1.1702682 [Accessed June 12, 2015].

Sirringhaus, H., Bird, M. & Zhao, N., 2010. Charge Transport Physics of Conjugated Polymer Field-Effect Transistors. *Advanced Materials*, 22(34), pp.3893–3898. Available at: http://onlinelibrary.wiley.com/doi/10.1002/adma.200902857/references [Accessed November 17, 2010].

Sonar, P. et al., 2007. A study of the effects metal residues in poly(9,9-dioctylfluorene) have on field-effect transistor device characteristics. *Synthetic Metals*, 157(21), pp.872–875. Available at: http://www.sciencedirect.com/science/article/pii/S0379677907002032 [Accessed September 3, 2011].

So, S.K., Choi, W.H. & Cheung, C.H., 2011. Thin-film transistor as a probe to study carrier transport in amorphous organic semiconductors. *Journal of Photonics for Energy*, 1(1), p.011011. Available at: http://link.aip.org/link/JPEOBV/v1/i1/p011011/s1&Agg=doi [Accessed August 4, 2011].

Svelto, O., 2010. *Principles of Lasers*, Boston, MA: Springer US. Available at: http://link.springer.com/10.1007/978-1-4419-1302-9 [Accessed October 11, 2015].

Tanase, C. et al., 2003. Unification of the Hole Transport in Polymeric Field-Effect Transistors and Light-Emitting Diodes. *Physical Review Letters*, 91(21), p.216601. Available at: http://link.aps.org/doi/10.1103/PhysRevLett.91.216601 [Accessed December 3, 2011].

Tessler, N. et al., 2009. Charge Transport in Disordered Organic Materials and Its Relevance to Thin-Film Devices: A Tutorial Review. *Advanced Materials*, 21(27), pp.2741–2761. Available at: http://onlinelibrary.wiley.com/doi/10.1002/adma.200803541/abstract [Accessed October 8, 2010].

Tessler, N., Denton, G.J. & Friend, R.H., 1996. Lasing from conjugated-polymer microcavities. *Nature*, 382(6593), pp.695–697. Available at: http://dx.doi.org/10.1038/382695a0 [Accessed November 13, 2010].

Tseng, H.-R. et al., 2014. High-Mobility Field-Effect Transistors Fabricated with Macroscopic Aligned Semiconducting Polymers. *Advanced Materials*, 26(19), pp.2993–2998. Available at: http://onlinelibrary.wiley.com/doi/10.1002/adma.201305084/abstract [Accessed April 22, 2015].

Tse, S.C., Tsang, S.W. & So, S.K., 2006. Polymeric conducting anode for small organic transporting molecules in dark injection experiments. *Journal of Applied Physics*, 100(6), p.063708. Available at: http://link.aip.org/link/JAPIAU/v100/i6/p063708/s1&Agg=doi [Accessed February 6, 2011].

Tsoi, W.C. et al., 2008. Observation of theβ-Phase in Two Short-Chain Oligofluorenes. *Advanced Functional Materials*, 18(4), pp.600–606. Available at: http://onlinelibrary.wiley.com/doi/10.1002/adfm.200700530/abstract [Accessed October 6, 2010].

Tsumura, A., Koezuka, H. & Ando, T., 1986. Macromolecular electronic device: Field-effect transistor with a polythiophene thin film. *Applied Physics Letters*, 49(18), p.1210. Available at: http://link.aip.org/link/APPLAB/v49/i18/p1210/s1&Agg=doi [Accessed December 4, 2010].

Turro, N.J., 1991. *Modern Molecular Photochemistry*, University Science Books.

Tyutnev, A. et al., 2012. Analysis of the carrier transport in molecularly doped polymers using the multiple trapping model with the Gaussian trap distribution. *Chemical Physics*, 404, pp.88–93. Available at: http://www.sciencedirect.com/science/article/pii/S0301010412001036 [Accessed October 17, 2014].

Uoyama, H. et al., 2012. Highly efficient organic light-emitting diodes from delayed fluorescence. *Nature*, 492(7428), pp.234–238. Available at: http://www.nature.com/nature/journal/v492/n7428/full/nature11687.html [Accessed June 3, 2013].

Veres, J. et al., 2004. Gate Insulators in Organic Field-Effect Transistors. *Chemistry of Materials*, 16(23), pp.4543–4555. Available at: http://dx.doi.org/10.1021/cm049598q [Accessed August 18, 2011].

Veres, J. et al., 2003. Low-k Insulators as the Choice of Dielectrics in Organic Field-Effect Transistors. *Advanced Functional Materials*, 13(3), pp.199–204. Available at: http://onlinelibrary.wiley.com/doi/10.1002/adfm.200390030/abstract [Accessed August 30, 2011].

Vissenberg, M.C.J.M. & Matters, M., 1998. Theory of the field-effect mobility in amorphous organic transistors. *Physical Review B*, 57(20), pp.12964–12967. Available at: http://link.aps.org/doi/10.1103/PhysRevB.57.12964 [Accessed May 25, 2015].

Wakayama, Y., Hayakawa, R. & Seo, H.-S., 2014. Recent progress in photoactive organic field-effect transistors. *Science and Technology of Advanced Materials*, 15(2), p.024202. Available at: http://iopscience.iop.org/1468-6996/15/2/024202 [Accessed May 27, 2015].

Wallace, J., 2009. *Carrier mobility in organic charge transport materials : methods of measurement, analysis, and modulation*. Available at: https://urresearch.rochester.edu/institutionalPublicationPublicView.action?institutionalItemId=10130 [Accessed October 18, 2014].

Wellinger, T., 2010. *Design and Characterisation of Blue Polymer Lasers*. Available at: http://spiral.imperial.ac.uk/handle/10044/1/6148.

Xia, Y. et al., 2012. Synthesis and characterization of alternating copolymers derived from indeno[1,2-b]fluorene for blue light-emitting diodes. *Journal of Applied Polymer Science*, 125(2), pp.1409–1417. Available at: http://onlinelibrary.wiley.com/doi/10.1002/app.35566/abstract [Accessed January 30, 2015].

Yamamoto, H. et al., 2004. Amplified spontaneous emission under optical pumping from an organic semiconductor laser structure equipped with transparent carrier injection electrodes. *Applied Physics Letters*, 84(8), pp.1401–1403. Available at: http://apl.aip.org/resource/1/applab/v84/i8/p1401_s1 [Accessed June 24, 2012].

Yang, L. et al., 2006. Theoretical investigations on the modulation of the polymer electronic and optical properties by introduction of phenoxazine. *Polymer*, 47(9), pp.3229–3239. Available at: http://www.sciencedirect.com/science/article/pii/S0032386106002576 [Accessed July 4, 2015].

Yap, B.K. et al., 2008. Simultaneous optimization of charge-carrier mobility and optical gain in semiconducting polymer films. *Nat Mater*, 7(5), pp.376–380. Available at: http://dx.doi.org/10.1038/nmat2165 [Accessed October 6, 2010].

Yasuda, T. et al., 2005. Carrier Transport Properties of Monodisperse Glassy-Nematic Oligofluorenes in Organic Field-Effect Transistors. *Chemistry of Materials*, 17(2), pp.264–268. Available at: http://dx.doi.org/10.1021/cm048532s [Accessed October 18, 2010].

Yokoyama, D., Moriwake, M. & Adachi, C., 2008. Spectrally narrow emissions at cutoff wavelength from edges of optically and electrically pumped anisotropic organic films. *Journal of Applied Physics*, 103(12), pp.123104–123104–13. Available at: http://jap.aip.org/resource/1/japiau/v103/i12/p123104_s1 [Accessed June 23, 2012].

You, J. et al., 2013. A polymer tandem solar cell with 10.6% power conversion efficiency. *Nature Communications*, 4, p.1446. Available at: http://www.nature.com/ncomms/journal/v4/n2/full/ncomms2411.html [Accessed July 9, 2015].

Yuanfu, P. et al., 2007. Synthesis and characterization of a novel electroluminescent polymer based on phenoxazine and fluorene derivatives. *Reactive and Functional Polymers*, 67(11), pp.1211–1217. Available at: http://www.sciencedirect.com/science/article/pii/S1381514807001526 [Accessed July 4, 2015].

Zaumseil, J. et al., 2008. Quantum efficiency of ambipolar light-emitting polymer field-effect transistors. *Journal of Applied Physics*, 103(6), pp.064517–064517–10. Available at: http://jap.aip.org/resource/1/japiau/v103/i6/p064517_s1 [Accessed June 21, 2012].

Zaumseil, J. & Sirringhaus, H., 2007. Electron and Ambipolar Transport in Organic Field-Effect Transistors. *Chemical Reviews*, 107(4), pp.1296–1323. Available at: http://dx.doi.org/10.1021/cr0501543 [Accessed October 18, 2010].

Zhang, M. et al., 2007. Field-Effect Transistors Based on a Benzothiadiazole−Cyclopentadithiophene Copolymer. *Journal of the American Chemical Society*, 129(12), pp.3472–3473. Available at: http://dx.doi.org/10.1021/ja0683537 [Accessed December 13, 2014].

Zhang, Q. et al., 2012. Design of Efficient Thermally Activated Delayed Fluorescence Materials for Pure Blue Organic Light Emitting Diodes. *Journal of the American*

Chemical Society, 134(36), pp.14706–14709. Available at: http://dx.doi.org/10.1021/ja306538w [Accessed May 30, 2013].

Zhang, W. et al., 2010. Indacenodithiophene Semiconducting Polymers for High-Performance, Air-Stable Transistors. *Journal of the American Chemical Society*, 132(33), pp.11437–11439. Available at: http://dx.doi.org/10.1021/ja1049324 [Accessed December 13, 2014].

Zhu, Y., Babel, A. & Jenekhe, S.A., 2005. Phenoxazine-Based Conjugated Polymers: A New Class of Organic Semiconductors for Field-Effect Transistors. *Macromolecules*, 38(19), pp.7983–7991. Available at: http://dx.doi.org/10.1021/ma0510993 [Accessed July 4, 2015].

APPENDIX

Table A. 1 Details of batches of the Indenofluorene-Fluorene copolymers in this thesis showing their molecular weights (in kg/mol) and polydispersity indices.

S50F3:50IF8	**S50F8:50IF8**	**S50F8:50IF1,4**
	SA181	**SA185**
	MW: ~110k, PDI ~3.5	MW: ~105k, PDI ~3.5
SA283	**SA284**	**SA279**
High MW: 63.9k, PDI: 1.75	High MW: 195.6k, PDI: 3.23	MW: 131k, PDI: 2.48
Low MW: 23.8k, PDI: 1.93	Low MW: 76.1k, PDI: 3.52	
SA314	**SA315**	**BS176**
High MW: 74.5k, PDI: 2.01	High MW: 63.7k, PDI: 1.88	High MW: 120 kg/mol, PDI=1.7
Low MW: 42.5k, PDI: 2.06	Low MW: 49.8k, PDI: 1.90	Low MW: 59 kg/mol, PDI=1.8

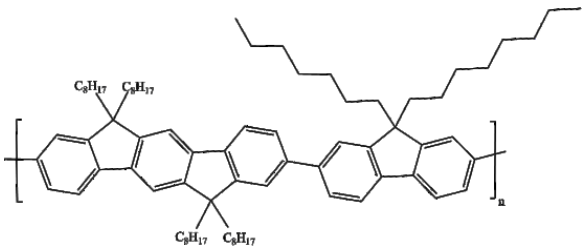

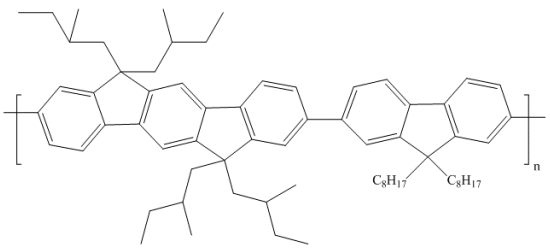

Table A. 2 Table of PLQE and hole mobility values for different batches of the S50F8:50IF1,4 copolymer.

	PLQE	**Hole Mobility (cm^2/Vs)**	**Square-root Electric Field $(V/cm)^{1/2}$ for hole mobility**
BS176-01-f1, first. batch	30.9%	5.36×10^{-3} 6.11×10^{-3}	576 751
BS176-01-f2, first. batch	37.9	5.35×10^{-3} 6.09×10^{-3}	169 280
BS176-01-f1-ii, re-precipitated	24.9%		
BS176-01-f2-ii, re-precipitated	31.5%	5.17×10^{-3} 5.36×10^{-3}	246 389
BS176-01, from GPC	28.4%	6.57×10^{-3}	341
Annealed 70°C		7.07×10^{-3}	341
120°C		1.02×10^{-2}	341
170°C		1.02×10^{-2}	341
BS176-02, newly synthesised batch	40.3%		341
70°C		6.88×10^{-3}	341
120°C		1.01×10^{-2}	341
170°C		9.68×10^{-3}	341